ION CONDUCTION MECHANISMS IN FAST ION CONDUCTING OXIDE GLASSES FOR RECHARGEABLE BATTERIES

THIEU DUC THO

NATIONAL UNIVERSITY OF SINGAPORE

2011

ION CONDUCTION MECHANISMS IN FAST ION CONDUCTING OXIDE GLASSES FOR RECHARGEABLE BATTERIES

BY

THIEU DUC THO

(*B. Eng. (Hons), Ho Chi Minh City Univ. of Tech.*)

A THESIS SUBMITTED

FOR THE DEGREE OF DOCTOR OF PHILOSOPHY

DEPARTMENT OF MATERIALS SCIENCE & ENGINEERING

NATIONAL UNIVERSITY OF SINGAPORE

2011

...To my beloved parents

...and grandparents

Acknowledgements

To complete this thesis, it required enormous effort and determination. However, successful result would not have been achieved if there was no help from some very special people.

First of all, I would like to express my utmost gratitude to my Professor, Dr. Stefan Adams, who has consistently given me invaluable advice and knowledge. Working with him during the whole course of this thesis was an enjoyable and inspiring journey.

Secondly, I am sincerely thankful to Dr. Rayavarapu Prasada Rao for his constructive direction and supervision. He led me to the right path of research. I am indebted to him for the on-time completion of this thesis.

Thirdly, I am very grateful to Advanced Batteries Laboratory team of Prof. B. V. R. Chowdari, especially Dr. M. V. Reddy, who always allowed me to access the lab facilities without hesitation.

I also take this opportunity to appreciate the helps from Prof. John Wang's group, who allowed me to use the heating furnace, and from Prof. Li Yi's group for letting me operate the Differential Scanning Calorimetry (DSC).

For my other group mates, Zhou YongKai, Li Kangle and some other friends whose names may not be mentioned here, thank you guys for the useful discussions and friendship.

Finally, from the bottom of my heart I would like to express my deepest affection to my mother (Tran Thi Mai), my father (Thieu Van Phuoc), my departed grandparents, and my special friend Ms Rachel Nguyen for their endless encouragement and support.

Table of Contents

Summary

Fast ion conducting glasses have been widely studied for technologically important applications such as solid electrolytes in electrochemical devices, especially all-solid-state rechargeable batteries. A detailed understanding of ion conduction mechanisms in these glasses is one of the key features for the development of solid electrolytes. However, such knowledge has yet to be thoroughly understood.

This thesis therefore deals with investigations of ion conduction mechanisms in fast ion conducting oxide glasses. Influence of network modifier (in lithium silicates) and halide dopant concentration (in lithium halide-doped phosphates), as well as of mixed glass former effect (in lithium borophosphates) on the structure, physical properties and Li^+ ion transport pathways is clarified using the combination of experimental and simulation techniques.

Chapter 1 introduces the field of solid state ionics, fast ion conductors or solid electrolytes. Classification of solid electrolytes and fundamentals of ion

transport in solids are mentioned. Literature on fast ion conducting glasses and especially a detailed survey on the oxide glasses under study are thoroughly reviewed. Theoretical models of ion conduction mechanisms in inorganic glasses are also discussed. Finally, motivation and objectives of the present study are stated.

Chapter 2 describes techniques used in this project, which include both experimental and simulation techniques. Various experimental techniques are employed to characterize structural and physical properties of the investigated glasses. Computer simulation techniques include Molecular Dynamics (MD) simulation and Bond Valence (BV) analysis.

Results of the present work are presented and discussed in Chapters 3, 4, 5. Chapter 3 and 4 investigate ion transport pathways in lithium silicate $xLi_2O - (1 - x)SiO_2$ and halide-doped phosphate $yLiX - (1 - y)(0.6Li_2O - 0.4P_2O_5)$ (where X = Cl, Br) glasses respectively. The results show clear evidence that density and connectivity of the percolating pathways for the motion of Li^+ ions rise (i) with the increase of the network modifier (Li_2O) content, or (ii) with the increase of halide LiX dopant concentration or with the doping by more polarisable halide X^- ions. BV analysis of the Li^+ transport pathways in the MD-simulated glass structures shows the same variation of the scaled pathway volume fraction with the experimental conductivity as previously observed from pathway models based on reverse Monte Carlo modelling. Further studies on structural variations, physical properties (glass transition temperature, ionic conductivity, etc) and ac conductivity have been conducted in these glassy systems.

Research on the formation, atomic structure, transport properties of lithium borophosphate glasses $0.45Li_2O - (0.55 - x)P_2O_5 - xB_2O_3$ ($0 \leq x \leq 0.55$) is given in Chapter 5. Correlation between structure and conductivity were scrutinized using FT-IR, Raman, XPS and impedance spectroscopy, as well as MD simulation and Bond Valence (BV) approach. Two proposed models to predict the variations of structure and ionic conductivity (σ_{dc}) with B_2O_3 addition are in very good agreement with experimental results. Structural studies from BV analysis qualitatively harmonize with those from Raman and XPS spectra. Analyses of impedance data in the borophosphate glasses indicate the existence of a universal ionic relaxation process in these materials. Similar to lithium silicates and halide-doped phosphates, in the borophosphate glasses the increase in the volume fraction of Li^+ ion transport pathways with the B_2O_3 content is in line with the decrease of activation energy (E_a) and the increase of σ_{dc}.

Conclusions from the present study and proposals for future work are presented in Chapter 6.

List of Tables

List of Figures

List of Publications / Conferences

Publications / Conference Papers

1. **Thieu Duc Tho**, R. Prasada Rao, Stefan Adams, "Glass formation, structure and ion transport in $0.45Li_2O - (0.55 - x)P_2O_5 - xB_2O_3$ glasses", ***Phys. Chem. Glasses: Eur. J. Glass Sci. Technol. B*** *52 (2011) 91-100.*

2. **Thieu Duc Tho**, R. Prasada Rao, Stefan Adams, "Structure and ion transport pathways in $0.45Li_2O - (0.55 - x)P_2O_5 - xB_2O_3$ glasses", ***Mater. Res. Soc. Symp. Proc.*** *1266 (2010) 1266-CC06-03*.

3. **Thieu Duc Tho**, R. Prasada Rao, Stefan Adams, "AC conductivity and mobile transport pathways in $0.45Li_2O - (0.55 - x)P_2O_5 - xB_2O_3$ glasses", ***ECS Transactions*** *28 (2010) 57-68*.

4. **Thieu Duc Tho**, R. Prasada Rao, Stefan Adams, "Mobile ion transport pathways in $(LiBr)_x [(Li_2O)_{0.6}(P_2O_5)_{0.4}]_{(1-x)}$ glasses", ***Journal of Solid State Electrochemistry*** *14 (2010) 1781-1786*.

5. **Thieu Duc Tho**, R. Prasada Rao, Stefan Adams, "AC conductivity studies and relaxation behaviour in $(LiX)_y [(Li_2O)_{0.6}(P_2O_5)0.4]_{(1-y)}$ glasses", ***Journal of Solid State Electrochemistry*** *14 (2010) 1863-1867.*

6. R. Prasada Rao, **Thieu Duc Tho**, Stefan Adams, "Ion transport pathways in molecular dynamics simulated lithium silicate glasses", ***Solid State Ionics*** *181 (2010) 1-6.*

7. R. Prasada Rao, **Thieu Duc Tho**, Stefan Adams, "Lithium ion transport pathways in xLiCl – (1 – x)($0.6Li_2O$ – $0.4P_2O_5$) glasses", ***Journal of Power Sources*** *189 (2009) 385-390*.

Oral presentations at International Conferences

1. **Thieu Duc Tho**, R. Prasada Rao, Stefan Adams, "Mobile ion transport pathways in $(LiBr)_x$ $[(Li_2O)_{0.6}(P_2O_5)_{0.4}]_{(1\ -\ x)}$ glasses", ***International Conference on Materials for Advanced Technologies (ICMAT)***, ***Singapore***, *28 June – 3 July 2009*.

2. **Thieu Duc Tho**, R. Prasada Rao, Stefan Adams, "Structure and ion transport pathways in $0.45Li_2O$ – $(0.55 - x)P_2O_5$ – xB_2O_3 glasses", ***MRS Spring Meeting, San Francisco, U.S.A.,*** *5 – 9 April 2010*.

3. **Thieu Duc Tho**, R. Prasada Rao, Stefan Adams, "AC conductivity and mobile transport pathways in $0.45Li_2O$ – $(0.55 - x)P_2O_5$ – xB_2O_3 glasses", ***217th ECS Meeting, Vancouver, Canada,*** *25 – 30 April 2010.*

Posters at International Conferences

1. **Thieu Duc Tho**, R. Prasada Rao, Stefan Adams, "Glass formation, ac conductivity and relaxation behaviour in $0.45Li_2O$ – $(0.55 - x)P_2O_5$ – xB_2O_3 glasses", ***4th Asian Conference on Electrochemical Power Sources, Taipei, Taiwan,*** *8 – 12 November 2009*. **(Winning the Best Poster Award (1st Prize))**

2. **Thieu Duc Tho**, R. Prasada Rao, Stefan Adams, "AC conductivity studies and relaxation behaviour in y(LiX) – (1 – y)[$0.60Li_2O$ – $0.40P_2O_5$] glasses", ***International Conference on Materials for Advanced Technologies (ICMAT)***, ***Singapore***, *28 June – 3 July 2009.*

3. **Thieu Duc Tho**, R. Prasada Rao, Stefan Adams, "Effect of intermediate range structure on conductivity in mixed glass former system $0.45Li_2O$ – $(0.55 - x)P_2O_5$ – xB_2O_3", ***4th MRS-S Conference on Advanced Materials, Singapore,*** *17 – 19 March 2010.*

Chapter 1

Introduction

1.1. Solid state ionics

1.1.1. Definitions and background

This research project focuses on studying the ion conduction mechanisms in fast ion conducting oxide glasses for the application in solid-state rechargeable batteries. Ionic conductors are materials, which can conduct electricity via the migration of highly mobile ions (cations and/or anions). While in general both liquids and solids could be ionic conductors, the objective of this project concentrates on solid state ionic conductors. Materials, which exhibit high ionic conductivity (10^{-4} to 1 S/cm) and negligible electronic conductivity at temperatures below their melting point, are termed as fast ion conductors (FIC) or solid electrolytes. Solid state ionic conductors differ from electronic conductors, e.g. metals and semiconductors, where the mobile charge carriers are electrons. Solids which exhibit both electronic and ionic conductivity in significant proportions are referred to as mixed conductors. In a battery mixed conductors cannot be used as solid electrolytes, as the electronic conduction leads to short circuiting. Instead, mixed conductors are important electrode materials for both battery (such as Li_xCoO_2, $Li_xMn_2O_4$, $LiFePO_4$ etc) and fuel cell (yttrium–zirconium–titanium oxides (YZT), $La_{0.4}Sr_{0.6}Ti_{1-x}Mn_xO_3$, $Sr_2Mg_{1-x}Mn_xMoO_{6-\delta}$ etc) applications.

Ionic conduction in solid state materials was first discovered in 1833 by Michael Faraday, who detected high ionic conductivity in Ag_2S and PbF_2 at elevated temperatures [1, 2]. However, it was not until 1914 Tubandt and Lorentz showed the first direct proof of Ag^+ ion transport in AgI and other

silver halides (in 1932), where a variation in mass of Ag electrodes separated by AgX (where X = I, Br, Cl) was observed, when an electric current was passed [3, 4]. In addition to Ag^+ conductors, Li^+ ion conducting materials were also discovered. Li_2SO_4 is one of the fast Li^+ conductors found as early as 1921 by Benrath and Drekopf [5]. Since then, many studies have focused on solid state ionics and a wide variety of solid materials with fast ionic conduction (or solid electrolytes) were identified subsequently.

Solid electrolytes find numerous applications in solid-state electrochemical devices, such as solid state batteries (where Li^+ ion-based solid electrolytes are mostly used), fuel cells, gas sensors, super-capacitors, electro-chromic displays, etc. [6 – 9]. In terms of battery applications, solid electrolytes range from LiI in Li-I_2 batteries for powering heart pacemakers, LIPON ($Li_{2y+3z-5}PO_yN_z$) or Li-B-O-N systems in rechargeable thin film batteries used for integrated circuits or smart cards, up to sodium β-alumina ($NaAl_{11}O_{17}$) in sodium-sulfur batteries for large scale electric energy storage. The first generation of Lithium ion rechargeable battery for portable devices was introduced by Sony in 1990, which used $LiPF_6$/alkyl carbonate as electrolyte, $LiCoO_2$ as cathode and graphite as anode.

Solid electrolytes offer many potential advantages when compared to liquid electrolytes, i.e. absence of leakage, avoidance of safety concerns due to flammable organic liquids or the possibility of short-circuiting by Li whisker formation, long shelf life, rugged construction, possibility of easy miniaturization (no need for mechanical separators between electrodes), wide temperature range of operation, better thermal durability, large electrochemical

stability window [9, 10]. Solid electrolytes can occur in crystalline, polymeric materials, glass and glass ceramics.

1.1.2. Crystalline solid electrolytes

Ion transport in crystalline solid electrolytes has been thoroughly investigated. Two types of defects accountable for ion transport in the crystals are Schottky and Frenkel defects. In Schottky defects, cation and anion leave their lattice site to create vacancies; while in Frenkel defects a lattice ion (cation or anion) moves to an interstitial position and leaves behind a vacancy. The mobility of one ion species in a stable crystal structure requires point defects that typically move via one of three elementary jump mechanisms: (i) vacancy mechanism: a particle at the regular site hops into a vacancy and leaves behind a vacancy (see Figure 1.1(a)); and two mechanisms involving interstitials: (ii) direct interstitial mechanism: an interstitial defect jumps directly into another interstitial site (see Figure 1.1(b)); (iii) interstitialcy or indirect interstitial mechanism: the interstitial defect pushes a particle at the regular site into an adjacent empty interstitial site (see Figure 1.1(c)) [11, 12]. For crystalline solid electrolytes more complex correlated motions have been found, such as paddle-wheel mechanism and percolation-type mechanism in alkali sulfate based materials [13 – 15]. There has been a long-standing debate on the ion transport mechanism of alkali sulfates. In the paddle-wheel mechanism which was proposed by Lundén [13], the strong enhancement of cation mobility at high temperatures is explained by the coupled rotational motion of translationally static sulfate ions and the Li^+ cation. The strong coupling between sulfate and Li^+ ion motion is attributed to insufficient space

for free rotation. On the other hand, in the percolation-type mechanism, Secco [14] assumed that the increase of lattice constants upon doping of guest ions, such as WO_4^{2-} or SiO_4^{4-} into sulfate (SO_4^{2-}) lattice, leads to an expansion of the "transport volume" for the cations and thus decreases the activation energy of the ion transport. It is now accepted that the high Li^+ ion conduction of alkali sulfates is linked to the relatively facile rotational motion of SO_4^{2-} tetrahedra via the paddle-wheel mechanism.

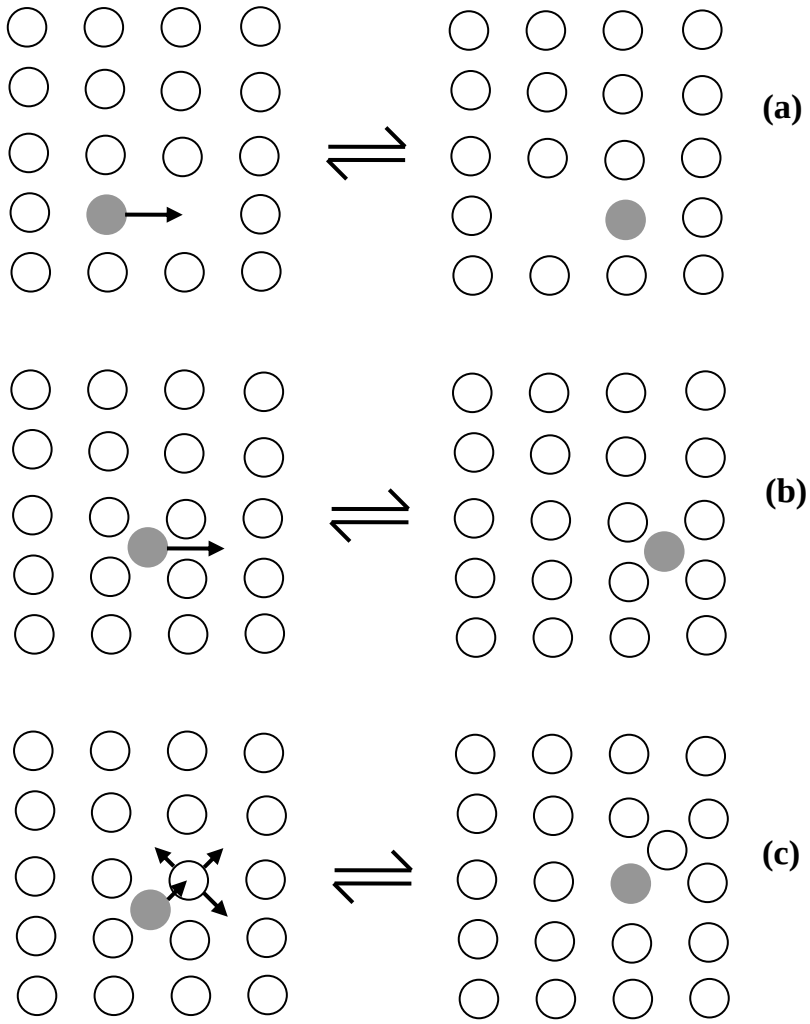

Figure 1.1. Elementary jump mechanisms in ionic crystal: (a) vacancy mechanism, (b) direct interstitial mechanism, (c) interstitialcy (indirect interstitial) mechanism. Reproduced from Ref. [12].

Selected examples of ionic conductivities for the crystalline solid electrolytes are given in Table 1.1. The best-known example of fast ion conductors is α – AgI, which can exhibit high ionic conductivity (σ_{dc}) up to 1 $S.cm^{-1}$ at 147^0C and an activation energy of around 0.05eV [16]. Another well-known ionic conductor is $RbAg_4I_5$, which has one of the highest values of σ_{dc} = 0.27 $S.cm^{-1}$ at room temperature and an activation energy around 0.10eV [17]. In the lithium thiophosphate systems, the crystalline phase $Li_7P_3S_{11}$ formed by heating the $70Li_2S - 30P_2S_5$ glass at 360^0C for 1h was reported to have the high σ_{dc} of 4.1 x 10^{-3} $S.cm^{-1}$ at room temperature and activation energy of 14 kJ/mol ($\approx$ 0.15eV) [18, 19]. Most recently, the $Li_7P_3S_{11}$ analogous phase, $Li_7P_3S_{11-z}$, was produced by thermal treatment at 360^0C for $70Li_2S - 29P_2S_5 - 1P_2S_3$ glass and possesses a higher room temperature σ_{dc} of 5.4 x 10^{-3} $S.cm^{-1}$ when compared to $Li_7P_3S_{11}$ phase without P_2S_3 doping [20]. Despite the high ionic conductivity, the crystalline materials have several disadvantages. Many FIC materials cannot be obtained as single crystals and their anisotropic nature possesses considerable difficulty in interfacing with electrodes in solid state batteries.

Table 1.1. Ionic conductivity (σ_{dc}) and activation energy (E_a) of some crystalline solid electrolytes.

Compound	σ_{dc} (S.cm^{-1})	E_a (eV)	Reference
α – AgI	1.0 (at 147^{0}C)	0.05	[16]
$RbAg_4I_5$	0.27 (at 25^{0}C)	0.10	[17]
Ag_8TiS_6	1×10^{-2} (at 23^{0}C)	0.18	[21]
$AgPbAsS_3$	6.2×10^{-6} (at 100^{0}C)	0.62	[22]
$Ag_8I_4V_2O_7$	8.6×10^{-4} (at 142^{0}C)	0.24	[23]
β – $NaAl_{11}O_{17}$	1.0 x 10^{-1} (at 200^{0}C)	0.16	[9, 16]
Li_4SiO_4	2×10^{-5} (at 300^{0}C)	0.87	[24]
Li_3N	4.0 x 10^{-4} (at 25^{0}C)	0.30	[25]
$Li_{0.34}La_{0.51}TiO_{2.94}$ (LLTO)	1.0 x 10^{-3} (at 27^{0}C)	0.40	[26, 27]
$Li_{0.25}La_{0.66}Ti_{0.75}Al_{0.25}O_3$ (LLTO)	7.7 x 10^{-5} (at 27^{0}C)	0.35	[28]
$Li_{1.3}Al_{0.3}Ti_{1.7}(PO_4)_3$ (NASICON)	3 x 10^{-3} (at 25^{0}C)	0.30 – 0.50	[29 – 31]
$Li_{1.5}Al_{0.5}Ge_{1.5}(PO_4)_3$ (NASICON)	4.2 x 10^{-3} (at 27^{0}C)	0.30 – 0.61	[32 – 34]
$Li_{14}ZnGe_4O_{16}$ (LISICON)	1 x 10^{-6} (at 25^{0}C)	0.40 – 0.60	[35, 36]
$Li_{3.4}Si_{0.4}P_{0.6}S_4$ (Thio−LISICON)	6.4 x 10^{-4} (at 27^{0}C)	0.29	[37, 38]
$Li_{3.25}Ge_{0.25}P_{0.75}S_4$ (Thio−LISICON)	2.2 x 10^{-3} (at 25^{0}C)	0.21	[39]
$Li_{2.2}Zn_{0.1}Zr_{0.9}S_3$ (Thio−LISICON)	1.2 x 10^{-4} (at 30^{0}C)	_	[40]
$Li_6La_2BaTa_2O_{12}$ (Garnet)	4 x 10^{-5} (at 22^{0}C)	0.40	[41, 42]
$Li_{5.5}La_3Nb_{1.75}In_{0.25}O_{12}$ (Garnet)	1.8 x 10^{-4} (at 50^{0}C)	0.51	[43]
$LiPO_3$	2.5 x 10^{-8} (at 280^{0}C)	1.40	[44]
$Li_7P_3S_{11}$	4.1 x 10^{-3} (at 25^{0}C)	0.15	[18, 19]
$Li_7P_3S_{11-z}$	5.4 x 10^{-3} (at 25^{0}C)	_	[20]

1.1.3. Polymeric solid electrolytes

Polymer electrolytes, notably polyethylene oxide (PEO) based salts exhibit moderate ionic conductivity at room temperature [45 – 61], which limits their applicability at lower temperatures, e.g. in car batteries for non-tropical regions. The mechanical strength of the polymer films is poor and as a result creeps under pressure while fabricating devices. In addition, thermal stability of the polymer film is not the expected level to buffer the temperature variation while in operation. Table 1.2 shows ionic conductivities for some selected polymeric solid electrolytes.

Table 1.2. Ionic conductivity (σ_{dc}) and activation energy (E_a) of some polymeric solid electrolytes.

Compound	σ_{dc} (S.cm^{-1})	E_a (eV)	Reference
$(PEO)_{20}LiClO_4$	1.0 x 10^{-7} (at 25^0C)	_	[45, 47 – 50]
$(PEO)_{20}$LiBOB	1.6 x 10^{-4} (at 50^0C)	_	[51]
$(PEO)_9$LiTf	6.7 x 10^{-7} (at 25^0C)	_	[52]
$(PEO)_9$LiTf + 15 wt.% Al_2O_3	7.8 x 10^{-6} (at 25^0C)	_	[52]
$(PEO)_9$LiTf + 15 wt.% Al_2O_3 + 50 wt.% [75% EC:25% PC]	1.2 x 10^{-4} (at 25^0C)	_	[52]
$(PEO)_{8.5}$LiBETI	1.8 x 10^{-4} (at 25^0C)	0.36 – 1.15	[53 – 55]
$(PEO)_{10}$ LiTFSI	3.2 x 10^{-5} (at 25^0C)	0.84	[56 – 61]
$(PEO)_6LiAsF_6$	9.0 x 10^{-8} (at 28^0C)	0.57	[46]
$(PEO)_6(LiAsF_6)_{0.97}(LiTFSI)_{0.03}$	9.0 x 10^{-7} (at 28^0C)	0.73	[46]
$(PEO)_{16}(SN)_{10}$LiBETI	3.2 x 10^{-4} (at 20^0C)	0.74	[55]
PEO:$LiClO_4$:PAA/PMAA/$Li_{0.3}$	9.9 x 10^{-4} (at 20^0C)	_	[50]

1.1.4. Glassy and glass-ceramic solid electrolytes

Glassy materials have many advantages over their crystalline counterparts from a technological point of view. Amorphous solids are generally easy to prepare; homogeneous thin films can be produced in different shapes and sizes for device applications. A bulk glass can readily be formed from the melt by relatively slow quenching procedures and near the glass transition temperature the material remains workable over a range of temperatures. Furthermore, the physical properties of bulk glasses are isotropic and homogeneous. The absence of microstructural defects, such as grain boundaries and dislocations, is important for their mechanical behaviors and mechanical engineering applications. Also, amorphous phases can often be formed in mixed-component systems over wide ranges of compositions. This allows their properties to be varied continuously simply by varying the composition. Figure 1.2 shows a comparison of the temperature-dependent conductivities of various crystalline and amorphous solid electrolytes. More details on glassy solid electrolytes will be discussed in Sections 1.3 and 1.4.

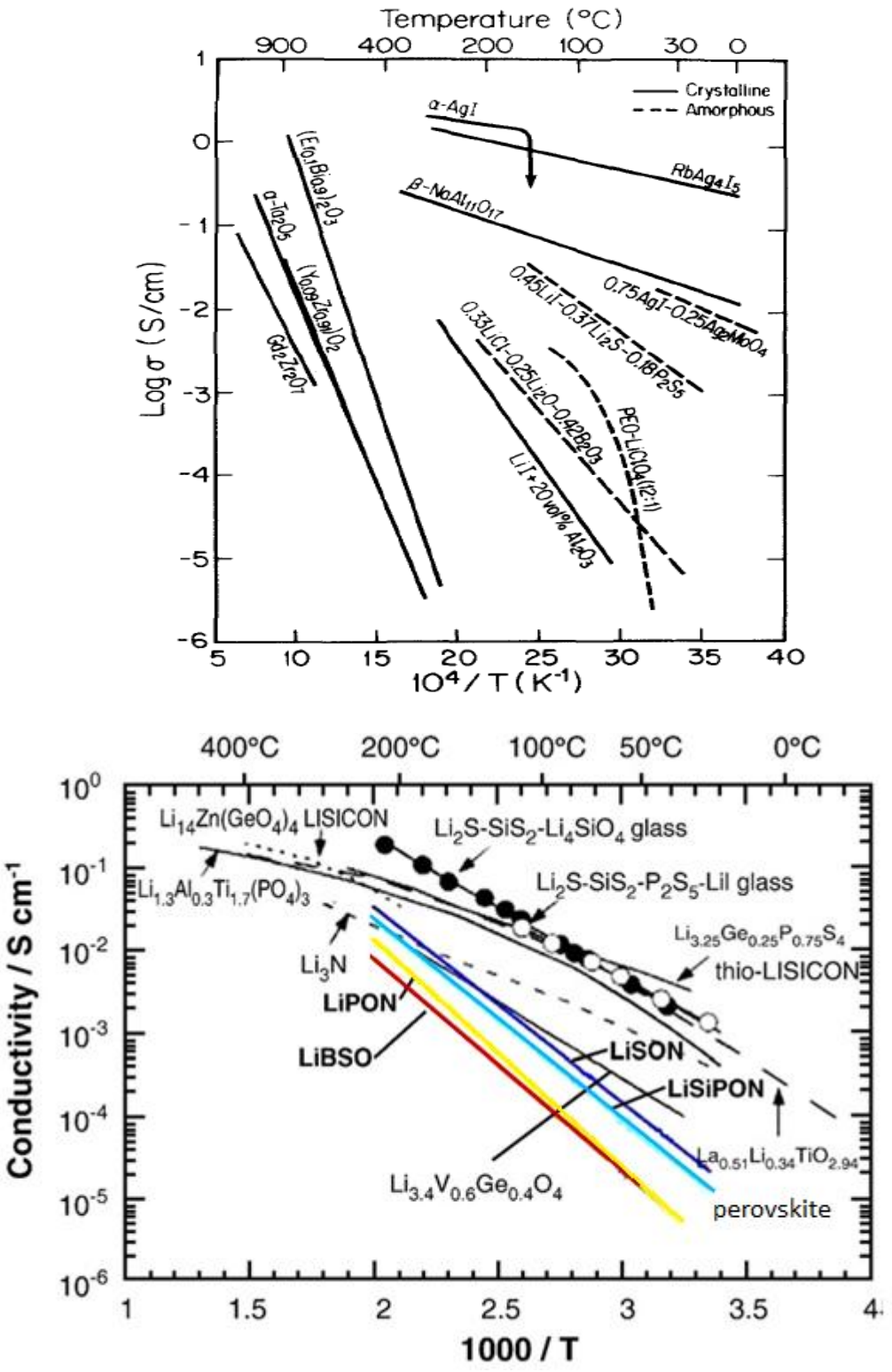

Figure 1.2. A comparison of the temperature-dependent conductivities of various crystalline and amorphous solid electrolytes. Reproduced from [10, 16]. LiPON: Lithium Phosphorous OxiNitride; LiBSO: $LiBO_2$ – Li_2SO_4; LiSON: Lithium Sulfur OxyNitride; LiSiPON: Nitrogen-incorporated Lithium SilicoPhosphate (Li_3PO_4 – Li_2SiO_3); LISICON: LIthium SuperIonic CONductor; thio-LISICON: Sulfide-based LIthium SuperIonic CONductor.

Glass ceramics are made through the heat treatment of bulk glasses above the glass transition temperature (T_g), close to the crystallization temperature (T_c) to bring about nucleation and to partially crystallize the material. Ionic conductivity of glass-ceramics can be lower or higher than that of their glassy counterparts depending on the system and the extent of the crystallization [19, 62 – 69]. The large glass-crystal interface area during the initial phase of crystallization often leads to enhanced conductivity, while for nearly complete crystallization conductivity is in most cases lower than in the glassy state [62, 63]. Figure 1.3 illustrates the variation of ionic conductivities with temperatures for the typical sulfide-based glass and glass-ceramics $Li_2S - P_2S_5$, for example.

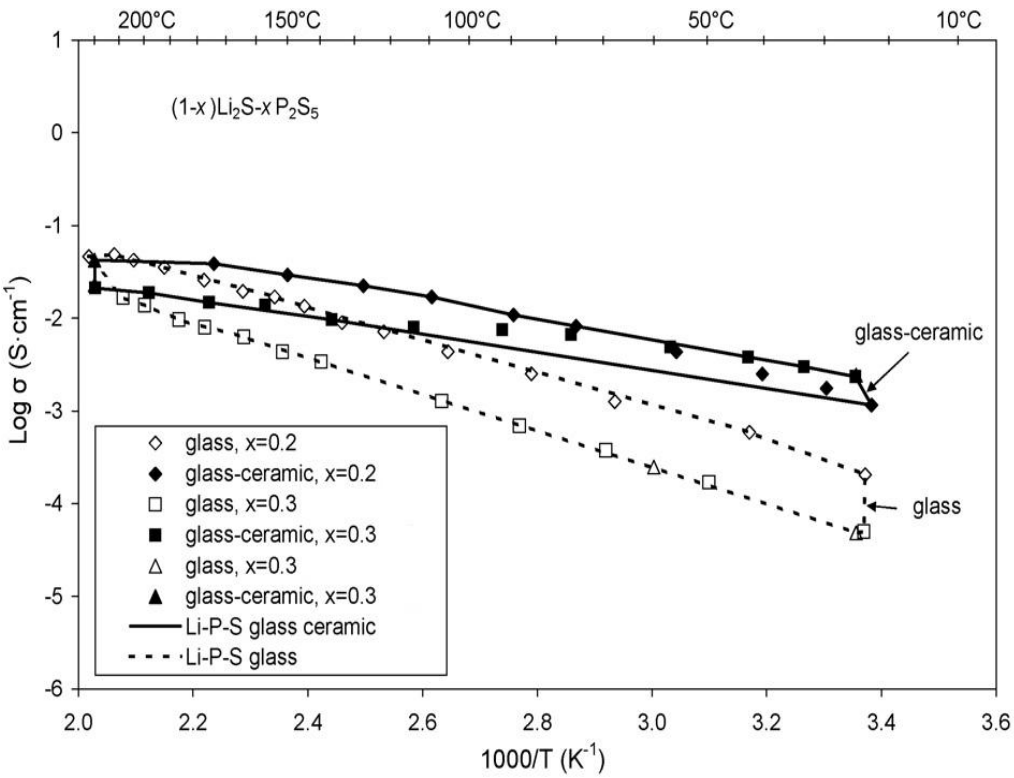

Figure 1.3. Variation of ionic conductivities with temperatures for $(1 – x)Li_2S – xP_2S_5$ glass and glass-ceramics. Reproduced from Ref. [70], data from [66 – 68].

1.2. Fundamentals of ion transport in solids

1.2.1. Ion diffusion

In general, there are two elementary types of ion diffusion: chemical diffusion (diffusion due to the gradient of concentration) and self diffusion (diffusion without the gradient of concentration).

In theory, total potential energy (U_i) of species i is composed of chemical potential (μ_i) and Coulombic interaction energy ($z_i q\Phi$) as follows:

$$U_i = \mu_i + z_i q\Phi \tag{1.1}$$

and also

$$\mu_i = \mu_0 + k_B T \ln c_i \tag{1.2}$$

where z_i and c_i (cm^{-3}) are the charge number and concentration of species i, respectively; q is the elementary amount of charge ($q = e = 1.6 \times 10^{-19}$ J), Φ is the electrostatic potential at a given position, k_B is Boltzmann constant ($k_B = 1.38 \times 10^{-23}$ $J.K^{-1}$) and T is temperature in Kelvin (K).

The force F_i acting on the species i is then calculated by:

$$F_i = -\nabla U_i = -\frac{\partial U_i}{\partial x} = -\left(\frac{\partial \mu_i}{\partial x} + z_i q \frac{\partial \Phi}{\partial x}\right) \tag{1.3}$$

The diffusive flux J_i of species i is subsequently estimated by:

$$J_i = c_i \beta_i F_i = -c_i \beta_i \left(\frac{\partial \mu_i}{\partial x} + z_i q \frac{\partial \Phi}{\partial x}\right) \tag{1.4}$$

where β_i is the mobility of species i, and *x* is the position.

1.2.1.1. Chemical diffusion

Since the diffusion is brought about by concentration gradient (∇c_i), the latter part ($z_i q \frac{\partial \Phi}{\partial x}$) in Equation (1.4) equals to 0. Thus, Equation (1.4) can be rewritten as:

$$J_i = -c_i \beta_i \frac{\partial \mu_i}{\partial x} = -\beta_i k_B T \frac{\partial c_i}{\partial x} \tag{1.5}$$

Besides, the diffusive flux J_i can also be described by:

$$J_i = -D_i \nabla c_i = -D_i \frac{\partial c_i}{\partial x} \tag{1.6}$$

which is known as Fick's law, where D_i the diffusion coefficient (cm^2/s). Comparing Equations (1.5) and (1.6), we have the following Einstein relation:

$$D_i = \beta_i k_B T \tag{1.7}$$

1.2.1.2. Self diffusion

Due to the diffusion without concentration gradient ($\frac{\partial \mu_i}{\partial x} = 0$), Equation (1.4) is now as follows:

$$J_i = -c_i \beta_i z_i q \frac{\partial \Phi}{\partial x} \tag{1.8}$$

In addition, the diffusive flux J_i is related to current density (I_i) of species i by the following equation:

$$I_i = z_i q J_i \tag{1.9}$$

According to Ohm's law, the current density I_i is linked to conductivity (σ_i) of species i by the relation:

$$I_i = -\sigma_i \frac{\partial \Phi}{\partial x} \tag{1.10}$$

Combining both Equation (1.9) and (1.10), we deduce that

$$J_i = -\frac{\sigma_i}{z_i q} \frac{\partial \Phi}{\partial x} \tag{1.11}$$

Again, by comparing Equation (1.8) and (1.11), we can conclude that

$$\beta_i = \frac{\sigma_i}{c_i (z_i q)^2} \tag{1.12}$$

By substituting Equation (1.12) into Equation (1.7), we finally obtain the relation between self-diffusion coefficient D_i and partial conductivity σ_i as follows:

$$D_i = \frac{\sigma_i k_B T}{c_i (z_i q)^2} \qquad \text{or} \qquad \sigma_i = \frac{c_i (z_i q)^2 D_i}{k_B T} \tag{1.13}$$

which is known as Nernst-Einstein relation. This equation is used in this thesis to estimate the ionic conductivities from the Molecular Dynamics simulations and then compare to those determined from impedance spectroscopy. It is noteworthy that the above derivation (Equation (1.13)) assumed that the mobile species move independently. For a correlated diffusion mechanism, the Haven ratio H_R, which is the ratio between tracer diffusion coefficient D_t and conductivity diffusion coefficient D_i, i.e. $H_R = D_t/D_i$, should be introduced. Hence the Nernst-Einstein relation between the diffusion coefficient and conductivity should be rewritten as:

$$D_t = \frac{H_R \sigma_i k_B T}{c_i (z_i q)^2} \qquad \text{or} \qquad \sigma_i = \frac{c_i (z_i q)^2 D_t}{H_R k_B T} \tag{1.14}$$

If the diffusion is caused by vacancy mechanism, H_R then equals the

correlation factor f, which ranges from 0 to 1 (f = 1 means no correlation; f = 0 indicates highly correlated diffusion).

1.2.2. Thermodynamics of ion conduction

If the conduction is predominantly due to a single ionic species, the electrical conductivity can be expressed by the following equation:

$$\sigma = c(zq)\beta \tag{1.15}$$

Here, c is the concentration of mobile ions with the charge (zq), and β represents the mobility of this ion type.

For an intrinsic ionic conductor, the mobile defect concentration c is given by:

$$c = c_0 \exp\left[-\frac{\Delta G_c}{k_B T}\right] \tag{1.16}$$

where c_0 is the concentration of investigated ions (i.e., (c/c_0) is the fraction of ions which are mobile), ΔG_c represents the change of free energy due to the formation of a single mobile defect.

In addition, the mobility (β) of the mobile species is described by:

$$\beta = \alpha a^2 (zq)\nu / k_B T \tag{1.17}$$

and also

$$\nu = \nu_0 \exp\left[-\frac{\Delta G_M}{k_B T}\right] \tag{1.18}$$

where α is the geometrical factor, a and ν are the distance and frequency of ion jump, respectively; ν_0 is the vibrational frequency of ions around the

equilibrium positions, and ΔG_M is the free energy barrier for ion migration.

Furthermore, it is well-known that:

$$\Delta G = \Delta H - T\Delta S \tag{1.19}$$

By substituting Equations (1.16), (1.17), (1.18) and (1.19) into Equation (1.15), the ionic conductivity (σ) can be rewritten as:

$$\sigma = \frac{\alpha a^2 (zq)^2 c_0 \nu_0}{k_B T} \exp\left[\frac{\Delta S_c + \Delta S_M}{k_B}\right] \exp\left[-\frac{\Delta H_c + \Delta H_M}{k_B T}\right] \tag{1.20}$$

Since in fast ion conductors (FIC) the degree of disorder in the mobile ion sublattice and the mobile ion concentration are expected to be high without the need of thermal generation, the additional formation of defects and ion migration will not significantly enhance the disorder of system. As a result, (ΔS_C + ΔS_M) may be considered to have a negligible value, and hence $\exp\left[\frac{\Delta S_c + \Delta S_M}{k_B}\right]$ nearly equals to 1. Then we can let

$$\sigma_0 = \frac{\alpha a^2 (zq)^2 c_0 \nu_0}{k_B} \exp\left[\frac{\Delta S_c + \Delta S_M}{k_B}\right] \approx \frac{\alpha a^2 (zq)^2 c_0 \nu_0}{k_B}$$

and also

$$E_a = \Delta H_c + \Delta H_M \approx \Delta H_M$$

where E_a is the activation energy.

The final simplified form of Equation (1.20) is as follows:

$$\sigma T = \sigma_0 \exp\left[-\frac{E_a}{k_B T}\right] \tag{1.21}$$

which is known as Arrhenius-type behavior of temperature-dependent ionic conductivity. As shown later in Chapters 4 and 5, the ionic conductivities of

glasses under study in this thesis follow this Arrhenius-type behavior.

The activation energy (E_a) for ion conduction can be determined by taking the natural logarithm of Equation (1.21) as follows:

$$\ln(\sigma T) = \ln\sigma_0 - \frac{E_a}{k_B}\frac{1}{T} \tag{1.22}$$

Consequently, the values of E_a are directly calculated from the slope (i.e., $-E_a/k_B$) of Arrhenius plot ln(σT) vs (1/T). The Arrhenius plots of some ionic conductors can be seen in Figures 1.2 and 1.3.

1.3. Fast ion conducting glasses

1.3.1. Definition of glass

According to J. Zarzycki (1991), "glass is a non-crystalline material that exhibits a glass transition, which is the temperature or range of temperatures that define the region where the properties of the material change continuously from those of a solid to those of a liquid." In other words, glasses are amorphous (and thus necessarily metastable) solids that exhibit a glass transition.

1.3.2. Silver-based glasses

Silver ion conducting glasses with various glass formers exhibit high ionic conductivity (σ_{dc}), as given in Table 1.3. Most of these glasses contain the dopant salt AgI. When iodide is introduced in glasses containing the modifier Ag_2O along with any glass former, the resulting glasses show high σ_{dc} even at

room temperature, though the room temperature phase of AgI is not a good ionic conductor. σ_{dc} increases with increasing AgI content. It should however be mentioned that the earlier hypothesis of AgI-like regions in the FIC glasses could not be confirmed, as typically nearly all silver ions have a mixed halide oxide environment [71, 72]. For equal AgX (X = Cl, Br, I) concentration, the conductivity decreases along with the anion polarisability in the order $\sigma_{AgI} > \sigma_{AgBr} > \sigma_{AgCl}$ and for the same silver halide, the variation in conductivity is larger when the ionic conductivity of the parent glass is low. The highest conductivities in glasses are reached when all anions exhibit high polarisability, such as in AgI doped silver sulfide glasses [73], where it seems that the fraction of mobile Ag^+ ion reaches a saturation level.

An analogous increase of conductivity with the halide dopant concentration and polarisability is observed in lithium-based glasses (see below). Maximum ionic conductivity at room temperature reaches 4×10^{-2} S/cm in AgI-doped Ag-based glasses and 2×10^{-3} S/cm in Li-based glasses with LiI addition. Despite the highest ionic conductivity, silver-based glasses have several disadvantages. They are expensive, exhibit low decomposition potential and batteries containing silver-based glassy electrolytes have low gravimetric energy density due to the greater mass of silver ion when compared to lithium ion.

1.3.3. Lithium-based glasses

Since lithium is light and highly electro-positive, lithium-based glasses find potential applications in high energy density solid state batteries even though their ionic conductivity (σ_{dc}) is not as high as that of silver-based

glasses. Ionic conductivities of some selected lithium oxide glasses are given in Table 1.3. Lithium ionic conductivity is observed in glasses with glass formers such as SiO_2, P_2O_5, V_2O_5, B_2O_3, SeO_2 and TeO_2. In all these glasses, σ_{dc} increases with increasing content of the network modifier Li_2O. σ_{dc} is further increased when more than one glass former is used, which is known as the mixed former effect or mixed anion effect [74 – 81]. Doping of these glasses with lithium halides such as LiCl, LiBr, LiI [82 – 85] typically enhances σ_{dc} by several orders of magnitude as exemplified in Table 1.3. In contrast σ_{dc} shows a pronounced minimum when two different mobile ions (such as two different alkali ions) are introduced into the oxide glasses, which is known as the mixed alkali effect or mixed mobile ion effect [86 – 92].

Lithium ion conducting sulfide glasses show an increase in σ_{dc} of more than three orders of magnitude when compared to the oxide glasses of analogous composition, as shown in Table 1.3, which is due to the higher polarisability of sulfur, though at the cost of decreasing stability of the glasses. SiS_2, P_2S_5, B_2S_3 and GeS_2 are the commonly used glass formers in Li_2S based glasses. When two glass formers such as P_2S_5 and P_2S_3, GeS_2 and P_2S_5, or SiS_2 and GeS_2 are incorporated in the same glass, σ_{dc} is shown to increase [68, 81, 93]. Besides, the addition of small amounts (up to 5 mol%) of lithium ortho-oxysalts Li_xMO_y (where M = Si (Li_4SiO_4), P (Li_3PO_4), Ge (Li_4GeO_4), B (Li_3BO_3), and Al (Li_3AlO_3)) to the sulfide-based glasses, which forms oxysulfide glassy systems, leads to a slight rise in σ_{dc} [94, 95]. Similar to the oxide glasses, doping of LiCl, LiBr or LiI into the sulfide-based glasses has been explored to further enhance σ_{dc}. The system of Li_2S – SiS_2 – P_2S_5 – LiI [96] glass exhibits the highest σ_{dc} among the lithium glasses so far reported.

Table 1.3. Ionic conductivity (σ_{dc}) and activation energy (E_a) of some ion conducting glasses.

Glasses	σ_{dc} (S.cm^{-1})	E_a (eV)	Reference
$75AgI - 25Ag_2SeO_4$	2.2×10^{-2} (at 25^0C)	0.20	[97 – 99]
$85AgI - 15Ag_4P_2O_7$	1.8×10^{-2} (at 25^0C)	0.23	[100]
$80AgI - 20Ag_2WO_4$	1.5×10^{-1} (at 25^0C)	0.16	[101]
$60AgI - 27Ag_2O - 13V_2O_5$	4.0×10^{-3} (at 25^0C)	0.21	[62, 63]
$50Ag_2O – 25B_2O_3 – 25P_2O_5$	2.9×10^{-4} (at 90^0C)	0.37	[102]
$0.4AgI – 0.6[0.525Ag_2S + 0.475B_2S_3:SiS_2]$	4.0×10^{-2} (at 25^0C)	0.25	[73]
$10Li_2O – 90SiO_2$	7.0×10^{-8} (at 150^0C)	0.71	[103]
$50Li_2O – 50SiO_2$	4.0×10^{-5} (at 150^0C)	0.58	[103]
$50Li_2O – 50P_2O_5$	2.4×10^{-9} (at 25^0C)	0.72	[104]
$62.5Li_2O – 37.5P_2O_5$	1.6×10^{-7} (at 25^0C)	0.58	[104]
$33.5Li_2O – 33.5P_2O_5 – 33LiI$	1.0×10^{-6} (at 25^0C)	0.51	[82]
$33.5Li_2O – 33.5P_2O_5 – 33LiBr$	3.2×10^{-7} (at 25^0C)	0.54	[82]
$35Li_2O – 35P_2O_5 – 30LiCl$	1.0×10^{-7} (at 25^0C)	0.60	[82]
$42.5Li_2O – 57.5B_2O_3$	7.1×10^{-8} (at 25^0C)	0.76	[78]
$34Li_2O – 61B_2O_3 – 5LiCl$	1.0×10^{-3} (at 300^0C)	0.60	[105]
$50Li_2O – 30P_2O_5 – 20B_2O_3$	1.8×10^{-5} (at 110^0C)	0.47	[79, 80]
$Li_{2.88}PO_{3.73}N_{0.14}$ (LiPON)	3.3×10^{-6} (at 25^0C)	0.45 – 0.55	[106 – 109]
$Li_{0.29}S_{0.28}O_{0.35}N_{0.09}$ (LiSON)	2.0×10^{-5} (at 25^0C)	0.47	[110]
$70Li_2S – 30P_2S_5$	9.2×10^{-5} (at 25^0C)	0.40	[111, 1112]
$75Li_2S – 25P_2S_5$	1.8×10^{-4} (at 25^0C)	0.30	[113, 114]
$75Li_2S – 20P_2S_5 – 5P_2S_3$	6.2×10^{-4} (at 25^0C)	0.36	[68, 115]
$37Li_2S – 18P_2S_5 – 45LiI$	1.0×10^{-3} (at 25^0C)	0.31	[116]

$67Li_2S - 10P_2S_5 - 23B_2S_3$	1.4×10^{-4} (at 25^0C)	0.40	[112]
$47Li_2S - 14SiS_2 - 9P_2S_5 - 30LiI$	2.1×10^{-3} (at 25^0C)	0.34	[96]
$57Li_2S - 38SiS_2 - 5Li_4SiO_4$	1.0×10^{-3} (at 25^0C)	0.34	[94, 117, 118]
$66.5Li_2S - 28.5B_2S_3 - 5Li_4SiO_4$	3.5×10^{-4} (at 25^0C)	0.34	[95]

Various methods of preparation of glasses have been reported in literature. The classical technique used to prepare glass is the melt quenching method. Recently, many groups have started using a new technology for the preparation of amorphous materials, namely, mechanical milling. In analogy to mechanical alloying of metals it is supposed that the amorphization via mechanical milling involves solid state inter-diffusion processes rather than local melt quenching [119 – 121]. Amorphous solid electrolytes in the system $Li_2S - P_2S_5$ were prepared from a mixture of crystalline Li_2S and P_2S_5 using a mechanical milling technique at room temperature by Tatsumisago et al. [113, 114]. Most recently, the sulfide-based glass-ceramics produced from heat treatment of corresponding mechanically milled glasses show the highest σ_{dc} of 5.4×10^{-3} S/cm at room temperature for the compositions of $70Li_2S - 29P_2S_5 - 1P_2S_3$ and $68.6Li_2S - 29.4P_2S_5 - 2GeS_2$ [20, 122]. The transport number of lithium ions in these mechanically prepared samples is close to one.

1.4. Review of oxide glasses under study

Research described in this thesis concentrates on studying the ion conduction mechanisms in technically relevant oxide-based glassy solid electrolytes, in particular lithium silicate, phosphate and borophosphate glasses. Therefore, a detailed review of the state of knowledge on these glass systems will be provided in the following sections.

1.4.1. Alkali silicate glasses

SiO_2 is the technically most important network former. Amorphous silica (SiO_2) is generally made up of SiO_4 tetrahedra linked by sharing an oxygen atom at a corner to form silicate network [123]. The disorder in the silicate network can be described by continuous random network (CRN) model, in which Si – O – Si angle lies between about 120^0 and 180^0, and there is very small variation in the bond length of Si – O (1.62 Å), O – O (2.65 Å) and O – Si – O tetrahedral angle (109.47^0) [124 – 127].

The introduction of alkali oxides, which are considered as network modifiers, into the silicate network breaks up the continuous random network by converting the bridging oxygens to non-bridging oxygens while maintaining silica SiO_4 tetrahedra. An oxygen atom covalently bonded to two silicon atoms in such a network is commonly referred to as bridging oxygen (BO), while non-bridging oxygen (NBO) is an oxygen atom forming a covalent bond to only one Si atom, leaving an ionic charge that is conventionally taken to be -1. This charge then gives rise to an ionic bond to modifier cations. The number of NBOs increases with increasing alkali oxide

content. The structure of alkali silicate glasses may be illustrated by the modified random network (MRN) model, as proposed by Greaves [128]. In this model, the local aggregation of network formers into network regions and of network modifiers into inter-network regions, which depend on the modifier content, may exhibit different morphologies, but should be characterized by a high concentration of NBOs.

As the NBOs are each coordinated by one Si atom, a given SiO_4 tetrahedron may have from 0 to 4 NBOs. These different SiO_4 tetrahedral units are normally described as Q_n, where Q symbolizes the TO_4 tetrahedron (T = Si, P, etc), and the index n represents the number of BOs linked to the central T atom and for the case of T = Si may also take values of 0 to 4. Consequently the number of NBOs per Si is then 4 – n. The simplest theoretical model to predict the concentration of Q_n units in alkali silicate glasses, $xM_2O - (1 - x)SiO_2$, is the idealized lever (binary) rule [127, 129, 130] as follows:

$$2Q_n + M_2O \rightarrow 2Q_{n-1} \tag{1.23}$$

In this model, it was assumed that only two types of Q_n units will exist in a particular glass, i.e. for $0 \leq x \leq 0.33$ there is only a progressive formation of Q_3 from Q_4 units, for $0.33 \leq x \leq 0.50$ the formation of Q_2 from Q_3 units, then for $0.50 \leq x \leq 0.60$ the formation of Q_1 from Q_2 units, and finally for $0.60 \leq x \leq 0.67$ the only formation of Q_0 from Q_1 units, without any formation of other Q_n units.

Various experimental techniques have been employed to investigate the network structure of the silicate glasses, including neutron and X-ray

diffraction, EXAFS, IR, XPS, Raman and NMR spectroscopy. Among these techniques, IR [131 – 134], Raman [135 – 137] and NMR [129, 130, 138 – 141] are often used to determine the distribution of Q_n units present in a glass. Different numbers of NBOs on a Q_n unit alter the vibration frequencies by modifying the network connectivity, and also alter the chemical shift of ^{29}Si NMR signal by modifying the charge density around Si atom. In alkali silicate glasses, the proportions of Q_n units with higher NBO/Si ratios were reported to increase with the increase of alkali oxide content [129, 130, 135 – 141]. Figure 1.4 shows the variations of Q_n units of lithium silicate glassy systems for example [130]. Since more than two types of Q_n units are found to be present in many of the glasses, the more precise description of distributions of Q_n units at each particular composition was proposed to include the equilibria:

$$2Q_n \rightleftharpoons Q_{n-1} + Q_{n+1} \qquad (1.24)$$

where n = 1, 2, 3.

Furthermore, Raman and NMR results also revealed that at the same alkali oxide concentration, the smaller alkali ions systematically favor considerable disproportionation, i.e. prefer to proceeds to the right-hand side of Equation (1.24) [129, 130, 135 – 141]. Based on this disproportionation reaction, Gurman [142] proposed a thermodynamic model named bond ordering model to predict the relative number of different Q_n units present in the glass. By providing an appropriate value of bond ordering energy for each alkali silicate system (e.g. $\Delta E/KT_g = 1.5 \pm 0.5$ for Li, 2.5 ± 0.5 for Na), the results from this model were reported to agree well with Raman and NMR data.

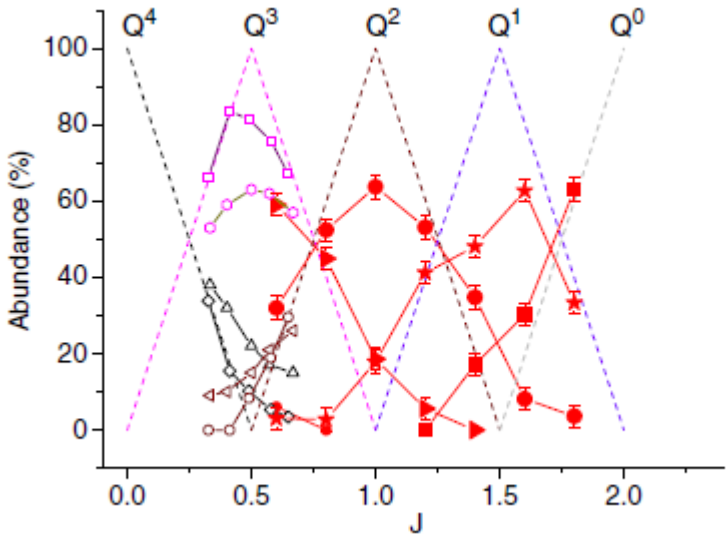

Figure 1.4. Fractions of Q_n units (index n refers to number of bridging oxygens (BOs) around Si atom) in $xLi_2O - (1 - x)SiO_2$ glasses as a function of J, where J is the molar ratio of Li_2O to SiO_2. Data were obtained from deconvolution of NMR spectra. Dotted lines are the idealized lever rule. Reproduced from Ref. [130].

The structural modifications due to the distributions of Q_n units control the physical and chemical properties of the silicate glasses. The addition of alkali oxide to silicate glasses reduces the viscosity of the melt and the glass transition temperature [127]. The densities, refractive indices, and thermal expansion coefficients of the glasses increase with the increase of alkali oxide content [127, 143]. Ionic conductivity of the alkali silicate glasses, which is due to the diffusion of alkali ions, increases and the activation energy logarithmically decreases with rising alkali oxide concentration [103, 144, 145]. The variations in these properties are essentially due to the creation of non-bridging oxygen, which leads to the reduction in the network connectivity of the glasses, i.e. the structure becomes more open.

Many efforts have been made to understand the relationships of composition-structure-properties, and underlying mechanisms of ion transport

in alkali silicate glasses. Computer based simulation techniques, e.g. Molecular Dynamics (MD) simulations, are the useful tools to correlate structure and properties, as well as to discover the ion dynamics by using various interatomic potential forms [146 – 151]. Cormack and Cao [149] have demonstrated the ion dynamics in sodium silicate glasses by MD and have observed a few sequences of jumps between selected sites. They interpreted the resulting dynamics as the motion of "vacancies" and suggested that the identification of all sites in the glass would be useful for a deeper understanding of the mechanism. The presence of conduction pathways (within the inter-network regions) has been proposed to understand the dynamics of mobile ions in alkali silicate and other ionic conducting glasses. The existence of conduction channels (formed by series of sites that are visited by many different ions) was reported for $Li_2O - SiO_2$ glasses by Lammert and Heuer [150], who conclude that the mobility of ions in single sites is found to depend strongly on the number of bridging oxygens in the coordinated shell. In addition, Sen and Mukerji [151] also proposed potential energy landscape of Li^+ mobile ions in lithium silicate glasses containing 3.3 – 15 mol% Li_2O to explain the logarithmic decrease of the activation energy for dc conductivity with increasing mobile ion concentration.

1.4.2. Alkali phosphate glasses

1.4.2.1. Vitreous phosphate glasses (v-P_2O_5)

Like vitreous silicates, the structure of vitreous phosphates is also based on a tetrahedral building block in which each P is surrounded by four O atoms. Since phosphorus is a pentavalent ion (P^{5+}), three of these oxygens are

bridging oxygens (BO), which link neighboring tetrahedra via P – O – P bonds to form three-connected network, and the fourth oxygen is a double-bonded non-bridging oxygen, P = O (NBO). Therefore, the basic units of v-P_2O_5 are Q_3 tetrahedra, as confirmed from neutron diffraction studies by Hoppe et al. and Suzuya et al. [152, 153] (using a Q_n notation as explained in 1.4.1). The structures of the three polymorphs of crystalline P_4O_{10}, i.e. one hexagonal and two orthorhombic forms, are also based on cross-linked Q_3 tetrahedra [154 – 156]. In v-P_2O_5, the bond length of the fourth bond P = O (1.42 – 1.43 Å) is significantly shorter than that of the P – BO bonds (1.58 Å), a consequence of its enhanced π-bond character [152, 153]. In general, the P = O bond lengths are shorter and the P – BO bond lengths are longer in the v-P_2O_5 than those in the different polymorphs of crystalline P_4O_{10} [153, 157 – 159]. In crystalline P_4O_{10}, the average O – P – O bond angle is 109.02^0, which is close to the tetrahedral angle of 109.47^0 [158]. Besides, the P – O – P bond angle lies between 123.01^0 and 135.72^0 in the crystalline P_4O_{10}, when compared to $137^0 \pm 3^0$ in the v-P_2O_5 [160].

In general, phosphate glasses have lower glass transition temperature, melting temperature, and higher thermal expansion coefficients, ionic conductivity than those found for silicate glasses [161, 162]. These properties make them useful candidates for fast ion conducting materials and other important applications such as laser hosts, glass-to-metal seals and bio-compatible materials [163].

1.4.2.2. Binary alkali phosphate glasses

The introduction of network modifying alkali oxides (M_2O) to v-P_2O_5 results in the creation of non-bridging oxygens (NBOs) at the expense of bridging oxygens (BOs). The resulting depolymerisation of the phosphate network with the addition of alkali oxide, M_2O, can be described by the pseudo-reaction model (cf. Equation (1.23)) [164], where the index n in Q_n (where n = 0, 1, 2, 3) is the number of bridging oxygens per PO_4 tetrahedron, consequently the number of non-bridging oxygens per PO_4 tetrahedron will be 4 – n. Figure 1.5 shows the possible phosphate structures existing in the phosphate glasses.

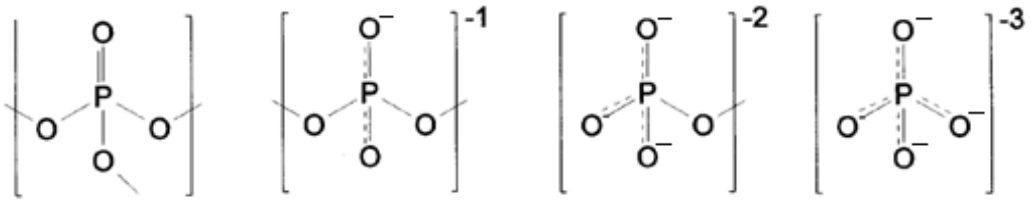

Figure 1.5. Phosphate tetrahedral units that can exist in the phosphate glasses. Reproduced from [165].

Equation (1.23) assumes that there are only two different Q_n units present at each composition of alkali phosphate glasses. In the ultraphosphate region of $xM_2O - (1 - x)P_2O_5$ glasses (where $0 \leq x \leq 0.50$) thereby only Q_3 and Q_2 units will be present, and more Q_2 units should be created at the expense of Q_3 units with the addition of M_2O up to x = 0.50.The distributions of Q_2 and Q_3 units can be predicted as follows [164]:

$$f(Q_2) = \frac{x}{1 - x} \tag{1.25a}$$

$$f(Q_3) = \frac{1 - 2x}{1 - x} \tag{1.25b}$$

At the metaphosphate composition, $x \approx 0.50$, the glass network is entirely formed by Q_2 units which connect via P – O – P bonds to form chains and rings. These chains and rings are linked by ionic bonds between metal cations and NBOs.

Polyphosphate glasses ($x > 0.5$) possess the chains, which are made up of Q_2 units terminated by Q_1 units. The average chain length progressively decreases with increasing the [O]/[P] ratio as a result of the disruption of long chain structures [166]. At the pyrophosphate composition, $x = 0.67$ or [O]/[P] = 3.5, the glass network is dominated by $(P_2O_7)^{4-}$ dimers, i.e. two Q_1 units linked by a common bridging oxygen. In the region between the metaphosphate ($x = 0.5$) and pyrophosphate ($x = 0.67$) compositions, the glass networks possess chains, which are made up of Q_2 units terminated by Q_1 units. The proportions of Q_1 and Q_2 species calculated from Equation (1.23) are given by:

$$f(Q_1) = \frac{2x - 1}{1 - x} \tag{1.26a}$$

$$f(Q_2) = \frac{2 - 3x}{1 - x} \tag{1.26b}$$

In the composition range between the pyrophosphates ($x = 0.67$) and orthophosphates ($x = 0.75$), $(P_2O_7)^{4-}$ dimers break down and only the isolated

Q_0 species should exist in the orthophosphates. The fractions of Q_0 and Q_1 estimated from Equation (1.23) are then given by:

$$f(Q_0) = \frac{3x - 2}{1 - x} \tag{1.27a}$$

$$f(Q_1) = \frac{3 - 4x}{1 - x} \tag{1.27b}$$

In the binary glass $xM_2O - (1 - x)P_2O_5$, the ratio of BO/NBO within the whole range of $0 \leq x \leq 0.75$ can be predicted by the following equation:

$$BO/NBO = 0.5(3 - 4x) \tag{1.28}$$

Martin et al. reported the glass forming region in binary lithium phosphate glasses $xLi_2O - (1 - x)P_2O_5$ up to x = 0.625 for conventional melt quenching technique [104]. Using the rapid quenching technique, the region of glass formation can be extended to x = 0.70 [167, 168]. In the binary alkali phosphate glasses, it was observed that there is a significant change in the physical properties near the alkali oxide content $x \approx 0.20$. Both glass transition temperature (T_g) and density of Li and Na phosphate glasses reduce with rising alkali oxide content (Li_2O or Na_2O) and reach a minimum at $x \approx 0.20$, and for $x > 0.20$, T_g and density increase again [104, 165, 169, 170]. Since T_g values of Li, Na and also Cs [170] phosphate glasses are lower than that of pure v-P_2O_5, it is apparent that the v-P_2O_5 with the 3-dimensional branched network is stronger than the binary alkali glasses for all values of x. The minimum of T_g at $x \approx 0.20$ also indicates that only when $x > 0.20$ do the modifier cations (e.g., Li^+, Na^+) start to strengthen the glass structure. In addition, ionic conductivity increases and corresponding activation energy decreases with rising alkali oxide content [103, 104].The increase of ionic

conductivity is due to the formation of more NBOs with the increase of alkali oxide content, which leads to the reduction in the network connectivity of the glasses and thus facilitates the Li^+ ion movement.

Several analytical techniques have been used for the investigation of glass structure and structure – property relationships in the phosphates such as neutron and X–ray diffraction (XRD), X–ray photoelectron spectroscopy (XPS), extended X–ray absorption fine structure (EXAFS), Infrared spectroscopy (IR), Raman spectroscopy, and Nuclear magnetic resonance spectroscopy (NMR).

XPS studies can effectively provide a quantitative analysis of oxygen bonding states in the binary phosphate glasses [171 – 174]. Generally, XPS O1s spectra can be decomposed into two components. The high and low binding energy peaks around 533.2eV and 531.5eV are assigned to bridging oxygen (BO), and non-bridging oxygen (NBO) respectively. In binary phosphate glasses with high P_2O_5 contents, NBO includes both double bonded P = O and $P – O^-$, and it is difficult to distinguish these two types of oxygen [173 – 175]. XPS spectra clearly showed that the number of NBOs increases, and the number of BOs decreases with increasing modifier content, and the quantification of BO/NBO ratios is similar to the analysis from NMR results as well as to the prediction from Equation (1.28) [173, 175].

The evolution of the cross-linked Q_3 network of v-P_2O_5 to the chain-like Q_2 network of the metaphosphate can be observed in NMR spectra [173, 176]. These spectra showed that typically in the ultraphosphate region ($0 \leq x \leq 0.50$) only Q_2 and Q_3 units are present, and no disproportionation of Q_2 units

($2Q_2 \rightarrow Q_1 + Q_3$) occurs, except for calcium metaphosphate glass [177]. According to Brow [163], distributions of Q_3 and Q_2 units in this region are in good agreement with the predictions from pseudo-reaction model (Eq. (1.25a) and (1.25b)). However, in the polyphosphate region ($x > 0.50$) NMR spectra indicate that Q_1 sites disproportionate to Q_0 and Q_2 groups ($2Q_1 \rightarrow Q_2 + Q_0$), as reported by Tatsumisago et al., Walter et al., and Brow et al. [178 – 181].

Raman and IR spectra for alkali ultraphosphate [165, 169, 173, 182] and polyphosphate [178, 183] glasses $xM_2O - (1 - x)P_2O_5$ also show the progression from the cross-linked Q_3 network to the chain-like Q_2 structure, and then to Q_1 and Q_0 species with the increase of modifier content. Results from Raman spectra are also consistent with the simple model in Equation (1.23). In the Raman spectra, with the increase of alkali oxide content, the dominant stretching band of P – NBO shifts from the frequency of 1390 cm^{-1} for $x = 0$ (symmetric P = O stretching mode on Q_3 phosphate tetrahedra) to near 1170 cm^{-1} for $x = 0.50$ (symmetric PO_2 stretching mode of NBO on Q_2 tetrahedra), then to 1050 cm^{-1} for $x = 0.67$ (symmetric PO_3 stretching mode of NBO on Q_1 tetrahedra), and further to 950 cm^{-1} for $x = 0.70$ (symmetric PO_4 stretching mode of NBO on Q_0 tetrahedra). These frequency shifts show the progressive depolymerisation of the phosphate network as well as the increase in the average bond length of P – NBO, which is also observed from neutron and X – ray diffraction studies for phosphate glasses [184]. Raman spectra of Li and Na phosphate glasses [165] also revealed that in the region of $0 \leq x \leq 0.20$ symmetric P = O stretching band on Q_3 units remains essentially unchanged. Therefore the decrease of T_g up to $x \approx 0.20$ mentioned earlier can be explained by the decrease of bridging oxygens (BOs), as Q_3 network

depolymerises to form Q_2 species. For x > 0.20, both IR [169] and Raman [165] showed the shift of (P = O) band to lower frequency with increasing alkali oxide content. This frequency shift reveals the delocalization of π-bonding on the Q_3 units, and hence lengthening of (P = O) bond. The increase of P = O bond length is also observed in NMR spectra in case of Li phosphate glasses [176].The π-bonding delocalization results in the increase of network strength due to the formation of alkali – oxygen bridges. Consequently, for x > 0.20 the glass transition temperature (T_g) rises with the increase of alkali oxide content [165].

X – ray diffraction and ^{6}Li NMR studies indicate that Li^+ ions has coordination number from 4 to 5 in case of phosphate glasses, while mostly 4 for ternary crystalline phosphates [185, 186]. The average coordination number of Li in a wider range of crystalline oxide salts is 5.02 [187]. Besides, the average bond lengths of Li – O and P – O are found to be around 2.02 – 2.04 Å and 1.52 – 1.53 Å in Li phosphate glasses, respectively [185]. The coordination number of Na^+ ions is about 5, as revealed from diffraction studies of sodium metaphosphate glass [188, 189]. Hoppe [184, 190] proposed a structural model, which is based on the coordination environments of modifier cations (CN_M) and the number of NBOs (N_{NBO}) available to coordinate the modifier cations, to explain the property minima (such as density, T_g) in the binary phosphate glasses at $x \approx 0.20$. This model predicts the transition from region I ($N_{NBO} > CN_M$) to region II ($N_{NBO} < CN_M$) occurring at x = 0.20 to 0.25, which is also observed in Raman and IR spectra, for Li and Na phosphate glasses. According to this model, for $x \leq 0.20$ the density decreases due to the expansion of Q_3 network to accommodate the

alkali ions, while for x > 0.20 density increases with rising alkali oxide content as more alkali ions share corners and edges.

In addition to experimental techniques mentioned above, an alternative way to study the relation between structure and properties in the glassy states is computer based simulation techniques, such as ab initio, reverse Monte Carlo (RMC), and Molecular Dynamics (MD) simulations. The main advantage of computer simulation is to bypass the experimental problems in glasses, such as difficulties in the preparation and property measurement of glasses due to their hygroscopic nature. Ab initio method can be used to predict the local structure and vibrational properties, such as pair and radial distribution functions, IR, Raman and XPS, and analyze coordination environment of alkali ion in the glassy systems [191 – 193]. The RMC method can generate static structural models that quantitatively agree with neutron and X-ray diffraction, EXAFS and NMR data, as well as other structural and chemical knowledge of the glasses [89, 194, 195]. This model is currently the only viable method to reproduce the structural models from the experimental data. However, no dynamical information can be extracted from RMC model. An alternative approach to obtain all the information about structure and dynamics (within the limitations imposed by the system size and the simulated period) is the MD simulation. The MD approach has shown to be a very useful tool in obtaining direct insight into the conduction mechanism and its correlation to the atomic structure [196 – 201]. Karthikeyan et al. [196] demonstrated the ion dynamics in $xLi_2O - (1 - x)P_2O_5$ glasses by MD simulation, and observed that the mean square displacement (MSD) of Li^+ ions increases with the increase in lithium oxide content. MSDs of both

phosphorous and oxygen are considerably lower than that of Li^+ ions, which confirmed that only Li^+ ions are the mobile species and contribute to ionic conductivity. He suggested that Li^+ ion migration is facilitated by the presence of an optimal NBO environment, and not directly linked to NBO – BO transformations (or bond flips). Vogel [199] performed MD simulation to investigate the lithium jumps in the $LiPO_3$ glasses. He found that short-lived dynamical heterogeneities, where the fast Li^+ ions participate in the correlated back – and – forth jumps between neighboring sites and migrate along the preferential pathways in the glassy network. He concluded that the sites featuring fast and slow Li^+ ion dynamics are intimately mixed and an exchange between the fast and slow Li populations is fast. Adams et al. [201 – 204] presented the bond valence (BV) approach, which is based on the local structure models derived from RMC or MD simulations, to predict quantitatively the ion transport pathways in the phosphate, as well as silicate and borate glasses. The authors revealed that the mobile ions in MD snapshots have a narrower distribution of BV sums and coordination numbers than RMC models. In case of $LiPO_3$ glass, the average BV sum V(Li) of Li atoms in the MD models (V(Li) = 0.83 ± 0.12 v.u.) was found to be lower than that of the RMC models (V(Li) = 0.93 ± 0.15 v.u.). His research clearly indicated that the analysis of energy landscape for mobile ions in terms of the BV approach can provide an effective tool to promote a better understanding of ion transport in glasses. More detail about this approach will be presented in Chapter 2 – Section 2.4.3 (Bond Valence approach).

1.4.2.3. Halide salt-doped lithium phosphate glasses

From the structural point of view, it is well established that the addition of metal halide salts into the binary oxide glasses has little effect on the connectivity of the parent glasses. Generally, introduced dopant ions dissolve into the glass structure and occupy its interstices without significantly modifying the glass network [185, 205 – 208].

The glass forming region in the ternary glass system $LiPO_3$ – LiX [X = I, Br, Cl] has been reported along with their ionic conductivity (σ) by Malugani et al. [82]. Glasses form up to 30 mol% of LiCl and 33 mol % of LiBr and LiI. σ increases with halogen ion size (and polarisability) and with increasing LiX content throughout the glass forming region. Another study conducted by Doreau et al. [209] in Li_2O – P_2O_5 – LiCl system reports glass forming region up to nearly 30 mol % of LiCl for R (R = Li_2O/P_2O_5) varying between 0.67 to 1.38 and up to 35 mol % for R value of 0.25. For all values of R studied, the glass transition temperature T_g decreases and σ increases as LiCl content increases. Conclusions from Raman spectroscopy studies of 0.30LiCl – 0.70($0.58Li_2O$ – $0.42P_2O_5$) glass in the same study indicate that the addition of Li_2O breaks up P – O – P bridges, creating non-bridging oxygens (NBOs) which reduce the lengths of chains formed by P – O – P bridges, while the addition of LiCl does not bring about any such modification of chain lengths in the glass network, though it reduces the T_g of the parent glass. X-ray diffraction study and MD simulation of $0.52Li_2O$ – $0.48P_2O_5$, $0.45Li_2O$ – $0.42P_2O_5$ – 0 .13LiCl and $0.39Li_2O$ – $0.36P_2O_5$ – 0.25LiCl glasses [185, 210] reports that the addition of Li_2O to P_2O_5 breaks up the 3-dimensional branched

structure creating more non-bridging oxygens, and the addition of LiCl makes the structure less rigid and creates wider channels for Li^+ movement, thus enhancing σ and decreasing T_g. Further structural reports for $Li_2O – P_2O_5 –$ LiCl glass [99, 178] confirm that no P – Cl bonds are formed and that LiCl dissolves interstitially in $LiPO_3$ glass network. In line with these findings, none of the six known complex oxyhalide crystal structures that contain P^{5+} shows a bond between phosphorous and the halide ion. In $Li_4X(BePO_4)_3$ with X = Cl or Br the halide ion is bonded exclusively to Li. In LiF-metal phosphates the second metal (e.g., Al, Ni, V) forms bonds with the F^- ions, but phosphorous is again coordinated by oxygen only. In all these structures Li^+ ions have mixed oxyhalide coordination. However, IR and XPS studies of $x(2LiCl)y(Li_2O)(100 – x – y)P_2O_5$ glasses (where x = 0, 10, 20, y = 50, 60) by Horiuchi et al. [211] suggest that the more open structure of the halide doped glasses is achieved by Cl^- ions, which alter the P – O – P glass network.

While Raman, IR spectroscopy and reverse Monte Carlo fits of diffraction data accordingly find that LiCl acts as a dopant only in lithium borate glasses [212, 213], the addition of LiCl in $Li_2O – TeO_2 –$ LiCl glasses [214, 215] is reported to produce NBOs leading to the formation of Te – Cl bonds in the equatorial position of the trigonal bipyramid TeO_4 unit. A comparative study of LiBr-doped lithium tellurite glasses, $Li_2O – TeO_2 –$ LiBr, with LiCl-doped glasses reported that the ionic conductivity (σ_{dc}) and thermal expansion values are lower, and T_g values are higher for LiBr-doped glasses than for LiCl-doped glasses. These phenomena are attributed to the strength of the Te – O_{ax} bond (ax denotes an axial position) and the amount of $(TeO_3)^{2-}$ trigonal pyramids; the extent of weakening of the Te – O_{ax} bond, which brings about the

formation of $(TeO_3)^{2-}$, is smaller in the LiBr-doped glasses than in the LiCl-doped glasses [216]. Another ^{11}B NMR and impedance spectroscopy study of $Li_2X - B_2O_3 - SiO_2$ (X = O, Cl_2) [217] reveals that Cl^- ion doping acts via modifying the B – O bond strengths and that the network dilatation brought about by the addition of Cl^- ion would be of influence for Li^+ ion conductivity.

A recent study in detail addressed the hypothesis of LiCl aggregates in the $LiCl - Li_2O - P_2O_5$ glasses by ^7Li MAS NMR [218]. Ogiwara et al. [218] found that no signs of LiCl aggregates can be observed for $x < 0.5$ in the case of $(LiCl)_x(Li_{1.4}PO_{3.2})_{1-x}$ or for $x < 0.3$ in the case of $(LiCl)_x(Li_{1.67}PO_{3.33})_{1-x}$. Instead it is concluded that all Li^+ ions in the glass matrix are interacting with both phosphate anions and Cl^- ions in this lower LiCl composition range. These authors indicated that amorphous LiCl aggregates only exist for high LiCl contents close to the limit of the glass forming region, and that these aggregates lead to the high mobility of Li^+ ions. They also suggested that the formation of amorphous metal-halide aggregate regions is a structural feature that is common for metal-halide-based fast ion conducting glasses only in the case of high metal-halide contents.

A large number of reports are available on theoretical models to explain the ionic conduction mechanism in disordered solid electrolytes [103, 219 – 223]. These reports emphasize the role of the shape and dynamic properties of the energy landscape predetermined by the local structure and composition of the glass. The commonly used models explain the conductivity from either microscopic hopping or macroscopic continuum models [220]. Hopping models are simple in approach and have been successfully adopted for a wide

range of electron conducting, semi-conducting and fast ion conducting systems. Especially, the random barrier model by Dyre et al. [220] is found to explain ionic conduction characteristics as a hopping process in an energy landscape with a random distribution of energy barrier heights.

1.4.3. Alkali borophosphate glasses

The properties of glasses can be modified by mixing more than one glass former to form competitive network, which is called “mixed glass former” or “mixed anion effect” [74, 78, 79, 224, 225]. Unlike the mixed alkali effect, which shows a pronounced minimum of ionic conductivity, the mixed glass former effect generally enhances the ionic conductivity and show high chemical durability when compared to individual glass former.

Alkali borophosphate glasses are of interest as model substances for the studies of mixed glass former effect. Borophosphate glasses have found many applications as fast ion conductors in solid state electrochemical devices (alkali and silver borophosphates) [102, 225 – 227], as low melting glass solders or glass seals (zinc borophosphates) [228], and applications in non-linear optical devices (niobium and calcium borophosphates) [229].

The structural properties of borophosphate glasses are distinct from those of either pure phosphate or borate glasses. The structure of pure v-P_2O_5 glasses consists of PO_4 tetrahedra linked via covalent bridging oxygens (P – O – P), while the structure of pure B_2O_3 glasses consists of boroxol rings and BO_3 triangles connected through B – O – B linkages [127]. The addition of a network modifier (e.g. Li_2O, Na_2O, K_2O etc.) to phosphate and borate

glasses results in opposite effects. In the phosphate glasses, the introduction of network modifier leads to the depolymerisation by breaking up the P – O – P bridges, creating non-bridging oxygens. On the contrary, in the borate glasses the addition of modifier increases the degree of polymerisation, in which the boron coordination converts from 3- to 4-fold and the basic units alter from trigonal BO_3 to tetrahedral BO_4 [230 – 233]. Therefore, in borophosphate glassy systems, the network structure is likely to be built by interconnection between phosphate and borate networks, which is formed by a combination of P and B coordination polyhedra.

Structural studies of borophosphate glasses have been reported using X-ray diffraction (XRD) and spectroscopic techniques. XRD confirms the glassy nature of the system $42.5Li_2O – xB_2O_3 – (57.5 – x)P_2O_5$ up to x = 57.5 mol% [78]. The glass forming region in the series of $0.50Li_2O – xB_2O_3 – (0.50 – x)P_2O_5$ is limited to $0 \leq x \leq 0.20$ [79]. Generally, glass forming regions of lithium borophosphate systems could be depicted as in Figure 1.6, as reported by Magistris et al. [225]. Crystalline Li_3PO_4 peaks were often identified in the Li_2O-rich compositions (the upper region of Figure 1.6) by XRD, whereas the formation of crystalline BPO_4 peaks occurs in the lower region of Figure 1.6. The remaining areas (shaded regions) in Figure 1.6 were located to be the glass forming regions.

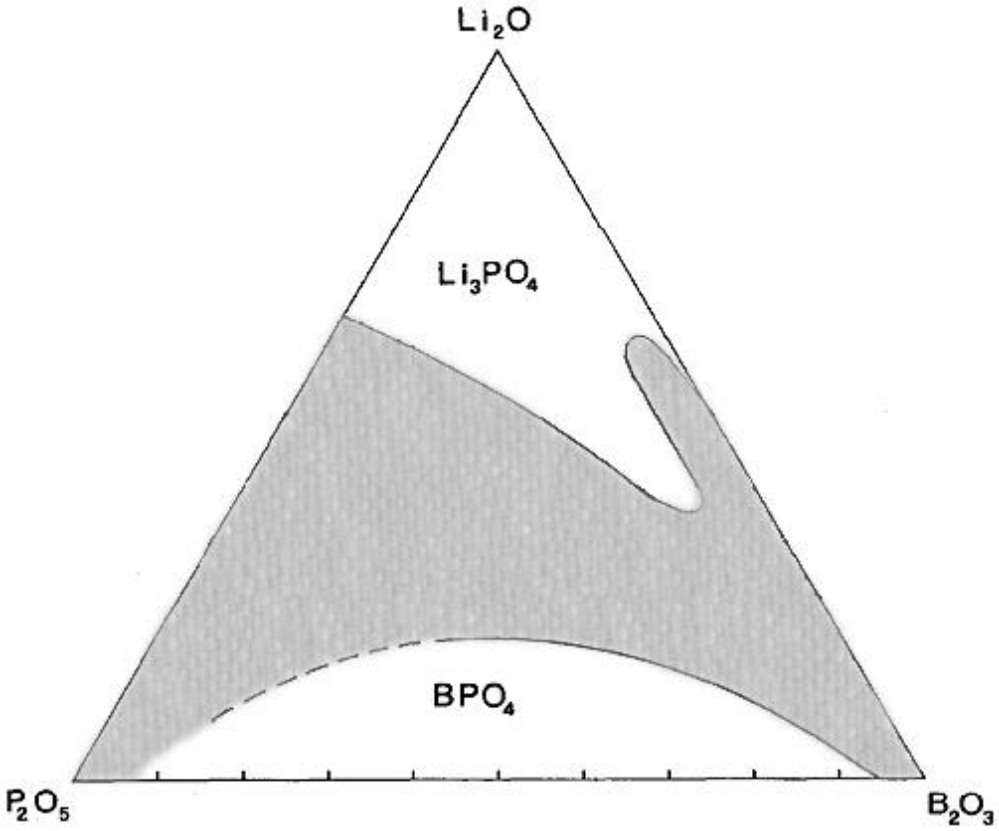

Figure 1.6. Glass formation regions of the $Li_2O – P_2O_5 – B_2O_3$ system. Shaded areas indicate the glass forming regions. Modified from Ref. [225].

X-ray photoelectron spectroscopy (XPS) has provided a quantitative measure of oxygen bonding in phosphate, borate glasses, as well as borophosphate glasses [171, 174, 175, 229, 234 – 236]. In the phosphate and borate glasses, contributions from bridging (BO) and non-bridging (NBO) oxygens to the O1s spectra can be clearly separated and their relative intensities depend on composition, namely, the modifier-to-former ratio. The high and low binding energy peaks around 533.2eV and 531.5eV are assigned to bridging oxygen (P – O – P bonds) and non-bridging oxygen ($P – O^-$ and P = O bonds) respectively in the phosphate glasses [171, 174, 234, 235]. In the zinc [175], calcium and sodium [229] borophosphate glasses, the third intermediate O1s component, assigned to P – O – B sites, is consistent with

the intermediate ionicity of this oxygen bonding, when compared to P – O – P and P – O^- bonds. By deconvoluting the XPS spectra of $(1 - y)Zn(PO_3)_2 - yB_2O_3$ glasses, Brow et al. [175] quantitatively found that proportions of P – O – P and P – O^- bonds decrease, and the concentration of P – O – B bonds increases with rising B_2O_3 content.

^{11}B and ^{31}P NMR spectra revealed that borophosphate glasses contain BO_3, BO_4 and (Q^1 and Q^2 type) PO_4 units, and form a substantial fraction of P – O – B linkages [80, 228, 237 – 240]. Thus their structure consists of a borophosphate network or a phosphate/borate network (when one of the glass formers is dominant). ^{11}B NMR studies of zinc [228], potassium [237], sodium [239], and lithium [80, 240] borophoshate glasses confirmed that in the phosphate-rich region boron atoms prefer a tetrahedral coordination (BO_4 units), and trigonal borons (BO_3 units) become increasingly important in the structural network of borate-rich region. In the glassy systems $0.45Li_2O - (0.55 - x)P_2O_5 - xB_2O_3$ ($0 \leq x \leq 0.30$), Feng et al. [240] revealed that N_4, i.e. the fraction of BO_4 units, increases from 0.7 (x = 0.05) to a maximum of 0.86 (x = 0.15) and remains $\geq$ 0.55 up to the maximum value of x (x = 0.3). Similarly, ^{11}B MAS NMR studies [80] on $0.50Li_2O - (0.50 - x)P_2O_5 - xB_2O_3$ glasses indicated that BO_4 units are predominant ($N_4 \approx 100\%$) up to x = 0.15, then N_4 progressively decreases and the fraction of BO_3 units increases with further B_2O_3 addition. ^{31}P MAS NMR spectra in this glassy system further showed that the increase of B_2O_3 content leads to the increase of Q_1 phosphate units as well as P – O – B linkages, and the decrease of Q_2 phosphate units. In addition, ^7Li MAS NMR confirmed that Li atoms remain four-coordinated environment with B_2O_3 addition in the $0.50Li_2O - (0.50 - x)P_2O_5 - xB_2O_3$

glasses [80].

Infrared spectroscopy has also been used to study the structure of borophosphate glasses [102, 241]. FT-IR spectra again revealed the presence of P – O – B linkages. In the glassy systems $xLi_2O – (1 – x)[0.50B_2O_3 – 0.50P_2O_5]$ and $xAg_2O – (1 – x)[0.50B_2O_3 – 0.50P_2O_5]$, the intensities of $[BO_3]^{2-}$, P = O vibrations, B – O – B stretching modes increase and the intensity of P – O – B stretching modes gradually decreases with the increase of network modifiers (Li_2O or Ag_2O) [102]. Symmetrical stretching vibrations in both PO_4 and BO_4 groups, as well as the bending modes of PO_4 and P – O – B were observed in the regions of 1045 cm^{-1} and 450 – 600 cm^{-1}, respectively.

Raman studies showed that the O – P – O stretching modes near 1170 cm^{-1} decrease and shift to lower frequencies as boron oxide replaces phosphorous oxide [79, 242 – 244]. With the addition of B_2O_3 the strong peak of P – O – P stretching vibrations near 700 cm^{-1} in pure phosphate glasses decreases rapidly and forms two new peaks at 660 – 640 cm^{-1}, which can be assigned to P – O – B bonds in different groups containing boron and phosphorous, and 720 cm^{-1}, which are the symmetric stretching vibrations of P – O – P [242, 244]. The formation of BPO_4, $(P_2O_7)^{4-}$, $(B – O – P)^-$ units around 1116 cm^{-1} and 1040 cm^{-1} was also observed [79, 243]. In lithium borophosphate glasses with the ratio of ([B + P]/[Li]) > 1, Scagliotti et al. [242, 245] suggested that the band around 1000 – 1100 cm^{-1} can be assigned to O – P – O vibrations of Q_2 phosphate units with either one or two oxygens bridging towards borons. The presence of BPO_4 units in borophosphate glasses, however, has not been universally supported. Ducel et al. [239, 241]

reported that there is no clear evidence of the presence of BPO_4 units in the ^{31}P and ^{11}B NMR spectra of $NaPO_3 – Na_2B_4O_7$ glasses. In the lithium and silver borophosphate glasses, Raman spectra showed the presence of BPO_4 units, whereas no definitive evidence was seen in ^{31}P NMR spectra; thus borophosphate glasses may consist of P – O – B linkages, but not the BPO_4 units [80, 242, 245].

Despite the controversy, the appearance of BPO_4 units was suggested to lead to high chemical stability, comparatively high glass transition temperature (T_g) and high ionic conductivity (σ_{dc}) in lithium borophosphate glasses [79, 225, 227, 246]. The addition of B_2O_3 increases T_g and hence the glass structure becomes more rigid [79, 102, 225, 244, 246]. T_g increases about 100 – 200^0C by the replacement of phosphorous with boron, and reaches either a plateau or maximum value near Y = 0.5 [225]. The increase of T_g is attributed to the increased cross-linking and connectivity of structural network through P – O – B linkages [80, 244].

An enhancement of σ_{dc} in lithium borophosphate glasses has been reported via the mixed glass former effect, when compared to the corresponding binary phosphate and borate glasses. Magistris et al. [225] found that a maximum of ionic conductivity takes place near Y = 0.5 (where Y = [B] / [B + P]), provided that these borophosphate compositions belong to the glass forming region. Salodkar et al. [78] also reported that there is an increase in the ionic conductivity with the B_2O_3 addition in the $42.5Li_2O – (57.5 – x)P_2O_5 – xB_2O_3$ glassy system. They observed two maxima of the ionic conductivity at Y = 0.3 and 0.7, which correspond to two minima of

activation energy (E_a) in these glasses, and explain this behaviour by using the thermodynamic approach. In the series of $0.30Li_2O - xB_2O_3 - (0.70 - x)P_2O_5$ and $0.40Li_2O - xB_2O_3 - (0.60 - x)P_2O_5$ [246], one maximum in σ_{dc} has been observed and attributed to the formation of BPO_4 units as evident from Raman spectra. The increase in σ_{dc} and the decrease in activation energy (E_a) up to glass forming limit x = 0.20 in the system $0.50Li_2O - xB_2O_3 - (0.50 - x)P_2O_5$ was also explained by the presence of BPO_4 units [79]. However, this explanation has recently been questioned by Munoz et al. [80], who emphasized the role of the predominant formation of BO_4 rather than BO_3 units for the conductivity enhancement, and assumed that the decrease of the Li – Li average distance further promotes Li^+ ion mobility.

1.5. Ion conduction mechanisms in glasses

Ion conduction in glasses has been studied in great detail for the last several decades. Various theoretical models were used to explain the mechanisms of ion conduction in these materials. However, no single unanimously accepted theoretical model exists to date that can explain completely the ion conduction mechanisms in glasses. Some of models are briefly discussed here.

1.5.1. The Anderson-Stuart model (A-S model)

In the A-S model [247], the activation energy for conduction is divided into two parts: the electrostatic binding energy of the original site (E_B) and the strain energy (E_s). E_B describes the Coulombic forces acting on the ion as it

moves away from its charge-compensating site, and E_s describes the mechanical forces acting on the ion as it dilates sufficiently the structure to allow the ion to move between the sites. The basic idea is that an ion makes a simple jump from one site to another, and passes through a "doorway" which opens as it passes through, where cation sites require only the presence of the non-bridging oxygens. The A-S model can be expressed as:

$$E_a = \frac{\beta_M}{\gamma}\left(\frac{zz_0e^2}{\delta+\delta_0} - \frac{zz_0e^2}{a/2}\right) + 4\pi G\delta_D(\delta-\delta_D)^2 \qquad (1.29)$$

where δ and δ_D are the radius of cation and the doorway respectively, a is the jump distance, γ is a covalency parameter arbitrarily taken equal to the relative permittivity ε_r, β_M is the Madelung constant which depends on the spatial arrangement of the ions. z_0 and δ_0 are the charge and radius of the O^{2-} ion, z is the charge of the cation and G is the elastic modulus. The covalency parameter (γ) was seen by Anderson and Stuart as expressing the "deformability of electron clouds on the oxygen atoms". The doorway radius δ_D can be estimated from diffusion data for noble gases such as He, Ne, Ar, since they are uncharged. A simplified version can be derived as the limiting value for $a \rightarrow \infty$:

$$E_a = \frac{\beta_M}{\gamma}\frac{zz_0e^2}{(\delta+\delta_0)} + 4\pi G\delta_D(\delta-\delta_D)^2 \qquad (1.30)$$

1.5.2. The weak electrolyte model

The weak electrolyte model can be applied to liquids or glasses for which the concentration of mobile ions (c) is less than the actual stoichiometric concentration. In this model, the ionic conductivity is expressed as in Equation

(1.15). The weak electrolyte model regards the solvent as a dielectric continuum. Based on this model, conductivity study of $Na_2O - SiO_2$ glasses [248, 249], where network former SiO_2 and the network modifier Na_2O are considered as the solvent and the solute respectively, found a correlation between ionic conductivity and thermodynamic activity of Na_2O (or Na^+) and explained the result by postulating the existence of an equilibrium:

$$Na_2O \leftrightarrow Na^+ + NaO^- \tag{1.31}$$

$$\sigma = \text{const} \times [Na^+] \tag{1.32}$$

in the glass. According to the weak electrolyte theory, the obvious way to improve the conductivity would be to increase the dissociation constant for the equilibrium in Equation (1.31). This can be done by choosing a glass network with highly polarisable atoms, which would give a high value of the dielectric constant, ε_r.

1.5.3. The cluster bypass model

The basis of the cluster bypass model [250] is the assumption that the liquid phase remains in small regions even far below the glass transition region. These regions of the liquid phase, which decrease in size with decreasing temperature, are situated between clusters of the glassy state. It is supposed that the liquid state forms an interconnected network of pathways, where the cation can diffuse by a percolation process. The decrease in conductivity with decreasing temperature is explained by a decreasing number of favorable pathways as the residual liquid phase progressively solidifies. An

advantage of the cluster bypass model is that it may provide a relatively straightforward explanation of the mixed mobile ion effect. The foreign cations are believed to be concentrated in the regions of the liquid phase and there "block" the most favorable pathways. The mobile host cations have to find less favorable pathways involving migration through the glass clusters. This would also explain why the activation energy increases when different cations are mixed.

1.5.4. The random site model

This model [251] proposes that the network modifier or dopant salt is homogenously dispersed in the glass and that its role for the enhanced ion conduction is to lower the average potential barriers within the glass. The cations are assumed to experience a Gaussian distribution of activation energies due to the randomness of the glass network. The average mobility then varies with the distribution of activation energies and thereby with the glass composition. All the cations are assumed to be potential charge carriers, which mean that it is mainly the mobility of the cations which increases with increasing modifier or dopant salt concentration. Thus, this model is different from the weak electrolyte model, where it is proposed that only a fraction of the cations are mobile and that their mobility is constant.

1.5.5. The diffusion pathway model

The diffusion pathway model [128, 252] was built on the assumption that the metal halide salt is introduced into the amorphous network in small clusters or micro domains, which form connected pathways for the ions to diffuse through the glass. These pathways were assumed to be built up by the halide ions and to be characterized by low energy barriers. While the basic assumption of micro-domain formation cannot be held up, the model remains relevant for network glasses with structures described by the modified continuous random network (CRN) model [128]. This includes metal oxide modified network glasses, where the percolation pathways are formed by inter-network channels of network modifiers and the non-bridging oxygens (NBOs) therein serve a corresponding purpose as the halide ions do for the doped glasses. Thus, the diffusion pathway model shows some similarities with the cluster bypass model, except that the interconnected regions are made up of the dopant salt or the network modifiers, instead of residual liquid in the cluster bypass model.

In this work, the Bond Valence approach, which is developed by our group, will be applied to shed new light on the ion conduction mechanisms in glasses. Details about this approach will be discussed in Chapter 2, Section 2.4.3 (Bond Valence approach).

1.6. Motivation and Objectives

In the view of the above review, most of the previous studies focus on understanding the structure and properties of the lithium based glasses from both experimental and simulation techniques. Although the computer-based simulations (e.g., ab initio, reverse Monte Carlo, empirical Molecular Dynamics) have been extensively used to correlate the structure and properties of glasses, the knowledge of composition-structure-property relationships which require a detailed understanding of the underlying mechanisms, e.g. the ion conduction mechanisms in glassy solid electrolytes, has yet to be understood thoroughly. There is still no unanimously accepted model that can explain some of the most interesting universal phenomena associated with ion conduction in glasses. In other words, the realization of the underlying mechanisms of ion dynamics in glassy solid electrolytes is still far from complete. Hence, understanding of the ion conduction mechanisms in glasses is one of the key features for the development of solid electrolytes and electrode materials for device applications, e.g. rechargeable batteries.

The overall objective of this thesis was therefore to achieve a detailed insight into ion conduction mechanisms in glassy solid electrolytes and exploit this knowledge to optimize the material properties. The followings are the specific aims of this project:

- Characterize structures and physical properties (e.g., glass transition temperature, ionic conductivity, etc.) of the investigated glasses.

- Simulate and visualize structures and ion transport pathways of the investigated glasses using both Molecular Dynamics simulations (with optimized potentials) and Bond Valence analysis.
- Reveal and analyze the features of lithium ion transport pathways (e.g., volume fraction, local dimensionality of percolating pathways).
- Clarify the influence of network modifier (in case of silicate glasses) and halide dopant concentration (for halide-doped phosphate glasses), as well as of mixed glass former effect (in case of borophosphate glasses) on the glass structure and Li^+ ion mobility.
- Explore ion dynamics of glasses (e.g., transport mechanism and relaxation behaviour).

To achieve these goals the following strategy has been adopted: The composition – structure – conductivity correlations in lithium silicate $xLi_2O – (1 – x)SiO_2$, halide-doped phosphate $(1 – y)(0.60Li_2O – 0.40P_2O_5) – yLiX$ (X = Cl, Br), and borophosphate $0.45Li_2O – (0.55 – x)P_2O_5 – xB_2O_3$ glasses were investigated using impedance spectroscopy as well as the combination of Molecular Dynamics (MD) simulation (with optimized potentials) and Bond Valence (BV) analysis. MD simulation aims to reproduce the experimentally observed properties (e.g., bond length, coordination number, ionic conductivity, etc.) and is one of the useful tools to appreciate the microscopic origin of the dynamics. In addition, BV analysis so far proved its helpfulness in predicting and quantifying the ion transport pathways, especially when it was applied to the low conductivity glasses, where the mobility of ions is too

small to be observed directly in room temperature MD simulation trajectories [195, 201 – 203, 253 – 256]. Furthermore, in case of the silicate and phosphate glasses, results of ion transport pathways from MD-simulated trajectories were compared to those from local structure models derived from experimental diffraction data by reverse Monte Carlo (RMC) modelling for related glassy solid electrolytes.

Besides, structural properties of halide-doped phosphate and borophopshate glasses were characterized by X-ray powder Diffractometry (XRD), SEM with Energy Dispersive X-ray Detection (EDX), as well as FT-IR, Raman and XPS spectroscopy (for borophosphate glasses). Glass transition temperatures of these glasses were determined by Differential Scanning Calorimetry (DSC). In case of borophosphate glasses, structural analyses from BV approach along with the deconvolution of Raman and XPS spectra were used to clarify the influence of mixed glass former effect on glass structure and ionic conductivity. Finally, in order to further understand ion transport mechanism and relaxation behaviour, ion dynamics in the $(1 - y)(0.60Li_2O - 0.40P_2O_5) - yLiX$ and $0.45Li_2O - (0.55 - x)P_2O_5 - xB_2O_3$ glassy systems is also explored using frequency dependent impedance spectroscopy.

The results obtained from this thesis are expected to promote a better understanding of ion transport in glassy solid electrolytes, and help to develop a systematic strategy for the design of highly ion-conducting glassy solid electrolytes that are suitable for application in electrochemical devices, especially all-solid-state rechargeable lithium batteries.

References

1. M. Faraday, Faraday's Diaries 1820-1862, Vol. II, (G. Bell and sons 1939), the entry dated 21st Feb 1883 and 19th Feb 1835.
2. C. A. C. Sequeira, A. Hooper, Solid State Batteries. Dordrecht; Boston: M. Nijhoff Publishers, c1985.
3. C. Tubandt, E. Lorenz, Z. Phys. Chem. 87 (1914) 513.
4. C. Tubandt, Hamb. Exp. Physi. 12 (1932) 383.
5. A. Beneath, K. Drekopf, Z. Phys. Chem. 99 (1921) 57.
6. R. Komiya, A. Hayashi, H. Morimoto, M. Tatsumisago, T. Minami, Solid State Ionics 140 (2001) 83.
7. W. Weppner, Fundamental Electrochemical Materials Aspects of Solid State Fuel cells, Ionics 4 (1998) 422.
8. N. Yamazoe, N. Miura, Solid State Ionics 86-88(2) (1996) 987.
9. P. R. Slater, Encyclopedia of Materials: Science and Technology (2008) 2848.
10. P. Knauth, Solid State Ionics 180 (2009) 911.
11. S. Chandra, Superionic solids: Principles and applications, North-Holland Publishing Company, 1981.
12. J. Maier, Physical Chemistry of Ionic Materials - Ions and Electrons in Solids. John Wiley & Sons, Ltd, 2004.
13. A. Lundén, Solid State Commun. 65 (1988) 1237.
14. E. A. Secco, Solid State Commun. 66 (1988) 921.
15. M. Jansen, Angew. Chem. lnt. Ed. Engl. 30 (1991) 1547.
16. H. L. Tuller, P. K. Moon, Mater. Sci. Eng. B1 (1988) 171.

17. S. Bredikhin, Solid State Ionics 136-137 (2000) 387.
18. H. Yamane, M. Shibata, Y. Shimane, T. Junke, Y. Seino, S. Adams, K. Minami, A. Hayashi, M. Tatsumisago, Solid State Ionics 178 (2007) 1163.
19. A. Hayashi, K. Minami, F. Mizuno, M. Tatsumisago, J. Mater. Sci. 43 (2008) 1885.
20. A. Hayashi, K. Minami, S. Ujiie, M. Tatsumisago, J. Non-Cryst. Solids 356 (2010) 2670.
21. H. Wada, M. Ishii, M. Onoda, M. Tansho, A. Sato, Solid State Ionics 86-88 (1996) 159.
22. E. R. Baranova, V. L. Kobelev, O. L. Kobeleva, N. V. Melnikova, V. B. Zlokazov, L. Ya. Kobelev, M. V. Perfiliev, Solid State Ionics 124 (1999) 255.
23. S. Adams, Z. Kristallogr. 211 (1996) 770.
24. Y. –W. Hu, I. D. Raistrick, R. A. Huggins, Mater. Res. Bull. 11 (1976) 1227.
25. J. R. Rea, D. L. Foster, Mater. Res. Bull. 14 (1979) 841.
26. Y. Inaguma, C. Liquan, M. Itoh, T. Nakamura, T. Uchida, H. Ikuta, M. Wakihara, Solid State Commun. 86 (1993) 689.
27. S. Stramare, V. Thangadurai, W. Weppner, Chem. Mater. 15 (2003) 3974.
28. A. Morata-Orrantia, S. García-Martín, E. Morán, M. A. Alario-Franco, Chem. Mater. 14 (2002) 2871.
29. H. Aono, E. Sugimoto, Y. Sadaoka, N. Imanaka, G. Adachi, J. Electrochem. Soc. 136 (1989) 590.

30. H. Aono, E. Sugimoto, Y. Sadaoka, N. Imanaka, G. Adachi, Solid State Ionics 47 (1991) 257.
31. K. Arbi, J. M. Rojo, J. Sanz, J. Eur. Ceram. Soc. 27 (2007) 4215.
32. J. S. Thokchom, B. Kumar, J. Power Sources 195 (2010) 2870.
33. J. S. Thokchom, N. Gupta, B. Kumar, J. Electrochem. Soc. 155(12) (2008) A915.
34. J. S. Thokchom, B. Kumar, J. Power Sources 185 (2008) 480.
35. P. G. Bruce, A. R. West, J. Electrochem. Soc. 130(3) (1983) 662.
36. A. D. Robertson, A. R. West, A. G. Ritchie, Solid State Ionics 104 (1997) 1.
37. R. Kanno, T. Hata, Y. Kawamoto, M. Irie, Solid State Ionics 130 (2000) 97.
38. M. Murayama, R. Kanno, M. Irie, S. Ito, T. Hata, N. Sonoyama, Y. Kawamoto, J. Solid State Chem. 168 (2002) 140.
39. R. Kanno, M. Murayama, J. Electrochem. Soc. 148 (2001) A742.
40. Z. Liu, F. Huang, J. Yang, B. Wang, J. Sun, Solid State Ionics 179 (2008) 1714.
41. V. Thangadurai, W. Weppner, Adv. Funct. Mater. 15 (2005) 107.
42. V. Thangadurai, W. Weppner, J. Am. Ceram. Soc. 88 (2005) 411.
43. V. Thangadurai, W. Weppner, J. Solid State Chem. 179 (2006) 974.
44. B. K. Money, K. Hariharan, Appl. Phys. A 88 (2007) 647.
45. C. Arbizzani, M. Mastragostino, L. Meneghello, X. Andrieu, T. Vicédo, J. Power Sources 45 (1993) 161.
46. A. M. Christie, S. C. Lilley, E. Staunton, Y. G. Andreev, P. G. Bruce, Nature 433 (2005) 50.

47. G. Derrien, J. Hassoun, S. Sacchetti, S. Panero, Solid State Ionics 180 (2009) 1267.

48. C. Shen, J. Wang, Z. Tang, H. Wang, H. Lian, J. Zhang, C. –N. Cao, Electrochim. Acta 54 (2009) 3490.

49. N. Li, L. Wang, X. He, C. Wan, C. Jiang, Ionics 14 (2008) 463.

50. S. Y. An, I. C. Jeong, M. –S. Won, E. D. Jeong, Y. –B. Shim, J. Appl. Electrochem. 39 (2009) 1573.

51. H. H. Sumathipala, J. Hassoun, S. Panero, B. Scrosati, Ionics 13 (2007) 281.

52. H. M. J. C. Pitawala, M. A. K. L. Dissanayake, V. A. Seneviratne, B. -E. Mellander, I. Albinson, J. Solid State Electrochem. 12 (2008) 783.

53. J. Kumar, S. J. Rodrigues, B. Kumar, J. Power Sources 195 (2010) 327.

54. N. Angulakshmi, T. P. Kumar, S. Thomas, A. M. Stephan, Electrochim. Acta 55 (2010) 1401.

55. L.-Z. Fan, X. -L. Wang, F. Long, X. Wang, Solid State Ionics 179 (2008) 1772.

56. M. Marzantowicz, J. R. Dygas, F. Krok, A. Tomaszewska, Z. Florjańczyk, E. Zygadło-Monikowska, G. Lapienis, J. Power Sources 194 (2009) 51.

57. Hekselman, M. Kalita, A. Plewa-Marczewska, G. Z. Żukowska, E. Sasim, W. Wieczorek, M. Siekierski, Electrochim. Acta 55 (2010) 1298.

58. T. Itoh, K. Hirai, T. Uno, M. Kubo, Ionics 14 (2008) 1.

59. T. Zhang, N. Imanishi, S. Hasegawa, A. Hirano, J. Xie, Y. Takeda, O. Yamamoto, N. Sammes, J. Electrochem. Soc. 155(12) (2008) A965.
60. C. Zhu, H. Cheng, Y. Yang, J. Electrochem. Soc. 155(8) (2008) A569.
61. T. Itoh, Y. Mitsuda, T. Ebina, T. Uno, M. Kubo, J. Power Sources 189 (2009) 531.
62. S. Adams, K. Hariharan, J. Maier, Solid State Ionics 75 (1995) 193.
63. S. Adams, K. Hariharan, J. Maier, Solid State Ionics 86-88 (1996) 503.
64. M. Tatsumisago, A. Hayashi, J. Non-Cryst. Solids 354 (2008) 1411.
65. A. Hayashi, Glass Tech.: Eur. J. Glass Sci. Technol. A 49(5) (2008) 213.
66. M. Tatsumisago, F. Mizuno, A. Hayashi, J. Power Sources 159 (2006) 193.
67. T. Minami, A. Hayashi, M. Tatsumisago, Solid State Ionics 177 (2006) 2715.
68. K. Minami, A. Hayashi, S. Ujiie, M. Tatsumisago, J. Power Sources 189 (2009) 651.
69. J. Trevey, J. S. Jang, Y. S. Jung, C. R. Stoldt, S. –H. Lee, Electrochem. Commun. 11 (2009) 1830.
70. J. W. Fergus, J. Power Sources 195 (2010) 4554.
71. S. Adams, J. Maier, Solid State Ionics 105 (1998) 67.
72. J. Swenson, S. Adams, Phys. Rev. B 64 (2001) 024204.
73. J. Kincs, S. W. Martin, Phys. Rev. Lett. 76 (1996) 70.
74. A. C. M. Rodrigues, R. Keding, C. Russel, J. Non-Cryst. Solids 273 (2000) 53.

75. A. C. M. Rodrigues, M. J. Duclot, Solid State Ionics 28-30 (1988) 729.

76. C. -H. Lee, K. H. Joo, J. H. Kim, S. G. Woo, H. -J. Sohn, T. Kang, Y. Park, J. Y. Oh, Solid State Ionics 149 (2002) 59.

77. Y. –I. Lee, J. –H. Lee, S. –H. Hong, Y. Park, Solid State Ionics 175 (2004) 687.

78. R. V. Salodkar, V. K. Deshpande, K. Singh, J. Power Sources 25 (1989) 257.

79. B. K. Money, K. Hariharan, Solids State Ionics 179 (2008) 1273.

80. F. Munoz, L. Montagne, L. Pascual, A. Duran, J. Non-Cryst. Solids 355 (2009) 2571.

81. V. K. Deshpande, A. Pradel, M. Ribes, Mater. Res. Bull. 23 (1988) 379.

82. J. P. Malugani, G. Robert, Mater. Res. Bull. 14 (1979) 1075.

83. P. P. Tsai, M. Greenblatt, J. Non-Cryst. Solids 103 (1988) 101.

84. J. Swenson, R. L. McGreevy, L. Borjesson, J. D. Wicks, Solid State Ionics 105 (1998) 55.

85. A. Hall, S. Adams, J. Swenson, J. Non-Cryst. Solids 352 (2006) 5164.

86. N. S. Rao, S. Bale, M. Purnima, K. S. Kumar, S. Rahman, J. Phys. Chem. Solids 68 (2007) 1354.

87. L. Abbas, L. Bih, A. Nadiri, Y. E. Amraoui, D. Mezzane, B. Elouadi, J. Mol. Struct. 876 (2008) 194.

88. L. Bih, L. Abbas, S. Mohdachi, A. Nadiri, J. Mol. Struct. 891 (2008) 173.

89. J. Swenson, A. Matic, C. Karlsson, L. Borjesson, C. Meneghini, W. S. Howells, Phys. Rev. B 63 (2001) 132202.
90. C. Karlsson, A. Mandanici, A. Matic, J. Swenson, L. Borjesson, Phys. Rev. B 68 (2003) 064202.
91. J. O. Isard, J. Non-Cryst. Solids 1 (1969) 235.
92. D. E. Day, J. Non-Cryst. Solids 21 (1976) 343.
93. H. Yamamoto, N. Machida, T. Shigematsu, Solid State Ionics 175 (2004) 707.
94. T. Minami, A. Hayashi, M. Tatsumisago, Solid State Ionics 136-137 (2000) 1015.
95. Y. Seino, K. Takada, B. –C. Kim, L. Zhang, N. Ohta, H. Wada, M. Osada, T. Sasaki, Solid State Ionics 177 (2006) 2601.
96. J. H. Kennedy, Z. Zhang, Solid State Ionics 28-30 (1988) 726.
97. T. Minami, K. Imazawa, M. Tanaka, J. Non-Cryst. Solids 42 (1980) 469.
98. C. Cramer, M. Buscher, Solid State Ionics 105 (1998) 109.
99. H. L. Tuller, D. P. Button, D. R. Uhlmann, J. Non-Cryst. Solids 40 (1980) 93.
100. T. Minami, Y. Takuma, M. Tanaka, J. Electrochem. Soc. 124 (1977) 1659.
101. M. Hosono, J. Kawamura, H. Itoigawa, N. Kuwata, T. Kamiyama, Y. Nakamura, J. Non-Cryst. Solids 244 (1999) 81.
102. S. Kumar, P. Vinatier, A. Levasseur, K. J. Rao, J. Solid State Chem. 177 (2004) 1723.

103. A. Bunde, M. D. Ingram, P. Maass, J. Non-Cryst. Solids 172-174 (1994) 1222.
104. S. W. Martin, C. A. Angell, J. Non-Cryst. Solids 83 (1986) 185.
105. A. Levasseur, J. C. Brethous, J. –M. Reau, P. Hagenmuller, Mater. Res. Bull. 14 (1979) 921.
106. J. B. Bates, N. J. Dudney, G. R. Gruzalski, R. A. Zuhr, Solid State Ionics 53-56 (1992) 647.
107. X. Yu, J. B. Bates, G. E. Jellison, F. X. Hart, J. Electrochem. Soc. 144 (1997) 524.
108. Y. Hamon, A. Douard, F. Sabary, C. Marcel, P. Vinatier, B. Pecquenard, A. Levasseur, Solid State Ionics 177(3-4) (2006) 257.
109. J. W. Long, B. Dunn, D. R. Rolison, H. S. White, Chem. Rev. 104 (2004) 4463.
110. K. -H. Joo, H. -J. Sohn, P. Vinatier, B. Pecquenard, A. Levasseur, Electrochem. Solid State Lett. 7 (2004) A256.
111. K. Minami, F. Mizuno, A. Hayashi, M. Tatsumisago, Solid State Ionics 178 (2007) 837.
112. Z. Zhang, J. H. Kennedy, Solid State Ionics 38 (1990) 217.
113. M. Tatsumisago, S. Hama, A. Hayashi, H. Morimoto, T. Minami, Solid State Ionics 154-155 (2002) 635.
114. A. Hayashi, S. Hama, H. Morimoto, M. Tatsumisago, T. Minami, J. Am. Ceram. Soc. 84(2) (2001) 477.
115. N. Machida, H. Yamamoto, S. Asano, T. Shigematsu, Solid State Ionics 176 (2005) 473.
116. J. P. Malugani, G. Robert, Solid State Ionics 1 (1980) 519.

117. H. Morimoto, H. Yamashita, M. Tatsumisago, T. Minami, J. Am. Ceram. Soc. 82(5) (1999) 1352.
118. M. Tatsumisago, H. Morimoto, H. Yamashita, T. Minami, Solid State Ionics 136-137 (2000) 483.
119. R. B. Schwarz, R. R. Petrich, C. K. Saw, J. Non-Cryst. Solids 76 (1985) 281.
120. H. –J. Fecht, Nanostruct. Mater. 6 (1995) 33.
121. S. Indris, D. Bork, P. Heitjans, J. Mater. Synth. Process. 8 (2000) 245.
122. K. Minami, A. Hayashi, M. Tatsumisago, J. Non-Cryst. Solids, In Press, doi:10.1016/j.jnoncrysol.2010.05.016.
123. W. H. Zachariasen, J. Am. Chem. Soc. 54 (1932) 3841.
124. R. A. B. Devine, J. Arndt, Phys. Rev. B 35 (1987) 9376.
125. G. N. Greaves, Glass Science and Technology, Vol. 4B, Academic Press, New York, 1990.
126. R. L. Mozzi, B. E. Warren, J. Appl. Cryst. 2 (1969) 164.
127. J. E. Shelby, Introduction to Glass Science and Technology, 2nd ed., Cambridge: RSC, 2005.
128. G. N. Greaves, J. Non-Cryst. Solids 71 (1985) 203.
129. H. Maekawa, T. Maekawa, K. Kawamura, T. Yokokawa, J. Non-Cryst. Solids 127 (1991) 53.
130. C. Larson, J. Doerr, M. Affatigato, S. Feller, D. Holland, M. E. Smith, J. Phys.: Condens. Matter 18 (2006) 11323.
131. R. Hanna, J. Phys. Chem. 69 (1965) 3846.
132. J. R. Ferraro, M. H. Manghnani, J. Appl. Phys. 43 (1972) 4595.

133. J. R. Ferraro, M. H. Manghnani, L. J. Basile, J. Appl. Phys. 44 (1973) 5391.

134. K. N. Dalby, P. L. King, American Mineralogist 91 (2006) 1783.

135. N. Umesaki, N. Iwamoto, J. Non-Cryst. Solids 106 (1988) 77.

136. S. A. Brawer, W. B. White, J. Chem. Phys. 63 (1975) 2421.

137. D. W. Matson, S. K. Sharma, J. A. Philpotts, J. Non-Cryst. Solids 58 (1983) 323.

138. R. Dupree, D. Holland, M. G. Mortuza, J. Non-Cryst. Solids 116 (1990) 148.

139. R. Dupree, D. Holland, P. W. McMillan, R. F. Pettifer, J. Non-Cryst. Solids 68 (1984) 399.

140. R. Dupree, D. Holland, D. S. Williams, J. Non-Cryst. Solids 81 (1986) 185.

141. J. F. Stebbins, J. Non-Cryst. Solids 106 (1988) 359.

142. S. J. Gurman, J. Non-Cryst. Solids 125 (1990) 151.

143. H. Doweidar, J. Non-Cryst. Solids 194 (1996) 155.

144. F. M. Ezz Eldin, N. A. El Alaily, Mater. Chem. Phys. 52 (1998) 175.

145. M. L. F. Nascimento, S. Watanabe, Mater. Chem. Phys. 105 (2007) 308.

146. A. Pedone, G. Malavasi, M. C. Menziani, A. N. Cormack, U. Segre, J. Phys. Chem. B. 110 (2006) 11780.

147. A. Pedone, G. Malavasi, A. N. Cormack, U. Segre, M. C. Menziani, Chem. Mater. 19 (2007) 3144.

148. H. Lammert, M. Kunow, A. Heuer, Phys. Rev. Lett. 90 (2003) 215901.

149. A. N. Cormack, Y. Cao, Mol. Eng. 6 (1996) 183.

150. H. Lammert, A. Heuer, Phys. Rev. B 70 (2004) 24204.

151. S. Sen, T. Mukerji, J. Non-Cryst. Solids 351 (2005) 3361.

152. U. Hoppe, G. Walter, A. Barz, D. Stachel, A. C. Hannon, J. Phys.: Condens. Matter 10 (1998) 261.

153. K. Suzuya, D. L. Price, C. K. Loong, S. W. Martin, J. Non-Cryst. Solids 232-234 (1998) 650.

154. B. Beagley, D. W. J. Cruickshank, T. G. Hewitt, Trans. Faraday Soc. 63 (1967) 836.

155. D. W. J. Cruickshank, Acta Crystallogr. 17 (1964) 677.

156. G. C. Hampson, A. J. Stiosick, J. Am. Chem. Soc. 60 (1938) 1814.

157. M. Jansen, B. Luer, Z. Kristallogr. 177 (1986) 149.

158. E. H. Arbib, B. Eloudi, J. P. Chaminade, J. Darriet, Solid State Chem. 127 (1996) 350.

159. D. Stachel, I. Svoboda, H. Fuess, Acta Crystallogr. C 51 (1995) 1049.

160. U. Hoppe, G. Walter, R. Kranold, D. Stachel, Z. Naturforsch. A 53 (1998) 93.

161. X. J. Xu, D. E. Day, Phys. Chem. Glasses 31 (1990) 183.

162. Y. B. Peng, D. E. Day, Glass Technol. 32 (1991) 200.

163. R. K. Brow, J. Non-Cryst. Solids 263-264 (2000) 1.

164. J. R. Van Wazer, Phosphorus and its Compounds, Volume 1, Interscience, New York, 1958.

165. J. J. Hudgens, R. K. Brow, D. R. Tallant, S. W. Martin, J. Non-Cryst. Solids 223 (1998) 21.

166. J. W. Wiench, M. Pruski, B. Tischendorf, J. U. Otaigbe, B. C. Sales, J. Non-Cryst. Solids 263-264 (2000) 101.

167. A. Pradel, T. Pagnier, M. Ribes, Solid State Ionics 17 (1985) 147.

168. M. Tatsumisago, Y. Kowada, T. Minami, J. Non-Cryst. Solids 150 (1992) 207.

169. J. J. Hudgens, S. W. Martin, J. Am. Ceram. Soc. 76 (1993) 1691.

170. R. K. Brow, C. A. Click, T. M. Alam, J. Non-Cryst. Solids 274 (2000) 9.

171. R. Gresch, W. Muller-Warmuth, H. Dutz, J. Non-Cryst. Solids 34 (1979) 127.

172. R. Bruckner, H. –U. Chun, H. Goretzki, M. Sammet, J. Non-Cryst. Solids 42 (1980) 49.

173. R. K. Brow, D. R. Tallant, J. J. Hudgens, S. W. Martin, A. D. Irwin, J. Non-Cryst. Solids 177 (1994) 221.

174. E. C. Onyiriuka, J. Non-Cryst. Solids 163 (1993) 268.

175. R. K. Brow, J. Non-Cryst. Solids 194 (1996) 267.

176. T. M. Alam, R. K. Brow, J. Non-Cryst. Solids 223 (1998) 1.

177. J. P. Fletcher, R. J. Kirkpatrick, D. Howell, S. H. Risbud, J. Chem. Soc. Faraday Trans. 89 (1993) 3297.

178. M. Tatsumisago, Y. Kowada, T. Minami, Phys. Chem. Glasses 29 (1988) 63.

179. G. Walter, J. Vogel, U. Hoppe, P. Hartmann, J. Non-Cryst. Solids 320 (2003) 210.

180. G. Walter, U. Hoppe, J. Vogel, G. Carl, P. Hartmann, J. Non-Cryst. Solids 333 (2004) 252.

181. R. K. Brow, D. R. Tallant, S. T. Myers, C. C. Phifer, J. Non-Cryst. Solids 191 (1995) 45.
182. K. Meyer, J. Non-Cryst. Solids 209 (1997) 227.
183. G. B. Pakhomov, S. L. Neverov, Solid State Ionics 119 (1999) 235.
184. U. Hoppe, G. Walter, R. Kranold, D. Stachel, J. Non-Cryst. Solids 263-264 (2000) 29.
185. K. Muruganandam, M. Seshasayee, S. Patnaik, Solid State Ionics 89 (1996) 313.
186. T. M. Alam, S. Conzone, R. K. Brow, T. J. Boyle, J. Non-Cryst. Solids 258 (1999) 140.
187. S. Adams, R. Prasada Rao, submitted to Physica Status Solidi B.
188. U. Hoppe, J. Non-Cryst. Solids 183 (1995) 85.
189. U. Hoppe, G. Herms, W. Gerike, J. Sakowski, J. Phys.: Condens. Matter 8 (1996) 8077.
190. U. Hoppe, J. Non-Cryst. Solids 195 (1996) 138.
191. T. Uchino, T. Yoko, J. Non-Cryst. Solids 263-264 (2000) 180.
192. E. D. Simandiras, D. G. Liakos, J. Phys. Chem. A 108 (2004) 3854.
193. D. G. Liakos, E. D. Simandiras, J. Non-Cryst. Solids 354 (2008) 1569.
194. R. L. McGreevy, J. Phys.: Condens. Matter 13 (2001) R877.
195. S. Adams, J. Swenson, J. Phys.: Condens. Matter 17 (2005) S87.
196. A. Karthikeyan, P. Vinatier, A. Levasseur, K. J. Rao, J. Phys. Chem. B 103 (1999) 6185.
197. J. -J. Liang, R. T. Cygan, T. M. Alam, J. Non-Cryst. Solids 263-264 (2000) 167.

198. T. M. Alam, J. -J. Liang, R. T. Cygan, Phys. Chem. Chem. Phys. 2 (2000) 4427.
199. M. Vogel, Phys. Rev. B 68 (2003) 184301.
200. R. K. Sistla, M. Seshasayee, J. Non-Cryst. Solids 349 (2004) 22.
201. S. Adams, Bull. Mater. Sci. 29(6) (2006) 587.
202. S. Adams, J. Swenson, Phys. Chem. Chem. Phys. 4 (2002) 3179.
203. S. Adams, J. Swenson, Solid State Ionics 175 (2004) 665.
204. A. Hall, S. Adams, J. Swenson, Ionics 10 (2004) 396.
205. L. Borjesson, L. M. Torell, U. Dahlborg, W. S. Howells, Phys. Rev. B 39 (1989) 3404.
206. L. Borjesson, L. M. Torell, W. S. Howells, Philos. Mag. B 59 (1989) 105.
207. G. Carini, M. Cutroni, A. Fontana, G. Mariotto, F. Rocca, Phys. Rev. B 29 (1984) 3567.
208. G. Chiodelli, A. Magistris, M. Villa, J. L. Bjorkstam, J. Non-Cryst. Solids 51 (1982) 143.
209. M. Doreau, A. A. E. Anouar, G. Robert, Mater. Res. Bull. 15 (1980) 285.
210. R. Prasada Rao, M. Seshasayee, Solid State Commun. 131 (2004) 537.
211. M. Horiuchi, T. Sei, T. Tsuchiya, J. Non-Cryst. Solids 177 (1994) 236.
212. A. Hall, S. Adams, J. Swenson, Phys. Rev. B 74 (2006) 174205.
213. M. Irion, M. Couzi, A. Levasseur, J. M. Reau, J. C. Brethous, J. Solid State Chem. 31 (1980) 285.

214. K. Tanaka, T. Yoko, H. Yamada, K. Kamiya, J. Non-Cryst. Solids 103 (1988) 250.

215. Y. Iwadate, H. Kenmotsu, T. Hattori, S. Nishiyama, K. Fukushima, N. Umeshki, T. Nakazawa, K. Noda, J. Alloys Compd. 305 (2000) 130.

216. K. Tanaka, T. Yoko, K. Kamiya, H. Yamada, S. Sakka, J. Non-Cryst. Solids 135 (1991) 211.

217. W. Muller, D. Kruschke, M. Torge, A. Grimmer, Solid State Ionics 23 (1987) 53.

218. Y. Ogiwara, K. Echigo, M. Hayana, J. Non. Cryst. Solids 352 (2006) 5192.

219. G. Garcia-Belmonte, J. Bisquert, J. Non-Cryst. Solids 337 (2004) 272.

220. J. C. Dyre, T. B. Schrøder, Rev. Modern Phys. 72 (2000) 873.

221. K. Funke, B. Roling, M. Lange, Solid State Ionics 105 (1998) 195.

222. M. D. Ingram, A. H. J. Robertson, Solid State Ionics 94 (1997) 49.

223. M. Vogel, Phys. Rev. B 70 (2004) 094302.

224. B. V. R. Chowdari, K. Radhakrishnan, J. Non-Cryst. Solids 108 (1989) 323.

225. A. Magistris, G. Chiodelli, M. Villa, J. Power Sources 14 (1985) 87.

226. A. P. Ahoussou, J. Rogez, A. Kone, J. Non-Cryst. Solids 353 (2007) 271.

227. G. Chiodelli, A. Magistris, M. Villa, Solid State Ionics 18-19 (1986) 356.

228. R. K. Brow, D. R. Tallant, J. Non-Cryst. Solids 222 (1997) 396.

229. V. Nazabal, E. Fargin, C. Labrugère, G. Le Flem, J. Non-Cryst. Solids 270 (2000) 223.

230. A. Levasseur, M. Menetrier, Mater. Chem. Phys. 23 (1989) 1.

231. E. I. Kamitsos, G. D. Chryssikos, J. Mol. Struct. 247 (1991) 1.

232. B. N. Meera, J. Ramakrishna, J. Non-Cryst. Solids 159 (1993) 1.

233. Y. H. Yun, P. J. Bray, J. Non-Cryst. Solids 44 (1981) 227.

234. R. K. Brow, R. J. Kirkpatrick, G. L. Turner, J. Am. Ceram. Soc. 73 (1990) 2293.

235. P. Y. Shih, Mater. Chem. Phys. 84 (2004) 151.

236. A. Hayashi, M. Nakai, M. Tatsumisago, T. Minami, C. R. Chimie 5 (2002) 751.

237. Y. H. Yun, P. J. Bray, J. Non-Cryst. Solids 30 (1978) 45.

238. J. F. Ducel, J. J. Videau, Mater. Lett. 13 (1992) 271.

239. J. F. Ducel, J. J. Videau, K. S. Suh, J. Senegas, Phys. Chem. Glasses 35 (1994) 10.

240. T. Feng, P. Linzhang, J. Non-Cryst. Solids 112 (1989) 142.

241. J. F. Ducel, J. J. Videau, M. Couzi, Phys. Chem. Glasses 34 (1993) 212.

242. M. Scagliotti, M. Villa, G. Chiodelli, J. Non-Cryst. Solids 93 (1987) 350.

243. J. Yifen, C. Xiangsheng, H. Xihuai, J. Non-Cryst. Solids 112 (1989) 147.

244. L. Koudelka, P. Mosner, J. Non-Cryst. Solids 293-295 (2001) 635.

245. M. Villa, M. Scagliotti, G. Chiodelli, J. Non-Cryst. Solids 94 (1987) 101.

246. T. Tsuchiya, T. Moriya, J. Non-Cryst. Solids 38-39 (1980) 323.

247. O. L. Anderson, D. A. Stuart, J. Am. Ceram. Soc. 37 (1954) 573.

248. D. Ravaine, J. L. Souquet, Phys. Chem. Glasses 18(2) (1977) 27.

249. D. Ravaine, J. L. Souquet, Phys. Chem. Glasses 19(5) (1978) 115.

250. M. D. Ingram, Mater. Chem. Phys. 23 (1989) 51.

251. A. M. Glass, K. Nassau, J. Appl. Phys. 51 (1980) 3756.

252. T. Minami, J. Non-Cryst. Solids 73 (1985) 273.

253. I. D. Brown, The Chemical Bond in Inorganic Chemistry – The Bond Valence Model, New York: Oxford University Press, 2002.

254. S. Adams, Acta Crystallogr. B, Struct. Sci. 57 (2001) 278.

255. S. Adams, J. Swenson, Solid State Ionics 154-155 (2002) 151.

256. S. Adams, softBV web pages: http://www.softBV.net (2003).

Chapter 2

Experimental Techniques

2.1. Introduction

This chapter will deal with the techniques utilized in this project to achieve the proposed objectives, which include both experimental and simulation techniques. The computer simulations, which include Molecular Dynamics (MD) simulation and Bond Valence (BV) approach, were conducted for all lithium silicate, halide-doped phosphate, and borophosphate glasses to visualize and analyze structure as well as ion conduction pathways in these glassy materials. Experimental synthesis and analysis were carried out for the halide-doped phosphate and borophosphate glasses. Density of these two glassy systems was determined by Archimedes' principle or Pycnometry. X-ray powder Diffractometry (XRD) was employed to confirm the glassy nature of prepared samples, while Differential Scanning Calorimetry (DSC) was used to reveal glass transition temperature (T_g). Scanning Electron Microscopy (SEM) with the aid of Energy Dispersive X-ray analysis (EDX) was exploited to find the exact composition of glassy samples after synthesis. Ionic conductivity of both halide-doped phosphate and borophosphate glasses was measured by Impedance Spectroscopy. In addition, Fourier Transformed Infrared (FT-IR), Raman and X-ray Photoelectron Spectroscopy (XPS) were further utilized to characterize the structure of lithium borophosphate glasses.

2.2. Glass synthesis

2.2.1. Lithium halide-doped phosphate glasses

Ternary glasses $yLiX - (1 - y)(0.60Li_2O - 0.40P_2O_5)$ glasses (where X = Cl, Br; y = 0, 0.10, 0.15, 0.20, 0.25) were prepared by conventional melt quenching. The starting raw materials used were ammonium dihydrogen phosphate ($NH_4H_2PO_4$), lithium carbonate (Li_2CO_3), and lithium halide salts (LiCl or LiBr). Appropriate amounts of $NH_4H_2PO_4$ and Li_2CO_3 were mixed, ground and kept in a platinum crucible at 300 ^{0}C for 1 hour to remove NH_3 and H_2O, and then heated up to 600 ^{0}C for 1 hour to remove CO_2 from the mixture. The mixture was subsequently melted at 800 ^{0}C for 30 minutes and stirred to homogenize the melt. After that, an appropriate amount of LiX was slowly added to the mixture inside the crucible at 800 ^{0}C, while stirring the melt. The melt was still kept at 800 ^{0}C for 5 minutes before quenching between two copper plates. To prevent the melt from crystallization, a fast quenching rate from a medium temperature range (800 ~ 200 ^{0}C) was very important. Furthermore, preheating the copper plates at 200 ^{0}C was helpful in avoiding shattering of the glassy samples during quenching. Both phosphate glasses and in particular the glasses with higher halide X content are hygroscopic, and thus have to be stored in a desiccator with silica. It was noticed that LiX partially evaporates during preparation and the amount of halide X present in the glass therefore had to be evaluated by Scanning Electron Microscopy (SEM) with the aid of Energy Dispersive X-ray (EDX) analysis, which will be mentioned later in this Chapter.

2.2.2. Lithium borophosphate glasses

Similar to halide-doped phosphate glasses, ternary borophosphate glasses $0.45Li_2O - (0.55 - x)P_2O_5 - xB_2O_3$ (where $0 \leq x \leq 0.55$) were also synthesized by conventional melt quenching method using $NH_4H_2PO_4$, Li_2CO_3 and boron oxide (B_2O_3) as starting materials. These analytical grade raw materials were thoroughly mixed, ground and heated in platinum crucibles at 600 ^{0}C for 1 hour to remove all the volatile products (NH_3, H_2O from $NH_4H_2PO_4$; CO_2 from Li_2CO_3). The mixture is then melted in the temperature range from 900 – 1100 ^{0}C for 30 minutes depending on composition (the melting temperature rises with the increase of B_2O_3 content). The homogenous melt was poured and quenched between two preheated (at 200 ^{0}C) copper plates to obtain glass samples with thickness ranging from 1 to 2 mm.

2.3. Experimental techniques

2.3.1. X-ray powder diffractometry

X-ray powder diffraction is a popular tool to obtain the information of atomic structure from solids such as space group, lattice constant, atomic positions, etc., of crystals. In a crystal, since the inter-planar spacing is generally of the order of several angstroms (Å), the atomic planes can diffract electromagnetic waves, like X-rays, whose wavelength is comparable to the inter-planar spacing. A monochromatic X-ray beam will be diffracted if the Bragg condition is satisfied:

$$n_O\lambda = 2d\sin\theta \quad (2.1)$$

where n_O is an integer that provides the order of diffraction, λ is the X-ray wavelength, d is the inter-planar spacing, and θ is the glancing angle between the incident beam and the scattering atomic planes. In practice, the diffraction angle is commonly specified as 2θ rather than θ.

It is well known that in the amorphous materials there is no long-range periodic structure, and thus Bragg's law is inappropriate. Therefore, unlike the crystals, the amorphous materials do not produce an X-ray or electron diffraction patterns with sharp Bragg peaks. Instead, characteristic diffuse haloes are observed. In the present study, the glassy nature of bulk glasses were characterized by X-ray powder diffractometry (XRD) using Cu Kα radiation (PANalytical X'Pert PRO, equipped with a fast linear X'Celerator detector, which can collect 100 steps at the same time). XRD data were collected in the 2θ range $10 - 80^0$ with a nominal scan rate of $70s.step^{-1}$ and a step size of 0.05^0 at room temperature. It is expected that only haloes and no sharp Bragg peaks are observed for the glasses.

2.3.2. Density measurement

Density of bulk glasses was measured using the Archimedes' principle with either density determination kit Mettler ME-3360 or a Pycnometer (AccuPyc 1330, Micromeritics).

For Mettler ME-3360, a liquid, such as toluene, with a known density ρ_0 was used as an immersing medium. The bulk glass was first weighed in air, then immersed into the toluene medium and weighed again. From these two weighings, the density of glass is calculated as:

$$\rho = \frac{W_a}{W_a - W_i} \cdot \rho_0 \qquad (2.2)$$

where W_a is the weight of the bulk glass in air, W_i is its weight when immersed in toluene, and ρ_0 is the density of toluene at a given temperature T (ρ_0 = 0.8669 g/ml at 20 ^{0}C).

In the AccuPyc 1330 Pycnometer, the amount of immersion fluid (helium gas) displaced by the sample (solid phase) was measured. The Pycnometer measures the sample volume by measuring the pressure change of helium and therefrom determines the density (incorporating the sample weight from external measurement). For each sample, the density value has been determined by taking the average of 10 volume measurements.

2.3.3. Scanning Electron Microscopy

Scanning electron microscopy (SEM) is a widely used technique in materials research. SEM uses a high-energy beam of incident (or primary) electrons for scanning the specimen surface to create 3-dimensional images (micrographs). The primary electrons are normally accelerated through a potential of 10 – 200 keV. When the primary electrons hit the specimen surface, their interaction with the specimen can be both elastic and inelastic. Back-scattered electrons (BSE) are the high-energy electrons (E_{BSE} > 50 eV) generated from an elastic interaction between the primary electrons and nuclei

of specimen atoms. Secondary electrons (SE) are lower-energy electrons ($E_{SE} \leq 50$ eV) produced by an inelastic interaction between the primary electrons and electrons of specimen atoms. These SE electrons are actually the valence electrons bombarded out of specimen atoms by the high-energy primary electron beam. In SEM, micrographs are often created from SE mode.

In addition to SE and BSE electrons, X-rays are also emitted when the primary electron beam strikes the specimen surface. Since X-ray energy is characteristic of the element from which X-rays were produced, they are effectively utilized in the Energy Dispersive X-ray spectroscopy (EDX) for elemental analysis. In principle, EDX is equipped with X-ray detector to detect characteristic X-rays emitted from the specimen. Depending on the type of window situated in front of the EDX detector, EDX can identify elements with atomic number $Z \geq 11$ (for Be window) or $Z \geq 4$ (for windowless detector or ultra-thin window).

In the present work, SEM (Philips XL-30 FE-SEM) equipped with EDX (EDAX XL-30, ultra-thin window) was employed to analyze the experimental composition of glassy samples after synthesis. In practice, the EDAX XL-30 model can detect the elements with $Z \geq 5$, i.e. from boron (B) onwards.

2.3.4. Differential Scanning Calorimetry

Thermal analysis in a material is conducted by observing changes in its physical and chemical properties as a function of temperature and time. Differential Scanning Calorimetry (DSC) is a common technique for determination of melting point of crystals, glass transition (T_g) and

crystallization temperatures of glasses. In principle, DSC measures the difference in the amount of heat energy (enthalpy) required to keep both sample (encapsulated inside an aluminum (or copper) pan) and the reference material (an empty aluminum (or copper) pan) at the same temperature, when both the sample and the reference are heated at a controlled (usually linear) rate. The calorimetric measurement is always carried out in an inert gas atmosphere, e.g. nitrogen (N_2).

Figure 2.1 shows a typical DSC curve for a glass on heating process. The first feature appearing in this curve is the glass transition temperature (T_g). The discontinuous change in the specific heat of the glassy sample, which happens when the glass converts from a solid to a liquid in the glass transformation region, is the indicative of T_g. In practice, T_g value of glass is determined by the intersection of the two tangents at the start of DSC endotherm, as shown in Figure 2.2. The second feature in the DSC curve (cf. Figure 2.1) is the exothermic peak due to crystallization of the glass, which involves the evolution of energy [1]. The third feature at the highest temperature in the DSC curve (cf. Figure 2.1) is the endothermic peak due to melting (the process is accompanied by the absorption of energy) of the crystals (formed during heating of glass).

In the present study, the glass transition temperature (T_g) of the investigated glasses was obtained by using DSC (TA Instruments 2920 Modulated DSC) at a heating rate of 10 $K.min^{-1}$ in the temperature range of 100 – 700^0C under constant flow of high purity N_2 gas.

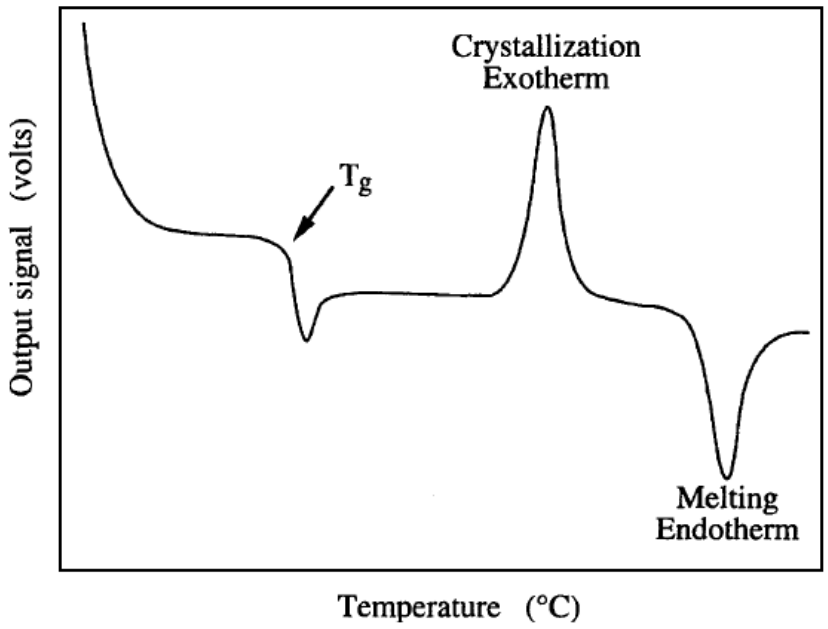

Figure 2.1. DSC curve exhibiting a change in specific heat at the glass transformation, an exothermic peak due to crystallization of the glass, and an endotherm due to melting of the crystals formed at the exotherm. Reproduced from Ref. [1].

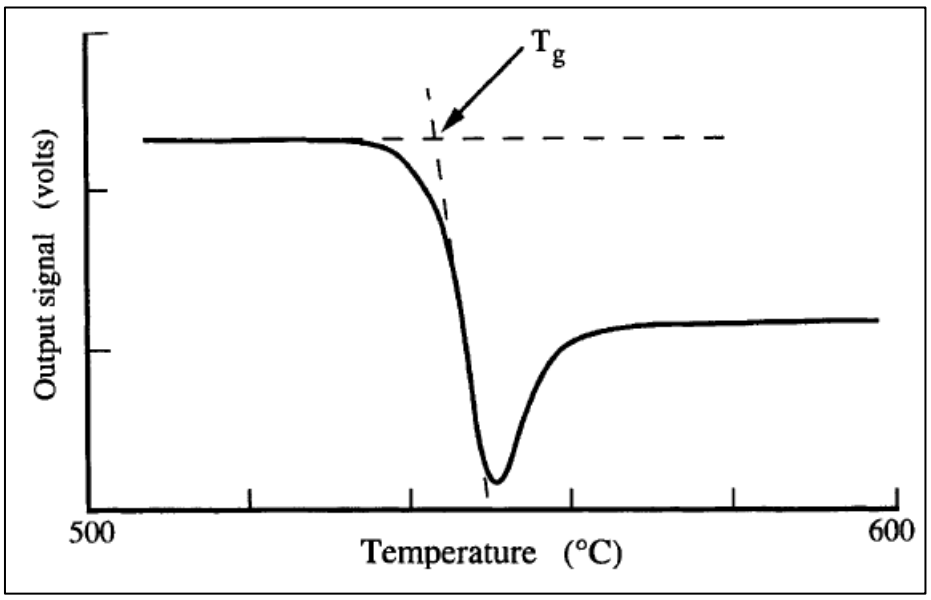

Figure 2.2. An example of the determination of T_g from a DSC curve. Reproduced from Ref. [1].

2.3.5. Fourier Transform – Infrared Spectroscopy

Fourier Transform – Infrared spectroscopy (FT-IR) is a preferred technique of infrared (IR) spectroscopy to identify the molecular compounds and local structures of materials. When an infrared light beam passes through a sample, some of the IR is absorbed by the sample while the other is passed through (transmitted). The IR wavelengths absorbed by the sample are characteristic of its molecular structure. The IR spectra can be presented in either transmission or reflection mode. The molecular vibrations appear as dips in the transmission spectra, and as peaks in the absorption and reflection spectra.

FT-IR employs an interferometer to encode all the wavelengths from the IR source. A detector is used to measure the intensity of transmitted or reflected light at each wavelength. The resulting signal from the detector is then analyzed with computer using the Fourier transformation to achieve the final FT-IR spectrum for study. The FT-IR spectra are normally portrayed as the percentage of light transmittance or absorbance versus wave number (in cm^{-1}), which is the reciprocal of wavelength.

In this work, FT-IR spectrometer (Varian Excalibur HE 3100 FTIR) in the wave number range of 400 – 4000 cm^{-1} (with the resolution of 4 cm^{-1}) at room temperature was utilized to investigate the structure of lithium borophosphate glasses. Dry potassium bromide (KBr) powder (with a quantity of 0.1 – 0.15 g) and a very small amount of glassy powder were mixed, grinded and then compressed to form thin pellets for measurements.

2.3.6. Raman Spectroscopy

Together with FT-IR spectroscopy, Raman spectroscopy is an indispensible tool for obtaining information about molecular structure of materials. Raman spectroscopy is a light scattering technique, where the energy of incoming photon is altered by an inelastic interaction between the photon and sample molecule. The scattered photon may have lower (Stokes – Raman scattering) or higher (anti-Stoke – Raman scattering) energy than that of the incident photon. The continuous-wave monochromatic lasers in the visible region such as Argon (λ = 351.1 – 514.5 nm), Krypton (λ = 337.4 – 676.4 nm), Helium-Neon (λ = 632.8 nm) are widely employed as an excitation source in Raman spectrometers. The basic components of Raman spectrometer are excitation source, sample illumination and light collection system, wavelength selector, detector, and computer processing system.

A typical Raman spectrum is plotted as intensity of the scattered light versus the energy difference between the incoming light and the scattered light. In Raman spectrum, the energy is usually presented as wave number (in cm^{-1}), and each energy peak represents a Raman shift from the incident photon energy.

In the present investigation, Raman spectrometer (Jobin Yvon Horiba MicroRaman HR800) using Argon ion green laser (λ = 514 nm) was used to characterize the structure of lithium borophosphate glasses. Data were collected at 4.16 cm^{-1} spectral resolution and an integration time of 30s. After that, Raman spectra were deconvoluted using the software PeakFit (version 4)

to clarify the influence of mixed glass former effect on the structure change.

2.3.7. X-ray Photoelectron Spectroscopy

X-ray photoelectron spectroscopy (XPS) is an analytical technique, which is sensitive to near-surface volume and widely applied for chemical characterization of solid materials. When a sample is irradiated with a monochromatic X-ray source under ultra-high vacuum environment, the absorption of the incident photons causes the emission of core-level electrons from atoms in the sample. The emitted core-level electrons have a kinetic energy (E_K) given by:

$$E_K = h\nu - E_B - \varphi \tag{2.3}$$

where $h\nu$ is the energy of incident photon, E_B is the binding energy of core electron in the atom, and φ is the work function defined as the potential difference between the Fermi level of material and the vacuum level.

In addition to the ejected core electron, Auger electron or characteristic X-ray is also emitted when an outer electron fills the vacancy left by the core electron. Both emitted core electron and Auger electron can be analyzed in the XPS. The present work mainly deals with the photoemissions from the core electrons (or photoelectrons).

A typical XPS spectrum is presented as the intensity (which is the number of emitted photoelectrons, in counts per second) versus their binding energy (in eV). In the spectrum, the E_B value of each peak is characteristic of one specific element present in the material, while the area under each peak is

indicative of relative amount of the element. The chemical states of the element (e.g. bridging and non-bridging in case of oxygen, etc.) is recognized by shape and position of the peak.

In the present study, X-ray photoelectron spectrometer (A Kratos Axis Ultra DLD XPS) using Al Kα monochromatic X-ray source of 1486.69eV with the vacuum of 10^{-10} mbar was utilized to investigate the structure of lithium borophosphate glasses. Besides the survey scans, high resolution scans for all elements (O1s, Li1s, B1s, and P2p) were conducted using 10eV band-pass energy. Drift of the electron binding energy (E_B) due to a surface charging effect was calibrated by referencing the measured E_B to the C1s peak (E_B = 284.6eV) of adventitious hydrocarbon impurity. Curve fitting and deconvolution of O1s spectra were carried out using the software XPSPeak (version 4.1) to quantify the influence of mixed glass former effect on the structure modification.

2.3.8. Electrochemical Impedance Analysis

To understand ion conduction mechanism, the most straightforward technique is the direct measurement of electrical conductivity. A particular problem when applying a DC bias to a sample via two standard metal electrodes is polarization at the electrodes due to the failure of the mobile ions to traverse the electrolyte/electrode interface (ionic current drops to zero). This problem may, in some cases, be solved by special four probe DC techniques such as the van der Pauw method, or two reversible electrodes (e.g. mixed conductors) which will allow ion transport across the electrolyte – electrode interface [2]. Nevertheless, AC techniques are generally simpler and more

applicable to conduct conductivity studies than their DC counterparts.

In AC impedance measurement, a small potential perturbation is applied to the sample. The AC response to the applied perturbation, which is normally sinusoidal, can be different in phase and amplitude from the applied signal. Data from the measurement must be collected at short times, otherwise diffusion rather than kinetics becomes the rate determining process. Measurement of the phase difference and the amplitude (i.e. the impedance) allows analysis of the electrode process relating to contributions from diffusion, kinetics, double layer capacitance, coupled homogeneous reactions, etc. It is widely applied in studies of ionic solids, solid electrolytes, conducting polymers, corrosion, membranes and liquid/liquid interfaces [3].

Electrochemical impedance is generally measured by applying an AC potential to an electrochemical cell, and then measuring the AC current through the cell. Assume that a sinusoidal potential:

$$E(t) = E_0 \exp(j\omega t) \tag{2.4}$$

is applied. Then the AC current responding to this potential can be expressed as follows [4]:

$$I(t) = I_0 \exp(j\omega t - j\psi) \tag{2.5}$$

The complex impedance (Z) can be determined by:

$$Z = \frac{E}{I} = Z_0 \exp(j\psi) = Z_0(\cos\psi + j\sin\psi), \tag{2.6}$$

where ω is the frequency, and ψ is the phase difference between the applied potential and response current.

As seen from Equation (2.6), the expression for Z(ω) consists of a real and an imaginary part. If the real part (Z') and the imaginary part (Z") multiplied by -1 are presented on the X axis and the Y axis respectively, a "Nyquist plot" is obtained, as shown in Figure 2.3. It should be noticed that in the Nyquist plots (cf. Figure 2.3) of electrochemical impedance spectroscopy data each point corresponds to the impedance at one specific frequency; low frequency data are on the right-hand side, while those of higher frequencies are on the left-hand side of the plot.

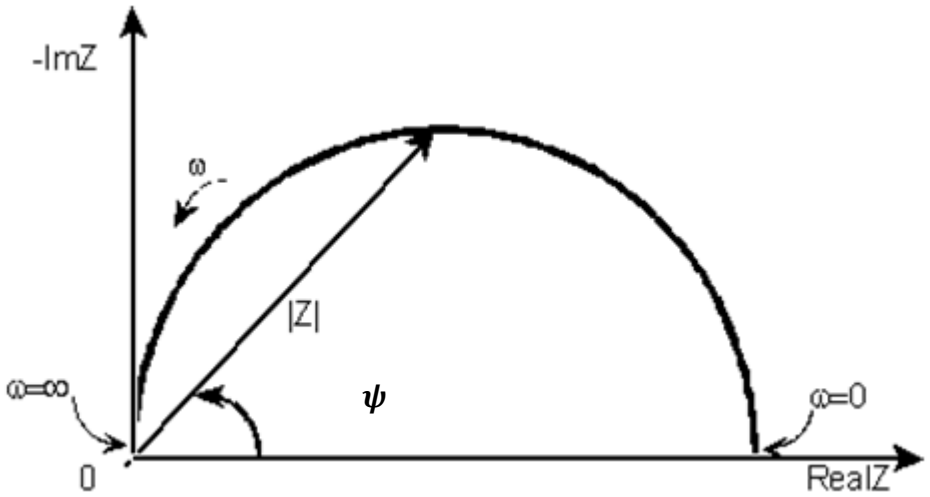

Figure 2.3. Nyquist plot with impedance vector. Reproduced from Ref. [5].

For glassy solid electrolyte materials, the Nyquist plot generally looks like Figure 2.4 [6 – 9]. The Equivalent Circuit of Figure 2.4 is shown in Figure 2.5. C_b is the geometric capacitor between the electrodes; CPE is a constant phase element due to the polarization distribution at the interface between blocking electrodes and glass. Normally, we are mostly interested in R_b, which characterizes the bulk DC resistance of the glass.

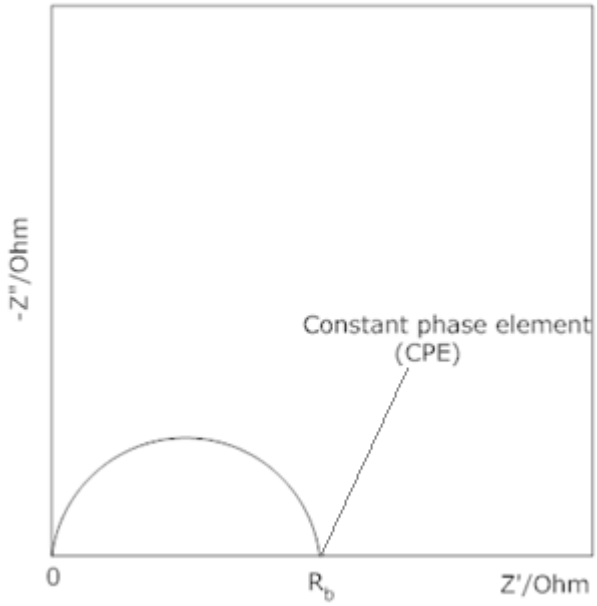

Figure 2.4. Nyquist plot of impedance for a glassy solid electrolyte with ion blocking electrodes.

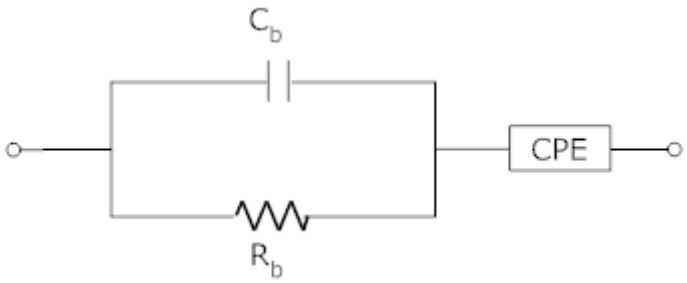

Figure 2.5. Equivalent circuit of Figure 2.4 with ion blocking electrodes.

In the case of glass ceramics, the Nyquist plot is generally described as Figure 2.6 and the corresponding equivalent circuit looks like Figure 2.7(b) [10, 11]. C_b and R_b are the capacitance and resistance attributed to the bulk, respectively. C_{gb} and R_{gb} are the capacitance and resistance due to grain boundary, and CPE is due to the polarization distribution at the interface between the electrolyte and ion blocking electrodes.

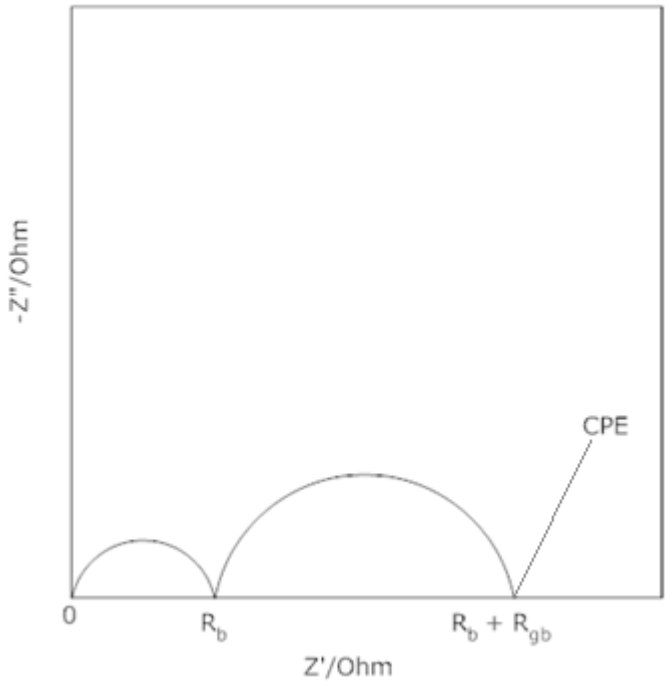

Figure 2.6. Nyquist plot of impedance for a glass-ceramic solid electrolyte with ion blocking electrodes.

The situation is comparable to the brick-layer model that has been derived for polycrystalline samples with (highly conducting) grain boundaries. This model distinguishes bulk, space charge layers and grain boundary core regions (which in the case of glass ceramics with a predominant crystalline phase may be identified with the residual glass matrix between the crystallites). The high frequency semicircle then includes both contributions from the bulk and the space charge zones of the parallel grain boundaries. The in-series contributions from perpendicular grain boundary cores appear as a separate low frequency semicircle and CPE is due to the polarization distribution at the interface between the electrolyte and ion blocking electrodes. Figure 2.7 shows the equivalent circuit for this situation.

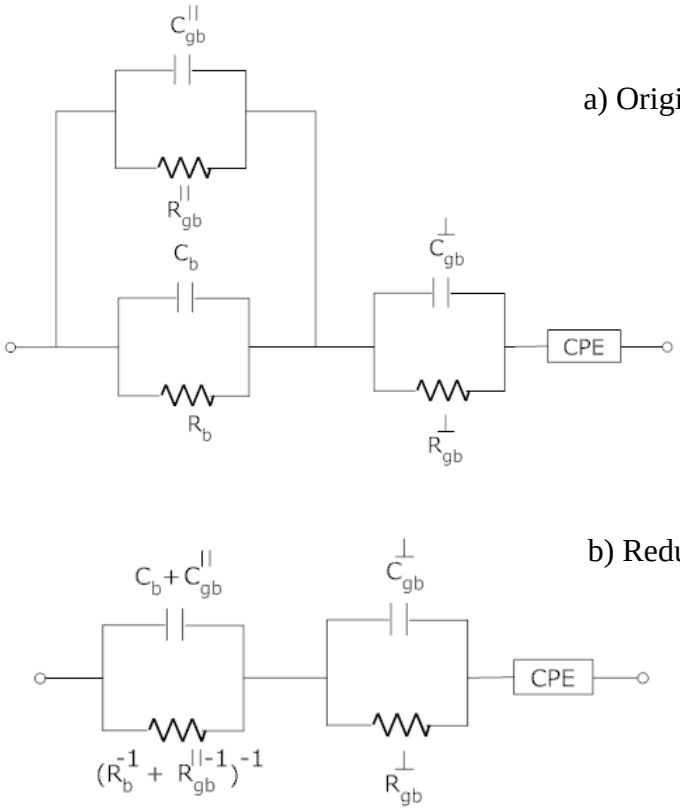

Figure 2.7. Equivalent circuit of Figure 2.6 according to the Brick-layer model. $C_{gb}^{\parallel}$, $R_{gb}^{\parallel}$ are the capacitance and resistance due to parallel grain boundary; $C_{gb}^{\perp}$, $R_{gb}^{\perp}$ are the capacitance and resistance due to perpendicular grain boundary.

In this study, ionic conductivity measurements of the halide-doped lithium phosphate and borophosphate glasses were carried out at different temperatures using the electrochemical impedance spectroscopy (Schlumberger Solartron SI 1260) in the frequency range of 1Hz to 15MHz. Commercially available Ag paint (ion blocking electrode) was applied on both sides of the glass sample to achieve a controlled contact area for the ionic conductivity determination. The sample was kept in a Kiel-type Electrochemical Cell (Ionic Systems), as shown in Figure 2.8. At each temperature the sample was kept for 10 min for thermal equilibration.

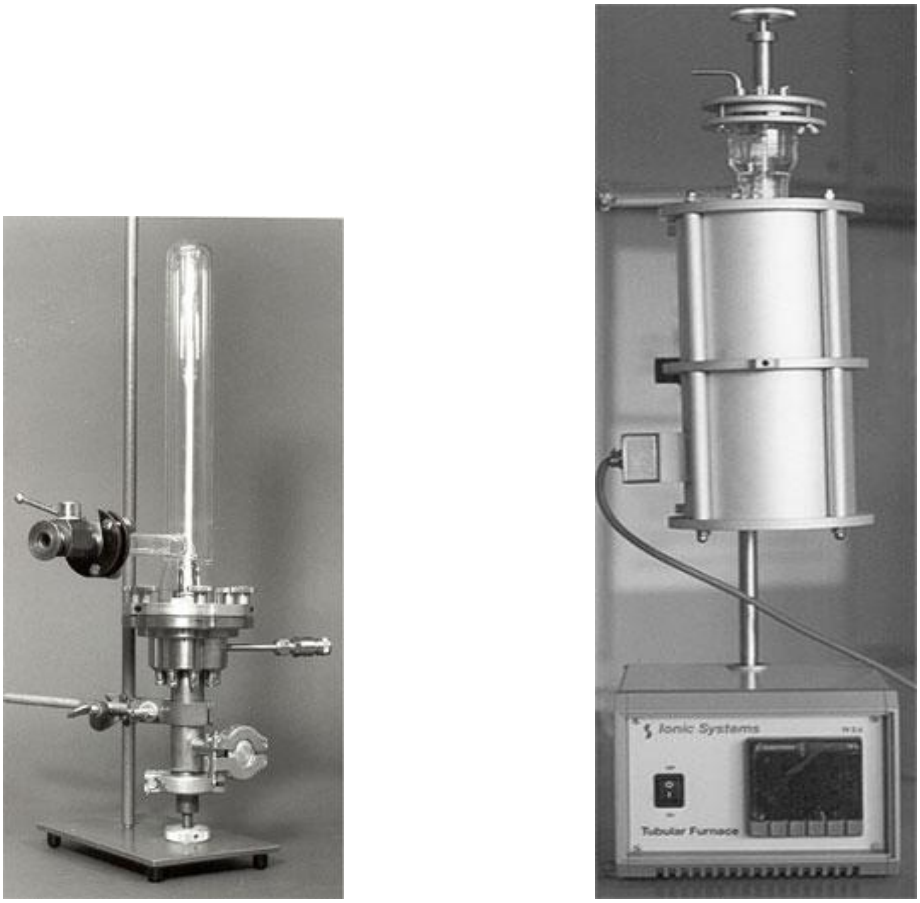

Figure 2.8. L.H.S.: A high-vacuum gas-tight quartz glass cylinder, in which sample is held to protect the arrangement from the air. R.H.S.: Set-up for ionic conductivity measurement at various temperatures, where the quartz glass cylinder is put inside the tubular furnace (with a temperature controller).

2.4. Computer simulation techniques

2.4.1. Molecular Dynamics Simulation

In the past, physical theories could only be tested in very simple cases; however, many problems of interest fall beyond the ability of computation power. With high-speed and low-cost personal computers, computer simulation becomes a very important tool in science today [12]. By setting simulation conditions very closely to experimental ones, the results obtained from simulation are convincingly comparable to those of experiment.

Furthermore, some experimentally inaccessible circumstances can also be predicted using these credible simulation models [13]. For conduction mechanism studies, a direct identification of the diffusing species in the electrolyte is very difficult when using experiment techniques. However, in Molecular Dynamics simulation, the motion of each single atom can be traced, and hence details inside a system can be clarified.

Molecular dynamics (MD) simulation is a deterministic simulation technique, which is commonly employed to provide information on macroscopic systems. It can be considered as a simulation of the evolution of a system over a certain time interval. In classical MD simulations, the motion of atoms obeys the laws of classical mechanics, i.e. Newton's equation,

$$F_i = m_i a_i(t) \tag{2.7}$$

where F_i is the force acting on atom i by surrounding atoms, m_i and a_i are the mass and the acceleration of atom i, respectively.

Positions (r) and velocities (v) of a particle at the next Δt are calculated as shown in Equations 2.8, 2.9, 2.10 using Verlet velocity algorithm [14]. The movement trajectory of the particle is shown in Figure 2.9.

$$r(t + \Delta t) = r(t) + \Delta t \cdot v(t) + \frac{\Delta t^2}{2m} F(t) \tag{2.8}$$

$$F(t + \Delta t) = -\nabla U(r(t + \Delta t)) \tag{2.9}$$

$$v(t + \Delta t) = v(t) + \frac{\Delta t}{2m} [F(t) + F(t + \Delta t)] \tag{2.10}$$

where U(r) is the potential energy of a system.

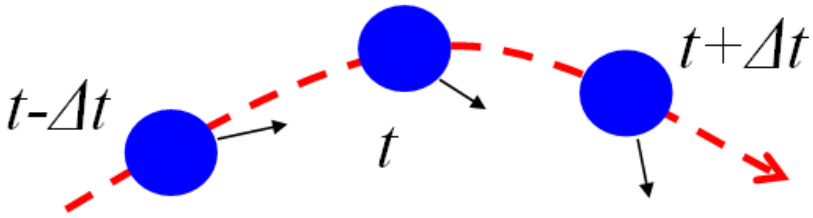

Figure 2.9. Trajectory of a particle in the Molecular Dynamics (MD) simulation.

Periodic boundary conditions (cf. Figure 2.10) are usually applied to the simulated system to eliminate the effect of unrealistic surface energies. After the system has reached its equilibrium, physical properties (which are generally a function of particle coordinates and velocities) can be determined by calculating their time averages over the system trajectory. Physical properties like energy, temperature, pressure, mean square displacement, pair correlation function and running coordination number are the most commonly measured.

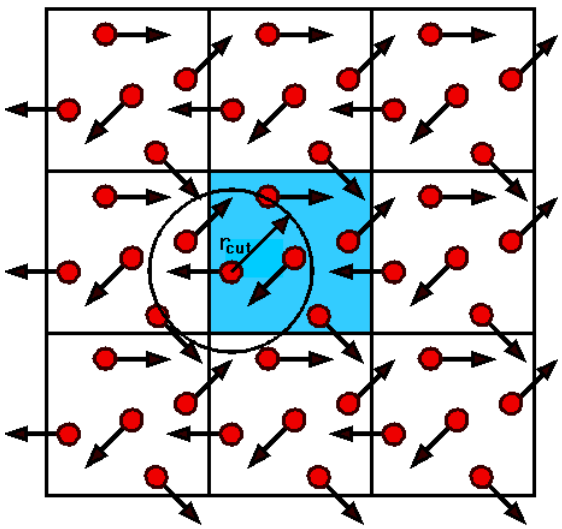

Figure 2.10. Illustration of periodic boundary conditions. Reproduced from Ref. [15].

The DL_POLY package has been used for MD simulations in the present work. From the measured density, size L of cubic cell (simulation cell) is determined. Typically, a few thousand atoms are taken for simulation, which usually (i.e. in not too complex glass systems) proved to be sufficient to get most of the macroscopic physical properties such as the diffusion coefficient. There are still properties which depend on the cell size. For example, MD simulation cannot give information on medium range order existing above L/2. The circumferential effect of the cell is taken care of by asserting that the ions are surrounded by replicas of the basic cell in all directions (periodic boundary condition).

Four main types of statistical ensembles used in MD simulations are **Microcanonical ensemble** (NVE; where the system has constant number of particles (N), volume (V) and energy (E)), **Canonical ensemble** (NVT; where N, V and temperature (T) are constant), **Isothermal-Isobaric ensemble** (NPT; where N, pressure (P) and T are constant) and **Grand canonical Ensemble** (μVT; where chemical potential (μ), V and T are constant). Among these ensembles, NVT was utilized for the studies of ion dynamics in all the investigated glasses.

In order to successfully explain the material properties by MD simulation, the selection of suitable potential parameters is an absolute necessity. There are various ways to obtain interatomic potentials for the simulation. The most accurate way is to compute the potential quantum mechanically using wave functions and the Schroedinger's equation by ab-initio methods. However, it is computationally very expensive. Alternatively, optimization techniques can be

used to achieve the interatomic potentials. Since the interatomic potentials in glasses are not very different from those in their crystalline counterparts, the structure and properties of the corresponding crystalline analogs can be used to optimize the potentials.

2.4.2. Computation of Physical Properties

2.4.2.1. Pair Correlation Function

Pair Correlation Function (PCF) provides information about the distribution of atoms j around atoms i, and is calculated using the following relationship:

$$g_{ij}(\delta) = \frac{1}{4\pi\delta^2\rho_j}\left(\frac{dN_j}{d\delta}\right) \tag{2.11}$$

where g_{ij} is the pair correlation function, ρ_j is the number density of atoms j. N_j is the mean number of atoms j lying between radii δ and (δ + dδ) around an atom i in a spherical shell centered at atom i.

2.4.2.2. Running Coordination Number

Running Coordination Number (RCN) gives information about the number of atoms j around an atom i up to a distance δ', and is determined as follows:

$$N_{ij}(\delta') = 4\pi\rho_j \int_0^{\delta'} \delta^2 g_{ij}(\delta) d\delta \tag{2.12}$$

where N_{ij} is the running coordination number.

In the present MD simulations, PCF and RCN were utilized in the process of deriving the optimized interatomic potentials for reproducing the structure of the investigated halide-doped phosphate and borophosphate glasses.

2.4.2.3. Mean Square Displacement, Self-diffusion Coefficient and Ionic Conductivity

Mean Square Displacement (MSD) can be expressed by the following equation:

$$\mathrm{MSD} = \langle [\mathrm{r}(\mathrm{t}_0) - \mathrm{r}(\mathrm{t}_0 + \tau)]^2 \rangle \tag{2.13}$$

where $\mathrm{r}(\mathrm{t}_0)$ and $\mathrm{r}(\mathrm{t}_0 + \tau)$ are the positions of a particle at the time t_0 and $\mathrm{t}_0 + \tau$ respectively; τ is the time step and $\langle \ldots \rangle$ symbolizes the ensemble average over the time steps.

Self-diffusion coefficient (D) is then determined from the slope of the linear part of MSD curve by the relation:

$$\mathrm{D} = \frac{1}{6} \frac{\mathrm{d}(\mathrm{MSD})}{\mathrm{d}\tau} \tag{2.14}$$

By applying the Nernst-Einstein relation between self-diffusion coefficient and ionic conductivity (cf. Equation (1.13) in Chapter 1), values of MD-simulated ionic conductivity of the investigated glasses can be calculated and compared to those measured from impedance spectroscopy.

2.4.3. Bond Valence Approach

Chemical bond is one of the most valuable concepts to appreciate the structures and properties of inorganic compounds. Empirical relationships between bond length and bond valence (BV) are widely used to identify plausible equilibrium sites for an atom in a crystal structure as sites where the BV sum of the atom matches its oxidation state [16]. A modification of the BV approach that improves the assessment of non-equilibrium site energies by a systematic adjustment of BV parameters to the bond softness [17 – 24] extends the application range of this simple tool to structure – property relationship studies in solid electrolytes.

In the BV approach, the bond valence s_{A-X} between a mobile ion A and an immobile counterion X can be estimated using the following empirical relationship:

$$s_{A-X} = \exp\left[\frac{(R_0 - R)}{b}\right] \tag{2.15}$$

where R is the bond length between a mobile ion A and an immobile counterion X, R_0 (the bond length of unit valence) and b are empirical parameters achieved from the refinement of well-defined crystal structures.

The bond valence sum V(A) of the ion A for bonds to all its adjacent counterions X is then calculated as:

$$V(A) = \sum_{X} s_{A-X} \tag{2.16}$$

The mismatch of the bond valence sum $|\Delta V(A)|$ is defined as the absolute

difference between the V(A) at the investigated site and the ideal bond valence sum (V_{id}(A)) of the ion A at the equilibrium site (which equals its oxidation state). The "accessible" sites for a mobile ion A in a local structure model can be identified as sites where |ΔV(A)| values remains small. However, to enhance the chemical plausibility of BV mismatch 'energy landscapes', |ΔV(A)| further contains a penalty function, p_{A-X}, that (i) discriminates against sites where a matching V(A) is achieved by unfavourable strongly asymmetric coordinations [20, 21, 24 – 26], and (ii) is complemented by truncated Coulomb repulsions between mobile and immobile cations only (e.g. Li and Si for lithium silicates, Li and P for lithium phosphates, etc) as well as soft coordination number constraints of mobile cation A (which is Li^+ ion in this study). A complete description of |ΔV(A)| is hence as follows:

$$|\Delta V(A)| = \left| \sum_X s_{A-X} - V_{id}(A) \right| + \sum_X p_{A-X} \tag{2.17}$$

where the penalty function, p_{A-X}, can be described by:

$$p_{A-X} = \begin{cases} \left(s_{A-X} - \frac{V_{id}}{CN_{min}} \right)^2, \text{if } s_{A-X} > \frac{V_{id}}{CN_{min}} \\ 0 \qquad\qquad\qquad\quad , \text{if } s_{A-X} < \frac{V_{id}}{CN_{min}} \end{cases} \tag{2.18}$$

where CN_{min} is the minimum coordination number, whose choice has to consider whether multiple bonds are possible for the respective atomic pair.

The bond valence sum mismatch |ΔV(A)| has been utilized to reveal transport pathways of mobile ions in various studies [20 – 23, 27 – 32]. In contrast to most conventional BV parameter sets, our *softBV* parameters [18]

are based on the assumption that not only the counterions of the first coordination shell but all counterions up to a cut-off radius of 4–8 Å (depending on sizes and polarisabilities of the ions involved) contribute to V(A). This is indispensable for modelling ion transport pathways as it avoids artefacts in the BV sum variation, when an ion moves across the border of its coordination shell. BV ion transport pathway models are based on the supposition that paths between accessible sites, along which $|\Delta V(A)|$ remains sufficiently low, represent probable ion transport paths. Isosurfaces of fixed maximum BV sum mismatch $|\Delta V(A)|$ for a certain ion type A will thus enclose regions that an A ion in the pathway may reach with a certain activation energy, E_a (as discussed more in detail in [24], E_a is proportional to $\Delta V(A)^2$). Low BV mismatch regions that include both occupied and vacant sites, therefore, enable local jumps of A. A long-range transport requires pathways that extend through the whole structure (cf. Figure 2.11). For periodic models this is equivalent to spanning the model box.

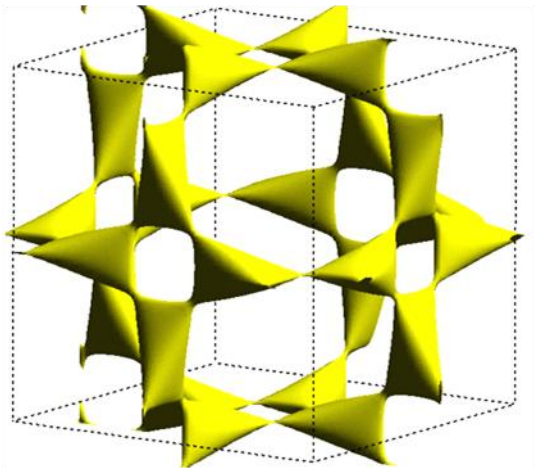

Figure 2.11. Ag^+ conduction pathways in α-AgI after Adams et al. [25].

In BV analysis, a volume element with a size of ca. $(0.2\ Å)^3$ is considered to belong to the conduction pathway if $|V(A) - V_{id}(A)|$ is below a fixed threshold value or if the sign of $(V(A) - V_{id}(A))$ alters within the volume element (the second condition cushions effects of the limited grid resolution). Accessible volume elements that share common faces or edges belong to the same 'pathway cluster'. It is assumed that these pathway clusters contribute to dc conductivity only if they percolate through the structure model. The volume fraction, F, of the percolating pathways turns out to be a suitable measure of E_a and thereby (in the case of glasses) also of the room temperature conductivity. The remaining restricted pathway clusters are considered to contribute only to ac conductivity.

As discussed in Ref. [21], a comparison of pathways for different types of mobile ions requires a mass scaling because for a fixed pathway volume fraction, the lighter cations with a higher polarizing power show higher values of activation energy and correspondingly reduced absolute conductivities. The polarisability differences should be reflected in the bond valence parameters and thus be already incorporated in the calculation of F, whereas the mass of the cation (M) does not directly modify the calculation of the bond valence landscape [22]. So the inclusion of the mass effect is required to convert a bond valence landscape into an energy landscape. Indeed a replacement of F (pathway volume fraction) by $FM^{1/2}$ leads to congruent linear structure-conductivity and structure-activation energy relations for the investigated glasses.

$$A_1 + B_1 \ln\left(\sigma T\sqrt{M}\right) \approx \left(F\sqrt{M}\right)^{1/3} \approx A_2 - B_2 \frac{E_a}{k_B T} \quad (2.19)$$

In this project, this dynamic bond valence analysis will be applied to molecular dynamics trajectories. Based on the trajectory of MD simulations, ion transport pathways are modelled in detail by the BV approach to investigate how the structure changes as a consequence of Li_2O modifier concentration variation in lithium silicate glasses, halide doping in lithium phosphate glass, and mixed glass former effect in lithium borophosphate glasses and thereby influences the ionic conductivity. In case of silicate and halide-doped phosphate glasses, characteristics of the resulting ion transport pathway models (such as volume fraction and local dimensionality of the percolating pathway) are compared to models for related glassy solid electrolytes based on reverse Monte Carlo (RMC) modelling of diffraction data previously reported by our group. It is expected to promote a better understanding of ion transport in the oxide-based glassy solid electrolytes.

References

1. J. E. Shelby, Introduction to Glass Science and Technology, 2nd ed., Cambridge: RSC, 2005.
2. C. A. C. Sequeira, A. Hooper, Solid State Batteries, Martinus Nijhoff Publishers, Dordrecht, 1985.
3. C. M. A. Brett, M. O. Brett, Electrochemistry - Principles, Methods, and Applications, Oxford University Press Inc., New York, 1993.
4. J. R. Macdonald, Impedance Spectroscopy - Emphasizing Solid Materials and Systems, John Wiley & Sons, New York, 1987.
5. E. Barsoukov, J. R. Macdonald, Impedance Spectroscopy - Theory, Experiment, and Applications, Second Edition, John Wiley & Sons, New Jersey, 2005.
6. C. -H. Lee, K. H. Joo, J. H. Kim, S. G. Woo, H. -J. Sohn, T. Kang, Y. Park, J. Y. Oh, Solid State Ionics 149 (2002) 59.
7. Y. -I. Lee, J. -H. Lee, S. –H. Hong, Y. Park, Solid State Ionics 175 (2004) 687.
8. J. Maier, Physical Chemistry of Ionic Materials - Ions and Electrons in Solids, John Wiley & Sons, Ltd, 2004.
9. I. D. Raistrick, Annu. Rev. Mater. Sci. 16 (1986) 343.
10. J. Fu, Solid State Ionics 104 (1997) 191.
11. C. J. Leo, PhD Thesis, Department of Physics, National University of Singapore, 2002.
12. F. Ercolessi, A Molecular Dynamics Primer, Spring College in Computational Physics, ICTP, Trieste, 1997.

13. R. P. Rao, Ph. D. thesis, Department of Physics, Indian Institute of Technology Madras, 2005.
14. L. Verlet, Phys. Rev. 159 (1967) 98.
15. A. S. Côté, B. Smith, P. J. D. Lindan, A Molecular Dynamics Tutorial, http://www.compsoc.man.ac.uk/~lucky/Democritus/Theory/pbc-mi.html, Daresbury Laboratory, 2001.
16. I. D. Brown, The Chemical Bond in Inorganic Chemistry - The Bond Valence Model, Oxford University Press, New York, 2002.
17. S. Adams, Acta Crystallogr. B, Struct. Sci. 57 (2001) 278.
18. S. Adams, softBV web pages: http://www.softBV.net (2003).
19. S. Adams, J. Swenson, Solid State Ionics 175 (2004) 665.
20. S. Adams, Solid State Ionics 177 (2006) 1625.
21. S. Adams, Bull. Mater. Sci. 29(6) (2006) 587.
22. S. Adams, J. Swenson, Phys. Chem. Chem. Phys. 4 (2002) 3179.
23. S. Adams, J. Swenson, Solid State Ionics 154-155 (2002) 151.
24. S. Adams, R. Prasada Rao, Phys. Chem. Chem. Phys. 11 (2009) 3210.
25. S. Adams, J. Maier, Solid State Ionics 105 (1998) 67.
26. S. Adams, J. Swenson, Phys. Rev. Lett. 84 (2000) 4144.
27. S. Adams, J. Power Sources 159 (2006) 200.
28. A. Hall, S. Adams, J. Swenson, Phys. Rev. B 74 (2006) 174205.
29. C. Muller, E. Zienicke, S. Adams, J. Habasaki, P. Maass, Phys. Rev. B 75 (2007) 014203.
30. V. Thangadurai, S. Adams, W. Weppner, Chem. Mater. 16 (2004) 2998.
31. S. Adams, J. Swenson, Phys. Rev. B 63 (2000) 054201.

32. S. Adams, Solid State Ionics 136 (2000) 1351.

Chapter 3

Ion Transport Pathways in Molecular Dynamics Simulated Lithium Silicate Glasses

3.1. Introduction

Solid state lithium batteries and electrochemical devices employing solid glass electrolytes have been the subject of numerous investigations. A systematic design of new materials with technologically interesting properties requires the knowledge of composition-structure-property relationships. Appreciation for such knowledge demands a detailed understanding of important underlying mechanisms.

Various silicate-based glass systems have been studied to explain these mechanisms. $xM_2O – (1 – x)SiO_2$ (M = Li, Na, K) have been among the most thoroughly investigated systems due to their great technological importance. Many reports are available in the literature to scrutinize the structure of these silicate glasses from NMR, IR and Raman spectroscopy, EXAFS, neutron and x-ray diffraction studies, as well as molecular dynamics simulations [1 – 6]. It is observed that the introduction of alkali oxides results in the formation of non-bridging oxygens (NBOs) by disruption of the Si – O – Si bonds and consequent reduction in glass connectivity [3]. These structural modifications affect the electrical and mechanical behaviour of alkali silicate glasses.

However, the realization of how such modification affects the behaviour of these glasses is far from complete. This requires a good understanding of ion migration mechanism, which is also one of the key features for the development of solid electrolytes and electrode materials for device applications.

Molecular dynamics (MD) simulations is one of the useful tools to

appreciate the microscopic origin of the dynamics. As mentioned in the literature review (see Chapter 1, Section 1.4.1), many studies have been done using this technique. However, most of the studies are based on high temperature simulations to increase ion mobility and cover only a few selected compositions (mostly x = 0.10 and x = 0.50). Moreover, there is still no unanimously accepted model that can explain some of the most interesting universal phenomena associated with ionic conduction in glasses.

As such, the main goal of this work is to investigate and quantify the ion transport pathways in the $xLi_2O - (1 - x)SiO_2$ glasses with different lithium ion concentrations at room temperature (300 K) for a detailed range of compositions (x = 0.10, 0.15, 0.20, 0.25, 0.30, 0.33, 0.40, 0.45, 0.50) using MD simulation and Bond Valence (BV) approach. BV method is applied to the equilibrated configurations at room temperature to analyse the structural variation in these glassy systems with increasing network modifier content, its consequence for Li^+ ion mobility, as well as the distribution of bridging and non-bridging oxygen atoms and the variation of the Q_n (where n is the number of bridging oxygens around Si atom) values. The result from this study is eventually compared with the reported experimental and reverse Monte Carlo (RMC) results. In a recent study, we could demonstrate that ion transport pathways derived directly from extended MD simulations correlate well with the ion transport pathways predicted by a BV approach [7, 8].

3.2. Techniques

3.2.1. Simulation Procedure

The structures of lithium silicate glasses $xLi_2O - (1 - x)SiO_2$ (with x = 0.10, 0.15, 0.20, 0.25, 0.30, 0.33, 0.40, 0.45, 0.50) have been modeled by means of NVT Molecular Dynamics (MD) simulations. For each composition, 1536 atoms were placed randomly in a cubic box using reported densities [1, 9, 10]. The DL_POLY [2, 11, 12] package has been employed for MD simulations. Integration of the equation of motion has been performed using the Verlet Leapfrog algorithm with a time step of 2 fs. Coulombic interactions have been calculated by the Ewald summation method. A pairwise potential reported by A. Pedone et al. has been employed [2]. This is based on a rigid ionic model with partial charges to handle the partial covalency of silicate systems. The potential is given by the sum of three terms: (i) the long-range Coulombic potential; (ii) the short-range forces, which are represented by a Morse function to account for covalent interactions; (iii) an additional repulsive term C/r^{12}, which has been added to model the repulsive contribution at high temperature and pressure. The DL_POLY code has been slightly modified to allow for the inclusion of this additional repulsive term. The overall expression for the interatomic potential U_{ij} between atoms i and j is then

$$U_{ij} = \frac{z_i z_j e^2}{r_{ij}} + D_{ij}\left[\left\{1 - \exp\left(-a_{ij}\left(r_{ij} - r_0\right)\right)\right\}^2 - 1\right] + \frac{C_{ij}}{r_{ij}^{12}} \qquad (3.1)$$

where z_i is the effective charge number of atom i, and r_{ij} is the interatomic

distance between atoms i and j; r_0 is the equilibrium bond distance. D_{ij}, a_{ij} and C_{ij} are potential parameters and the indices i and j refer to the different atomic species. The ionic charges used in MD simulations for Li, Si, O atoms are +0.6e, +2.4e and -1.2e respectively. The systems have been cooled down uniformly from 5000 K to 2000 K over in steps of 500 K over 770 ps, followed by a slower cooling rate of 5 ns/500 K for 1500 K – 500 K and finally for 300 K. The total cooling time is 20.77 ns with a nominal cooling rate of 10^{11} K/s.

Bond valence analysis is applied to the final equilibrated MD configurations at 300 K to calculate different structural units present in the systems under investigation.

3.2.2. Bond valence approach

More details of this approach can be found in Section 2.4.3.

In practice, the structure model (containing 1536 atoms) is divided into a primitive grid containing ~ 3.3 million cubic volume elements with a size of ca. $(0.2\ Å)^3$. It should be noticed that a description of the pathways at ambient temperatures has to rely on an energy-landscape type of approach, since in the silicate glasses the mobility of ions is too small to be observed directly in room temperature MD simulation trajectories.

Determining which oxygens are bridging or not is frequently done using radial cut-off criterion: how many Si atoms there are within a specified distance of the oxygen. Here $s_{(Si-O)} = 0.16$ is used to decide whether an oxygen atom is BO or NBO. Therefore, the Q_n species for the simulated xLi_2O –

$(1 - x)SiO_2$ glass structures is calculated and compared to the Q_n distribution as determined by NMR, Raman [13 – 15] and theoretical models. According to the bond ordering model by Gurman [16], the number of Q_n (n is the number of bridging oxygens around silicon atom) units present in $xLi_2O - (1 - x)SiO_2$ glasses can be described by the following relations.

$$\frac{Q_4 Q_2}{Q_3^2} = \frac{Q_3 Q_1}{Q_2^2} = \frac{Q_2 Q_0}{Q_1^2} = e^{-2\Delta E/kT_g} \tag{3.2}$$

$$Q_0 + Q_1 + Q_2 + Q_3 + Q_4 = 1 \tag{3.3}$$

where ΔE, T_g are the bond ordering energy and glass transition temperature, respectively.

3.3. Results and Discussion

Figure 3.1 shows that the variation of the fraction of bridging oxygens (BOs) with the addition of modifier Li_2O as calculated from the equilibrated configurations at room temperature using the above-mentioned BV criterion practically coincides with the assumption that the addition of each Li_2O creates two non-bridging oxygen (NBO) atoms. Only for higher alkali contents the simulated systems include up to 0.3% 'free oxygen' i.e. O^{2-} ions unlinked to a silicon atom. The existence of such free oxygens is also found experimentally by Raman spectroscopy in lithium silicate glasses of very high alkali content [14]. The number of BOs is decreasing as expected with the concentration of lithium ions. This indicates the role of modifier in decreasing the connectivity of network.

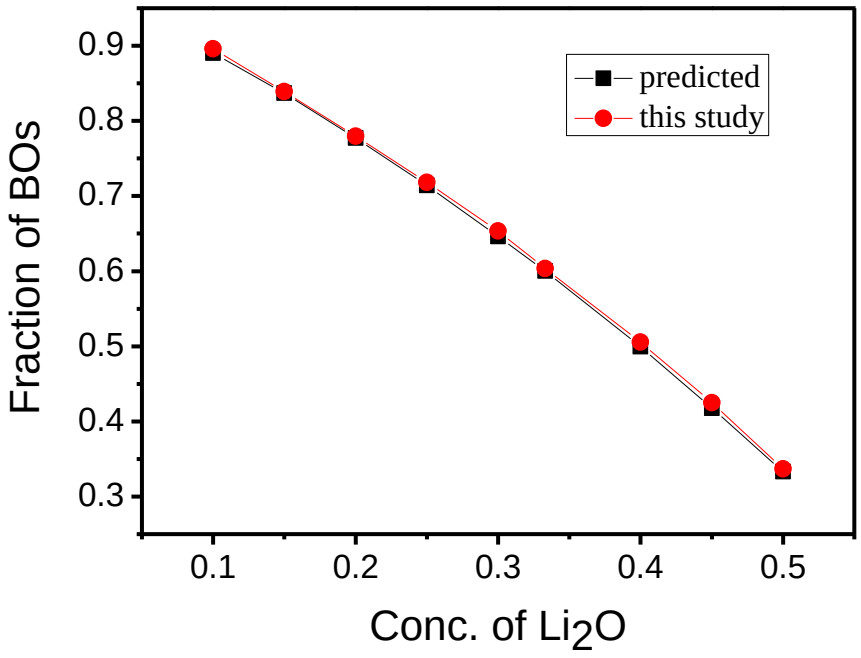

Figure 3.1. Comparison of observed and expected fractions of bridging oxygens (BOs) as a function of Li_2O concentration.

Figure 3.2 shows how the fraction of the Lithium bond valence sum that originates from bonds Li-NBO varies with the concentration of Li_2O. As to be expected this fraction exhibits an overall increase, as the number of NBOs rises with the Li_2O concentration. What is more interesting is that a transition can be seen, when the Li_2O concentration reaches 33%. For lower Li_2O contents, there is a strong preference of Li to be bonded by the few available NBOs, whereas for high Li_2O contents the connection between the Li and NBO sites is less pronounced. As shown in Figure 3.2 the trivial variation of the average V(Li-NBO)/[V(Li-NBO)+V(Li-BO)] can be expressed by a linear regression for the high Li_2O concentration region, while the values in the low Li_2O concentration region are characterized by an excess contribution characterizing the degree of localization of Li ions in the vicinity of NBOs. It should be expected that this localization affects the Li ion mobility.

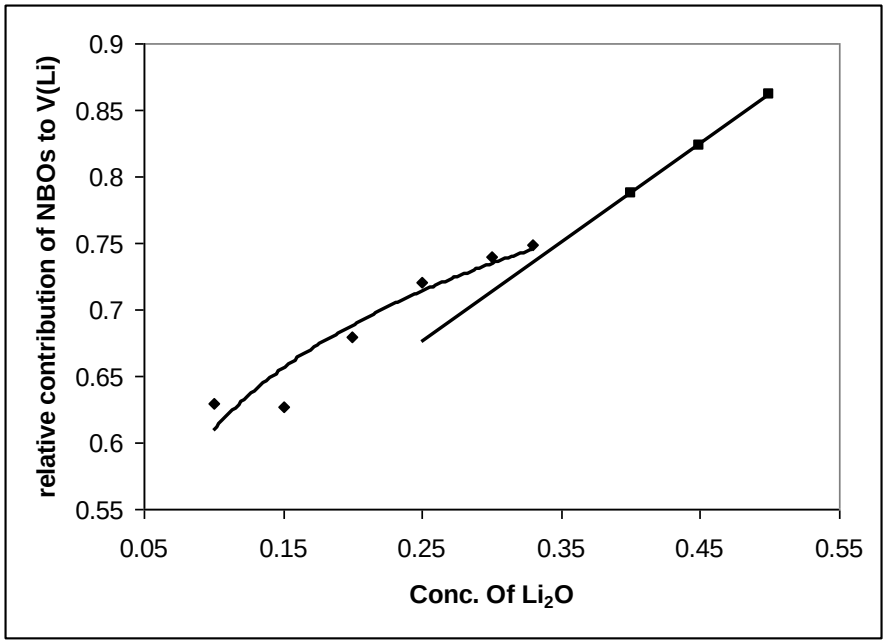

Figure 3.2. Contribution of bonds to NBO's to the Li bond valence sum vs. concentration of Li_2O.

The concentration of the various Q_n species, $c(Q_n)$ (where the index n refers to the number of bridging oxygens around Si) is a further useful measure for characterizing the intermediate range structure of glasses. Obviously the values of $c(Q_n)$ are controlled by the number and spatial distribution of non-bridging oxygens. Q_n distributions can be determined experimentally, e.g. by NMR and Raman. Figures 3.3 and 3.4 compares the distribution of Q_n for $xLi_2O - (1 - x)SiO_2$ observed in our simulations with the values calculated based on bond order model and with experimental values [13 – 17].

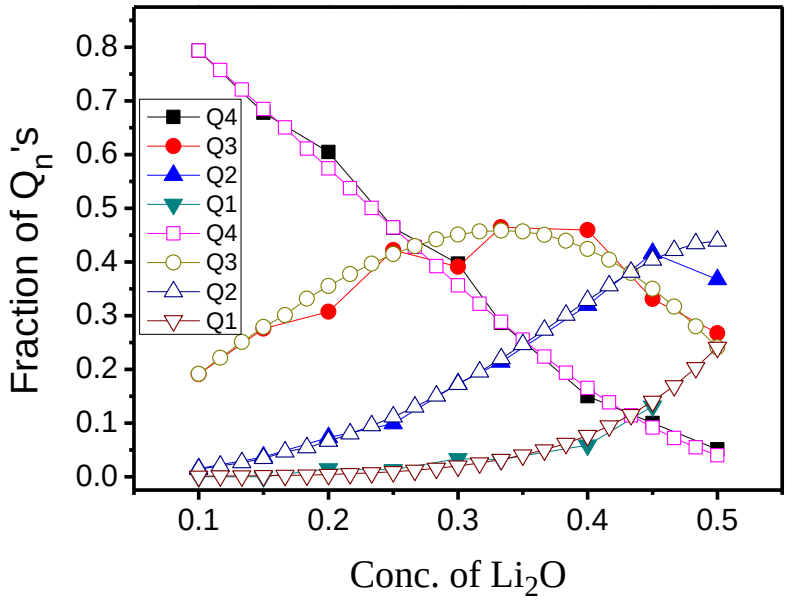

Figure 3.3. Variation of fraction of Q_n units for $xLi_2O - (1 - x)SiO_2$. Open symbols: calculated values for bond order model [16] with $\Delta E/kT_g = 0.6$; solid symbols: this study.

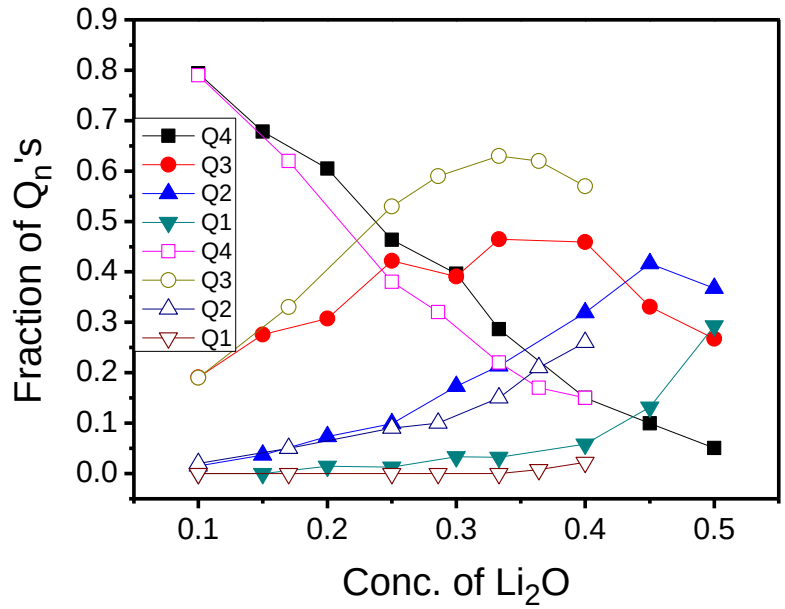

Figure 3.4. Variation of fraction of Q_n units for $xLi_2O - (1 - x)SiO_2$. Open symbols: reported values from NMR and Raman spectroscopy [13 – 15, 17]; Solid symbols: this study.

As seen from Figure 3.4, experimental values (based on NMR and Raman studies) show that the $c(Q_4)$ decreases from x = 0.10 to 0.50, while $c(Q_3)$ increases up to 0.33 and then decreases, and Q_2 can be identified for $x \geq 0.17$ and $c(Q_2)$ increases from x = 0.17 to 0.50. No Q_1 units were reported from Raman and NMR studies below x = 0.5. Similarly, in our simulations $c(Q_4)$ decreases monotonically, whereas $c(Q_3)$ reaches a maximum for x = 0.33. $c(Q_2)$ and $c(Q_1)$ rise over the investigated composition range (except $c(Q_2)$ for x = 0.10). No Q_0 (isolated SiO_4) units were observed.

Though there is a qualitative agreement between the variation of the $c(Q_n)$ as a function of x and the experimental values for the lithium silicate glasses of our study, there is no quantitative agreement of the $c(Q_n)$ values. Both suggest that the distribution of the Q_n units is not completely random, but the preference for values of $c(Q_n)$ close to the expectation value $\tilde{n}(x) = (4 - 6x)/(1 - x)$ is more pronounced for the experimental data. Our results are consistent with the distribution of $c(Q_n)$ found in the simulations in Ref. [1, 2] that used the same force field, but an independent algorithm for the determination of $c(Q_n)$.

To achieve a more quantitative description of the variation of the $c(Q_n)$ with x ordering, a certain degree of spatial ordering of the NBO atoms has to be assumed. As discussed in detail in Ref. [16] the extent of ordering may be approximated in a thermodynamic model as being formally caused by a bond ordering energy ΔE (cf. Equation (3.2)). As seen in Figure 3.3, the simulation results quantitatively match with the bond order model for $\Delta E = 0.6\ kT_g$. Simulation results by Voigt et al. [17] based on the force field by Habasaki et

al. [18] for the range $0.10 < x < 0.33$ correspond to a slightly lower bond ordering energy value. Experimental studies on Q_n distributions exhibit a large scatter, but are generally found to correspond to somewhat larger values of $\Delta E = 1.0\ kT_g$ (based on data from Ref. [15]) or $\Delta E = 1.5\ kT_g \pm 0.5\ kT_g$ [16], i.e. a more pronounced ordering of the NBOs. It might be assumed that the differences in the degree of NBO ordering between experimental and simulated Q_n distributions are due to the inevitable difference in the cooling rate, and an imperfect treatment of polarisation effects by the force fields. Recent work by Tilocca et al. [19] showed that the more detailed description of polarisability by core-shell models can help to further improve the description of the intermediate range order of the silicate network and the local environment of modifier cations.

Figure 3.5 shows slices of the MD generated configurations for glasses with x = 0.10, 0.30 and 0.50. The slices visualize that the NBOs are to some extent clustered in the simulated structure models in accordance with the observation that the Q_n distribution follows a bond order model. Along with the arrangement of NBOs, the distribution of Li^+ ions changes with the Li_2O content from micelle-like for x = 0.10, via interconnected larger Li-rich regions for x = 0.30 to a nearly homogeneous distribution for x = 0.50. The same tendency, but less pronounced, is seen in slices through the bond valence Li^+ conduction pathways (modelled as isosurfaces of constant Li bond valence sum mismatch) as shown in Figure 3.6 for the same three glasses. As we move from glass x = 0.10 to 0.50 the density of pathways, their local diameter and the number of connections increase due to the addition of modifier ions, in line with the increase of ionic conductivity in these lithium silicate glasses. While

in the displayed slices for the glasses with low Li_2O concentrations pathways may look like discontinuous ribbons, about one half (for x = 0.10) to about 98% (for x = 0.50) of the displayed pathway sections belong to the percolating pathway cluster.

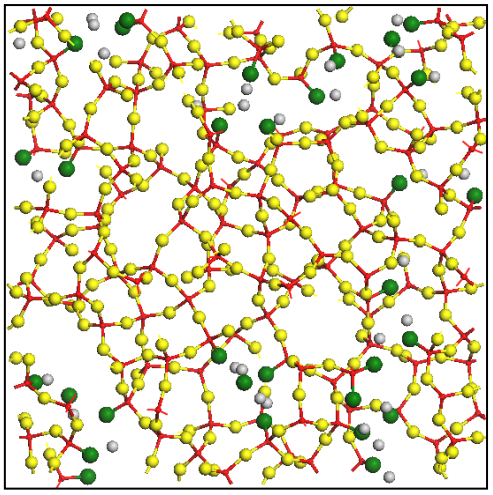

x = 0.10

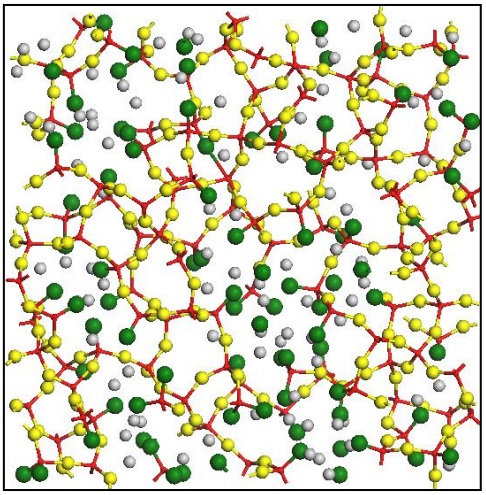

x = 0.30

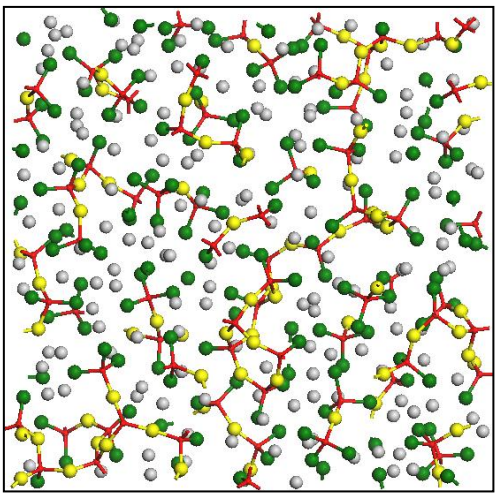

x = 0.50

Figure 3.5. Structures of glasses with x = 0.10, 0.30, 0.50 (top to bottom) (oxide atoms are around red Si tetrahedra, Li: small grey spheres, NBO: green spheres, BO: yellow spheres). Only the central 1/3 of the structure model is shown along z (perpendicular to the plane of view) to reduce overlap.

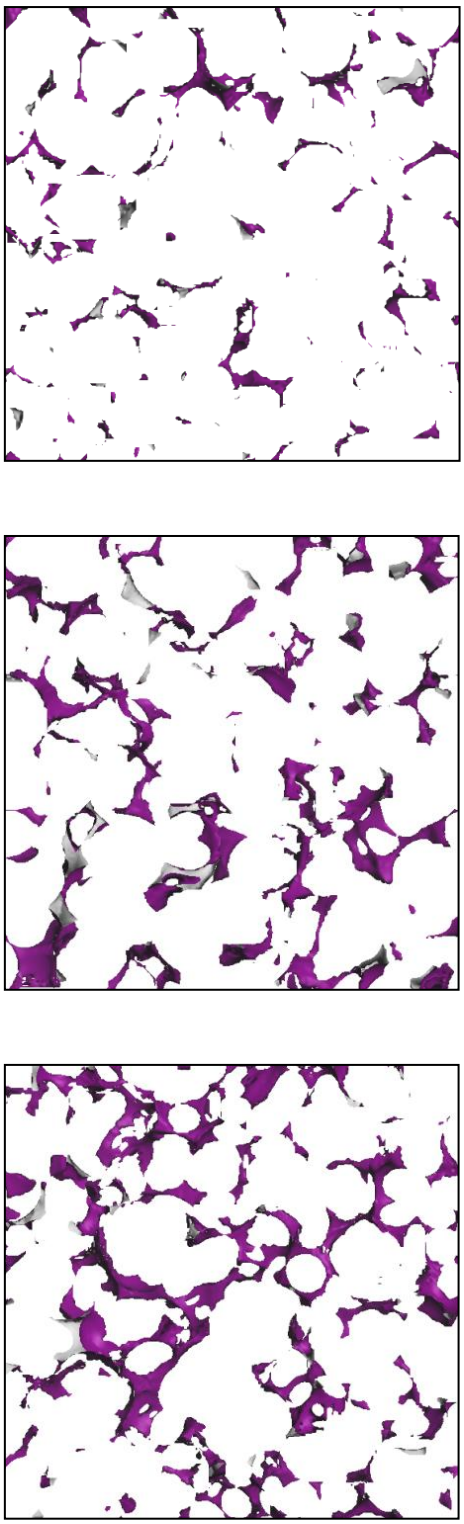

Figure 3.6. Slices of the isosurfaces of constant Lithium bond valence sum mismatch $|\Delta V(Li)|$ in the glasses $xLi_2O - (1 - x)SiO_2$ for x = 0.10, 0.30, 0.50 (top to bottom), projected along the z-axis (thickness nearly 5 Å). Note that although the pathways appear to be discontinuous ribbons in the displayed thin slices, about one half (for x = 0.10) to about 98% (for x = 0.50) of the displayed pathway sections belong to the percolating pathway cluster if the complete 3-dimensional model is considered.

With increasing network modifier content the percolating pathway clusters change in their volume fraction (the "cluster weight") and as a consequence also in their local pathway dimensionality. Figures 3.7 and 3.8 relate the volume fraction F of the percolating ion conduction pathways in the investigated Li^+ ion system to the experimentally observed absolute values of their ionic conductivity (σ_{dc}) and activation energy (E_a) [20]. The figures compare the results of the present MD study with a set of values that we reported previously on the basis of RMC-generated structure models of various alkali and Ag-conducting glasses. As discussed in Section 2.4.3, such a comparison of pathways for different types of mobile ions requires a mass scaling, as for a fixed pathway volume fraction the lighter cations with a higher polarising power show high values of activation energy and correspondingly reduced absolute conductivities. (The polarisability differences should be reflected in the bond valence parameters and thus be already incorporated in the calculation of F, whereas the mass of the cation does not directly modify the calculation of the bond valence landscape [21]). After the mass scaling, it was found that the MD-simulated Li silicate glass models nearly follow the same linear correlation between the structure-derived quantity $(F \times M^{1/2})^{1/3}$ and the experimentally determined transport properties (i.e., ionic conductivity, activation energy) as the previously investigated glass systems. It should be noticed that this simple formalism permits to estimate the order of magnitude of the conductivity and the activation energy for the glasses of this study. This may also be understood as an indication that the recent force field used in this study produces plausible structure models of silicate glasses.

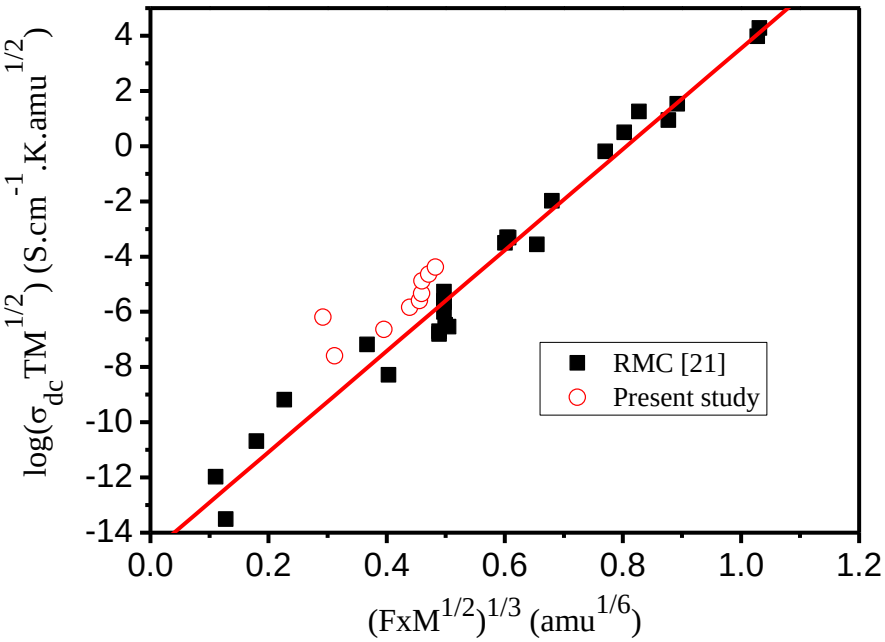

Figure 3.7. Variation of pathway volume fraction of Li^+ ions with experimental ionic conductivity (σ_{dc}). Solid symbols refer to data from RMC models for a wide range of Ag and alkali conducting glasses [21]. Open circles refer to MD-simulated structures of the glasses in this study.

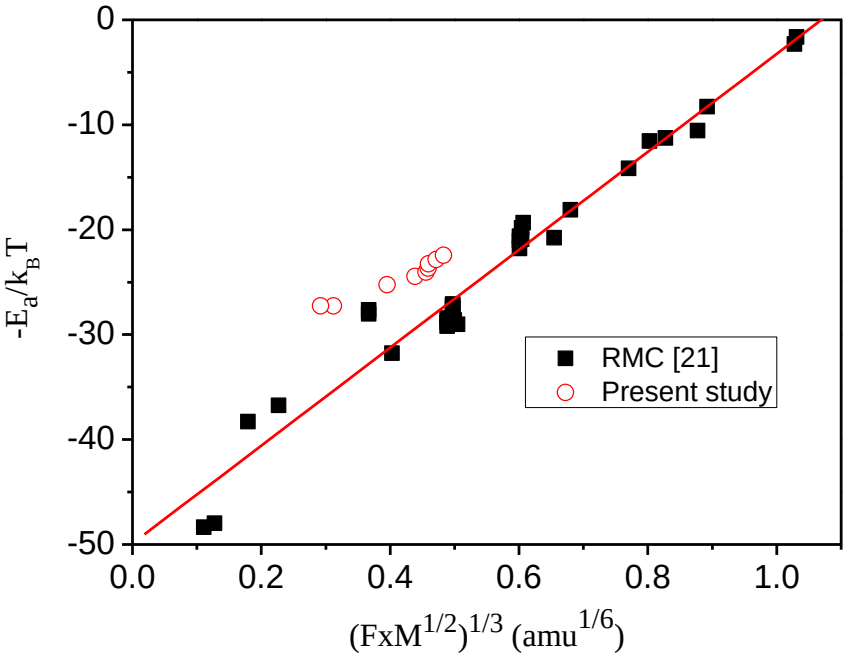

Figure 3.8. Variation of pathway volume fraction of Li^+ ions with activation energy (E_a). Solid symbols refer to data from RMC models for a wide range of Ag and alkali conducting glasses [21]. Open circles refer to MD-simulated structures of the glasses in this study.

Figure 3.9 reveals the variation in the local pathway dimensionality, as determined from the increase of the average number of pathway volume elements within a sphere around a random cluster site with the radius of the sphere. As to be expected the minimum of the local pathway dimension (*d*) increases with the Li_2O content. This increase is most pronounced for $0.10 < x < 0.25$, but only subtle for higher Li_2O contents ($d = 1.1$ for $x = 0.10$, $d \approx 1.5$ for $x = 0.15$, $d \approx 5/3$ for $x \geq 0.25$). For $x = 0.10$ the bottleneck of the pathway also appears at a larger distance than for the other glasses, which might indicate that the nearly one-dimensional pathways connecting pockets of NBO-coordinated Li sites in the glass with $x = 0.10$ are qualitatively different in nature from the pathways of the glasses with higher network modifier contents. All the glasses show a noticeable medium-range ordering of the pathways, as indicated by further maxima and minima of the pathway dimension in the range up to ca. 10 Å.

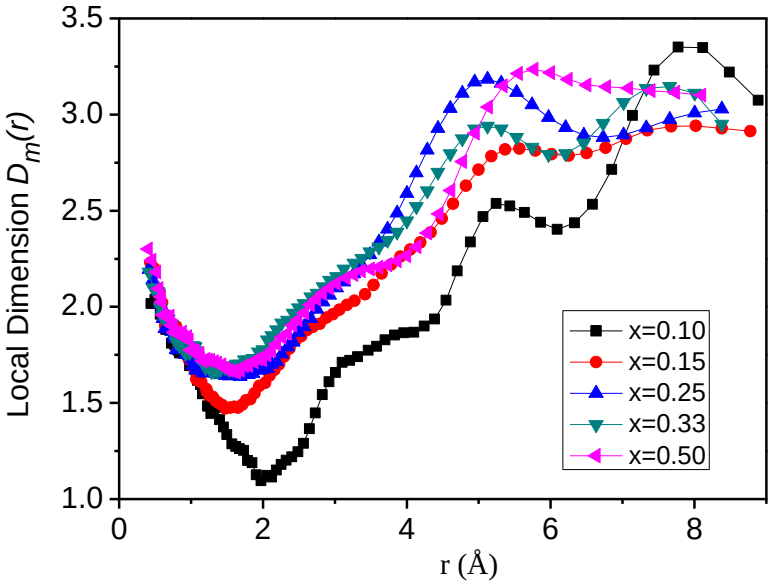

Figure 3.9. Local pathway dimension $D_m(r)$ of Lithium transport pathways in 5 of the studied lithium silicate glasses as a function of distance, highlighting the reduced dimensionality of pathways on the length scale of elementary hopping processes. Minima in $D_m(r)$ may be largely thought of as characterizing the width of Li^+ transport pathway at the bottleneck of elementary transport steps.

3.4. Conclusions

As the modifier concentration x increases the fraction of BOs and thereby the connectivity of the glass network decreases. Within the large range of compositions covered in this study, it appears that this variation in the network (and the Li^+ ion pathways in between) is more pronounced around x = 0.30 indicating a qualitative change in the glass structure with the Li_2O contents.

The variation of Q_n units indicates the reduction of branched network, which leads to the increase of the density and connectivity of pathways for the motion of Li^+ ions in the glasses. As known from previous experimental studies, the non-random distribution of Q_n units can be approximately described by a bond order model, though the extent of ordering is somewhat less pronounced in the simulated glass structures, probably due to the faster quenching rate.

The BV analysis of the lithium transport pathways in the MD-simulated lithium silicate structures shows the same variation of the scaled pathway volume fraction with the experimental conductivity as previously observed from RMC-generated structure models. Thereby it is possible to apply the BV method to MD simulated structure models in the same way as for the RMC-generated models to predict transport properties directly from the structure model. This permits to analyse transport properties even for glass systems or temperatures, where the ion mobilities are too low to be derived directly from mean square displacements in the MD simulation trajectories.

References

1. A. Pedone, G. Malavasi, M. C. Menziani, A. N. Cormack, U. Segre, J. Phys. Chem. B. 110 (2006) 11780.
2. A. Pedone, G. Malavasi, A. N. Cormack, U. Segre, M. C. Menziani, Chem.Mater. 19 (2007) 3144.
3. H. Lammert, M. Kunow, A. Heuer, Phys. Rev. Lett. 90 (2003) 215901.
4. A. N. Cormack and Y. Cao, Mol. Eng. 6 (1996) 183.
5. H. Lammert, A. Heuer, Phys. Rev. B 70 (2004) 24204.
6. S. Sen, T. Mukerji, J. Non-Cryst. Solids 351 (2005) 3361.
7. C. Müller, E. Zienicke, S. Adams, J. Habasaki, P. Maass, Phys. Rev. B 75 (2007) 014203.
8. S. Adams, R. Prasada Rao, Phys. Chem. Chem. Phys. 11 (2009) 3210.
9. H. Doweidar, J. Non-Cryst. Solids 194 (1996) 155.
10. A. Heuer, M. Kunow, M. Vogel, R. D. Banhatti, Phys. Chem. Chem. Phys. 4 (2002) 3185.
11. I. T. Todorov, The DL_POLY Molecular Simulation Package, web pages: http://www.cse.scitech.ac.uk/ccg/software/DL_POLY/.
12. W. Smith, T. R. Forester, J. Mol. Graphics 14 (1996) 136.
13. R. Dupree, D. Holland, M. G. Mortuza, J. Non-Cryst. Solids 116 (1990) 148.
14. N. Umesaki, N. Iwamoto, J. Non-Cryst. Solids 106 (1988) 77.
15. H. Maekawa, T. Maekawa, K. Kawamura, T. Yokokawa, J. Non-Cryst. Solids 127 (1991) 53.

16. S. J. Gurman, J. Non-Cryst. Solids 125 (1990) 151.
17. U. Voigt, H. Lammert, H. Eckert, A. Heuer, Phys. Rev. B 72 (2005) 64207.
18. J. Habasaki, I. Okada, Y. Hiwatari, Phys. Rev. E 52 (3) (1995) 2681.
19. A. Tilocca, N. H. De Leeuw, A. Cormack, Phys. Rev. B 73 (2006) 104209.
20. A. Bunde, M. D. Ingram, P. Maass, J. Non-Cryst. Solids 172-174 (1994) 1222.
21. S. Adams, J. Swenson, Phys. Chem. Chem. Phys. 4 (2002) 3179.

Chapter 4

Mobile Ion Transport Pathways and AC Conductivity Studies in Halide Salt Doped Lithium Phosphate Glasses $yLiX – (1 – y) (0.60Li_2O – 0.40P_2O_5)$

4.1. Introduction

In addition to increasing network modifier Li_2O as mentioned in Chapter 3 for lithium silicate glasses, the doping of halide salt into the glass network is also expected to enhance the ionic conductivity of the glassy systems. Therefore, in this project the halide salt doped lithium phosphate glasses $yLiX – (1 – y)(0.60Li_2O – 0.40P_2O_5)$ (where X = Cl, Br) were investigated to clarify the effect of halide dopant concentration on the glass structure and Li^+ ion mobility.

Lithium phosphate glasses possess technological importance due to their simple composition with strong glass forming character and low glass transition temperature. With the addition of appropriate doping agent, these glasses find a wide variety of applications in optoelectronic devices, laser host materials and as solid electrolytes in solid state ionic devices. Fast alkali ion conducting glasses with high ionic conductivity are potential candidates for applications in solid state electrochemical devices such as batteries, sensors, etc. due to their advantageous characteristics over the conventional crystalline materials. A systematic design of new materials with technologically interesting properties requires the knowledge of composition-structure-property relationships. Appreciation for such knowledge demands a detailed understanding of important underlying mechanisms.

Many investigations have been carried out on lithium phosphate glassy systems to explain these mechanisms. Structural studies of binary $Li_2O – P_2O_5$ and ternary $Li_2O – P_2O_5 – LiX$ (where X = Cl for most of the cases) glasses

have been reported using neutron and X-ray diffraction, spectroscopic techniques, and computer based simulations, such as RMC and MD simulations (see literature review of phosphate glasses). Generally the introduction of Li_2O breaks up P – O – P bridges, creating non-bridging oxygens (NBOs) which reduce the phosphate chain lengths. The addition of dopant LiX does not cause any such modification of chain length in the glass network, though it makes the structure less rigid and create wider channels for Li^+ ion movement, and thus enhancing ionic conductivity (σ) and decreasing glass transition temperature (T_g) [1 – 6].

Most studies focus on LiCl doped phosphate glasses, whereas the structure and properties of LiBr doped glasses have not been investigated thoroughly. Therefore, a detailed understanding of effect of halide dopant in the lithium phosphate glasses is far from complete.

As mentioned in the literature review (see Chapter 1, Section 1.4.2), MD simulations have been used to investigate the structure and ion dynamics in the lithium phosphate glasses. However, most of these MD studies were conducted on the binary Li_2O – P_2O_5 phosphate systems, while to my knowledge only one structural study using MD simulation for ternary phosphate glasses Li_2O – P_2O_5 – LiCl was available when we started our works [2]. Moreover, there is still no unanimously accepted model that can explain the mechanism of ionic conduction in these glasses and in particular the effect of halide dopant on the ion transport pathways in the ternary glasses.

As such, halide salt doped lithium phosphate glassy systems yLiX – $(1 - y)(0.60Li_2O – 0.40P_2O_5)$ (where X = Cl, Br; y = 0, 0.10, 0.15, 0.20, 0.25)

were chosen to study in details the ion conduction mechanism.

The first objective of this research is to investigate the relation between the conductivity and the transport pathways for mobile Li^+ ions, as well as the influence of halide doping in these glassy systems. To achieve this aim, $yLiX – (1 – y)(0.60Li_2O – 0.40P_2O_5)$ glasses were prepared, characterized by impedance spectroscopy, while their structures were modelled by MD simulation. Based on the equilibrated configurations of these MD simulations, ion transport pathways are modelled in detail by the bond valence (BV) approach to clarify the influence of the halide dopant concentration on the glass structure and its consequence for Li^+ ion mobility.

The second objective is to have a complete knowledge on the ion transport mechanism and relaxation behaviour in these glasses. Therefore, the variation of ac conductivity ($\sigma(\omega)$) and electric modulus (M^*) with the addition of LiCl and LiBr to $0.60Li_2O – 0.40P_2O_5$ glassy system will be investigated using frequency-dependent impedance spectroscopy.

4.2. Techniques

4.2.1. Sample synthesis and properties characterization

Please see Section 2.2.1 for the preparation of halide salt doped lithium phosphate glasses $yLiX – (1 – y)(0.60Li_2O – 0.40P_2O_5)$ (where X = Cl, Br; y = 0, 0.10, 0.15, 0.20, 0.25).

Because LiCl and LiBr partially evaporate during the preparation, the

exact composition of the prepared sample was determined from scanning electron microscopy (SEM) with the aid of energy dispersive X-ray analysis (EDX). Weight percentage of halide X obtained from EDX was used to quantify the exact composition for each prepared glass [y = (wt% of X/100)*(M_{glass}/M_X), where M: atomic mass in g/mol]. Table 4.1 shows a comparison between the expected and the observed halide X contents in the corresponding glasses. Hereafter, experimental data will refer to the observed compositions, while MD simulations are conducted for the expected (nominal) compositions.

The quenched samples were characterized by X-ray powder diffractometry (XRD) using Cu K_α radiation (PANalytical X'Pert PRO, equipped with a fast linear X'Celerator detector, which can collect 100 steps at the same time). XRD data were collected in the 2θ range $10–80^0$ with a nominal scan rate of $70s.step^{-1}$ and a step size of 0.05^0 at room temperature. Except for y = 0.25LiBr, no sharp Bragg peaks were observed for other compositions, confirming glassy nature of the samples with up to y = 0.25 for LiCl-doped and y = 0.20 for LiBr-doped glasses (cf. Figure 4.1). Density of glasses was measured by Archimedes' principle or Pycnometry. The glass transition temperature (T_g) was determined using Differential Scanning Calorimetry (DSC; TA Instruments 2920 Modulated DSC) at a heating rate of $10K.min^{-1}$ under constant flow of high purity N_2 gas.

Table 4.1. Results of composition analysis of yLiX – (1 – y)($0.60Li_2O$ – $0.40P_2O_5$) glasses (X = Cl, Br).

Nominal composition	Theor. (Exp.) /wt_X%	Experimental composition
$0.60Li_2O$–$0.40P_2O_5$	-	$0.60Li_2O$–$0.40P_2O_5$
$0.54Li_2O$–$0.36P_2O_5$–0.10LiCl	4.96 (4.87)	$0.54Li_2O$–$0.36P_2O_5$–0.098LiCl
$0.51Li_2O$–$0.34P_2O_5$–0.15LiCl	7.61 (7.14)	$0.51Li_2O$–$0.34P_2O_5$–0.141LiCl
$0.48Li_2O$–$0.32P_2O_5$–0.20LiCl	10.39 (10.26)	$0.48Li_2O$–$0.32P_2O_5$–0.198LiCl
$0.45Li_2O$–$0.30P_2O_5$–0.25LiCl	13.30 (13.20)	$0.45Li_2O$–$0.30P_2O_5$–0.248LiCl
$0.54Li_2O$–$0.36P_2O_5$–0.10LiBr	10.52 (10.13)	$0.54Li_2O$–$0.36P_2O_5$–0.096LiBr
$0.51Li_2O$–$0.34P_2O_5$–0.15LiBr	15.66 (15.65)	$0.51Li_2O$–$0.34P_2O_5$–0.150LiBr
$0.48Li_2O$–$0.32P_2O_5$–0.20LiBr	20.72 (20.59)	$0.48Li_2O$–$0.32P_2O_5$–0.199LiBr

Ionic conductivity measurements for a temperature range of 300 to 492 K were carried out by impedance spectroscopy in the frequency range of 1 Hz to 15 MHz (see Section 2.3.8 for more details). The bulk resistance (R_b) was determined from fitting impedance data to Nyquist plots (-Z" versus Z') using an equivalent circuit model. The equivalent circuit consists of C_b, R_b and CPE, where C_b is the geometric capacitance of the sample between the electrodes, and CPE is the constant phase element due to the polarization distribution at the interface between blocking electrodes and glass.

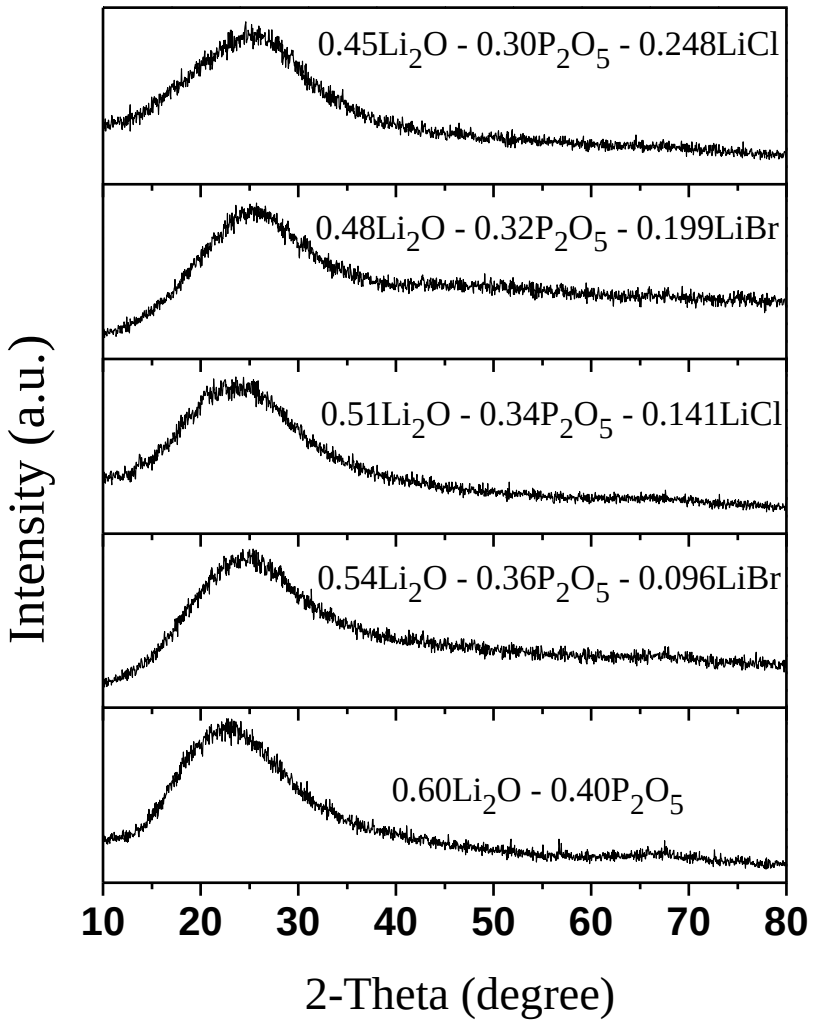

Figure 4.1. XRD patterns of some yLiX – (1 – y)($0.60Li_2O$ – $0.40P_2O_5$) glasses.

4.2.2. Computer simulations

Constant volume (NVT) MD simulations were performed on structure models of yLiX – (1 – y)($0.60Li_2O$ – $0.40P_2O_5$) glasses (where X = Cl, Br; y = 0.10, 0.15, 0.20, 0.25). The volume of the simulation box is derived from our density determinations (Table 4.2). The optimized potential parameters shown in Tables 4.3, 4.4 and 4.5 for LiCl- and LiBr-doped glasses have been derived in the frame of this project by fitting to experimentally known bond

lengths and coordination numbers. Low pressure has been observed in the simulations.

Table 4.2. Physical parameters of $yLiX – (1 – y)(0.60Li_2O – 0.40P_2O_5)$ glasses (X = Cl, Br).

Nominal composition	Mass density /g.cm^{-3}	Number density/Å^{-3}	T_g/K	E_a^{dc}/eV
$0.60Li_2O–0.40P_2O_5$	2.348	8.70 x 10^{-2}	583	0.650
$0.54Li_2O–0.36P_2O_5–0.10LiCl$	2.324	8.50 x 10^{-2}	565	0.601
$0.51Li_2O–0.34P_2O_5–0.15LiCl$	2.298	8.34 x 10^{-2}	551	0.584
$0.48Li_2O–0.32P_2O_5–0.20LiCl$	2.271	8.17 x 10^{-2}	535	0.568
$0.45Li_2O–0.30P_2O_5–0.25LiCl$	2.249	8.03 x 10^{-2}	519	0.543
$0.54Li_2O–0.36P_2O_5–0.10LiBr$	2.392	8.23 x 10^{-2}	573	0.575
$0.51Li_2O–0.34P_2O_5–0.15LiBr$	2.421	8.01 x 10^{-2}	555	0.555
$0.48Li_2O–0.32P_2O_5–0.20LiBr$	2.443	7.78 x 10^{-2}	540	0.535

Starting at a temperature of 1500 K, the system containing 1975 – 2170 atoms was cooled by scaling velocities to 1000, 700, 500, 400 K and finally cooled to 300 K with a time step of 2 fs. At 1500, 1000 and 700 K, equilibration time was 300 ps followed by a NVT simulation (Hoover thermostat) for 200 ps. At 500, 400, 300 K the equilibration time was increased to 600 ps and the production run after equilibration was also increased to 400 ps. Thus the calculation of mean square displacement (MSD) for all atoms was based on the final 200 ps at 1500, 1000, 700 K, and the final 400 ps for the temperatures 500, 400 and 300 K below the glass transition temperature (T_g). The interatomic potential U_{ij} between atoms i and j used in MD simulations is as follows:

$$U_{ij} = \frac{z_i z_j e^2}{r_{ij}} + A_{ij}\exp\left(\frac{-r_{ij}}{\rho_{ij0}}\right) + \frac{k_{ij}}{8(\theta_{jik} - \pi)}\left\{\left[(\theta_0 - \pi)^2 - (\theta_{jik} - \pi)^2\right]^2\right\}\exp\left[-\frac{r_{ij}}{\rho_{ij}} - \frac{r_{ik}}{\rho_{ik}}\right] \quad (4.1)$$

Here U_{ij} is the interatomic potential between atoms i and j, z_i is the effective charge number of atom i, θ_0 is the equilibrium angle subtended by r_{ij} and r_{ik}. A_{ij}, ρ_{ij0}, k_{ij}, ρ_{ij} and ρ_{ik} are potential parameters.

The first term in Equation (4.1) is the Coulomb potential where ze is the ionic charge. Since it is a long range (1/r) interaction, it is slowly convergent. The convergence is enhanced by applying Ewald summation, where electrostatic potential experienced by one ion in the presence of all the other ions in the system is calculated by splitting the slowly convergent direct summation into two fast converging series with one in direct and the other in reciprocal space. The ionic charges used in MD simulations for Li, P, O, X (Cl, Br) are +0.6*e*, +3.0e, -1.2e, -0.6e, respectively. They are generally lower than the nominal charges of the ions to account for partial covalency of phosphate systems.

The second term in Equation 4.1 is the Buckingham pair-wise potential (see Equation 4.2), which includes both Born repulsion and Van der Waals interactions, and accounts for the short range interactions.

$$U_{buck}(r) = A\exp\left(-\frac{r}{\rho}\right) - \frac{C}{r^6} \quad (4.2)$$

In practice the Van der Waals-attraction term ($-\frac{C}{r^6}$) is often approximated

by a modification of the effective charge in the Coulomb term and the parameter C is chosen to be zero. In that case the Buckingham potential is simplified to a pure Born repulsion term as shown in Equation 4.1.

The third term in U_{ij} (cf. Equation 4.1) is the three-body Screened Vessal term, which is introduced to account for the angle-dependent nature of covalent interactions. Bond valence analysis is then applied to the final equilibrated configuration obtained at 300 K.

Table 4.3. Optimized two-body potential parameters for LiCl doped phosphate glasses.

Interaction (i - j)	A_{ij}/eV	ρ_{ijo}/Å
P – O	2900.57	0.212
O – O	2100.43	0.295
Li – O	25500.42	0.170
Li – Cl	150000.00	0.176
P – Cl	2500.00	0.450
Cl – Cl	1500.00	0.600

Table 4.4. Optimized two-body potential parameters for LiBr doped phosphate glasses.

Interaction (i - j)	A_{ij}/eV	ρ_{ijo}/Å
P – O	2700.57	0.212
O – O	4000.43	0.295
Li – O	26000.42	0.170
Li – Br	80000.00	0.196
P – Br	2000.00	0.300
Br – Br	1000.00	0.600

Table 4.5. Potential parameters for the three-body Vessal term in the forcefield for LiX doped phosphate glasses (X = Cl, Br).

Interaction (i – j – k)	O – P – O	P – O – P
k/eV	0.0129	0.0129
θ_0	109.47	135.58
ρ_{ij}/Å	0.2252	1.5000
ρ_{jk}/Å	0.1191	1.2321
r_c^*/Å	1.90	1.90

r_c*: cut off in r_{ij} and r_{jk}.

4.2.3. Bond valence approach

More details of this approach can be found in Section 2.4.3.

In practice, the structure model is divided into a primitive grid containing ~ 3.3 million cubic volume elements with a size of ca. $(0.2\ Å)^3$, i.e. about 1600 volume elements per atom.

4.3. Results and Discussion

4.3.1. Density, glass transition temperature (T_g)

The mass density of LiCl-doped glasses decreases and the mass density of LiBr-doped glasses increases with rising of LiX (X = Cl, Br) content (see Table 4.2). However in both cases the number density decreases with the increase of LiX content (cf. Table 4.2), indicating that the glass network becomes more open. This leads to the decrease of glass transition temperature (T_g) (cf. Table 4.2) and the increase of Li^+ ion mobility. The decrease in T_g with the increase of LiX content proves that the glass matrix becomes less rigid with the LiX addition, in line with the literature reports for lithium halide-doped phosphate glasses [2, 5]. It may still be noticed that for the same value of y and Li_2O/P_2O_5 ratio, T_g values are ca. 5 K higher for the LiBr-doped glasses than for the corresponding LiCl-doped glasses.

4.3.2. Impedance analysis

Complex impedance spectra of the glasses were measured over the temperature range from 300 to 492 K. The Nyquist plots were fitted by using an equivalent circuit model of one RC couple (representing the bulk resistance and geometric capacitance) in series with one CPE (representing polarization at the electrode: electrolyte interface) (see Figure 4.2). A series of Nyquist plots of $0.54Li_2O - 0.36P_2O_5 - 0.096LiBr$ glass at different temperatures is shown in Figure 4.2. The bulk ionic conductivities from these fits follow the Arrhenius-type temperature dependence as expected (see Figure 4.3). Table 4.6 shows the values of experimental and MD simulated ionic conductivity

(σ_{dc}) at room temperature for yLiX – (1 – y)(0.60Li_2O – 0.40P_2O_5) glasses. For the same value of y and Li_2O/P_2O_5 ratio, LiBr-doped glasses exhibit higher σ_{dc} values than those of LiCl-doped glasses.

The slope of Arrhenius plots (cf. Figure 4.3) decrease with the increase of LiX content, consequently activation energies (E_a^{dc}) decreases from 0.601eV for y = 0.10LiCl to 0.543eV for y = 0.25LiCl, and from 0.575eV for y = 0.10LiBr to 0.535eV for y = 0.20LiBr (see Table 4.2). For the same value of y and Li_2O/P_2O_5 ratio, LiBr-doped glasses exhibit lower E_a^{dc} values than those of LiCl-doped glasses (cf. Figure 4.4). The drop in E_a^{dc} as a function of y can be approximated as $E_a^{dc} = 0.65 - c_1 y + c_2 y^2$ with c_1 = 0.92, c_2 = 1.75 for LiBr- and c_1 = 0.59, c_2 = 0.90 for LiCl-doped glasses (cf. Figure 4.4). The coefficient c_1 of the linear term is related to the softness of the network atoms. A higher value of c_1 for LiBr-doped glasses when compared to LiCl-doped glasses means the free volume in-between the network structure is more accessible when doping with the more polarisable Br^- ions. More work on the complete range of compositions would be required to reveal the detailed significance of the quadratic correction term c_2.

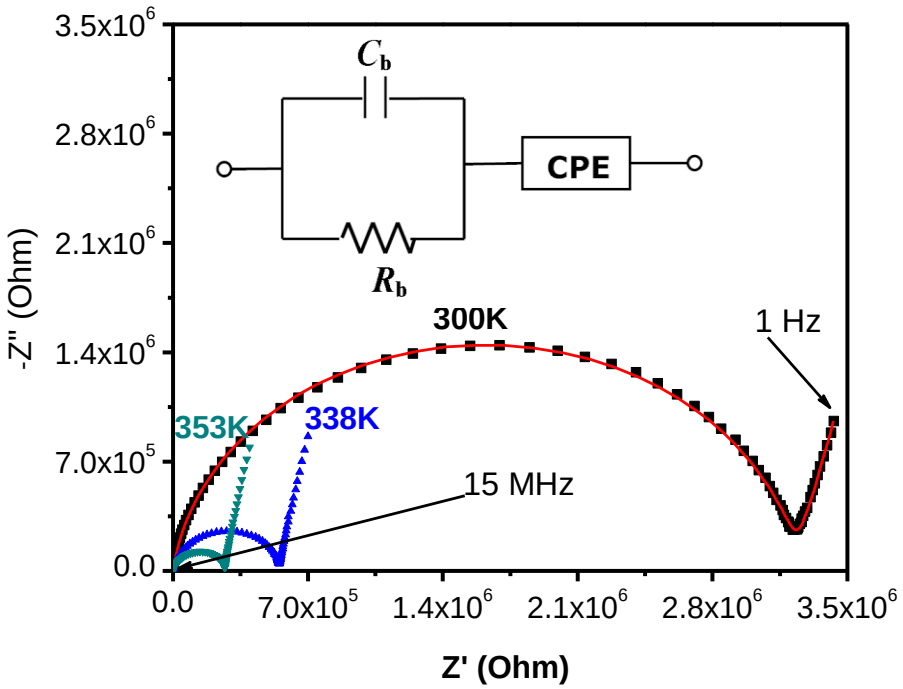

Figure 4.2. Nyquist plots of $0.54Li_2O - 0.36P_2O_5 - 0.096LiBr$ glass at different temperatures and equivalent circuit used for fitting. Red solid line: fit at T = 300 K.

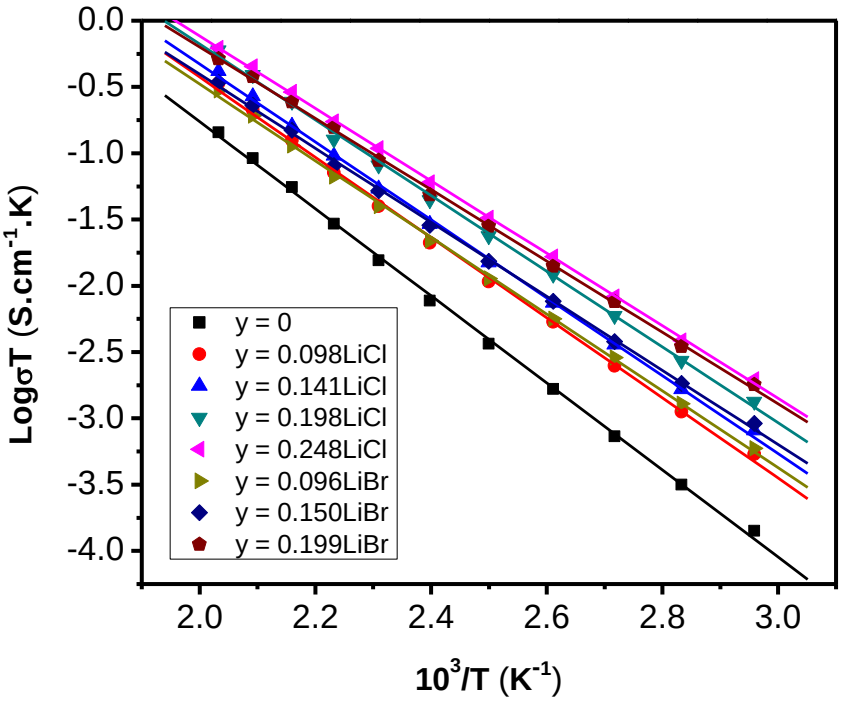

Figure 4.3. Arrhenius plots of dc ionic conductivities obtained from impedance spectroscopy for different yLiX – (1 – y)(0.60Li_2O – 0.40P_2O_5) glasses.

Table 4.6. MD and experimental ionic conductivities of yLiX – (1 – y)(0.60Li_2O – 0.40P_2O_5) glasses (X = Cl, Br) with nominal and experimental glass compositions at 300 K.

Nominal (experimental) composition	σ_{MD} (S.cm^{-1})	σ_{exp} (S.cm^{-1})
0.54Li_2O–0.36P_2O_5–0.10LiCl (0.098LiCl)	4.28 x 10^{-7}	2.89 x 10^{-7}
0.51Li_2O–0.34P_2O_5–0.15LiCl (0.141LiCl)	7.32 x 10^{-7}	4.74 x 10^{-7}
0.48Li_2O–0.32P_2O_5–0.20LiCl (0.198LiCl)	1.26 x 10^{-6}	0.93 x 10^{-6}
0.45Li_2O–0.30P_2O_5–0.25LiCl (0.248LiCl)	2.38 x 10^{-6}	1.56 x 10^{-6}
0.54Li_2O–0.36P_2O_5–0.10LiBr (0.096LiBr)	3.53 x 10^{-7}	3.18 x 10^{-7}
0.51Li_2O–0.34P_2O_5–0.15LiBr (0.150LiBr)	1.13 x 10^{-6}	0.98 x 10^{-6}
0.48Li_2O–0.32P_2O_5–0.20LiBr (0.199LiBr)	2.97 x 10^{-6}	2.72 x 10^{-6}

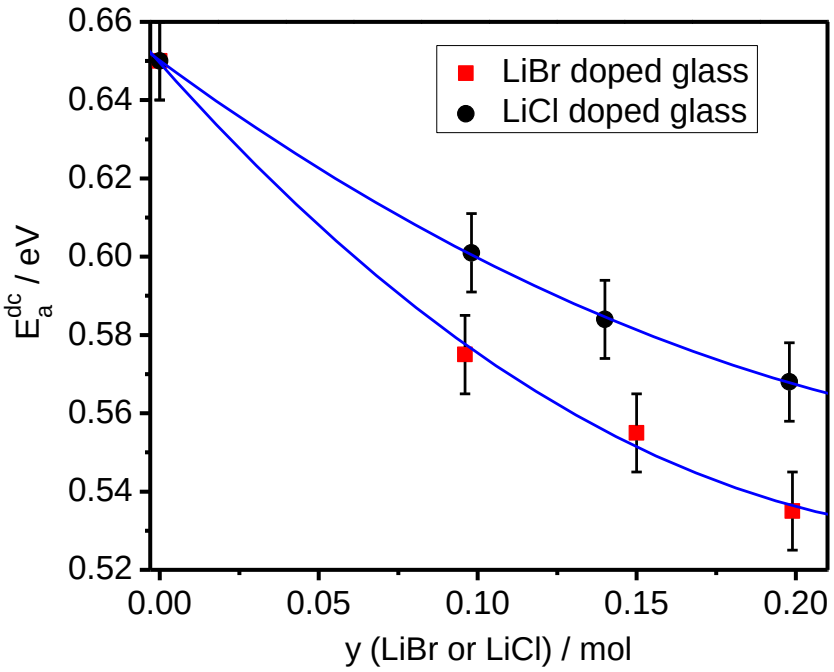

Figure 4.4. Activation energies (E_a^{dc}) versus LiX contents for yLiX – (1 – y)(0.60Li_2O – 0.40P_2O_5) glasses. The lines are polynomial fits of data.

4.3.3. Frequency dependence of ionic conductivity

Analysis of the frequency dependence of ionic conductivity at various temperatures of the electrolytes helps to reveal insights into the hopping frequency of the ions, their temperature dependence, extrapolated dc conductivity and also whether the mobile ion concentration is thermally activated [7 – 10]. Figure 4.5 shows frequency-dependent conductivity plot of log(σ) versus log(ω) for the glass composition 0.54Li_2O – 0.36P_2O_5 – 0.098LiCl. Three distinct regions in the conductivity spectra are observed for the compounds at above room temperatures: (i) the high frequency dispersive region ($\omega > 10^4$ Hz), (ii) the central plateau region, which is also called dc regime; and (iii) the low frequency dispersive region arising from

electrolyte:electrode polarisation.

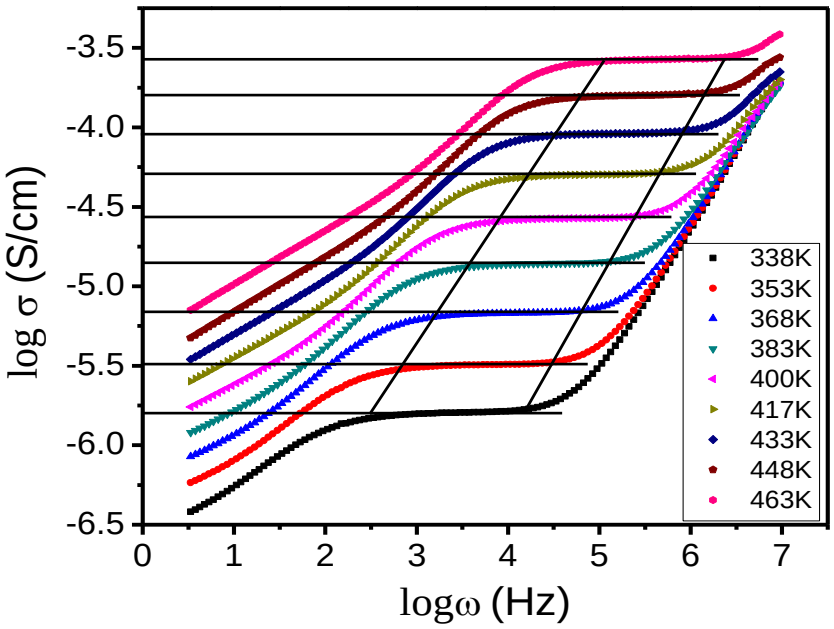

Figure 4.5. Log-log of σ versus ω at different temperatures for $0.54Li_2O - 0.36P_2O_5 - 0.098LiCl$ glass.

The frequency dispersion characteristics in the high frequency and central plateau regions can be analyzed using Jonscher's universal power law relation,

$$\sigma(\omega) = \sigma(0) + A_T\omega^n \qquad (4.3)$$

where σ(0) is the frequency-independent dc conductivity of the sample, A_T is a weakly temperature-dependent quantity (≈ 4 x 10^{-11} $S.cm^{-1}.rad^{-n}$ for $0.60Li_2O - 0.40P_2O_5$ glass, and ≈ 3 x 10^{-11} $S.cm^{-1}.rad^{-n}$ for LiX-doped glasses) and n is the power law exponent ($0 < n < 1$). The n values for all glasses are summarised in Table 4.7. As the temperature increases, the frequency at which the dispersion becomes prominent shifts to higher frequency region, as the kinetic energy of the ions and hence their vibrational frequency increases (cf. Figure 4.5). In addition, the onset points of the high-frequency conductivity dispersion at different temperatures lie on a straight line inclined at an angle of

45° (slope = 1) as shown in Figure 4.5 for $0.54Li_2O – 0.36P_2O_5 – 0.098LiCl$ glass. This suggests that dc conductivity $\sigma_{dc}(T)$ and onset frequency ω are proportional to each other and both are thermally activated with nearly the same activation energy, indicating a general feature of the power law proposed by Funke [11]. An analogous behaviour was observed when varying the content of LiX.

Table 4.7. Activation energies (E_a) and fitting parameters of ac conductivity and modulus analysis for $yLiX – (1 – y)(0.60Li_2O – 0.40P_2O_5)$ glasses (X = Cl, Br).

Experimental composition	E_a^{dc}/eV	$E_a^{\omega_p}$/eV	n	β	τ (s)
$0.60Li_2O–0.40P_2O_5$	0.650	0.625	0.91	0.87	1.86×10^{-6}
$0.54Li_2O–0.36P_2O_5–0.098LiCl$	0.601	0.588	0.94	0.90	6.58×10^{-7}
$0.51Li_2O–0.34P_2O_5–0.141LiCl$	0.584	0.569	0.94	0.91	2.88×10^{-7}
$0.48Li_2O–0.32P_2O_5–0.198LiCl$	0.568	0.547	0.94	0.93	1.81×10^{-7}
$0.45Li_2O–0.30P_2O_5–0.248LiCl$	0.543	0.525	0.94	0.94	1.34×10^{-7}
$0.54Li_2O–0.36P_2O_5–0.096LiBr$	0.575	0.565	0.95	0.90	3.92×10^{-7}
$0.51Li_2O–0.34P_2O_5–0.150LiBr$	0.555	0.544	0.95	0.91	2.76×10^{-7}
$0.48Li_2O–0.32P_2O_5–0.199LiBr$	0.535	0.521	0.95	0.94	1.39×10^{-7}

n: power law exponent in Equation (4.3); β and τ are stretching exponent and relaxation time, respectively, in the KWW function (cf. Equation 4.7).

Scaling of ac conductivity data for ionically conducting glasses and amorphous semiconductors to construct a master curve in order to realise a common underlying behaviour was reported previously [12 – 14]. The ac conductivities obtained at different temperatures follow the relation,

$$\frac{\sigma(\omega)}{\sigma_{dc}} = f\left(\frac{\omega}{\omega_p}\right) \tag{4.4}$$

where *f* is a temperature-independent scaling function, and ω_p is the hopping frequency at which $\sigma = 2\sigma_{dc}$. The hopping frequency ω_p is found to increase with temperature (see Figure 4.6), LiX addition, and halide size. For the same composition and temperature, ω_p of LiBr-doped glasses is higher than that of LiCl-doped glasses. The temperature dependence of ω_p obeys the Arrhenius behaviour. Also, as shown in Table 4.7, the hopping activation energies ($E_a^{\omega_p}$) are comparable to those of dc conductivity (E_a^{dc}). This suggests that the relaxation mechanism requires the charge carriers to cross the same energy barrier as for the conduction process [13].

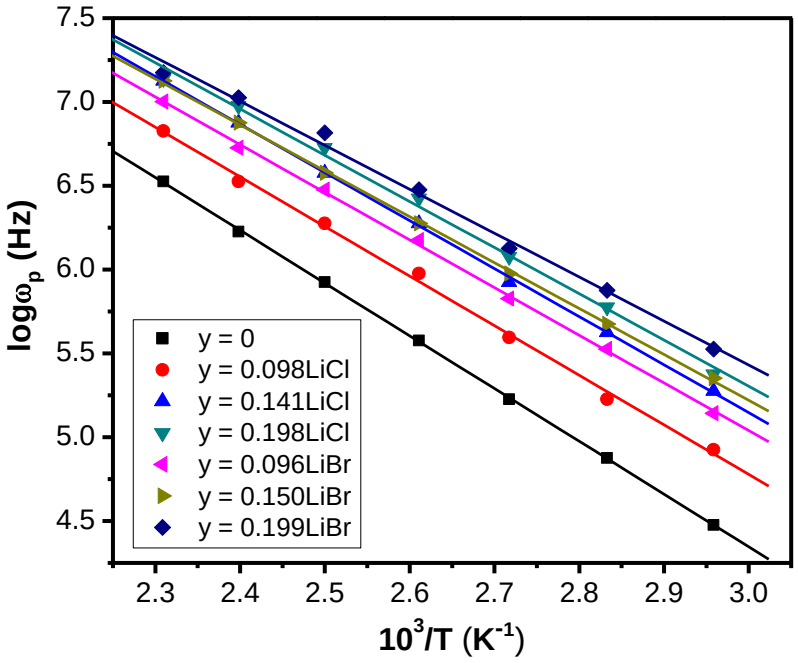

Figure 4.6. Arrhenius plots of hopping frequencies (ω_p) for different yLiX – (1 – y)(0.60Li_2O – 0.40P_2O_5) glasses.

Figure 4.7(a) shows the scaling of the ac conductivity spectra of 0.54Li_2O – 0.36P_2O_5 – 0.098LiCl glass at different temperatures. The value of ω_p at various temperatures obtained from frequency dependent conductivity $\sigma(\omega)$ approximately follows the relation,

$$\sigma(\omega) = \sigma_{dc}\left[1 + \left(\frac{\omega}{\omega_p}\right)^n\right] \quad (4.5)$$

As the characteristic frequency is activated by the same thermal energy as $\sigma_{dc}T$, the scaling parameter can also be chosen as $\sigma_{dc}T$ instead of ω_p. The advantage of using this scaling parameter is that it employs the directly available quantities σ_{dc} and T rather than the value of ω_p that has to be derived from the conductivity dispersion. Figure 4.7(b) shows the same data as Figure 4.7(a) with ω now scaled by $\sigma_{dc}T$. The exponent n in Equation (4.5) is found to decrease slightly with increasing temperatures and to exhibit a minute increase with LiX content. The values of n observed for all compounds are ~0.94±0.04. Nearly the same values of n would follow from Equation (4.3) (as n is close to 1). Since the Li^+ ion number densities of the investigated systems vary only slightly, the master curves for different glasses nearly fall on a super master curve (except for the low frequency region), and it can hardly be decided whether the additional scaling by the mobile ion concentration (as proposed by Roling et al. [12, 15]) improves the agreement among the curves. The low frequency dispersion observed for compositions at various temperatures is due to the electrode polarization as a result of the accumulation of mobile ions at the interface. The development of the space charge accumulation is more effective at lower frequencies [16]. Therefore, the total conductivity (σ) of the compound decreases as frequency decreases at a given temperature. The drop in σ can be seen in Figures 4.5 and 4.7 for frequencies below the middle plateau dc frequency regime. The dispersion is steeper and also the onset point of the low frequency dispersion shifts to a higher frequency value with increasing temperature. This is due to the fact that the higher ion mobility at

higher temperatures results in faster and more pronounced accumulation of ions and hence a corresponding drop in σ. As for high frequency dispersion, the onset points of low frequency dispersion at different temperatures lie on a straight line inclined at a slope of 0.83 (cf. Figure 4.5).

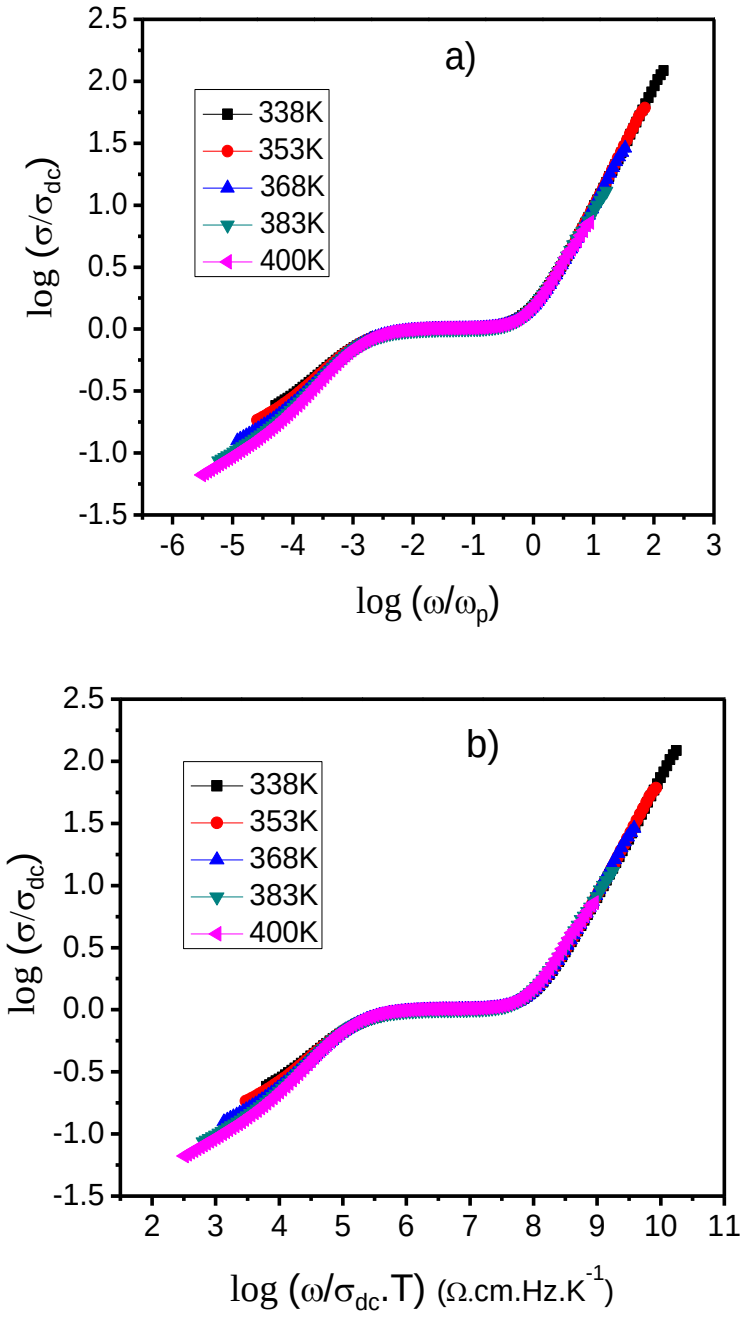

Figure 4.7. Conductivity master curves of (a) $\log(\sigma/\sigma_{dc})$ vs. $\log(\omega/\omega_p)$; (b) $\log(\sigma/\sigma_{dc})$ vs. $\log(\omega/\sigma_{dc}T)$ of $0.54Li_2O - 0.36P_2O_5 - 0.098LiCl$ glass at various temperatures.

4.3.4. Modulus analysis

The analysis of impedance data in the modulus formalism assumes importance, as it suppresses the electrode effects in extracting the conductivity relaxation times. The electric modulus data can be obtained from the complex impedance data using the relation,

$$M^* = M' + jM'' = \frac{1}{\varepsilon} = j\omega C_0 Z^* \quad (4.6)$$

where C_0 is the vacuum capacitance ($C_0 \approx 0.2 – 0.4$ pF for all the glasses), Z^* the complex impedance. Figure 4.8 shows the variation of the real part of electric modulus with frequency at different temperatures for $0.51Li_2O – 0.34P_2O_5 – 0.15LiBr$ glass. At lower frequencies, M' tends to be very small, confirming that the electrode effects make a negligible contribution, and hence may be ignored when the data are analysed in modulus formalism. For all temperatures M' reaches a constant value M_∞ at high frequencies, due to relaxation processes that spread over a range of frequencies.

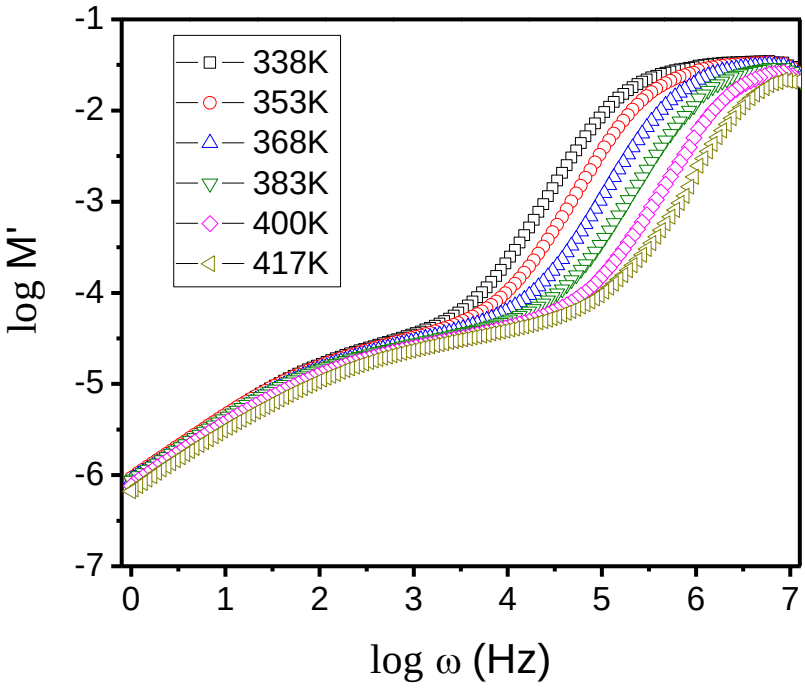

Figure 4.8. Logarithmic variation of real part of modulus (M') with frequency (ω) for $0.51Li_2O - 0.34P_2O_5 - 0.15LiBr$ glass.

The peaks of imaginary part of electric modulus (M") are asymmetric and broader on both sides of the maxima than predicted by ideal Debye behaviour (see Figure 4.9). The frequency range where the peak occurs indicates the transition from long-range to short-range mobility. The peak in M″ shifts toward higher frequencies with increase in temperature. The asymmetric M″ plot is suggestive of stretched exponential character of relaxation times. The stretched exponential function is defined by the empirical Kohlrausch-Williams-Watts (KWW) function:

$$\phi(t) = \exp\left(-\frac{t}{\tau}\right)^{\beta} \tag{4.7}$$

where τ is the relaxation time and $0 < \beta < 1$ characterises the departure from a linear exponential behaviour ($\beta = 1$).

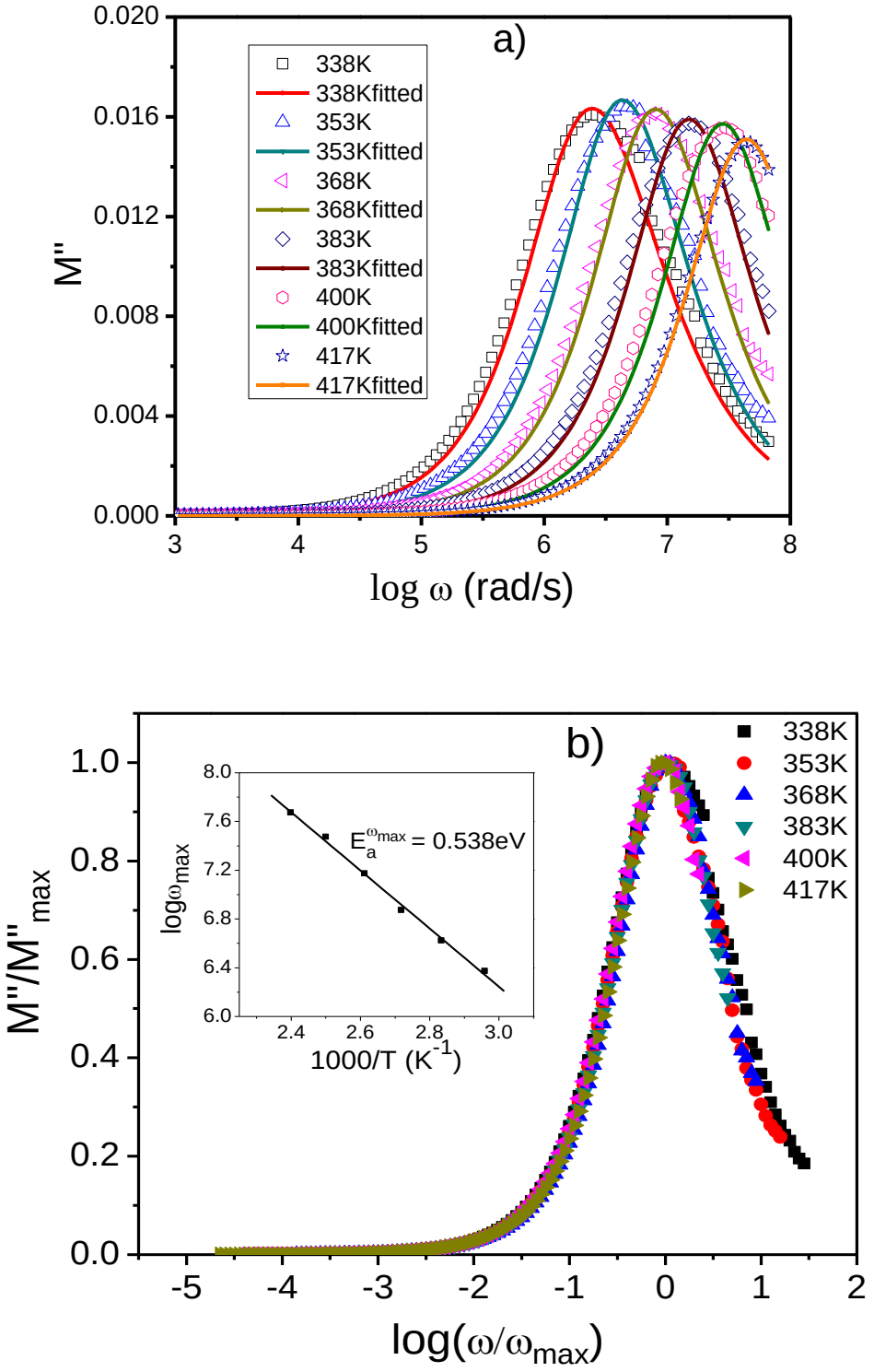

Figure 4.9. (a) Variation of imaginary part of modulus (M”) with frequency (ω) for $0.48Li_2O - 0.32P_2O_5 - 0.199LiBr$ glass. (b) Normalised plots (M''/M''_{max}) vs. $\log(\omega/\omega_{max})$ for $0.48Li_2O - 0.32P_2O_5 - 0.199LiBr$ glass. Inset: Arrhenius plot of peak frequencies ω_{max}.

In fitting to Equation (4.7), β and M_∞ have been taken as freely adjustable parameters at each temperature. The solid lines through the modulus spectra in Figure 4.9(a) show the fits are in good agreement with the experimental data. The average β value is found to depend on LiX content and temperature (see Table 4.7). The frequency exponent β does not obey Ngai's relation $\beta = 1 - n$ [10], because the KWW function used for fitting the modulus spectra leaves the high frequency component unaccounted for, whereas the conductivity formalism takes it into account. Besides, as seen in Table 4.7 the average relaxation time (τ) decreases (i) when increasing the LiX content or rising the temperature, or (ii) when replacing Cl^- by the same amount of Br^- ion.

The superimposed plots of M''/M''_{max} *vs* log (ω/ω_{max}) suggest that the dynamical processes governing conductivity relaxations at different frequencies remain the same over the investigated temperature range in these glassy systems (cf. Figure 4.9(b)). The temperature dependence of ω_{max} obeys the Arrhenius relation $\omega_{max} = \omega_0 \exp\left[-E_a^{\omega_{max}}/kT\right]$, where $E_a^{\omega_{max}}$ is the activation energy for the electrical relaxation (cf. Figure 4.9(b)). The values of $E_a^{\omega_{max}}$ are found to be comparable with the values obtained from temperature-dependent conductivity study.

4.3.5. MD simulations

Figure 4.10(a) shows the pair correlation function (PCF) and running coordination (RCN) of P – O for a typical glass y = 0.20LiBr, indicating the presence of PO_4 tetrahedra. PCF and RCN of Li – O are shown in Figure 4.10(b). The simulated bond lengths of P – O, Li – O, Li – Cl, Li – Br are

around 1.51 Å, 2.04 Å, 2.57 Å, and 2.78 Å respectively, which agree very well with their experimentally reported values for P – O, Li – O in Li phosphate glasses [1], as well as for crystalline LiCl [17] and LiBr [18]. The structure of $0.45Li_2O$ – $0.30P_2O_5$ – 0.25LiCl glass in MD-generated configuration at 300 K is illustrated in Figure 4.11, as an example.

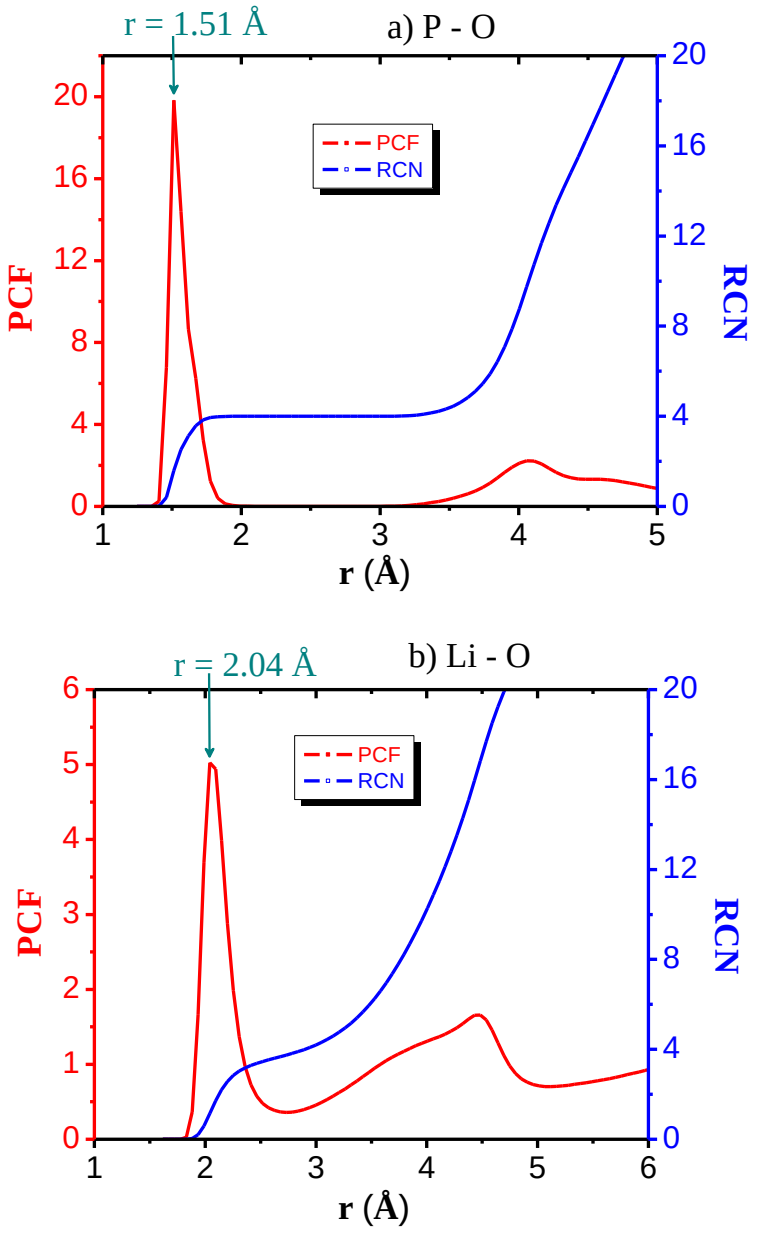

Figure 4.10. Pair correlation function (PCF) and running coordination number (RCN) of a) P – O; b) Li – O for $0.48Li_2O$ – $0.32P_2O_5$ – 0.20LiBr glass.

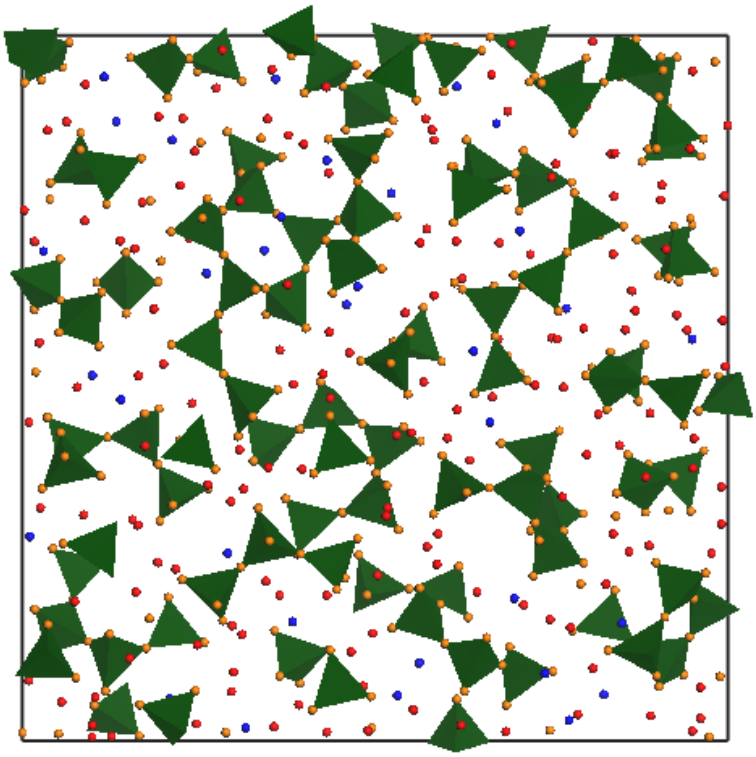

Figure 4.11. Slice from MD-simulated structure model of $0.45Li_2O – 0.30P_2O_5 – 0.25LiCl$ glass at 300 K. Oxide atoms (orange spheres) are around P atoms (shown as olive tetrahedra), Li atoms: red spheres, Cl atoms: blue spheres. Only 1/4 of the structure model is shown along the z-axis (perpendicular to the plan of view) to reduce overlap.

Figure 4.12 illustrates mean square displacement (MSD) as a function of time (τ) of Li, P, O, Cl at 300 and 1000 K for $0.45Li_2O – 0.30P_2O_5 – 0.25LiCl$ glass as an example. These plots confirm that the mobility of Li^+ ion is very much higher than those of P, O, X (Cl, Br) at 300 K, thus identifies Li^+ ion as the mobile ion which contributes to ionic conductivity in the $yLiX – (1 – y)(0.60Li_2O – 0.40P_2O_5)$ glasses. The mobility of Li^+ ions increases with temperature. Diffusion coefficient (D) of Li^+ ions was calculated from the slope of the MSD plots. Simulated ionic conductivity was then determined using the Nernst-Einstein equation. Figure 4.13 shows a comparison of ionic conductivity of both experimental and simulations for LiX-doped glasses. As seen from Figure 4.13, MD values are of the same order of the experimental

ones. The trend of increment of conductivity is the same in both cases. For LiBr-doped glasses, MD simulation can quantitatively reproduce the experimental values within experimental uncertainties, which are ca. 10% of σ_{dc} values (see Figure 4.13(b)).

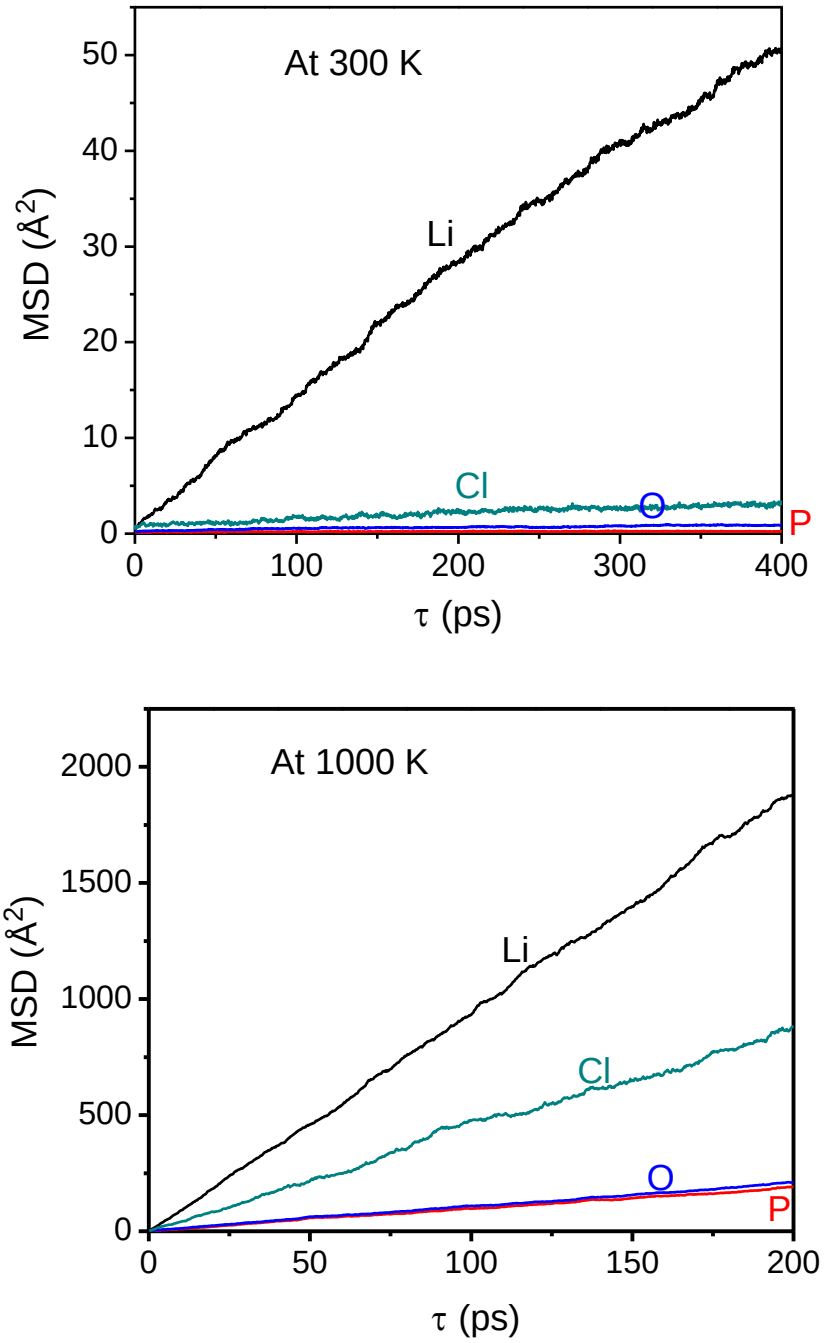

Figure 4.12. Mean square displacement (MSD) versus time (τ) for $0.45Li_2O - 0.30P_2O_5 - 0.25LiCl$ glass at 300 K (below T_g) and 1000 K (above T_g).

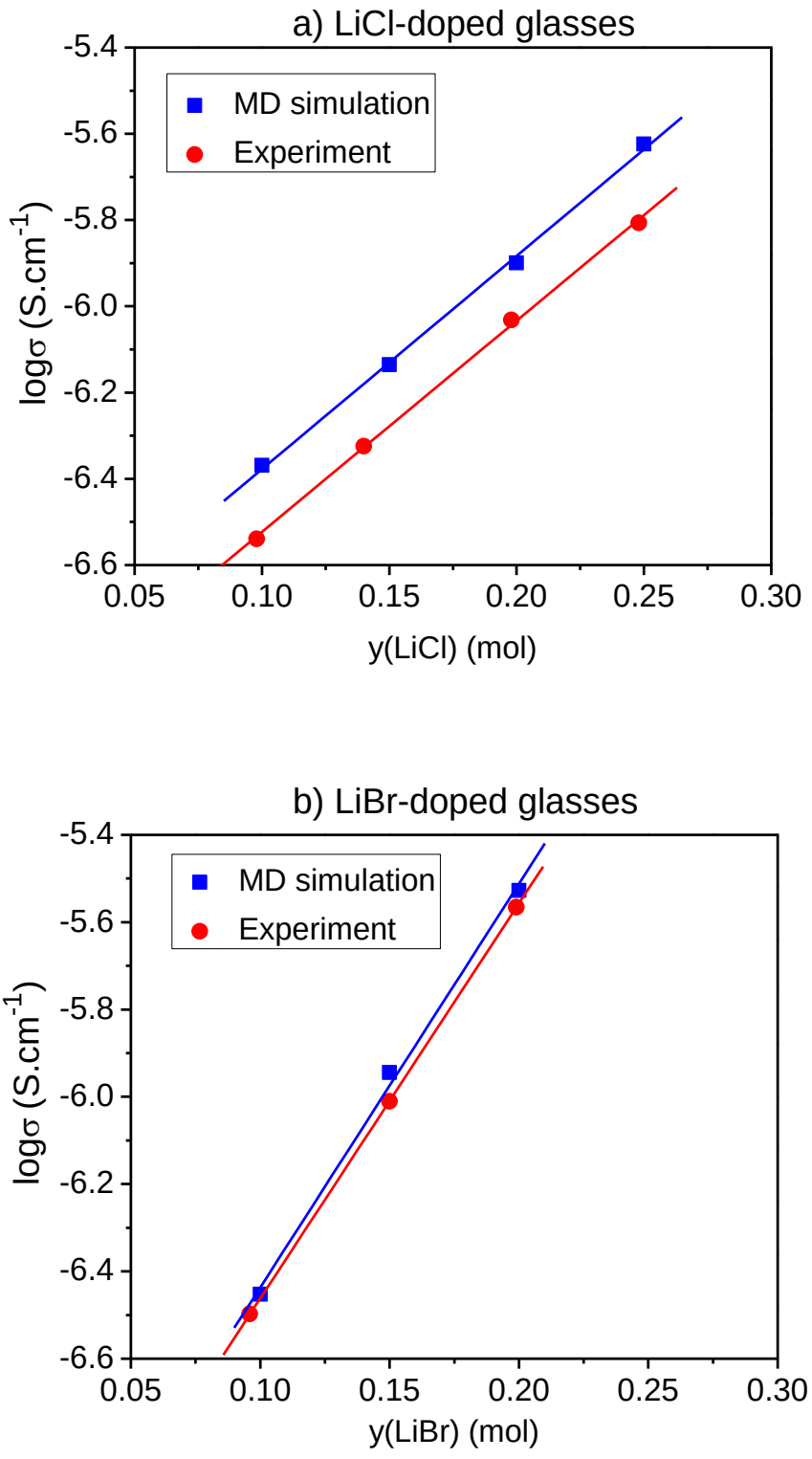

Figure 4.13. Comparison of ionic conductivities for a) LiCl-doped glasses; b) LiBr-doped glasses with composition at 300 K. The lines are linear fits of data.

4.3.6. BV analysis

Final equilibrated MD configurations of $yLiX - (1 - y)(0.60Li_2O - 0.40P_2O_5)$ glasses were used for Bond Valence (BV) analysis. It was confirmed that the percentage of bridging and non-bridging oxygen (23% and 77%, respectively) did not vary with the addition of LiX (X = Cl, Br).

The BV approach can be employed to clarify whether the Li^+ ions form LiX clusters in the investigated glass structures, as has been discussed previously in the literature for related systems [19, 20]. It is found that this hypothesis can be ruled out for the system under study: The distribution of relative contributions of Li – Cl or Li – Br bonds to the Lithium BV sums in the corresponding LiCl- or LiBr-doped glasses (cf. Figure 4.14) demonstrates that, as to be expected for a modified random network glass, only a small fraction of the Li atoms are bonded predominantly by chloride or bromide ions (< 2% for all glasses). None of the Li atoms in these glasses is coordinated exclusively by Cl^- or Br^- ions. In the case of LiCl-doped glasses (cf. Figure 4.14(a)), more than 95% oxide contribution occurs for 20% (y = 0.25, O/Cl ratio 7.8:1) to 64% (y = 0.10, O/Cl ratio 23.4:1) of the Li atoms. Similarly, for LiBr-doped glasses (cf. Figure 4.14(b)), more than 95% oxide contribution occurs for 18% (y = 0.20, O/Br ratio 10.4:1) to 64% (y = 0.10, O/Br ratio 23.4:1) of the Li atoms. Therefore, any Lithium ion transport pathway has to run along sites with mixed oxide/halide or exclusive oxide coordination.

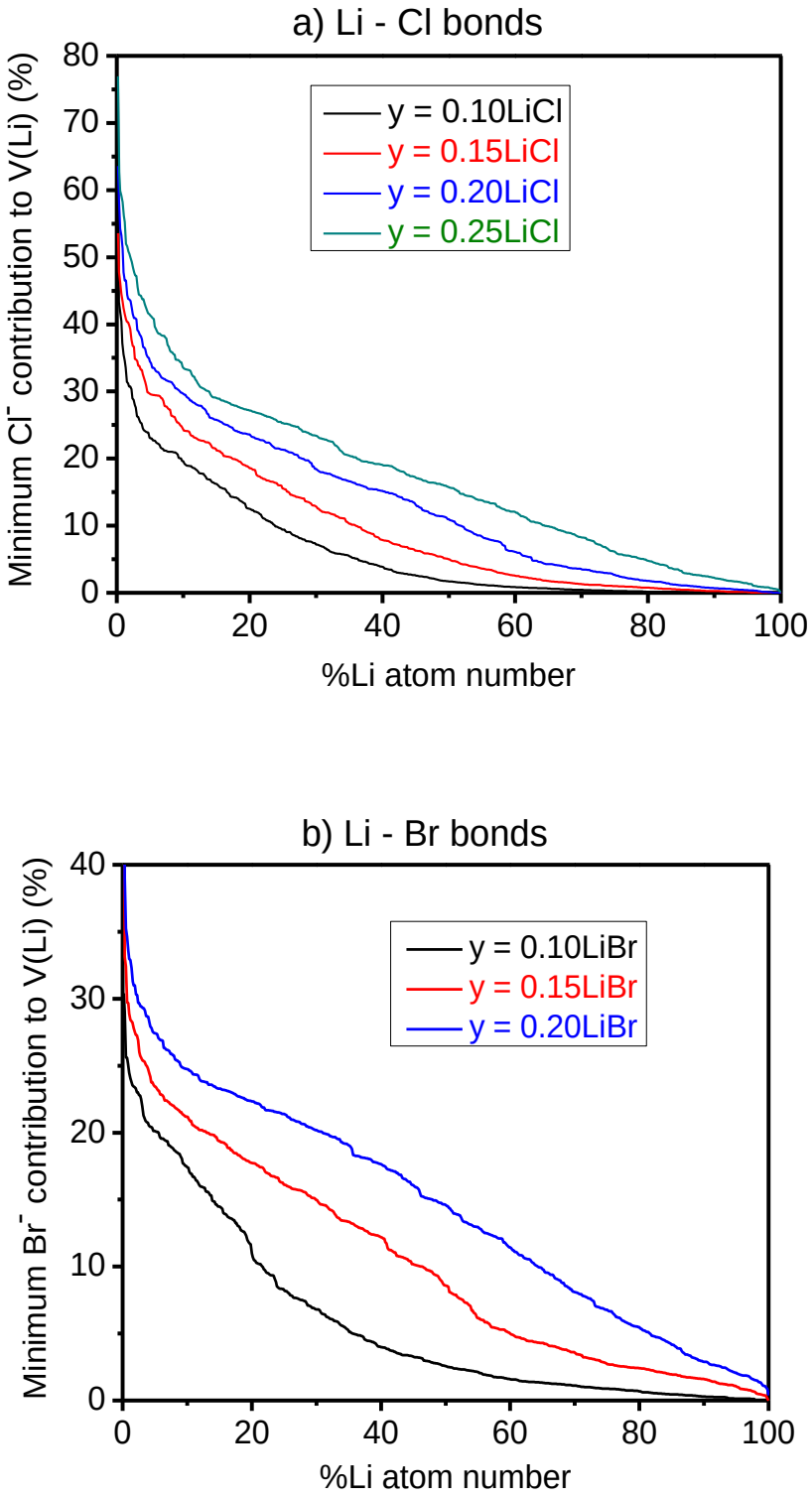

Figure 4.14. Distribution of relative contributions of a) Li – Cl bonds; b) Li – Br bonds to the BV sum of Li^+ ions in the yLiX – (1 – y)(0.60Li_2O – 0.40P_2O_5) glasses for X = Cl, Br and y = 0.10, 0.15, 0.20, and 0.25 for LiCl only.

Figures 4.15 and 4.16 show the local environment of the Li^+ ion sites located in the conduction pathways of investigated glasses (modelled as isosurfaces of constant Li bond valence sum mismatch) at 300 K. Although the pathways appear to be discontinuous ribbons in the displayed thin slices, nearly all the displayed pathway sections belong to the percolating pathway cluster if the complete 3-dimensional model is considered. The density of pathways slightly increases with increasing halide content (cf. Figures 4.15 and 4.16), in line with the slight increase of ionic conductivity in these glasses, except for y = 0.15LiCl. It was noticed that the volume fraction of percolating pathways (F) in the LiBr-doped glasses increases from 6.67% at y = 0.10LiBr to 6.93% at y = 0.20LiBr, which is higher than that of LiCl-doped glasses correspondingly (F increases from 5.40% at y = 0.10LiCl to 5.80% at y = 0.25LiCl). This contributes to higher ionic conductivity of LiBr-doped glasses when compared to LiCl-doped glasses for the same value of LiX doping (X = Cl, Br).

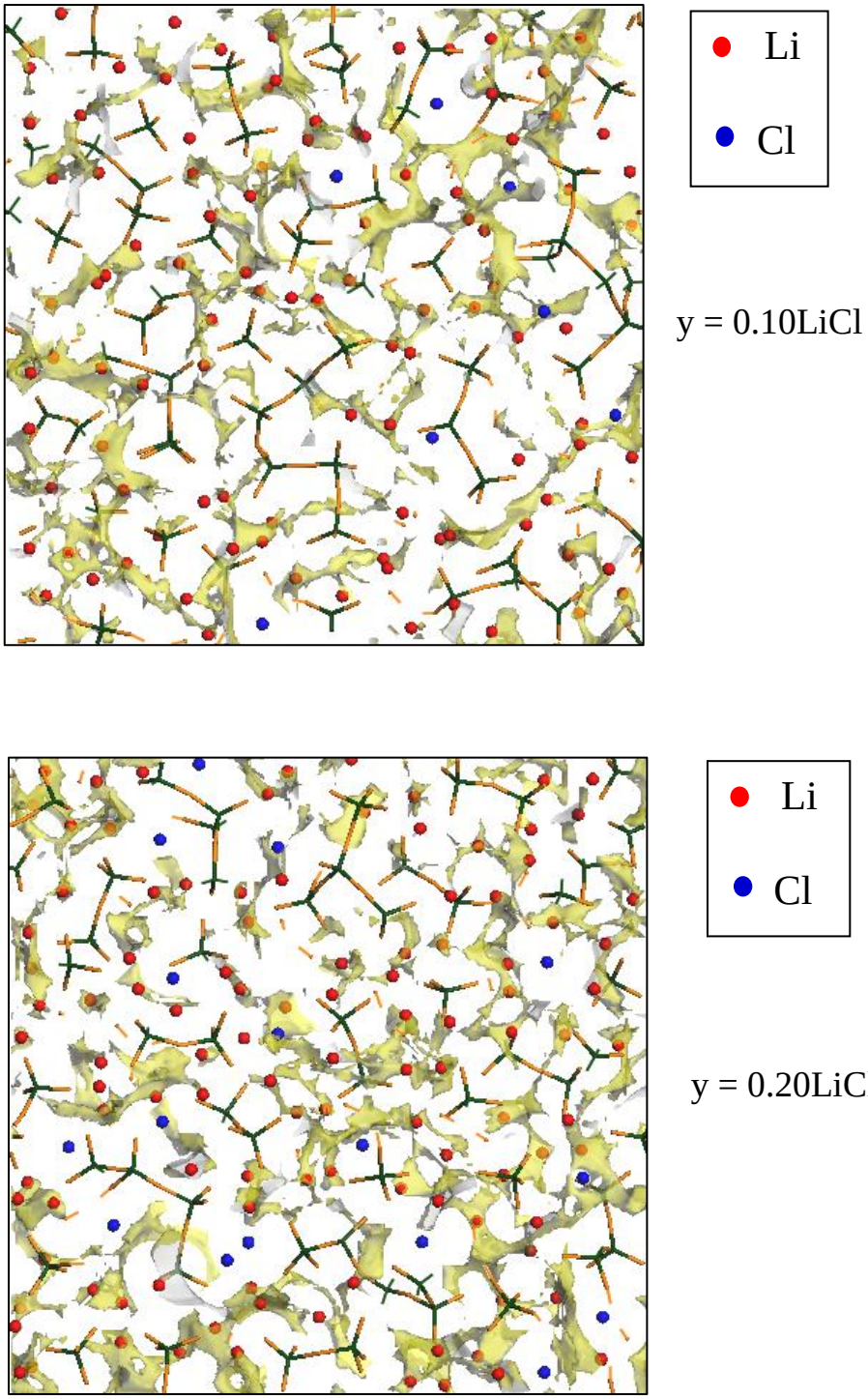

Figure 4.15. Slices through the Lithium migration pathway network visualized as isosurfaces of constant Lithium bond valence sum mismatch |ΔV(Li)| in the glasses yLiCl – (1 – y)(0.60Li_2O – 0.40P_2O_5) (y = 0.10 (top), 0.20 (bottom)) at 300 K, projected along the z-axis and superimposed on the respective glass structure model. Oxide atoms (orange sticks) are around P atoms (shown as olive tetrahedra).

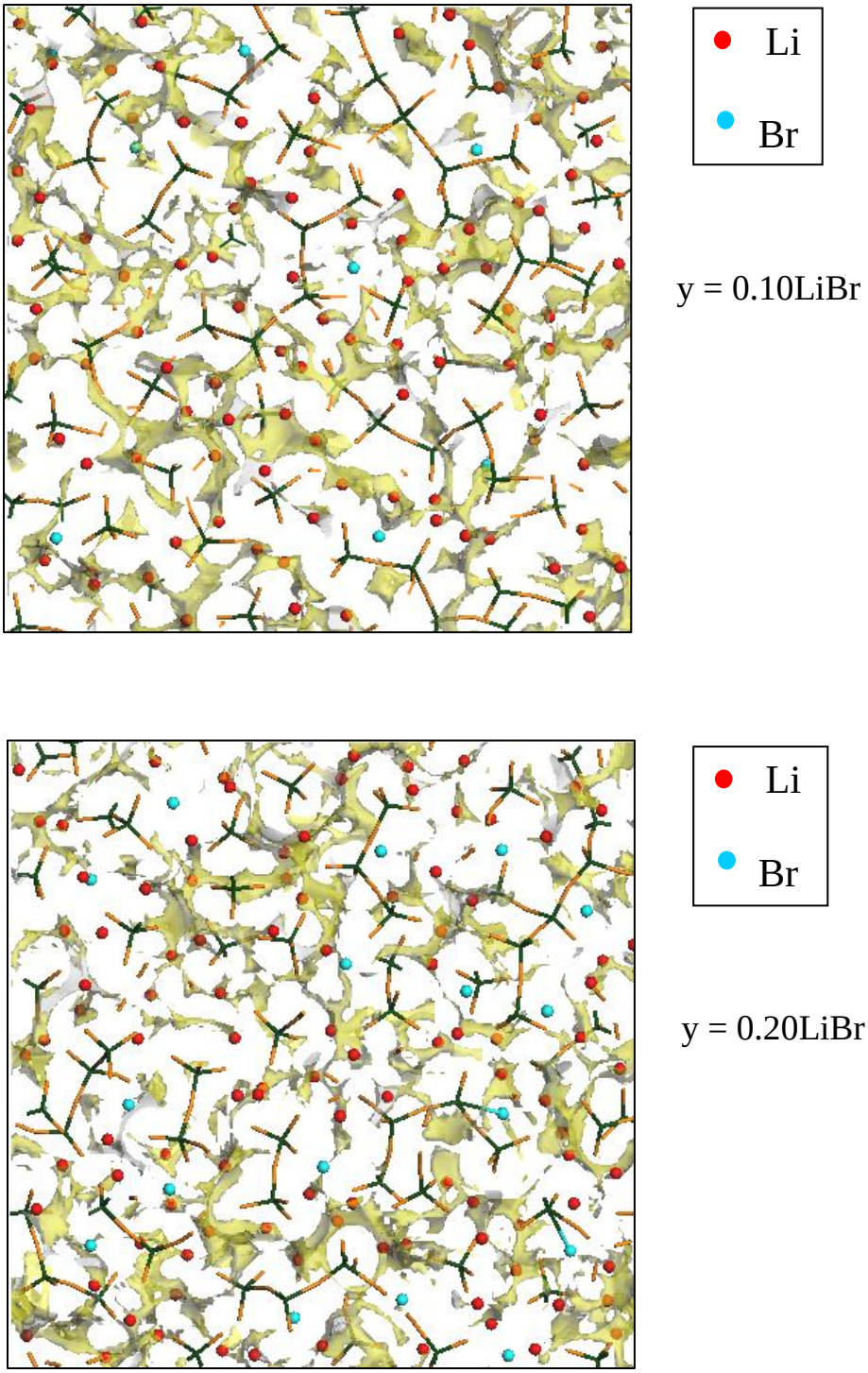

Figure 4.16. Slices through the Lithium migration pathway network visualized as isosurfaces of constant Lithium bond valence sum mismatch |ΔV(Li)| in the glasses yLiBr – (1 – y)(0.60Li_2O – 0.40P_2O_5) (y = 0.10 (top), 0.20 (bottom)) at 300 K, projected along the z- axis and superimposed on the respective glass structure model. Oxide atoms (orange sticks) are around P atoms (shown as olive tetrahedra).

Using a bond valence mismatch value $|\Delta V(Li)|$ of 0.10 valence units (to allow for a comparison with existing reference data for a wide range of other oxide glasses), we could also show that the room temperature ionic conductivity in these glasses can be semi-quantitatively predicted from the structure model. Figure 4.17 relates the volume fraction of the percolating ion conduction pathways (F) in the investigated glasses to their experimentally observed absolute values of the ionic conductivity (σ_{dc}) and activation energy (E_a^{dc}). Results of the present MD studies are compared with the previously reported reverse Monte Carlo (RMC) values [21]. As seen from Figure 4.17, the slight increase in F (i) when increasing the LiX (X = Cl, Br) dopant concentration y, or (ii) when replacing Cl^- ions by the same amount of more polarisable Br^- ions, leads to a slight increase in the ionic conductivity (σ_{dc}) and a correspondingly slight decrease in the activation energy (E_a^{dc}), except for y = 0.15LiCl.

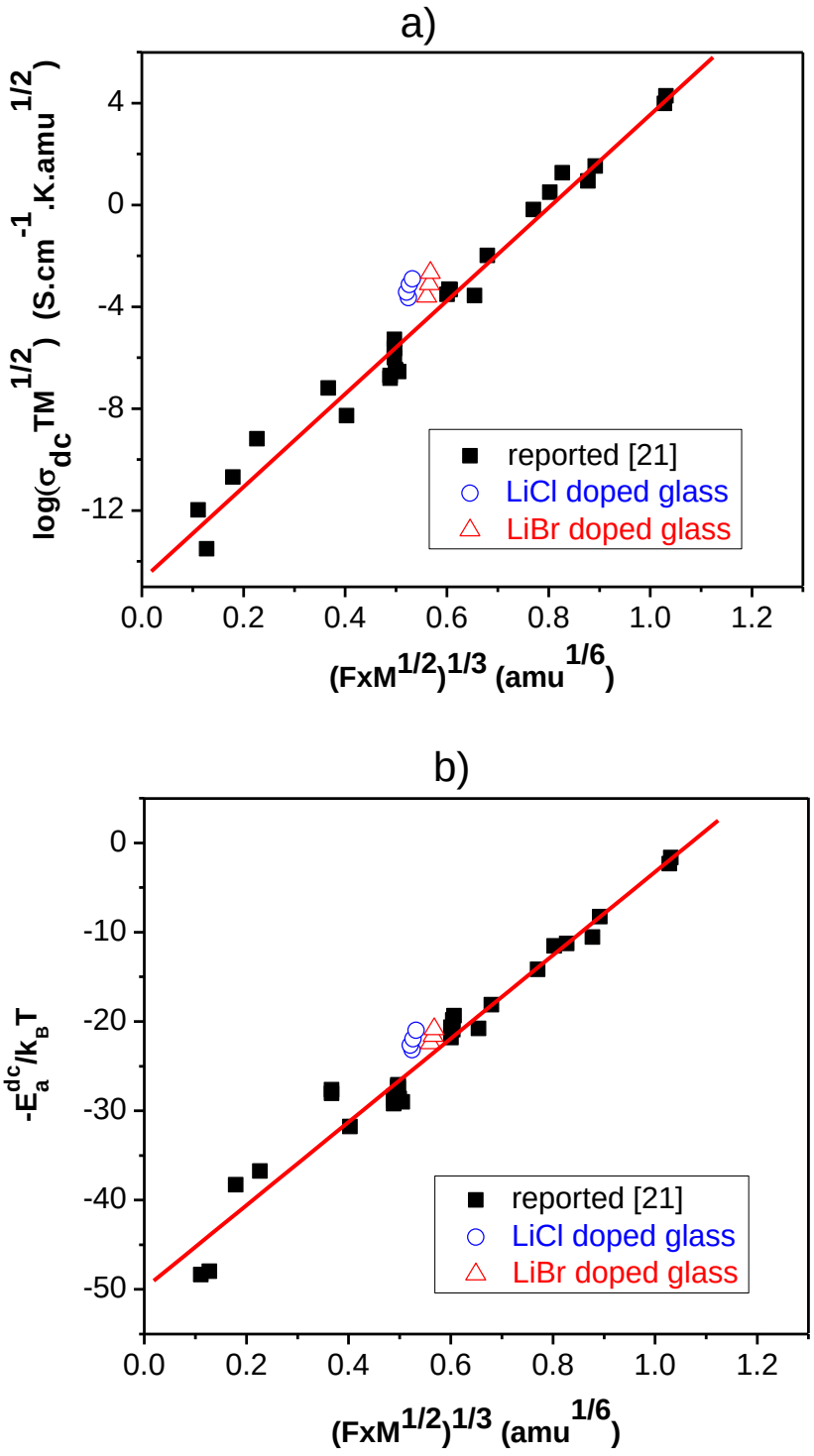

Figure 4.17. Variation of Li^+ ion pathway volume fractions with a) Experimental room temperature ionic conductivity (σ_{dc}); b) Activation energy (E_a^{dc}). Solid symbols refer to data from RMC models [21]. Open symbols refer to MD-simulated data of $yLiX - (1 - y)(0.60Li_2O - 0.40P_2O_5)$ glasses (where X = Cl, Br; y = 0.10, 0.15, 0.20, and 0.25 for LiCl only).

Using the concept of mass-radius dimension [22], we can further investigate details of the pathway structure. Firstly, as seen from Figure 4.18, the minimum value of local pathway dimension increases with rising LiX content, again except for y = 0.15LiCl. This minimum value of local dimension may be largely thought of as characterizing the width of the Li^+ ion transport pathway at the bottleneck of elementary transport steps. Thus the increase of the local pathway dimension as a result of doping by the more polarisable X^- ions indicates that channels accessible for Li^+ ion movement are widened by the doping. Secondly, it was noticed that the minima of local dimension for LiBr-doped glasses (increasing from 1.969 at y = 0.10LiBr to 2.145 at y = 0.20LiBr) are higher than those for LiCl-doped glasses (rising from 1.876 at y = 0.10LiCl to 1.967 at y = 0.25LiCl). This is attributed to the higher polarisability and larger size of Br^- than Cl^- ions. Consequently, the reorganization of the bridged P – O – P chains by creating more space between them, which is caused to accommodate the X^- ion, is more effective for Br^- ion, thus leading to broader channels for Li^+ ion transport, when compared to Cl^- ion. This also contributes to the decrease of activation energy and the increase of ionic conductivity (i) when increasing LiX dopant content or (ii) when replacing Cl^- by the same amount of more polarisable Br^-.

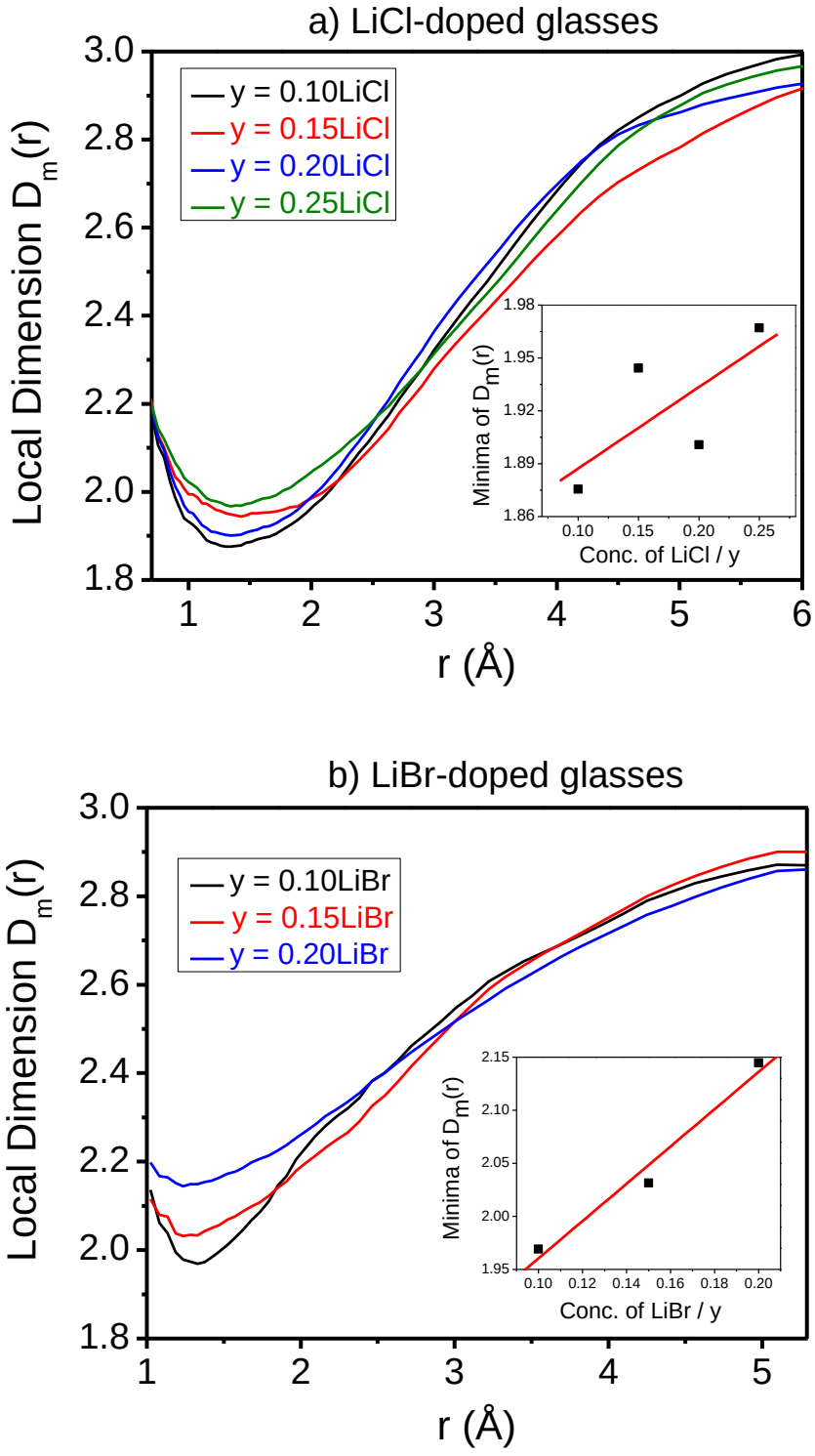

Figure 4.18. The local Li^+ ion transport pathway dimension, $D_m(r)$ versus radius (r) for $yLiX - (1 - y)(0.60Li_2O - 0.40P_2O_5)$ glasses. Inside graphs indicate the variation of local dimension minima with respect to LiX variation.

4.4. Conclusions

Halide salt doped lithium phosphate glasses $yLiX – (1 – y)(0.60Li_2O – 0.40P_2O_5)$ (where X = Cl, Br; y = 0, 0.10, 0.15, 0.20, 0.25) were prepared using melt quenching method. Number density and glass transition temperature (T_g) decrease with the increase of LiX content, indicating that the glass matrix becomes less rigid with the LiX addition. Replacement of Cl^- ions by the same amount of more polarisable Br^- ions leads to a higher T_g value.

Ac conductivity and relaxation behaviour of $0.60Li_2O – 0.40P_2O_5$ glass doped with LiX have been studied as a function of temperature and frequency. The frequency dependent conductivity at different temperatures has been analysed using Jonscher's power law approach. The exponent *n* is ~0.9 and slightly depends on temperature, while the superposition of the reduced conductivity at all temperatures shows that the relaxation mechanism is temperature independent. Data have been analysed in the modulus formalism with a distribution of relaxation times using KWW stretched exponential function. The stretching exponent, β, is found to depend on temperature and LiX content. In addition, the average relaxation time (τ) decreases (i) when increasing the LiX content or rising the temperature, or (ii) when replacing Cl^- by the same amount of Br^- ion, which is in line with the decrease of activation energy and the increase of ionic conductivity. The analysis of the temperature variation of the M″ peak indicates that the observed relaxation process is thermally activated. The inferences drawn from the above analysis (i) Arrhenius dependence of relaxation peak on temperature and (ii) comparable values of activation energy obtained from conductivity and modulus analysis

suggest that the ion transport in the investigated materials follows the hopping mechanism.

Optimised potential parameters reproduce the reported bond lengths and coordinations in the $yLiX - (1 - y)(0.60Li_2O - 0.40P_2O_5)$ glasses. Moreover, experimental and simulated values of the ionic conductivity are in good agreement. For the investigated compositions ion transport cannot be related to the (previously presumed) LiX (X = Cl, Br) aggregates as such aggregates do not exist – at least in the simulated structures. Nearly all Li atoms have mixed oxide-halide coordinations.

The effect of halide addition on the pathways for the mobility of Li^+ ions is quantified for the phosphate glasses $yLiX - (1 - y)(0.60Li_2O - 0.40P_2O_5)$. Volume fraction for Li^+ ion transport pathways and experimental conductivities accordingly exhibit an unusually small effect of halide doping. The volume fraction and the minimum value of the local pathway dimension increase (i) when increasing the LiX (X = Cl, Br) dopant concentration or (ii) when replacing Cl^- ions by the same amount of more polarisable Br^- ions. The higher minimum local dimension means the Li^+ ion transport pathway is more open, i.e. channels for Li^+ ion hopping become wider. As a result, doping by the more polarisable X^- ions causes lower activation energy (E_a^{dc}) and higher ionic conductivity (σ_{dc}).

References

1. K. Muruganandam, M. Seshasayee, S. Patnaik, Solid State Ionics 89 (1996) 313.
2. R. Prasada Rao, M. Seshasayee, Solid State Commun. 131 (2004) 537.
3. M. Tatsumisago, Y. Kowada, T. Minami, Phys. Chem. Glasses 29 (1988) 63.
4. H. L. Tuller, D. P. Button, D. R. Uhlmann, J. Non-Cryst. Solids 40 (1980) 93.
5. J. P. Malugani, G. Robert, Mat. Res. Bull. 14 (1979) 1075.
6. M. Doreau, A. Abou El Anouar, G. Robert, Mat. Res. Bull. 15 (1980) 285.
7. S. R. Elliott, Solid State Ionics 27 (1988) (3) 131.
8. D. P. Almond, A. R. West, Solid State Ionics 9-10 (1983) 277.
9. K. Funke, R. D. Banhatti, Solid State Ionics 177 (2006) 1551.
10. K. L. Ngai, A. K. Rajagopal, S. Teitler, J. Chem. Phys. 88 (1988) 5086.
11. K. Funke, Prog. Solid State Chem. 22 (1993) 111.
12. B. Roling, A. Happe, K. Funke, M. D. Ingram, Phys. Rev. Lett. 78 (1997) 2160.
13. P. S. Anantha, K. Hariharan, Mat. Sci. Eng. B 121 (2005) 12.
14. A. Bhide, K. Hariharan, Mat. Chem. Phys. 105 (2007) 213.
15. K. Funke, B. Roling, M. Lange, Solid State Ionics 105 (1998) 195.

16. C. J. Leo, G. Subba Rao, B. V. R. Chowdari, J. Mat. Chem. 12 (2002) 1848.
17. S. H. Bauer, T. Ino, R. F. Porter, J. Chem. Phys. 33 (1960) 685.
18. S. Matsuo, P. Nachimuthu, D. W. Lindle, H. Wakita, R. C. C. Perera, J. Phys. Chem. B 107 (2003) 12562.
19. S. Adams, Bull. Mater. Sci. 29(6) (2006) 587.
20. Y. Ogiwara, K. Echigo and M. Hayana, J. Non. Cryst. Solids 352 (2006) 5192.
21. S. Adams, J. Swenson, Phys. Chem. Chem. Phys. 4 (2002) 3179.
22. A. Hall, S. Adams, J. Swenson, Phys. Rev. B 74 (2006) 174205.

Chapter 5

Glass Formation, Structure, AC Conductivity Studies and Mobile Ion Transport Pathways in Borophosphate Glasses $0.45Li_2O – (0.55 – x)P_2O_5 – xB_2O_3$

5.1. Introduction

Besides the increase of network modifier (Li_2O) and halide dopant (LiX) concentration as mentioned in Chapter 3 and 4 for lithium silicate and phosphate glasses, mixed glass former effect is also expected to further increase the ionic conductivity of the glassy systems. Therefore, in this project lithium borophosphate glasses $0.45Li_2O - (0.55 - x)P_2O_5 - xB_2O_3$ ($0 \leq x \leq 1$) were studied by keeping the molar ratio $[Li_2O]/([P_2O_5] + [B_2O_3])$ constant to focus on the effect of mixed glass formers on the glass structure and Li^+ ion mobility.

Lithium borophosphate glasses are of technical interest as fast ion conductors with high chemical durability but also of theoretical interest as model substances for studies of the mixed glass former effect [1 – 5]. Since lithium borophosphate glasses present an ionic conductivity with orders of magnitude higher than their binary counterparts, these glasses are promising candidates for improved solid electrolytes in the next generation lithium batteries. Therefore, a detailed knowledge of composition-structure-property relationships plays an important role for a systematic design of these materials for the above applications.

As mentioned in literature review, various studies have been done to understand the effect of compositions on structure and properties of borophosphate glasses. However the correlation of macroscopic dynamic properties such as glass transition temperature, ionic conductivity, etc. with structure in these materials is still not fully understood. There is still a debate

whether BPO_4 units exist to a significant extent in the structural network of borophosphates and contribute to the enhancement of ionic conductivity. Besides, the role of cross-linking P – O – B linkages on the macroscopic properties also needs to be clarified. Therefore, further investigation on the structures and properties of borophosphate glasses have been undertaken in this work.

There are very few studies on the structure and ion dynamics of mixed glass former systems using computational simulation such as ab initio, reverse Monte Carlo (RMC) Molecular Dynamics (MD) simulations. This may be due to their complex structures, which make it difficult to derive optimized potentials for modelling. MD simulations for borosilicate- and aluminosilicate-based glasses have been reported [6 – 8], but to my knowledge no such activities has been published so far for borophosphate glasses. Furthermore, the understanding of ion conduction mechanism in the borophosphate glassy systems and in particular the effect of B_2O_3 dopants on the ion transport pathways is still lacking.

For the above reasons, the main aim of my study here is to investigate borophosphate glassy system $0.45Li_2O – (0.55 – x)P_2O_5 – xB_2O_3$ in order to further understand the influence of mixed glass former effect on cation mobility, as well as the relation between structure and ion transport pathways in these materials.

Firstly, to attain this objective, $0.45Li_2O – (0.55 – x)P_2O_5 – xB_2O_3$ glasses are synthesized and characterized using XRD, DSC, electrochemical impedance spectroscopy. Structures of the investigated glasses are analyzed by

using FT-IR, Raman and XPS spectroscopy. Ion dynamics in this system is also explored using analysis of frequency dependent conductivity and modulus formalisms to provide more information on ion transport mechanism and relaxation behavior.

Secondly, structures of the borophosphate glasses are modelled by using MD simulation, followed by the quantification of ion transport pathways using bond valence (BV) approach, which is applied for the MD simulated borophosphate glasses. Bridging (BOs) and non-bridging oxygens (NBOs) of the simulated $0.45Li_2O - (0.55 - x)P_2O_5 - xB_2O_3$ glass structures are calculated and compared to those as determined from deconvolution of XPS spectra in this study.

It is noticed that for easier comparison with borophosphate glass series of slightly different network modifier content, the relative B_2O_3 content $Y = [B_2O_3]/([B_2O_3]+[P_2O_5])$ instead of x will be used where appropriate.

5.2. Techniques

5.2.1. Sample synthesis and properties characterization

Please see Section 2.2.2 for the preparation of Li borophosphate glasses.

The quenched samples were characterized by XRD (cf. Section 2.3.1). Density of glasses was measured by Pycnometry (cf. Section 2.3.2). The glass transition temperature (T_g) was determined using DSC (cf. Section 2.3.4).

Ionic conductivity measurements of these glasses were carried out in the

frequency range of 150 Hz to 15 MHz and temperature range of 300 K to 479 K (cf. Section 2.3.8).

Fourier Transformed Infrared (FT-IR) spectra of the glasses were recorded in the wave number range of 400 – 4000 cm^{-1} at room temperature with the resolution of 4 cm^{-1} (cf. Section 2.3.5).

Raman spectra were measured at room temperature on bulk glassy samples using Argon green laser (cf. Section 2.3.6). Deconvolutions of the spectra were carried out within the wave number range of 500 – 1400 cm^{-1}. To achieve the best fits for all the experimental spectra, each Raman spectrum was fitted with Gaussian peaks using a least-square curve-fitting algorithm. The position of each band, band width, and its intensity are the adjustable parameters during the fitting.

X-ray photoelectron spectroscopy (XPS) analyses of the glassy samples were also carried out (cf. Section 2.3.7 for more details). Each O1s spectrum was fitted with Gaussian peaks using a least-square curve-fitting algorithm. Peak positions, band widths and intensities were varied to obtain the best fit to each experimental spectrum.

5.2.2. Molecular Dynamics (MD) simulations

Constant volume (NVT) Molecular Dynamics (MD) simulations have been performed on structure models of $0.45Li_2O – (0.55 – x)P_2O_5 – xB_2O_3$ (where $0.05 \leq x \leq 0.35$ or $0.09 \leq Y \leq 0.64$). The volume of the simulation box is derived from our density determinations (Table 5.1). Optimized potential parameters shown in Tables 5.2 and 5.3 have been derived by fitting to

experimentally known bond lengths and coordination numbers.

Table 5.1. Physical parameters of $0.45Li_2O – (0.55 – x)P_2O_5 – xB_2O_3$ glasses, where $Y = [B_2O_3]/([B_2O_3]+[P_2O_5])$.

x	Y	Mass density (g/cm^3)	Molar volume (cm^3)	Number density ($Å^{-3}$)	T_g (K)	$F_{1/2}$
0	0.00	2.330	39.28	7.98×10^{-2}	561	0.342
0.05	0.09	2.344	37.51	8.19×10^{-2}	606	0.326
0.10	0.18	2.398	35.15	8.56×10^{-2}	636	0.333
0.15	0.27	2.434	33.14	8.90×10^{-2}	659	0.339
0.20	0.36	2.447	31.49	9.18×10^{-2}	682	0.350
0.25	0.45	2.435	30.15	9.38×10^{-2}	692	0.380
0.30	0.55	2.405	29.03	9.54×10^{-2}	698	0.396
0.35	0.64	2.372	27.91	9.71×10^{-2}	705	0.421
0.40	0.73	2.334	26.81	9.88×10^{-2}	720	0.458
0.45	0.82	2.315	25.47	10.16×10^{-2}	n.d.*	-
0.50	0.91	2.287	24.20	10.45×10^{-2}	738	0.341
0.55	1.00	2.246	23.04	10.71×10^{-2}	715	0.346

*n.d.: not determined; T_g: glass transition temperature; $F_{1/2}$: thermodynamic fragility.

Table 5.2. Optimized two-body potential parameters for $0.45Li_2O – (0.55 – x)P_2O_5 – xB_2O_3$ glasses.

Interaction (i – j)	A_{ij} (eV)	ρ_{ijo} (Å)
P – O	740.25	0.290
B – O	600.75	0.245
Li – O	350.50	0.280
O – O	6000.00	0.245
P – P	3000.13	0.290
B – P	3576.88	0.250
Li – P	510.63	0.290
B – B	2000.13	0.290
Li – B	510.63	0.290
Li – Li	1437.50	0.290

Table 5.3. Potential parameters for the three-body Vessal term in the forcefield for $0.45Li_2O – (0.55 – x)P_2O_5 – xB_2O_3$ glasses (r_c*: cut-off in r_{ij} and r_{ik}).

Interaction (j – i – k)	k (eV)	θ_0	ρ_{ij} (Å)	ρ_{ik} (Å)	r_c^* (Å)
O – P – O	4.5000	109.47	2.8252	2.8252	3.00
P – O – P	0.0129	135.58	1.5000	1.2322	2.60
O – B – O	7.0000	109.47	2.2700	2.2700	2.10

Starting at a temperature of 1500 K, the system was cooled by scaling velocities to 1000, 700, 500, 400 K and finally to 300 K with a time step of 2 fs and equilibration time of 100 ps. Equilibration runs at each of these temperatures were followed by production runs as a basis for the determination of the mean square displacement (MSD), which for the temperatures 1500 – 700 K extended over 400 ps, or over 900 ps for the temperatures 500 – 300 K below the glass transition temperature. Besides the Coulomb interactions the potential function U_{ij} between atoms i and j involves a Born repulsion term (Buckingham potential with C_{ij} =0) and a Vessal-type three-body term as follows:

$$U_{ij} = \frac{z_i z_j e^2}{r_{ij}} + A_{ij}\exp\left(\frac{-r_{ij}}{\rho_{ij0}}\right) + \frac{k_{ij}}{8(\theta_{jik} - \pi)}\left\{\left[(\theta_0 - \pi)^2 - (\theta_{jik} - \pi)^2\right]^2\right\}\exp\left[-\frac{r_{ij}}{\rho_{ij}} - \frac{r_{ik}}{\rho_{ik}}\right] \quad (5.1)$$

Here, U_{ij} is the interatomic potential between atoms i and j, z_i is the effective charge number of atom i, θ_0 is the equilibrium angle subtended by r_{ij} and r_{ik}. A_{ij}, ρ_{ij0}, k_{ij}, ρ_{ij} and ρ_{ik} represent potential parameters. The ionic charges used in MD simulations for Li, P, B, O are +0.6*e*, +3.0*e*, +1.8*e*, -1.2*e*, respectively.

Bond valence analysis is then applied to the final equilibrated configuration obtained at 300 K.

5.2.3. Bond valence (BV) approach

More details of the Bond Valence approach can be found in Section 2.4.3.

Determining which oxygens are bridging or not is frequently done by using radial cut-off criterion: how many P or B atoms there are within a specified distance of the oxygen. Here a threshold value of $s_{(X\text{-}O)} = 0.16$ (where X = P or B) is used to decide whether an X – O interaction should be treated as a bond and hence whether an oxygen atom is bridging or non-bridging. Therefrom, bridging (BO) and non-bridging oxygens (NBO) of the simulated $0.45Li_2O – (0.55 – x)P_2O_5 – xB_2O_3$ glass structures are calculated and compared to those as determined from deconvolution of XPS spectra in this study.

5.3. Results and Discussion

5.3.1. XRD, density and thermal studies

No sharp Bragg peaks were observed from XRD within the ranges of $0 \leq Y \leq 0.73$ ($0 \leq x \leq 0.40$) and $0.91 \leq Y \leq 1$ ($0.50 \leq x \leq 0.55$), confirming the glass forming regions of $0.45Li_2O – (0.55 – x)P_2O_5 – xB_2O_3$ system for usual melt quenching rates, as shown in Figure 5.1. Transparent glasses were obtained in these regions. However, at Y = 0.82 (x = 0.45), some Bragg peaks corresponding to crystalline Li_3PO_4 phase were identified on the amorphous

background (see Figure 5.1). This finding is in harmony with the phase diagram proposed by Magistris et al. [2].

The mass density, molar volume, number density, glass transition temperature (T_g) and thermodynamic fragility ($F_{1/2}$) values of all the investigated glasses are listed in Table 5.1. As the B_2O_3 content increases, T_g increases (cf. Figure 5.2(a)), while the glass density passes through a maximum at Y = 0.36 (x = 0.20) and then decreases (in agreement with the findings in [9]). Likewise, the number density exhibits a positive deviation from the general trend that is again most pronounced for Y = 0.36 (cf. Figure 5.2(b)). The rise in T_g indicates that the glass matrix overall becomes stronger and more rigid with increasing B_2O_3 content, and with increased cross-linking of the glass network between phosphate chains through B – O – P bonds [4, 5]. Therefore the T_g versus Y curve exhibits a pronounced positive deviation from a Vegard-type linear interpolation between single glass former cases Y = 0 and Y = 1 (cf. Figure 5.2(a)).

Thermodynamic fragility ($F_{1/2}$) values were calculated according to:

$$F_{1/2} = (0.151 - \Theta)/(0.151 + \Theta) \tag{5.2}$$

where $\Theta = \Delta T_g/T_g$, and ΔT_g is the width of the glass transition [10]. The increase of $F_{1/2}$ with B_2O_3 content up to Y = 0.73 indicates that the glass system becomes more fragile, especially when the relative B_2O_3 content is in the range $0.30 < Y \leq 0.73$, the limit of the phosphate-rich glass forming region. For higher borate contents, $F_{1/2}$ then decreases again towards the pure borate side ($Y \geq 0.91$).

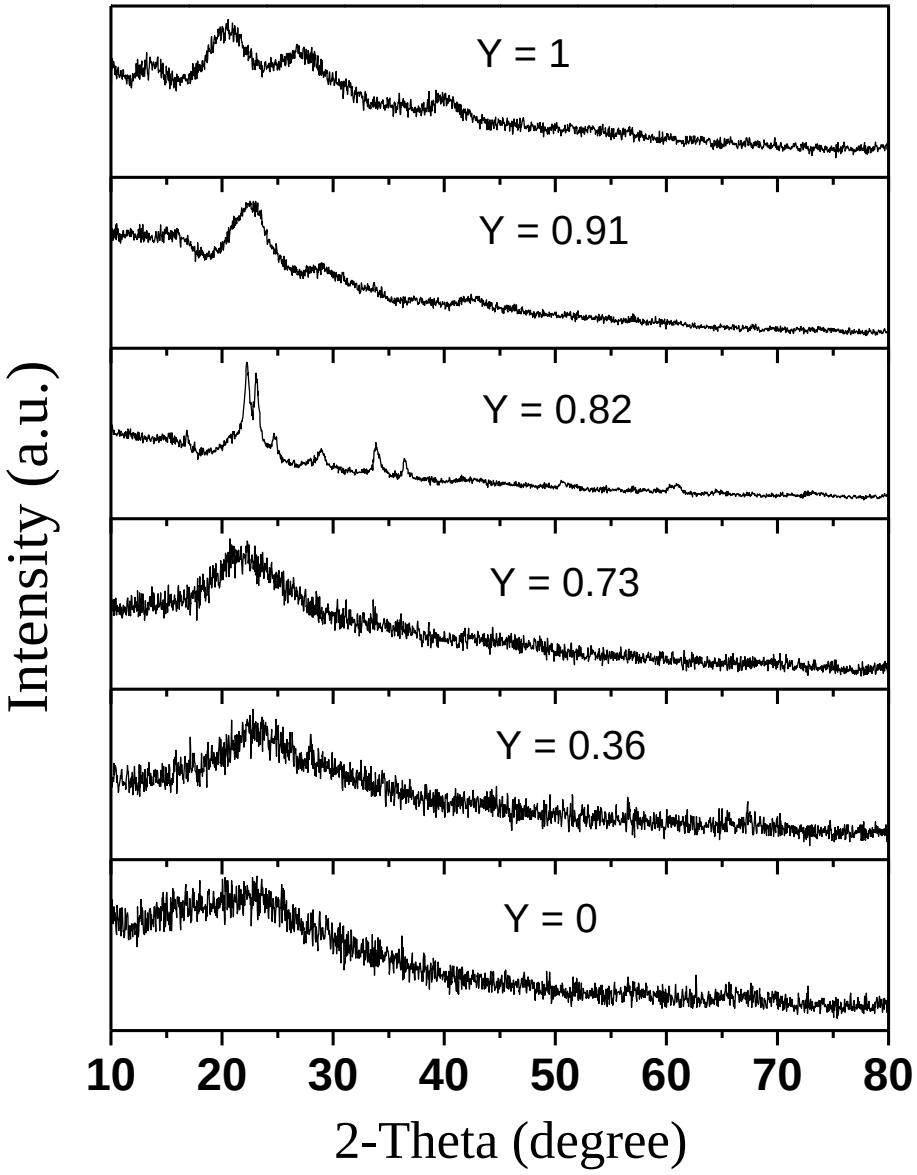

Figure 5.1. XRD patterns of some $0.45Li_2O - (0.55 - x)P_2O_5 - xB_2O_3$ ($0 \leq x \leq 0.55$ or $0 \leq Y \leq 1$) glasses. The crystalline Li_3PO_4 peaks only present at Y = 0.82 (x = 0.45).

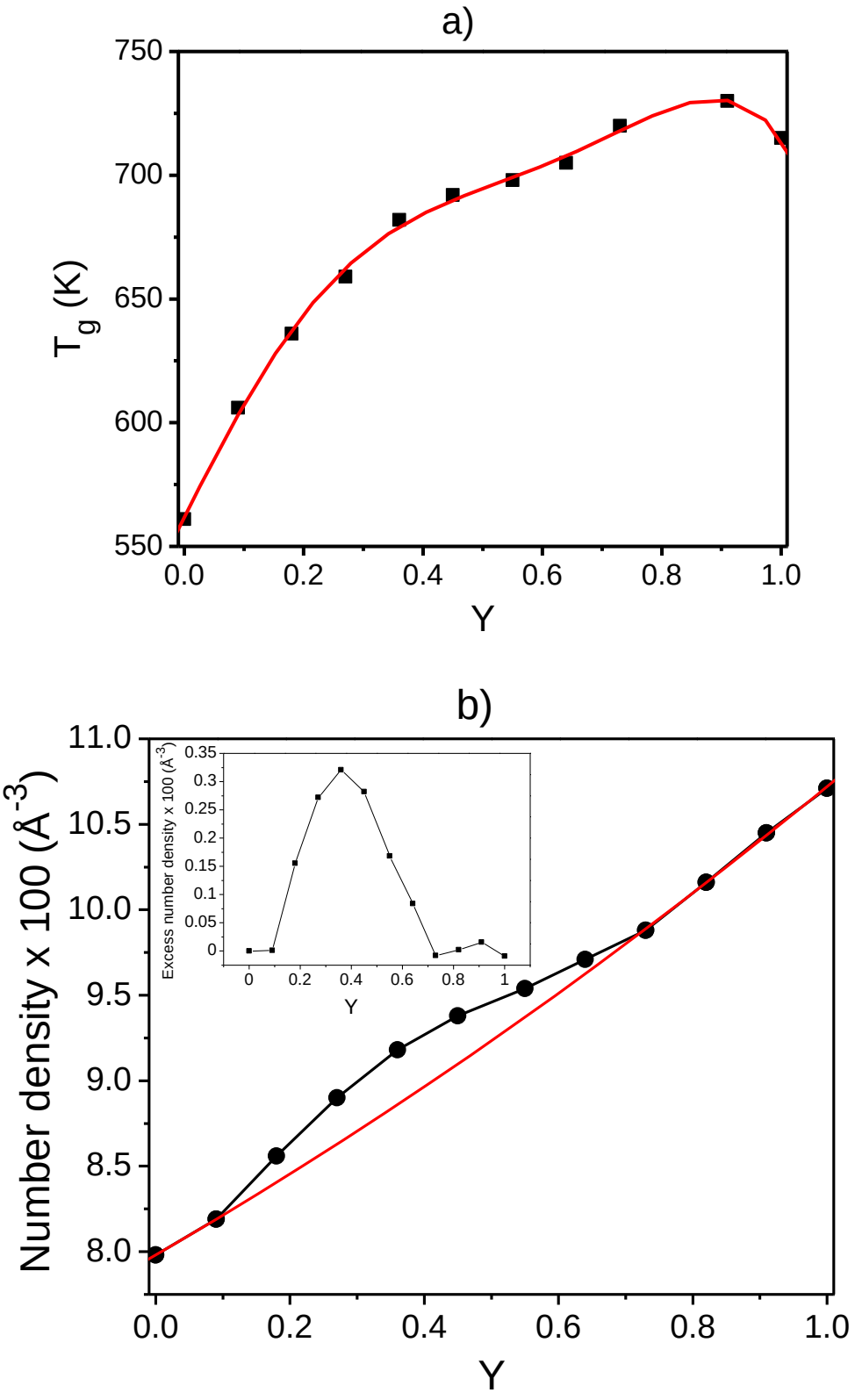

Figure 5.2. Variation of a) Glass transition temperature (T_g); b) Number density with the relative B_2O_3 content Y (where Y = $[B_2O_3]/([B_2O_3]+[P_2O_5])$) in the $0.45Li_2O$ – $(0.55 – x)P_2O_5$ – xB_2O_3 glasses. The inset displays the excess number density when compared to the overall variation between the single glass former systems.

5.3.2. FT-IR, Raman and XPS spectra

5.3.2.1. FT-IR spectra

FT-IR spectra of $0.45Li_2O - (0.55 - x)P_2O_5 - xB_2O_3$ glasses are shown in Figure 5.3. The band around 1330 – 1450 cm^{-1} contributes to the B – O stretching vibrations of trigonal BO_3 units, and is clearly evident in the spectra of compositions $Y \geq 0.64$ ($x \geq 0.35$) [11]. The band near 1260 – 1280 cm^{-1} is assigned to out-of-chain $(PO_2)_{AS}$ vibrations of Q^2 units, the asymmetric stretching mode of the two non-bridging oxygen atoms bonded to phosphorous atoms in the PO_4 tetrahedra [12 – 15]. This band shifts to lower wave numbers with the increase of B_2O_3 content, and for $0.36 \leq Y \leq 0.73$ is replaced by the band near 1200 cm^{-1}, which can be assigned to P = O vibrations, then disappear for $Y > 0.73$ [16]. In the pure borate glass $0.45Li_2O - 0.55B_2O_3$, the relatively weak band at 1200 – 1280 cm^{-1} is also attributed to the B – O stretching vibrations of metaborate chains (BO_3 with one non-bridging oxygen) [17].

The absorption band at around 1160 cm^{-1}, which can be ascribed to the PO_2 symmetric stretching mode, ($(PO_2)_S$ in Figure 5.3), gradually loses intensity when Y increases and disappears for $Y > 27$ ($x > 0.15$) [12]. The band near 1100 cm^{-1} is assigned to P – O^- units of PO_4 tetrahedra in the chain structure [18, 19]. The absorption band near 1000 – 1055 cm^{-1} may be attributed to the symmetrical stretching modes in both PO_4 and BO_4 groups [11, 16]. The relatively weaker absorption bands near 950 – 960 cm^{-1}, which increase in intensity towards boron side, and 840 cm^{-1} can be assigned to B – O stretching modes of BO_4 units and symmetric stretching (P – O – B)

linkages, respectively [11, 16].

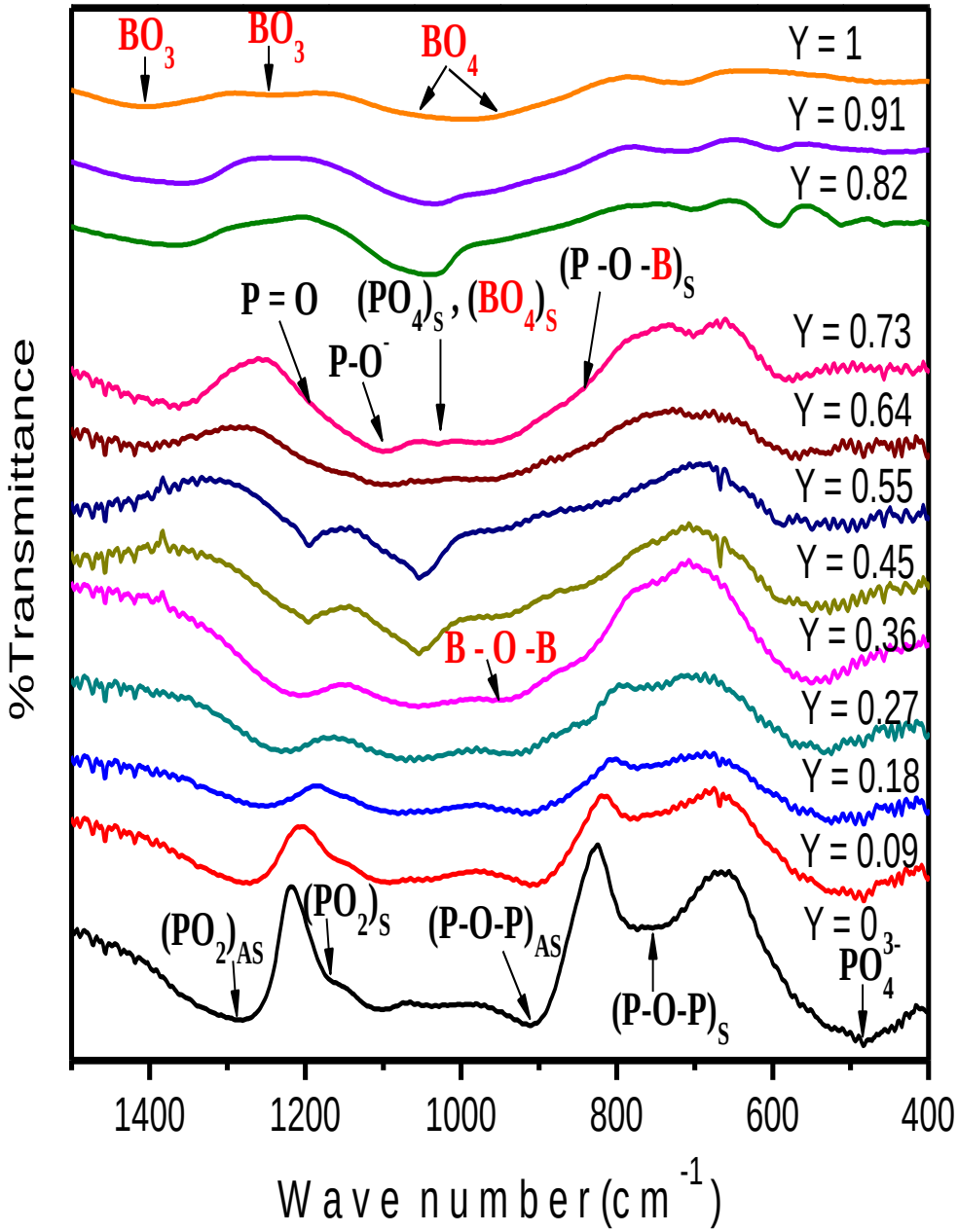

Figure 5.3. FT-IR spectra of $0.45Li_2O - (0.55 - x)P_2O_5 - xB_2O_3$ glasses ($0 \leq x \leq 0.55$ or $0 \leq Y \leq 1$); where $Y = [B_2O_3]/([B_2O_3]+[P_2O_5])$.

As seen in Figure 5.3, the absorption bands near 910 cm^{-1} and 745 – 775 cm^{-1} are attributed to the asymmetric, $(P - O - P)_{AS}$, and symmetric stretching modes, $(P - O - P)_S$, of the in-chain P – O – P linkages respectively [18].

These bands gradually lose intensity with the increase of B_2O_3 content and disappear for Y > 0.27. The band 700 – 750 cm^{-1}, which emerges at the rich-borate side (Y ≥ 0.64), is ascribed to the bending vibrations of O – B – O bridges of borate network [11]. The absorption bands near 450 – 600 cm^{-1} are ascribed to the bending modes of PO_4 and P – O – B [16, 18].

It should be noticed that FITR spectra were only used as a supporting tool to firstly identify the possible structural units existing in the glass structures (due to their limited resolution). Thereafter, a more detailed investigation of the variation in the glass structures with B_2O_3 addition was carried out using Raman and XPS studies.

5.3.2.2. Raman spectra

Structural changes with the replacement of P_2O_5 by B_2O_3 in these glasses are also observed in the Raman spectra (see Figure 5.4). Money et al. [4] have reported the formation of borophosphate units (BPO_4) at 1116 cm^{-1} in the Raman spectra of $0.50Li_2O – (0.50 – x)P_2O_5 – xB_2O_3$ glasses for Y ≥ 0.30 (or x ≥ 0.15). They suggested that these BPO_4 units account for the increase in the conductivity and decrease in the activation energy for ion migration, while – as mentioned in the literature review – Munoz et al. [5] have recently offered an alternative explanation since a formation of BPO_4 units is not seen in their NMR data. To clarify this question, our Raman spectra of $0.45Li_2O – (0.55 – x)P_2O_5 – xB_2O_3$ (0 ≤ Y ≤ 1) glasses were deconvoluted to see in detail the effects of structural modifications.

Because the bands below 500 cm^{-1} are attributed to bending and torsional

vibrations in phosphate glasses [20, 21], the range of wave number for deconvolution of Raman spectra is taken from 500 – 1400 cm^{-1}. Figure 5.5 illustrates the deconvolution of spectrum for $0.45Li_2O – 0.30P_2O_5 – 0.25B_2O_3$ (Y = 0.45) glass as an example. From the deconvolution, the fraction of structural units is taken as proportional to the area of their characteristic component bands.

For pure phosphate glass $0.45Li_2O – 0.55P_2O_5$ (Y = 0), the bands at around 1290 and 1172 cm^{-1} are assigned to the asymmetric and symmetric stretching vibrations O – P – O of two non-bridging oxygens in the PO_4 tetrahedra, respectively [22 – 24]. With the addition of B_2O_3, the band at 1290 cm^{-1} steadily shifts to lower frequencies down to 1200 cm^{-1} at Y = 0.64 and disappears for $Y \geq 0.73$, while the band at 1172 cm^{-1} similarly shifts to the lower frequencies around 1100 cm^{-1} up to Y = 0.91 [22 – 24]. From our deconvolution it could not be clarified, whether the band near 1100 cm^{-1} includes a contribution from BPO_4 units (as claimed by Money et al. [4]).

For the glass compositions within the range $0 \leq Y \leq 0.73$, the band at around 700 cm^{-1} is attributed to stretching vibration of P – O – P groups of $(PO_3)_n^{n-}$ chains [22 – 24]. From Raman deconvolutions, the total fraction of the bands at 1290 – 1200 cm^{-1}, 1172 – 1100 cm^{-1} and 710 cm^{-1}, which are responsible for the stretching vibrations of O – P – O and P – O – P groups of various phosphate chains, is found to decrease with B_2O_3 addition, as shown in Figure 5.6(a).

In the lithium borophosphate glasses, the band around 1045 – 1000 cm^{-1}, which appears for $0.27 \leq Y \leq 0.91$, is previously assigned to overlapping

vibrations of pyrophosphate, and $(P - O - B)^-$ groups which are P – O – B bonds where the excess negative charge on the BO_4 units is compensated by Li^+ cations [22 – 24]. However, in the pure borate glasses, this band is also attributed to diborate groups (see Figure 5.4 for Y = 1) [27]. Furthermore, as suggested in [5], pyrophosphate $(P_2O_7)^{4-}$ units cannot be considered as completely detached structural entities, as they may be involved in P – O – B linkages. Therefore, the band around 1045 – 1000 cm^{-1} is finally attributed to P – O – B bonds. Besides, the band around 670 – 620 cm^{-1}, which appears for $0.09 \leq Y \leq 0.73$, is also assigned to P – O – B bonds [22, 24]. Figure 5.6(a) shows the contribution of P – O – B bonds from the two bands 1045 – 1000 cm^{-1} and 670 – 620 cm^{-1}. The fraction of P – O – B bonds rises with the increase of B_2O_3 content, and passes through a maximum at Y = 0.55.

For the pure borate glass $0.45Li_2O - 0.55B_2O_3$ (Y = 1), the bands at 930, 970 and 1100 cm^{-1} are observed and attributed to diborate groups [25]. The appearance of 770 cm^{-1} band may be assigned to triborate groups [22, 25]. Besides, the very weak bands at 844 cm^{-1} and 694 cm^{-1} in the $0.45Li_2O - 0.55B_2O_3$ glass are characteristic of pyroborate and chain-type metaborate groups, respectively [11, 25]. These pyroborate and chain-type metaborate bands are also observed with the small addition of P_2O_5 content, i.e. for Y = 0.91 and 0.82 (cf. Figure 5.4). The diborates band at 900 – 970cm^{-1} and 1100 cm^{-1} emerges for $0.18 \leq Y \leq 1$ and $Y \geq 0.82$ respectively. The peak at 950 cm^{-1} observed in the borophosphate glasses for $0.64 \leq Y \leq 0.82$ is the indication of isolated $(PO_4)^{3-}$ units [22, 24]. This assignment is supported by the formation of crystalline Li_3PO_4 from XRD pattern at Y = 0.82. Similarly, in the $0.45Li_2O - (0.55 - x)P_2O_5 - xB_2O_3$ glasses the band around 770 cm^{-1} is

observed for Y ≥ 0.64 (x ≥ 0.35) and accounts for triborate groups [22]. In addition, the band at 500 cm^{-1}, which is attributed to loose BO_4 and loose diborate units, appears for 0.09 ≤ Y ≤ 0.73 [11, 25].

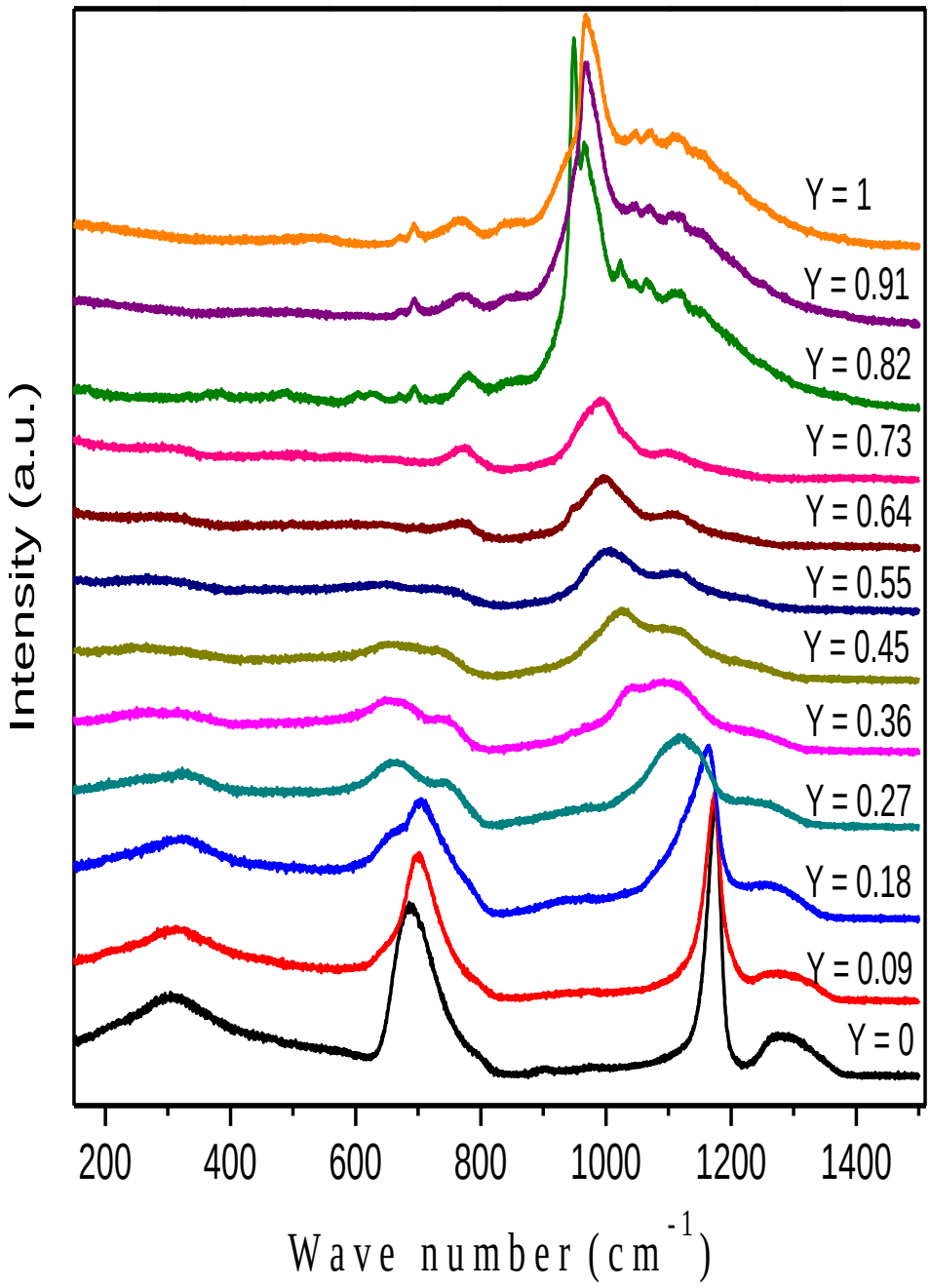

Figure 5.4. Raman spectra of all the $0.45Li_2O - (0.55 - x)P_2O_5 - xB_2O_3$ glasses (0 ≤ x ≤ 0.55 or 0 ≤ Y ≤ 1); where $Y = [B_2O_3]/([B_2O_3]+[P_2O_5])$.

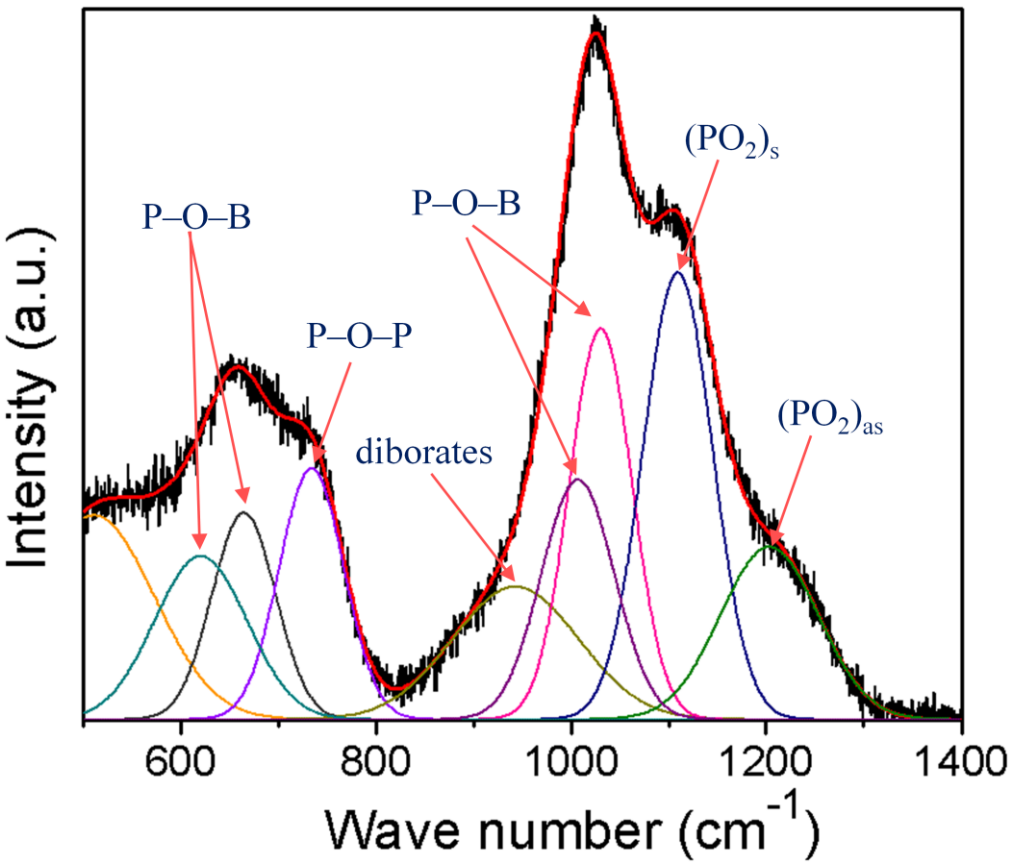

Figure 5.5. Band deconvolution for Raman spectrum of $0.45Li_2O - 0.30P_2O_5 - 0.25B_2O_3$ (Y = 0.45) glass. Black dots: experimental spectrum, red line: fitted spectrum.

Figure 5.6(b) shows the total fraction of all the bands (500, 694, 770, 844, 900 – 970, 1100 cm^{-1}) related to the vibrations of borate groups as discussed above. The fraction of these bands firstly increases for $0.09 \leq Y \leq 0.27$, which is due to the increase of loose BO_4 units and diborate groups, as supported from NMR studies where the fractions of BO_4 units are predominant and increase up to Y = 0.27 for the same system [26]. For $0.36 \leq Y \leq 0.55$, the reduction of these bands is due to the rise of P – O – B linkages, which lead to the decrease of separate borate and phosphate entities (cf. Figure 5.6(a) and 5.6(b)). With higher boron contents ($Y \geq 0.64$), the increase in the fraction of borate groups up to 100% for the pure borate composition (Y = 1) is certainly

due to the decrease of B – O – P linkages and phosphate groups.

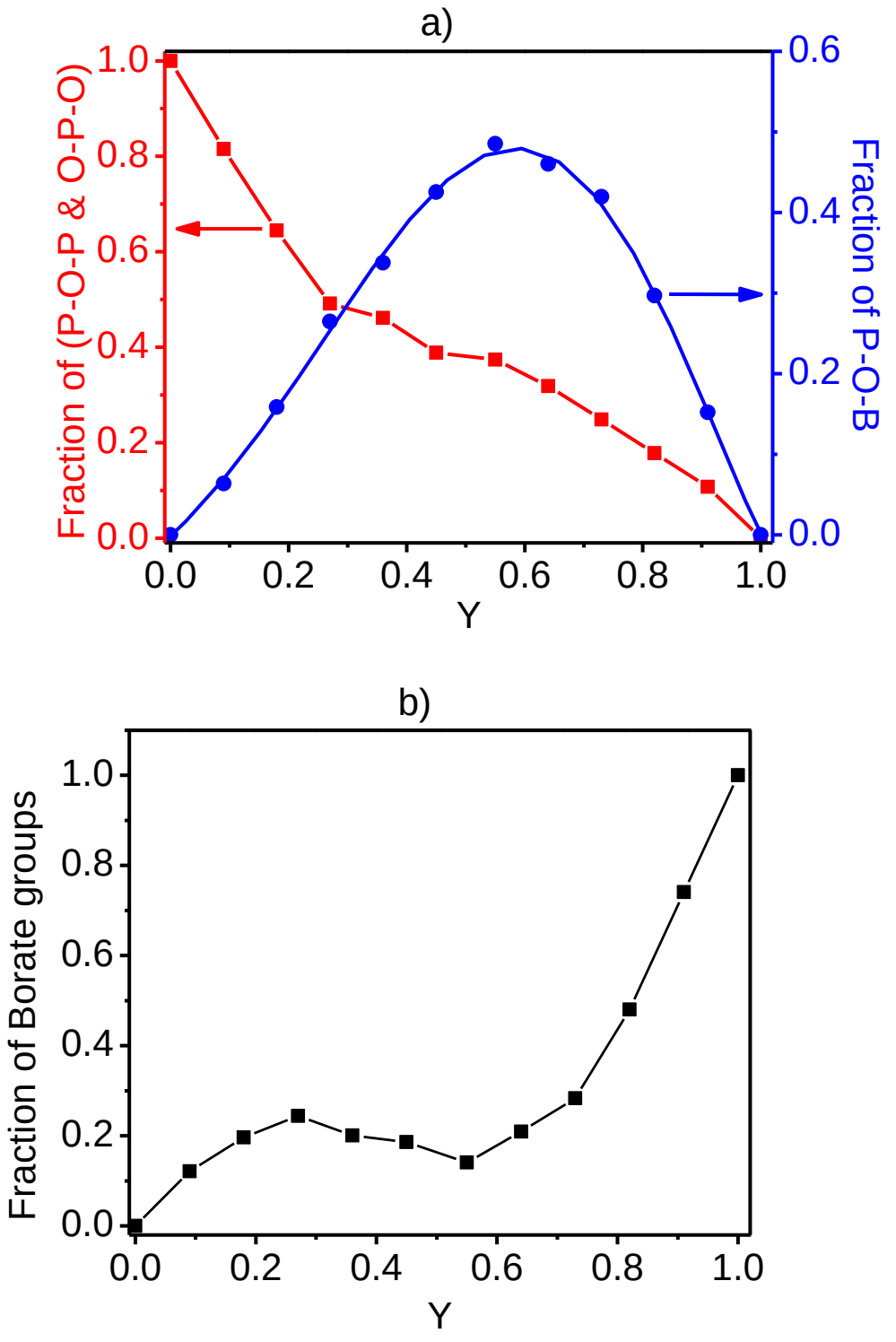

Figure 5.6. Fractions of a) (P – O – P & O – P – O) and P – O – B; b) overlapping vibrations of various borate groups (loose BO_4 and loose diborate units, diborates, pyroborates, chain-type metaborates, triborates) as estimated from Raman spectra; Y = $[B_2O_3]/([B_2O_3]+[P_2O_5])$.

5.3.2.3. XPS spectra

Typical O1s XPS spectra for the $0.45Li_2O - (0.55 - x)P_2O_5 - xB_2O_3$ ($0 \leq x \leq 0.55$ or $0 \leq Y \leq 1$) glasses together with curve fittings are illustrated in Figure 5.7. Since oxide ions in the lithium borophosphate system have different types of chemical bonding, a deconvolution of the O1s spectrum can be used to analyze the bonding states of oxide ions. As seen from Figure 5.7(a), O1s spectra for the parent phosphate glass (Y = 0) can be decomposed into two components: The high and low binding energy peaks around 533.2eV and 531.5eV are assigned to P – O – P (bridging oxygens (BOs)) bonds, and non-bridging oxygens (NBOs) respectively. In the pure phosphate glasses with high P_2O_5 contents, NBOs include both double bonded P = O and $P - O^-$, and it is difficult to distinguish these two types of oxygen [18, 27, 28]. In the borate glasses, the high and low binding energy peaks are analogously attributed to B – O – B (BOs) bonds, and $B - O^-$ (NBOs) bonds, respectively [29]. It was noticed that the separation between bridging (BOs) and non-bridging (NBOs) oxygens for the pure borate glass (cf. Figure 5.7(f)) is not pronounced as that for pure phosphate glass (cf. Figure 5.7(a)), but the distribution of BOs and NBOs (fraction of NBOs = 0.205, and fraction of BOs = 0.795) in the $0.45Li_2O - 0.55B_2O_3$ (Y = 1) glass from this XPS analysis (cf. Figure 5.8) is in very good agreement with the values obtained from NMR studies [30].

With the addition of B_2O_3 into the parent phosphate glass, the high (around 533.2 ± 0.4eV) and low binding energy peak (around 531.4 ± 0.3eV) should represent the overlapping contributions from P – O – P and B – O – B

bonds, and from P = O, P – O^- and B – O^- (NBOs) bonds, respectively. For $0.09 \leq Y \leq 0.55$, besides P – O – P, B – O – B, P = O, P – O^-, B – O^- bonds, a third intermediate O1s peak around 532.4 ± 0.4eV emerges that can be assigned to P – O – B bonds in line with the intermediate bond asymmetry of this oxygen bonding [28, 31]. With further addition of B_2O_3 content ($Y > 0.55$), there is a shift of (P – O – P and B – O – B) peak from 532.9eV for $Y = 0.64$ to a lower binding energy up to 531.8eV corresponding to B – O – B peak for $Y = 1$, while the P – O – B peak shifts down from 532eV ($Y = 0.64$) to 531.6eV ($Y = 0.91$). The position of NBO peaks of 531.4eV remains nearly unchanged with the B_2O_3 addition in the investigated system.

It was found that the fraction of (P – O – P & B – O – B) bonds decreases and the fraction of P – O – B bonds increases with rising B_2O_3 content up to $Y = 0.55$, as shown in Figure 5.8(a). In good agreement with the finding from Raman analysis (cf. Figure 5.6(a)) the observed increase of cross-linking P – O – B bonds is the main cause for the pronounced increase of T_g (cf. Table 5.1) up to $Y = 0.55$. For $Y > 0.55$ the contribution of (P – O – P & B – O – B) bonds increases suddenly due to the increase of B – O – B bonds (as Raman analysis showed that the number of P – O – P bonds continues to decrease with rising B_2O_3 content also for $Y > 0.55$, while as to be expected the contributions of borate groups increase up to 100% for $Y = 1$ (cf. Figure 5.6). Consequently, P – O – B bonds decrease for $Y > 0.55$ (cf. Figure 5.8(a)).

In addition, the fraction of non-bridging oxygens (NBOs) was found to decrease continuously with the increase of B_2O_3 content for $Y \geq 0.18$, and reach to a value of 0.205 for $Y = 1$ (cf. Figure 5.8(b)). This finding is similar to

that of Brow for Zn borophosphate glasses [28]. The correlation between these structural changes and conductivity will be discussed hereafter.

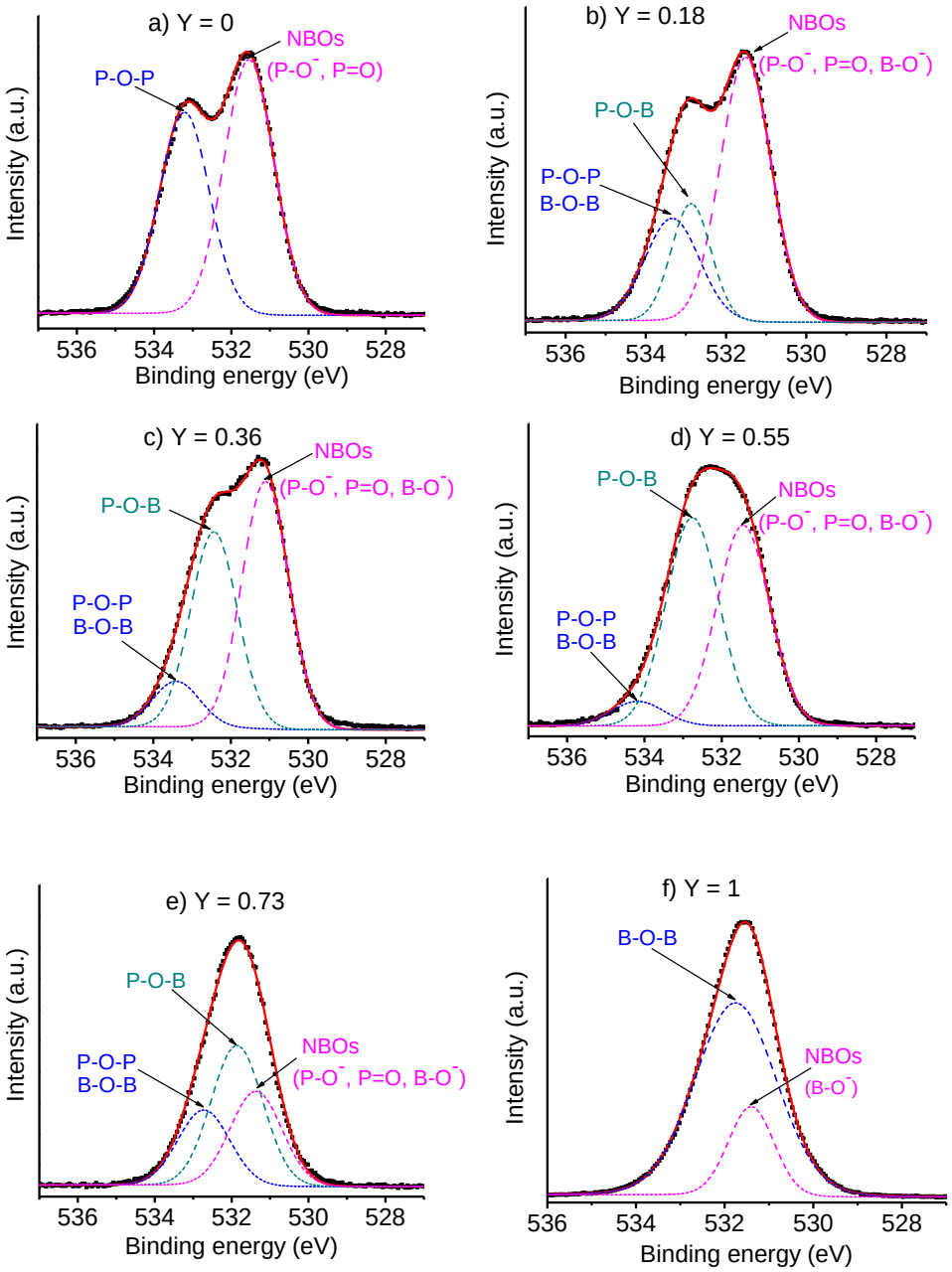

Figure 5.7. O1s spectra of $0.45Li_2O - (0.55 - x)P_2O_5 - xB_2O_3$ ($0 \leq x \leq 0.55$ or $0 \leq Y \leq 1$) glasses and their peak deconvolution; $Y = [B_2O_3]/([B_2O_3]+[P_2O_5])$. Black dots: experimental spectrum, red line: fitted spectrum, dashed lines with blue, cyan and pink colours: O1s components from deconvolution.

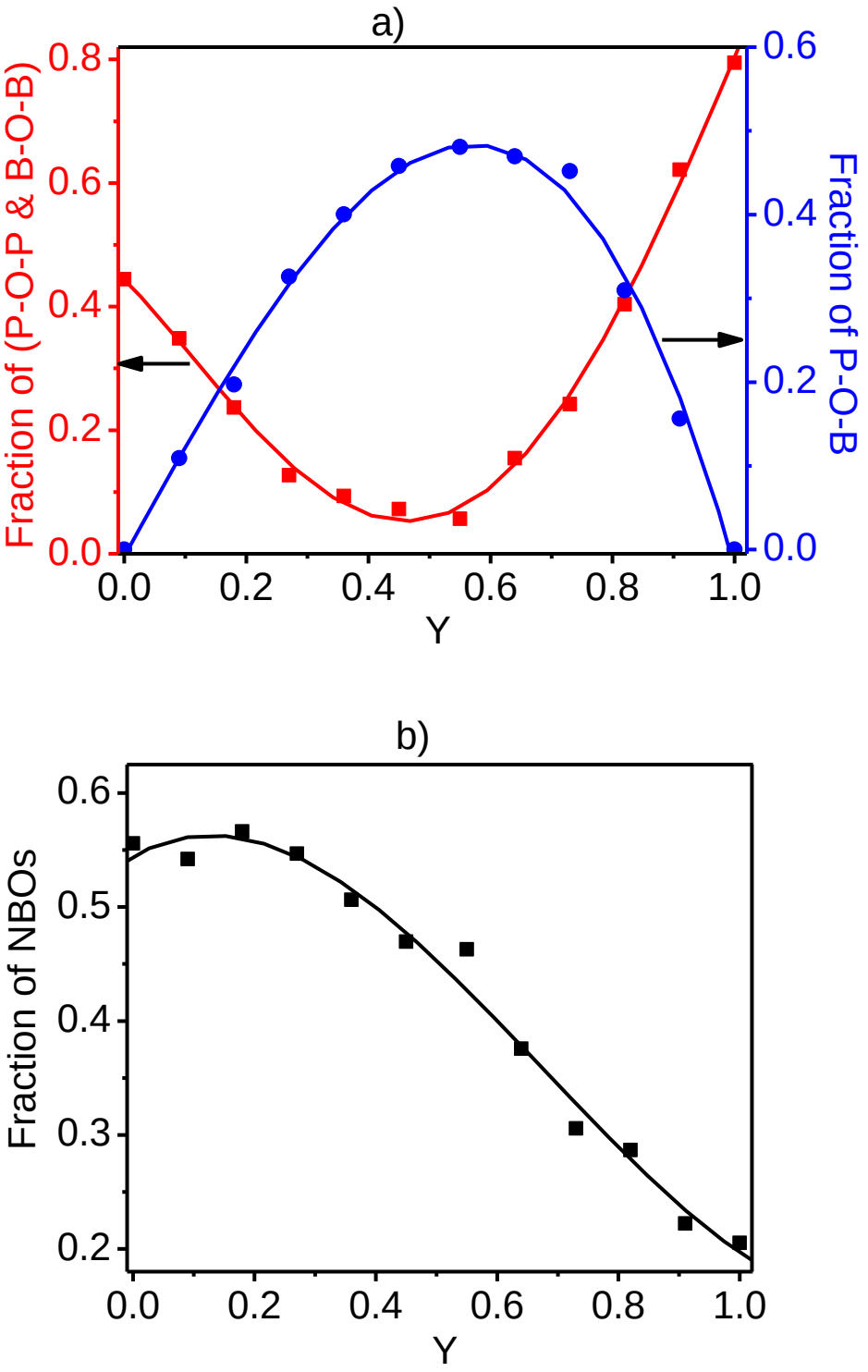

Figure 5.8. Fractions of a) (P – O – P & B – O – B) and P – O – B; b) Non-bridging oxygens (NBOs) with the relative B_2O_3 content (Y) as determined from O1s spectra decomposition; Y = $[B_2O_3]/([B_2O_3]+[P_2O_5])$.

5.3.3. Structure model

A model of the borophosphate structure is developed that allows one to check the plausibility of the various experimental findings, such as the relative fractions of non-bridging oxygens (NBOs), bridging oxygens (BOs) (i.e., P – O – P, B – O – B and P – O – B bonds) present in the borophosphate glassy system $0.45Li_2O – (0.55 – x)P_2O_5 – xB_2O_3$ or equivalently $0.45Li_2O – 0.55[(1 – Y)P_2O_5 – YB_2O_3]$ $(0 \leq Y \leq 1)$.

In the pure phosphate glass $0.45Li_2O – 0.55P_2O_5$ (Y = 0), the expectation value for the fraction of NBOs ($f_{NBO} = 0.62$) and BOs ($f_{BO} = 1 – f_{NBO} = 0.38$) can be calculated using the Equation (1.28) in Chapter 1. Since this phosphate glass is close to the metaphosphate composition, its structure is mostly made up of Q_2 units with two NBOs (cf. Equations 1.25(a) and 1.25(b)). It should be kept in mind that the replacement of one formula unit of P_2O_5 by B_2O_3 will also reduce the number of oxygens in the system by 2. With the B_2O_3 addition, both BO_3 and BO_4 units can be incorporated into the parent phosphate network. Therefore the number of NBOs in the glass will be reduced by 2 for each BO_4 unit or by 1 for each BO_3 unit that is introduced. As the fraction of BO_4 units (N_4) and hence the fraction of BO_3 units (N_3, where $N_3 = 1 – N_4$) were known for this borophophate system, in which N_4 ranges from 0.70 for Y = 0.09 up to the maximum of 0.86 for Y = 0.27 and then continuously decreases to the value of 0.42 for Y = 1 (pure borate) [26, 30], it becomes feasible to predict the variation of the NBO fraction as a function of the relative borate content Y.

To judge the role of P – O – B units for the borophosphate glass structure,

their concentration variation as a function of Y is compared to expectation values for any type of bridging oxygens that would result from a random distribution of B and P in the network. To quantify the deviation of the experimentally observed concentrations from this random distribution, a relative preference factor ξ for the P – O – B formation is introduced, assuming that the P – O – P and B – O – B concentrations are uniformly reduced by the respective factor. Therefore, for a $0.45Li_2O – 0.55[(1 – Y)P_2O_5 – YB_2O_3]$ glass, the relative fractions of the four possible oxygen species can be described by:

$$f_{NBO} = \left[N_{NBOp} - Y \times (N_4 \times 2 + N_3 \times 1)\right]/N_O \quad (5.3a)$$

$$f_{POB} = \xi \times 2 \times Y \times (1 - Y) \times (1 - f_{NBO}) \quad (5.3b)$$

$$f_{POP} = \left(\frac{1 - f_{POB} \times \xi}{1 - f_{POB}}\right) \times (1 - Y)^2 \times (1 - f_{NBO}) \quad (5.3c)$$

$$f_{BOB} = \left(\frac{1 - f_{POB} \times \xi}{1 - f_{POB}}\right) \times Y^2 \times (1 - f_{NBO}) \quad (5.3d)$$

$$f_{NBO} + f_{POB} + f_{POP} + f_{BOB} = 1 \quad (5.3e)$$

where f_{NBO}, f_{POB}, f_{POP}, f_{BOB} are the relative fractions of NBOs, P – O – B, P – O – P and B – O – B bonds respectively. N_{NBOp} represents the number of NBOs in one formula unit of the parent phosphate glass, and equals to $N_{NBOp} \approx 1.80$ in the case of $0.45Li_2O – 0.55P_2O_5$ (Y = 0). N_O is the total number of oxygens per formula unit, while N_4, N_3 are the relative fractions of BO_4 and BO_3 units, respectively, in the glass. ξ is the preference factor for the

P – O – B formation. A comparison of the model to the P – O – B bond fractions determined from XPS data yields a value of $\xi = 1.65$ for the only fit parameter in the model, indicating that for the glass composition $0.45Li_2O – 0.55[(1 – Y)P_2O_5 – YB_2O_3]$ P – O – B groups occur 1.65 times more frequently than they should for a random distribution of P and B. Thus there is a highly significant preference for the formation of networks in which the cations P and B alternate (as they also do in crystalline BPO_4).

Figures 5.9 and 5.10 shows the estimated values (solid lines) for NBOs, P – O – P, B – O – B and P – O – B bonds together with the experimental values from XPS data. A good agreement is observed for both the estimated from the relationships in Equations 5.3(a) – 5.3(d) and the experimental results.

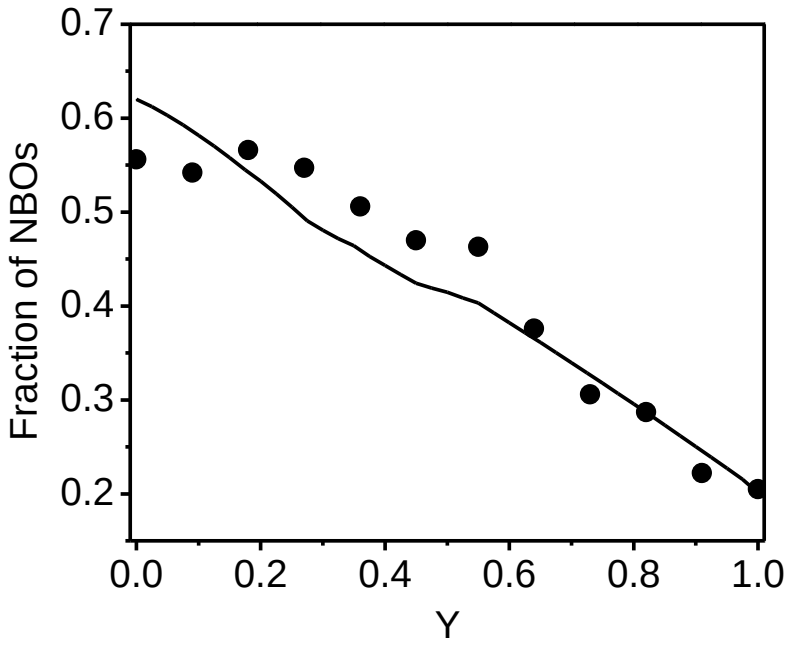

Figure 5.9. Relative fraction of non-bridging oxygens (NBOs) estimated from the proposed structure model and XPS data. Solid line represents the values predicted from the model, while the symbols (full circles) are the experimental values from XPS.

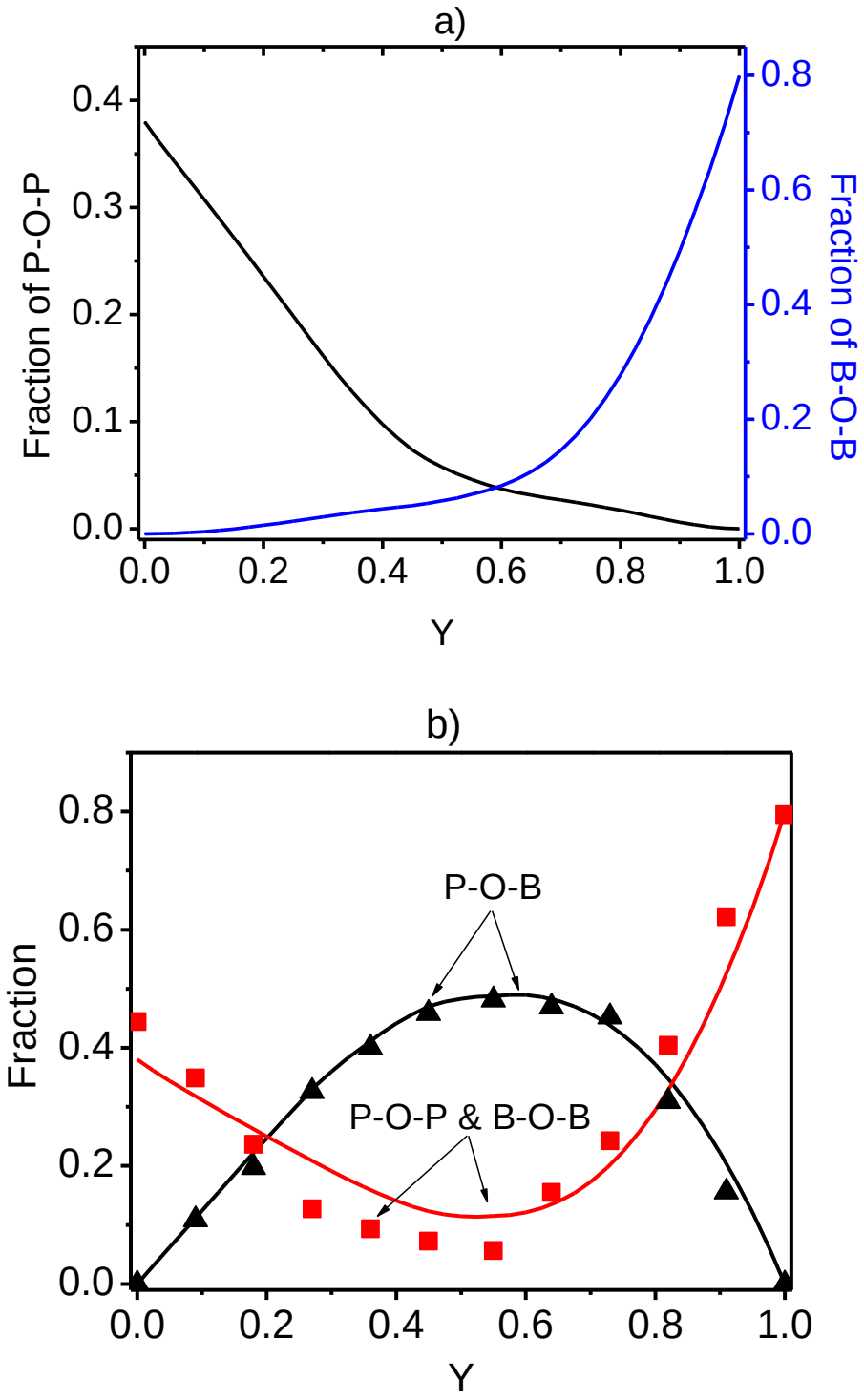

Figure 5.10. Relative fractions of the estimated values from the proposed structure model and XPS data for a) P – O – P and B – O – B bonds; b) P – O – B and (P – O – P & B – O – B) bonds. Solid lines represent the values predicted from the model with a preference factor of $\xi = 1.65$, while the symbols (full triangles and squares) are the experimental values from XPS.

5.3.4. Impedance analysis

A series of Nyquist plots of $0.45Li_2O - 0.40P_2O_5 - 0.15B_2O_3$ (Y = 0.27) glass at different temperatures together with equivalent circuit for curve fittings is shown in Figure 5.11. Figure 5.12 then demonstrates that the dc ionic conductivity follows the Arrhenius-type behaviour.

$$\sigma_{dc}T = \sigma_0 exp\left[-\frac{E_a}{k_B T}\right] \quad (5.4)$$

where σ_0 is the pre-exponential factor and k_B is Boltzmann's constant. Activation energies (E_a) for ion migration calculated according to Equation (5.4) are shown in Figure 5.13 together with dc ionic conductivity (σ_{dc}) values at room temperature.

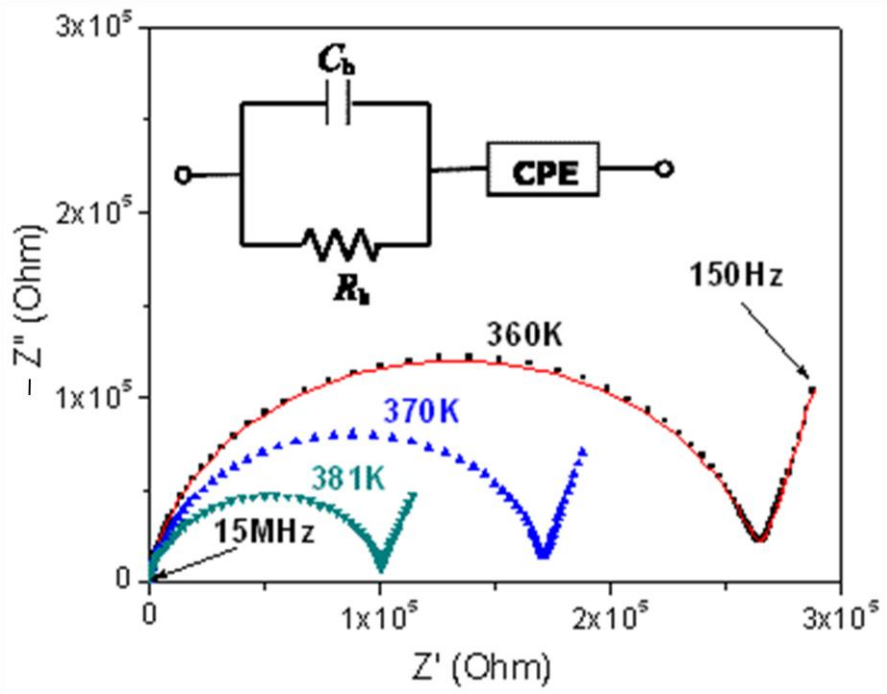

Figure 5.11. Nyquist plots of $0.45Li_2O - 0.40P_2O_5 - 0.15B_2O_3$ (Y = 0.27) glass at different temperatures and their equivalent circuit.

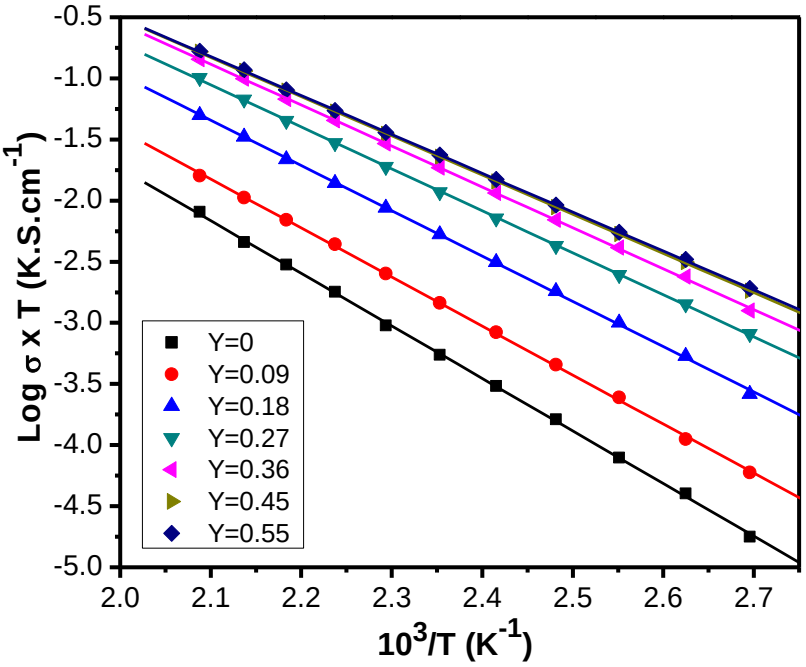

Figure 5.12. Arrhenius plots for the temperature dependence of the conductivity of $0.45Li_2O - 0.55[(1 - Y)P_2O_5 - YB_2O_3]$ glasses with $0 \leq Y \leq 0.55$; $Y = [B_2O_3]/([B_2O_3]+[P_2O_5])$.

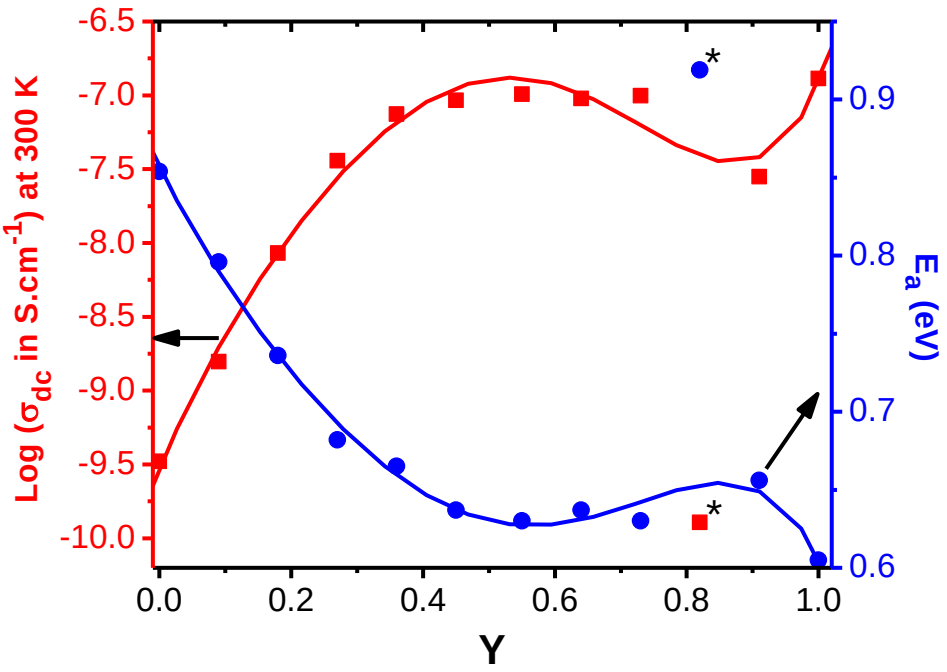

Figure 5.13. Logarithm of ionic conductivity (σ_{dc}) at room temperature and activation energy (E_a) as a function of the relative B_2O_3 content (Y). Solid lines: polynomial fits (ignoring the values of σ_{dc} and E_a in the crystallized sample with Y = 0.82 (marked with asterisk (*)) using the function: $f(y) = a + b_1y + b_2y^2 + b_3y^3 + b_4y^4 + b_5y^5$; for σ_{dc}: a = -9.52; b_1 = 10.36; b_2 = -16.83; b_3 = 31.51; b_4 = -50.59; b_5 = 28.13; for E_a: a = 0.86; b_1 = -0.84; b_2 = 1.23; b_3 = -2.24; b_4 = 3.65; b_5 = -2.06.

As seen from Figure 5.13, the ionic conductivity (σ_{dc}) rises and the activation energy (E_a) drops with the increase of B_2O_3 content in the $0.45Li_2O - 0.55[(1 - Y)P_2O_5 - YB_2O_3]$ glasses. Both σ_{dc} and E_a then reach nearly constant plateaus of $\sigma_{dc} = 1 \times 10^{-7}$ S.cm^{-1} at room temperature and $E_a \approx 0.63$eV for $0.45 \leq Y \leq 0.73$. It was noticed that the much lower value of σ_{dc} at $Y = 0.82$, which corresponds to a much higher value of E_a, is due to the appearance of crystalline lithium orthophosphate (Li_3PO_4) within the glass matrix (as mentioned above in the discussion of XRD and Raman data), which obstruct Li^+ ion movement and hence reduce significantly the ionic conductivity. The borate-rich glass phase with Y close to 1 then again exhibits a slight increase of σ_{dc} and a drop in E_a with the increase of B_2O_3 content up to $\sigma_{dc} = 1.3\times10^{-7}$ S.cm^{-1} and $E_a = 0.61$eV for the pure borate glass ($Y = 1$), though the statistical precision of the latter trend is limited by the small number of data points for this composition range.

The increase in σ_{dc} up to $Y \approx 0.5$ is in good agreement with reports by Magistris et al. for similar borophosphate glasses [2]. The variation of ionic conductivity can be explained in terms of cross-linking of phosphate chains through P – O – B bonds. Here, P – O – B bonds containing BO_4 units ("B-$(OP)_4$") can be expected to have a stronger structure modifying – and hence conductivity enhancing – effect than the (initially few) bonds by BO_3 units ("B-$(OP)_3$").

The linear variation of $\log(\sigma_{dc})$ and E_a in the region $0 \leq Y \leq 0.27$ (cf. Figure 5.13) may be linked to the linear increase of P – O – B bonds (cf. Figure 5.6(a) and 5.8(a)), which are mostly B-$(OP)_4$ linkages [26]. The

maximum fraction of P – O – B bonds at Y = 0.55 may be responsible for the maximum in σ_{dc} and the minimum in E_a at this composition for $0 \leq Y \leq 0.91$. For $0.36 \leq Y \leq 0.55$, N_4 values (i.e. the fraction of BO_4 units) decrease from 0.78 for Y = 0.36 to 0.55 for Y = 0.55, which means that N_3 values (fraction of BO_3 units) increase [26]. The gradual decrease of B-$(OP)_4$ bonds and the corresponding increase of BO_3 units limits the further conductivity enhancement. For $0.55 < Y \leq 0.91$, the decrease of P – O – B bonds, which may be due to the more pronounced decrease of B-$(OP)_4$ linkages, accounts for a plateau of the ionic conductivity.

5.3.5. Model for the calculation of ionic conductivity

To achieve a more quantitative insight into the leading order factors determining the conductivity variation, the room temperature ionic conductivity (σ_{dc}) is linked to the relative concentration of the different oxygen species in the simple structure model explained in section 5.3.3 (cf. Equation 5.3(a) – 5.3(d)). After eliminating terms with the lowest effect on the conductivity variation, the room temperature ionic conductivity (σ_{dc}) of the borophosphate glass $0.45Li_2O - 0.55[(1 - Y)P_2O_5 - YB_2O_3]$ as a function of the borate content Y may be expressed using the following relationship:

$$log\sigma_{dc} = -6.961 - 7.024f_{POP} + 0.12f_{BOB} + 12.8f_{POP}f_{POB} - 0.316f_{POP}f_{BO.} \quad (5.5)$$

The values of σ_{dc} at room temperature determined from the above relationship are shown together with the experimental ones from impedance spectroscopy (except for the data points at Y = 0.82 and 0.91 that might be

affected by minor fractions of crystalline phases) in Figure 5.14. As seen there, the model provides a quantitative description of the experimental conductivity variation.

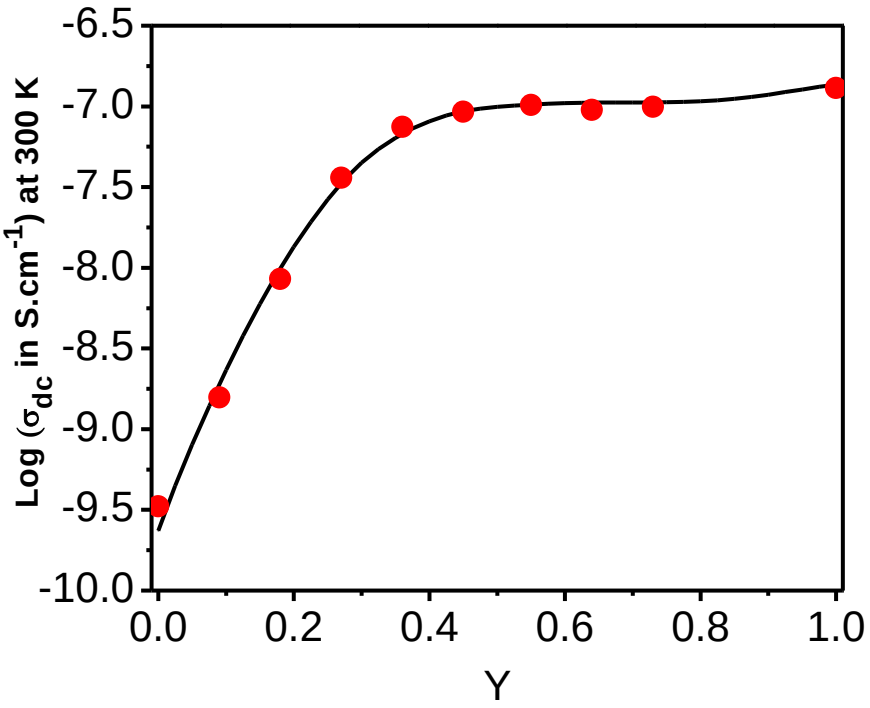

Figure 5.14. Ionic conductivities (σ_{dc}) at room temperature estimated from the proposed model and from the impedance spectroscopy. Solid line represents the values predicted from the model (cf. Equation 5.5), while the full circles are the experimental values from impedance spectroscopy.

While the absolute values of the coefficients may have a limited reliability, it is clear that extended P – O – P regions will seriously reduce the conductivity, while introducing P – O – B units into a P – O – P region is the main contributing factor for the conductivity enhancement. Without introducing the cross term $f_{POP}f_{POB}$ an accurate description of the conductivity variation is not possible. While P – O – B units are important for the high conductivity of the mixed glass former system, it is not just the P – O – B concentration, but also the intermediate range arrangement of the elementary

structure building blocks that controls the conductivity variation.

5.3.6. Frequency dependence of ionic conductivity σ(ω)

Figure 5.15 shows frequency-dependent conductivity plot of log(σ) versus log(ω) at different temperatures for the composition $0.45Li_2O - 0.45P_2O_5 - 0.10B_2O_3$ (Y = 0.18). Three distinct regions in the conductivity spectra are observed for the compounds at above room temperatures: (i) the high frequency dispersion region ($\omega > 10^4$ Hz), (ii) the central plateau region, which is also called dc regime and (iii) the low frequency dispersion region.

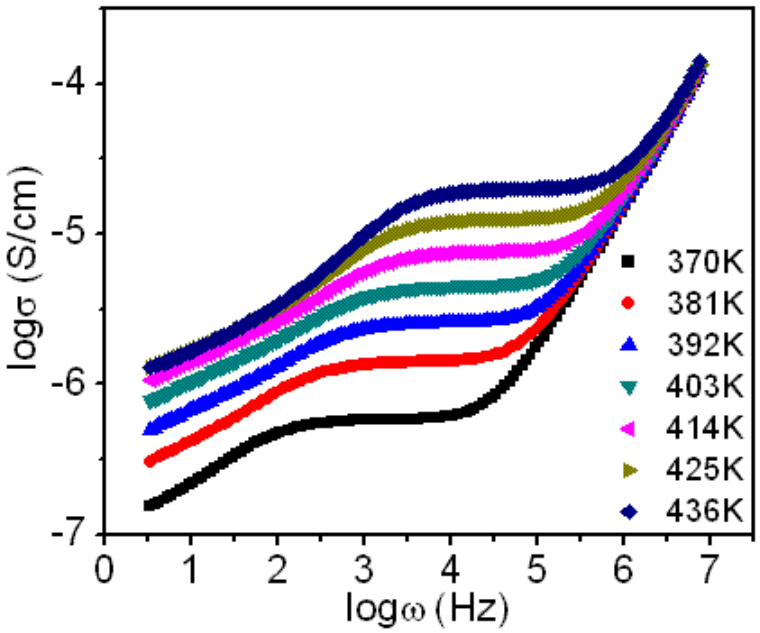

Figure 5.15. Log-log plot of σ *vs.* ω at different temperatures for $0.45Li_2O - 0.45P_2O_5 - 0.10B_2O_3$ (Y = 0.18) glass (From bottom to top: 370 K to 436 K).

The frequency dispersion characteristics in the high frequency and central plateau regions can be analyzed using Jonscher's universal power law relation,

$$\sigma(\omega) = \sigma(0) + A_T\omega^n \quad (5.6)$$

where $\sigma(0)$ is the frequency-independent dc conductivity of the sample, A_T is a weakly temperature-dependent quantity and n is the power law exponent ($0 < n < 1$). As the temperature increases, the frequency at which the dispersion becomes prominent shifts to higher frequencies, as the kinetic energy of the ions increases. The low frequency dispersion observed for compositions at various temperatures is due to the electrode polarization as a result of the accumulation of mobile ions at the interface. This space charge accumulation is more effective at lower frequencies. Therefore, the total conductivity (σ) of the compound decreases as frequency decreases at a given temperature as seen in Figure 5.15.

The characteristic frequency corresponding to the onset of high frequency conductivity dispersion is identified with the hopping frequency (ω_p), and is determined using the relation $\sigma(\omega_p) = 2\sigma_{dc}$ [32]. ω_p is found to increase with temperature and B_2O_3 content up to Y = 0.73 (cf. Figure 5.16). For Y > 0.73, the variation of ω_p follows the variation of dc conductivity (σ_{dc}). The temperature dependence of ω_p obeys the Arrhenius-type behaviour. The resulting hopping activation energies ($E_a^{\omega_p}$) are comparable to those of dc conductivity (E_a^{dc}) as shown in Figure 5.17, which suggests that the relaxation mechanism requires charge carriers to cross the same energy barriers as for the dc conduction process [32].

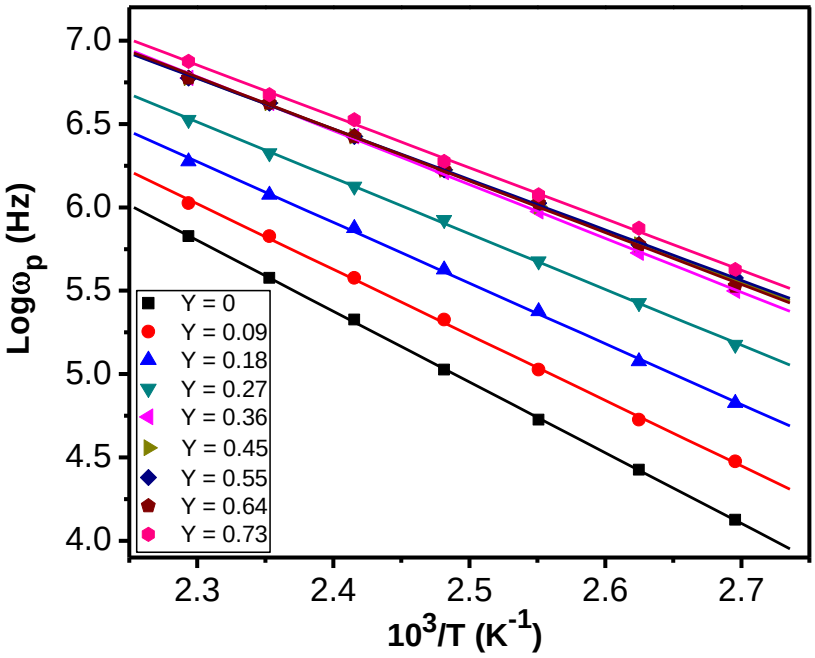

Figure 5.16. Arrhenius plots for the temperature dependence of the hopping frequency (ω_p) of the $0.45Li_2O - 0.55[(1 - Y)P_2O_5 - YB_2O_3]$ glasses.

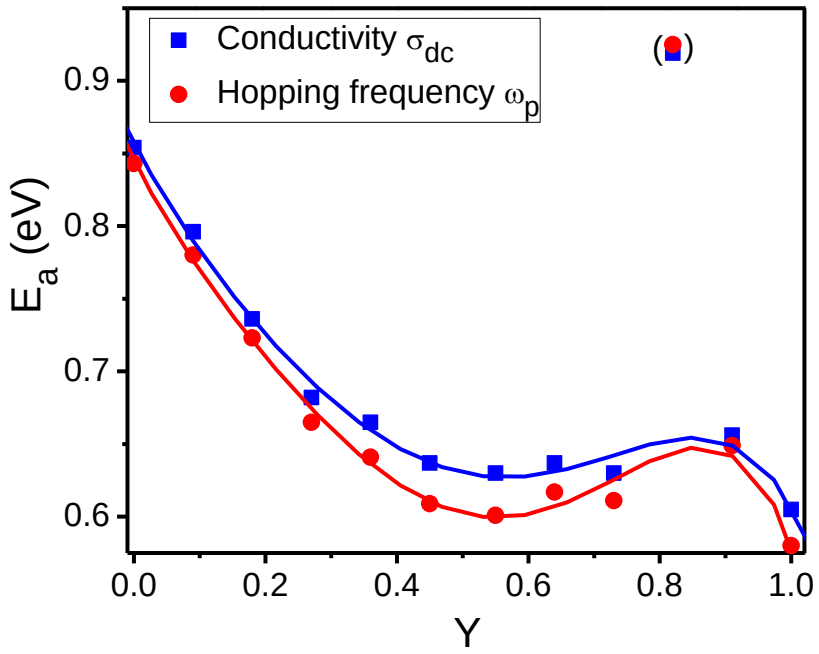

Figure 5.17. Comparison of activation energies (E_a) for dc conductivity (σ_{dc}) and hopping frequency (ω_p); Y = $[B_2O_3]/([B_2O_3]+[P_2O_5])$. Solid lines: polynomial fits (ignoring values of the crystallized sample Y = 0.82).

Scaling of ac conductivity data for ionically conducting glasses and amorphous semiconductors to construct a master curve in order to realize a common underlying behaviour was reported previously [32 – 34]. The ac conductivities obtained at different temperatures follow the relation,

$$\frac{\sigma(\omega)}{\sigma_{\mathrm{dc}}} = F\left(\frac{\omega}{\sigma_{dc}T}\right) \tag{5.7}$$

where F is a temperature-independent scaling function, T is temperature in Kelvin. Figure 5.18 shows the scaling of the ac conductivity spectra of $0.45Li_2O – 0.45P_2O_5 – 0.10B_2O_3$ (Y = 0.18) glass at different temperatures. A single master curve is obtained, indicating the relaxation behaviour is temperature-independent. Since the concentration of the network modifier Li_2O and hence the mobile ion concentration remain constant in the investigated system, the master curves for different glasses fall on a common super master curve (except for the low frequency region) (cf. Figure 5.19) without the need for an additional scaling by the mobile ion concentration as proposed by Roling et al. [33]. This corroborates the hypothesis of a universal ionic relaxation process in these glasses. It should be noticed that the findings from σ(ω) analysis in these borophosphate glasses are consistent with our earlier findings in the halide-doped lithium phosphate glasses (see Chapter 4, Sections 4.3.3).

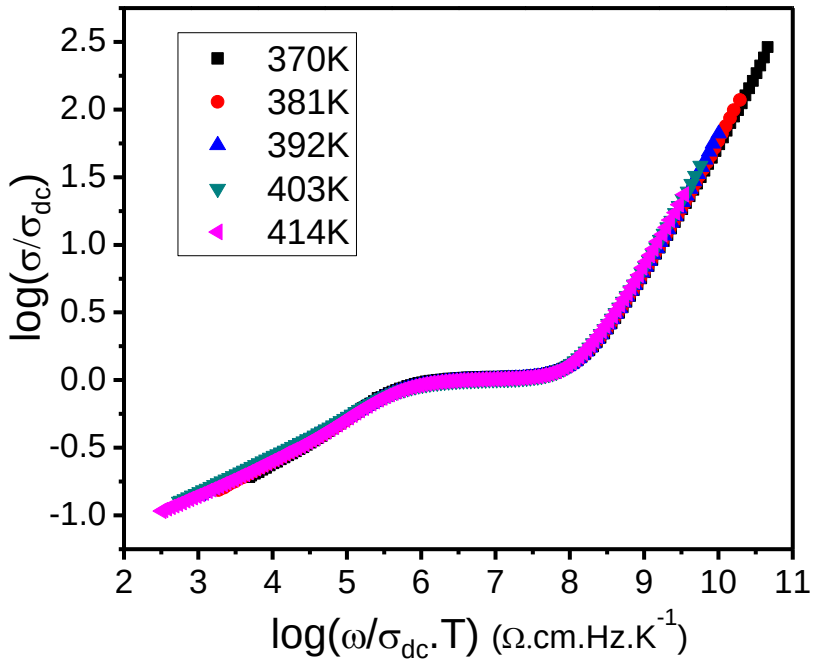

Figure 5.18. Logarithm of (σ/σ_{dc}) vs. ($\omega/\sigma_{dc}T$) for $0.45Li_2O - 0.45P_2O_5 - 0.10B_2O_3$ (Y = 0.18) glass at various temperatures (T).

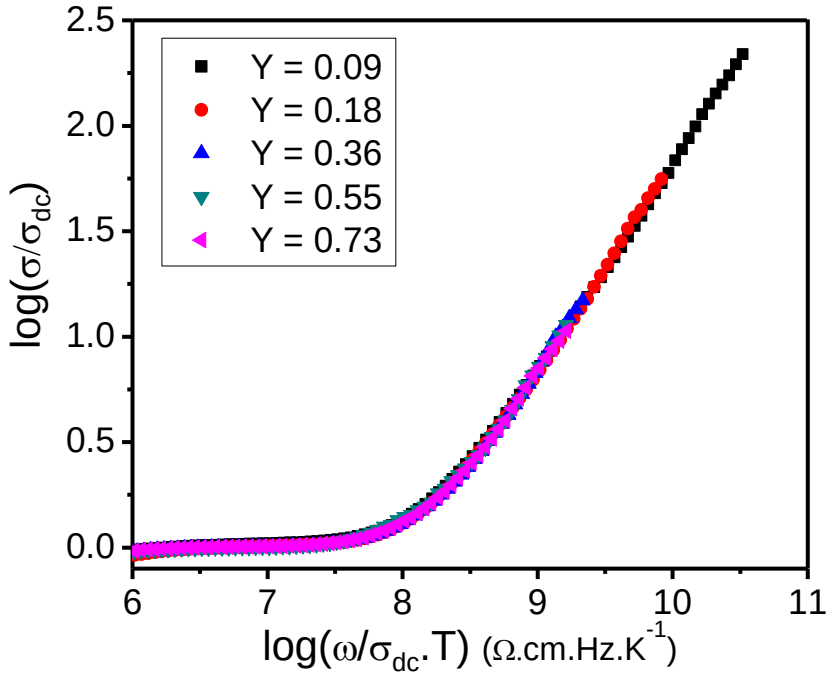

Figure 5.19. Conductivity super master curve for the borophosphate glasses $0.45Li_2O - 0.55[(1 - Y)P_2O_5 - YB_2O_3]$.

5.3.7. Modulus analysis

The analysis of impedance data in the modulus formalism suppresses the electrode effects in extracting the conductivity relaxation times. The electric modulus data can be obtained from the complex impedance data using the relation,

$$M^* = M' + M'' = j\omega C_0 Z^* \quad (5.8)$$

where C_0 is the vacuum capacitance, Z^* is the complex impedance.

Figure 5.20 shows the variation of the imaginary part of electric modulus (M") with frequency (ω) at different temperatures for $0.45Li_2O - 0.35P_2O_5 - 0.20B_2O_3$ (Y = 0.36). The M″ peaks are asymmetric and broader on both sides of the maxima than to be expected for an ideal Debye behaviour. The peak in M″ shifts toward higher frequencies with increase in temperature. The asymmetric M″ peak indicates a stretched exponential character of relaxation times (τ) of the material, which can be described by the empirical KWW function (see Equation (4.7)).

The solid lines through the modulus spectra in Figure 5.20 show the fits in good agreement with the experimental data. The average β value is found to depend on B_2O_3 content and temperature. The superimposed plots of M''/M''_{max} *vs.* log (ω/ω_{max}) onto a single master curve at different temperatures suggest that the dynamical processes governing conductivity relaxations at different frequencies remain the same over the investigated temperature range (cf. Figure 5.21). Furthermore, as mobile ion concentration of the investigated

glasses keeps constant, the M”/M”$_{max}$ master curves for different glasses overlap onto a common super master curve (cf. Figure 5.22) without any additional scaling, indicating that the ionic relaxation is universal in these glasses.

The temperature dependence of peak frequencies (ω_{max}) also obeys the Arrhenius relation $\omega_{max} = \omega_0 \exp\left[-E_a^{\omega max}/kT\right]$, where $E_a^{\omega max}$ is the activation energy for the electrical relaxation (cf. Figure 5.21). The values of $E_a^{\omega max}$ are comparable with the values obtained from temperature-dependent conductivity study, and the peak frequency (ω_{max}) is found to rise with temperature and B_2O_3 content, except for the crystallized sample Y = 0.82.

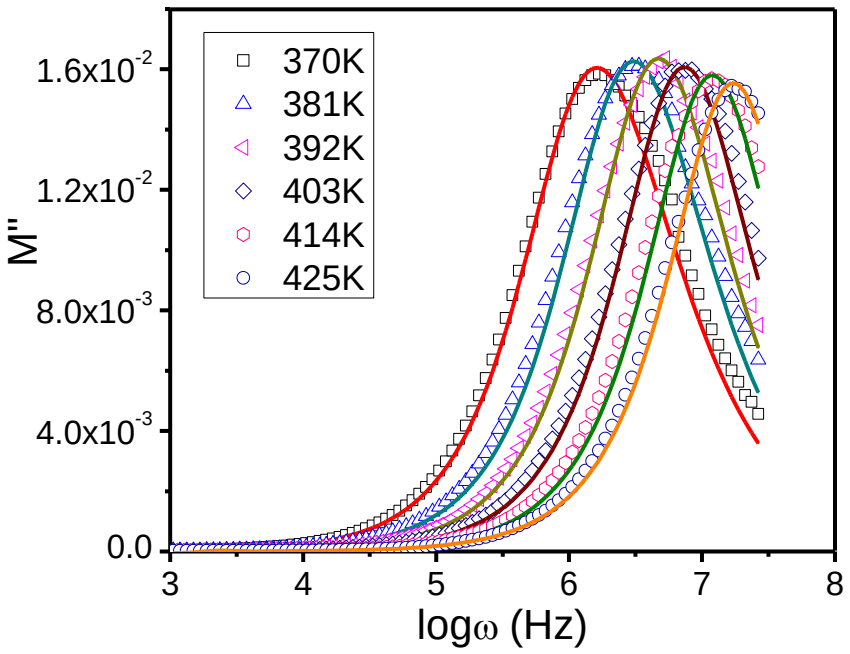

Figure 5.20. Variation of M” with frequency (ω) at different temperatures for $0.45Li_2O – 0.35P_2O_5 – 0.20B_2O_3$ (Y = 0.36) glass. Solid lines: fitted data.

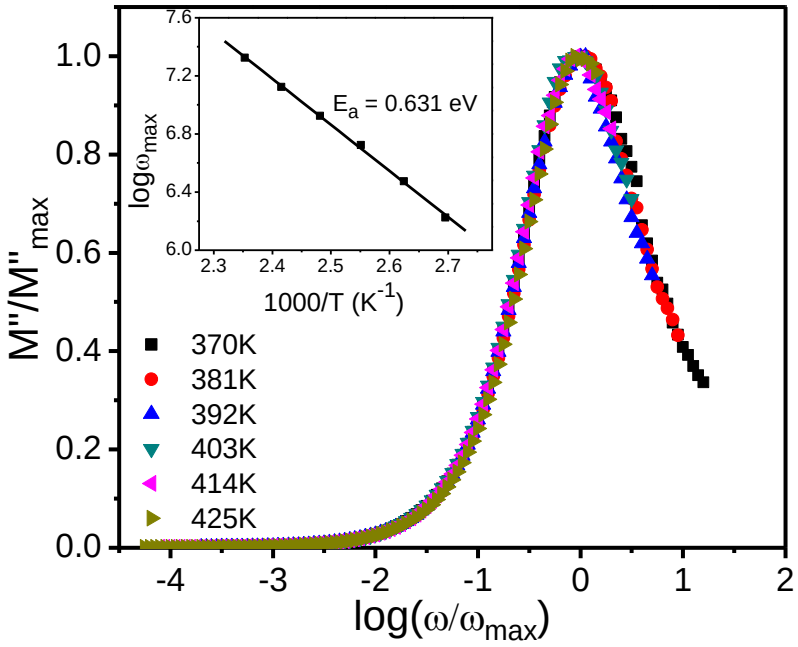

Figure 5.21. Normalized plots of M"/M"max vs. $\log(\omega/\omega_{max})$ at different temperatures for $0.45Li_2O - 0.35P_2O_5 - 0.20B_2O_3$ (Y = 0.36) glass. Inset: Arrhenius plot of peak frequencies ω_{max}.

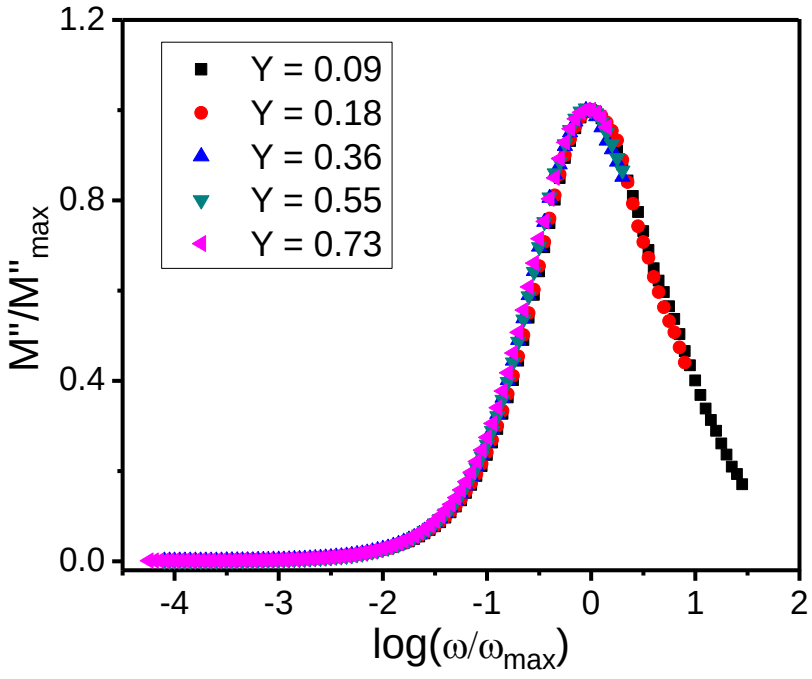

Figure 5.22. Modulus super master curve for the borophosphate glasses $0.45Li_2O - 0.55[(1 - Y)P_2O_5 - YB_2O_3]$.

5.3.8. MD simulations and BV analysis

Figures 5.23 and 5.24 show the pair correlation function (PCF) and running coordination (RCN) of different bonds for the typical glass $0.45Li_2O - 0.20P_2O_5 - 0.35B_2O_3$ (Y = 0.64). The simulated bond lengths of P – O, B – O, Li – O are around 1.53 Å, 1.42 Å and 2.05 Å respectively, which agree very well with their experimentally reported values [35, 36]. The plateau region of RCN for P – O at 4 (cf. Figure 5.23) implies the presence of PO_4 tetrahedra, while there is a gradual increase of RCN for B – O from 3 to 4 (cf. Figure 5.24(a)), which indicates the existence of both trigonal BO_3 and tetrahedral BO_4 units in these borophosphate glasses as revealed from NMR studies [26].

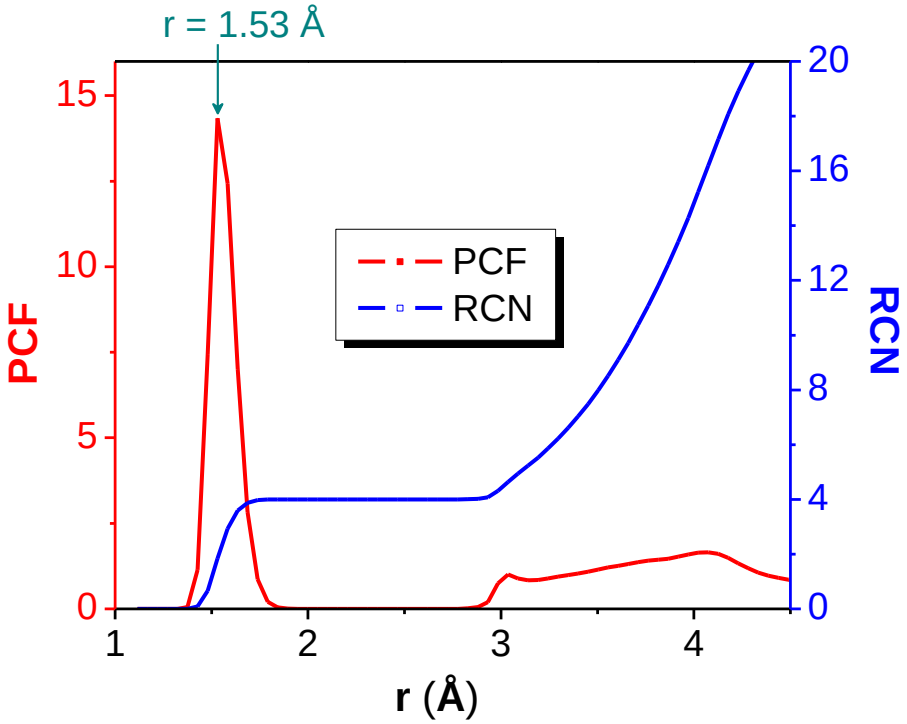

Figure 5.23. Pair correlation function (PCF) and running coordination (RCN) of P – O for $0.45Li_2O - 0.20P_2O_5 - 0.35B_2O_3$ (Y = 0.64) glass.

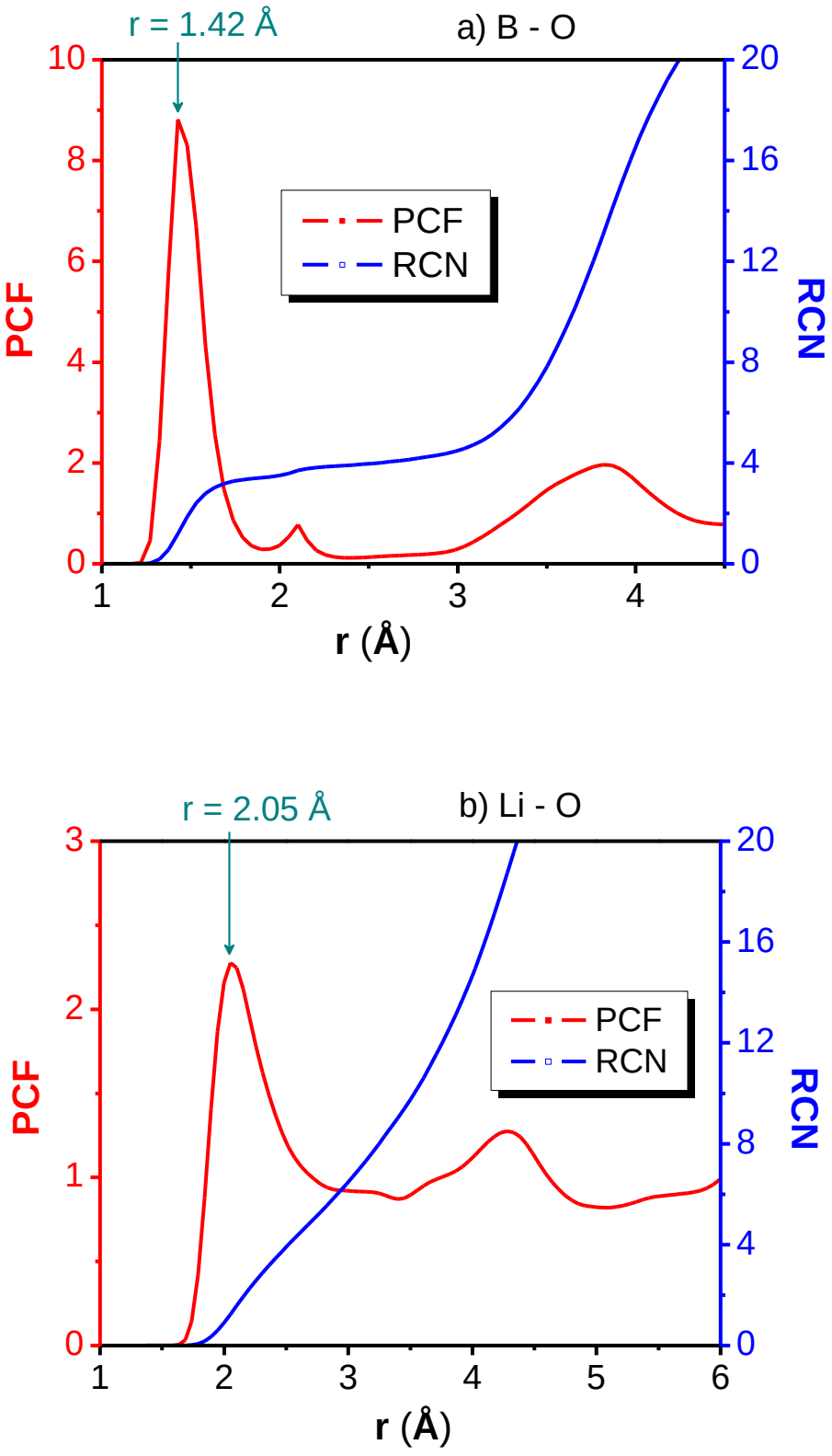

Figure 5.24. Pair correlation function (PCF) and running coordination (RCN) of a) B – O; b) Li – O for $0.45Li_2O - 0.20P_2O_5 - 0.35B_2O_3$ (Y = 0.64) glass.

Figure 5.25 depicts the presence of PO_4, BO_4 tetrahedra and BO_3 triangles in the MD generated configuration of $0.45Li_2O - 0.35P_2O_5 - 0.20B_2O_3$ (Y = 0.36) glass at 300 K. The cross-linking of the glass network between phosphate chains through P – O – B bonds is clearly observed in the simulated structures. MD simulations also quantitatively reproduce the experimental values of ionic conductivity, as shown in Figure 5.26.

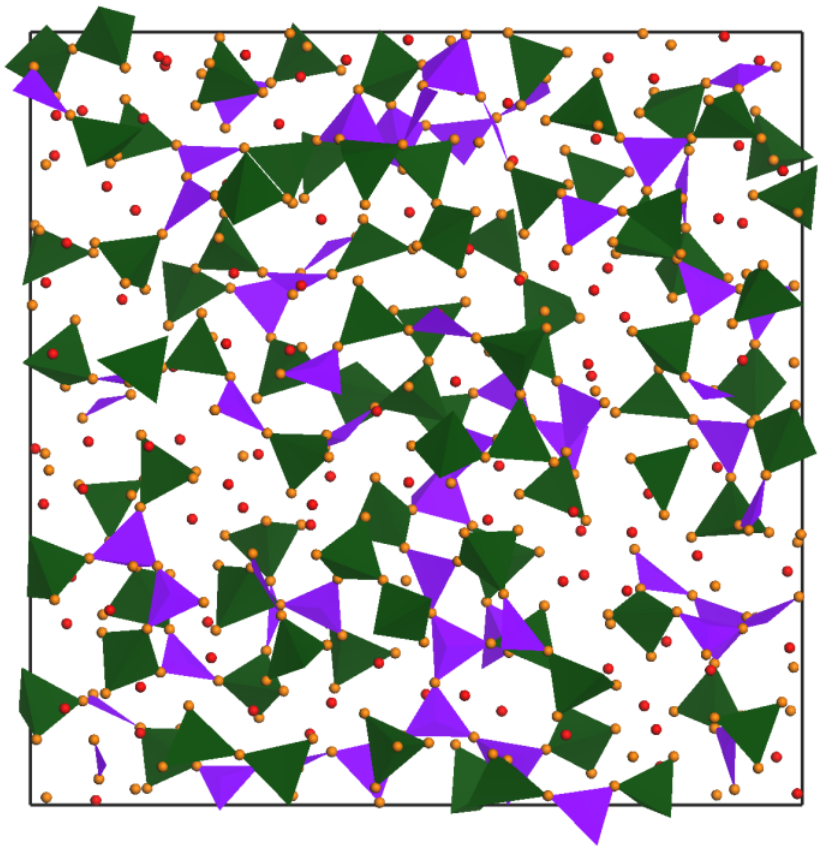

Figure 5.25. Structure of $0.45Li_2O - 0.35P_2O_5 - 0.20B_2O_3$ (Y = 0.36) glass at 300 K. Oxide atoms (orange spheres) are around P (olive tetrahedra) and B (violet tetrahedra and triangles). Li atoms: red spheres. Only 1/4 of the structure model is shown along z (perpendicular to the plane of view) to reduce overlap.

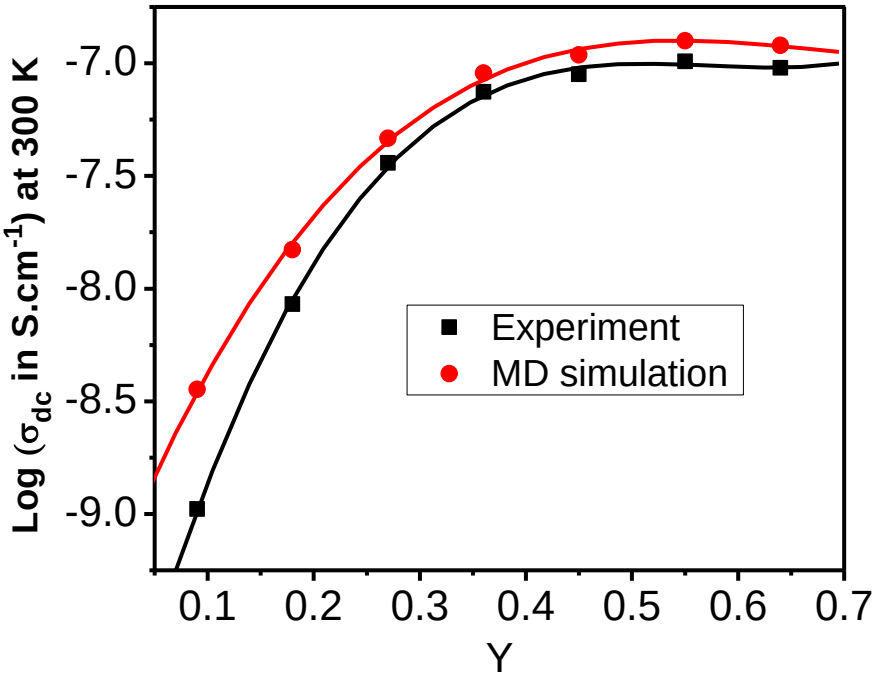

Figure 5.26. Comparison of ionic conductivities for the borophosphate glasses $0.45Li_2O - 0.55[(1 - Y)P_2O_5 - YB_2O_3]$ ($0.09 \leq Y \leq 0.64$) with the relative B_2O_3 content (Y) at 300 K . The lines are polynomial fits of data.

Final equilibrated MD configurations at 300 K of the borophosphate glasses $0.45Li_2O - 0.55[(1 - Y)P_2O_5 - YB_2O_3]$ ($0.09 \leq Y \leq 0.64$) are used for bond valence (BV) analysis. The fractions of bridging (P – O – P, B – O – B, P – O – B) and non-bridging oxygens (NBOs) are quantified using the above-mentioned BV criterion. The number of P – O – P bonds decreases and B – O – B bonds increases as expected with the rise of B_2O_3 content (cf. Figure 5.27(a)). The total fraction of simulated (P – O – P and B – O – B) bonds shows a decrease up to Y = 0.45, then increase (cf. Figure 5.27(b)). In addition, the fraction of simulated P – O – B bonds rises with the increase of B_2O_3 content and passes through a maximum at Y = 0.45 (cf. Figure 5.28(a)). This trend is qualitatively similar to the variation on the P – O – B bond concentration assessed experimentally from XPS spectra (and also from

Raman spectra), except that the peak value of the experimental data is shifted slightly to Y = 0.55. A description of the MD-simulated glasses by our preference factor approach described in section 5.3.3 shows that P – O – B units again occur more frequently than to be expected for a random distribution of P and B. The somewhat lower preference factor $\xi \approx 1.4$ observed for the MD-simulated structure when compared to the XPS results ($\xi \approx 1.65$) probably indicates that the structure evolution in the simulated glass corresponds to a system with a significantly faster quenching rate and correspondingly higher degree of disorder. The close correlation between experimental and simulated characteristic parameters of the glasses also includes the values of T_g (cf. Table 5.1) and ionic conductivity σ_{dc} (cf. Figure 5.13) observed in this study, as well as from Magistris et al. for similar borophosphate glasses [2]. Besides, the fraction of NBOs is found to decrease continuously with the rise of the B_2O_3 content, as shown in Figure 5.28(b), in good agreement with both the structure model in section 5.3.3 and the findings in our XPS analysis.

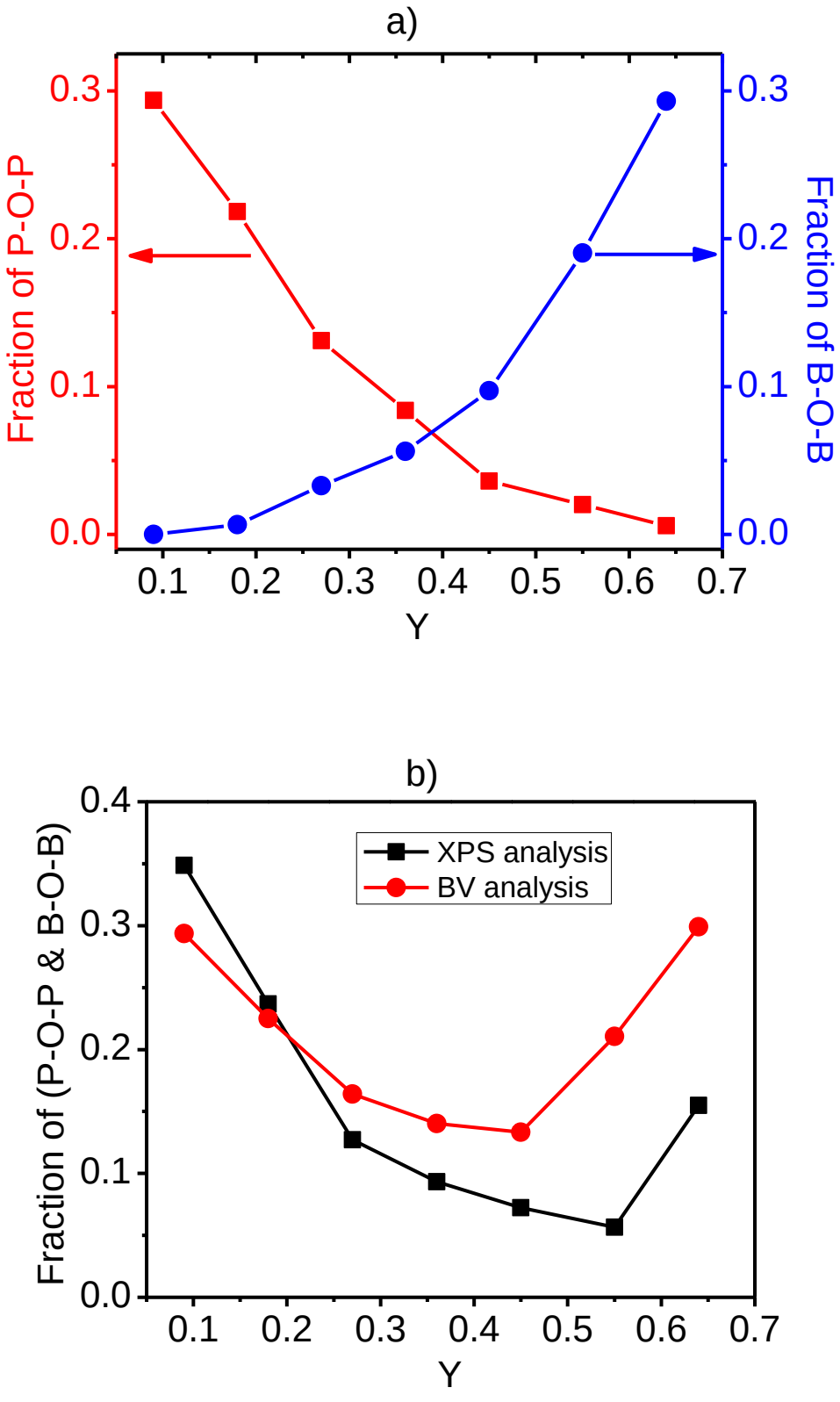

Figure 5.27. a) Fraction of P – O – P and B – O – B bonds from bond valence (BV) analysis; b) Comparison of (P – O – P & B – O – B) from XPS data and BV analysis for the glassy system $0.45Li_2O - 0.55[(1 - Y)P_2O_5 - YB_2O_3]$ ($0.09 \leq Y \leq 0.64$) with the relative B_2O_3 content (Y).

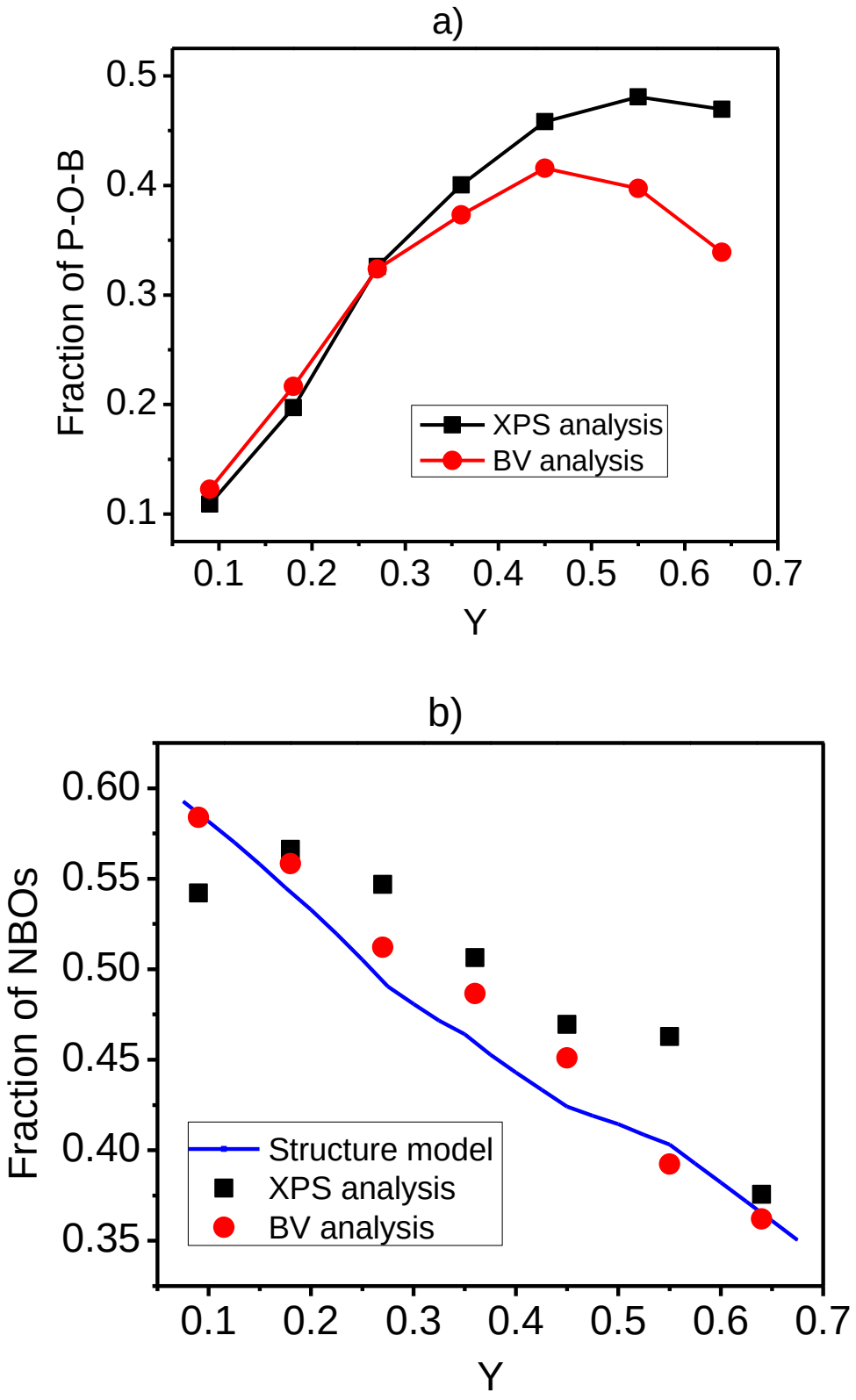

Figure 5.28. Comparison of a) P – O – B bonds; b) Non-bridging oxygens (NBOs) from XPS and BV analysis for the borophosphate glassy system $0.45Li_2O - 0.55[(1 - Y)P_2O_5 - YB_2O_3]$ ($0.09 \leq Y \leq 0.64$) with the relative B_2O_3 content (Y).

Figure 5.29 shows the local environment of the Li^+ ion sites located in the conduction pathways of the investigated borophosphate glasses. The yellow isosurfaces here represent the percolating Li^+ ion conduction pathways. The density of pathways increases with rising B_2O_3 content from Y = 0.09 to 0.64 (the volume fraction of percolating pathways (F) increases from 5.7% to 8.3%), in line with the decrease of activation energy (E_a) as shown in Figure 5.30, and the corresponding increase of experimental ionic conductivity (σ_{dc}) at 300 K. Besides, all the data points in Figure 5.30, except for the last point at Y = 0.64, fall approximately on a straight line.

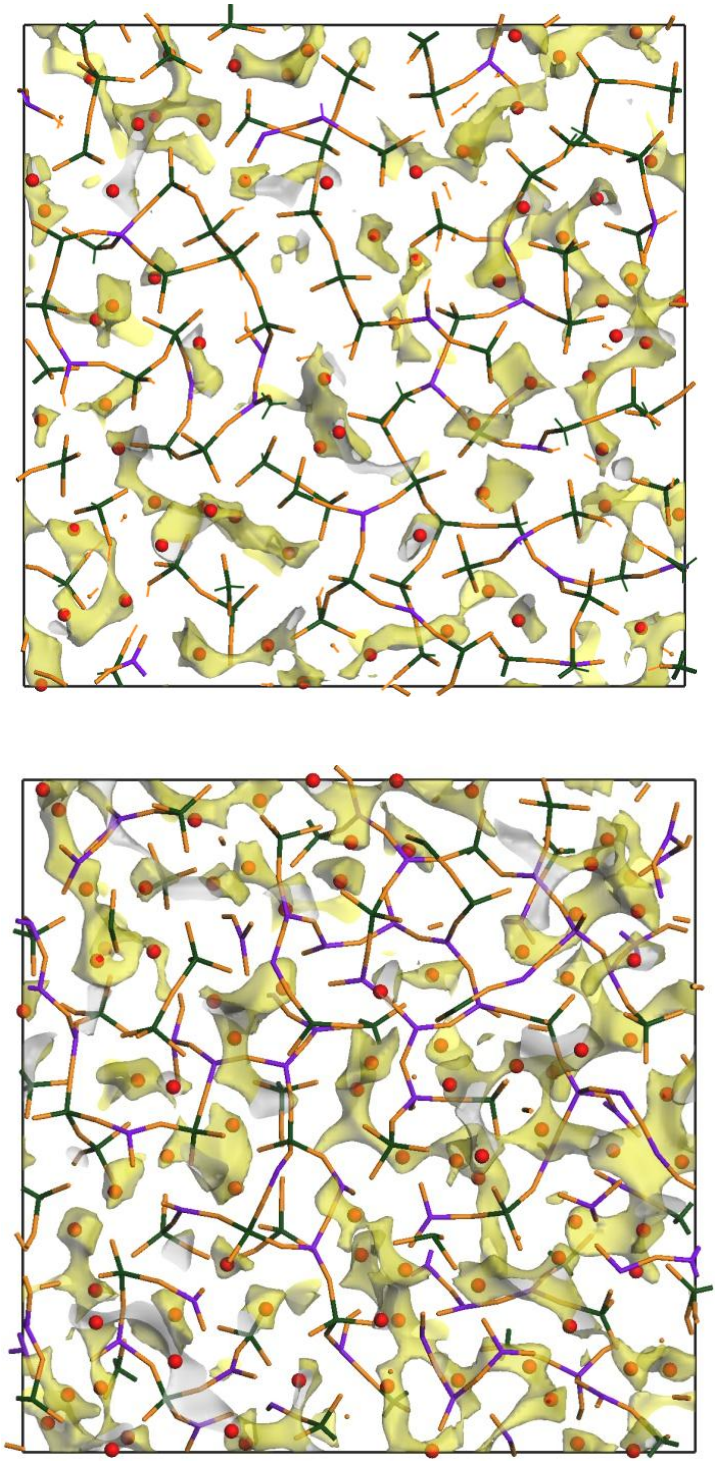

Figure 5.29. Slices through the lithium migration pathway network visualized as isosurfaces of constant Li bond valence sum mismatch $|\Delta V(Li)|$ for the relative B_2O_3 contents Y = 0.18 (top) and Y = 0.55 (bottom) at 300 K superimposed on the respective glass structure model. Li atoms: red spheres.

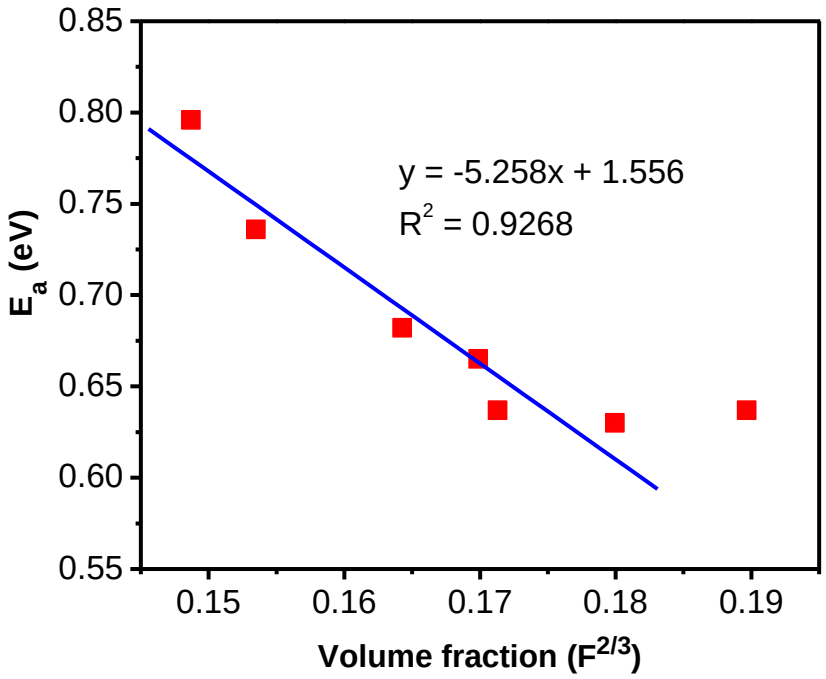

Figure 5.30. Variation of pathway volume fraction of Li^+ ions with activation energy (E_a) for $0.45Li_2O - 0.55[(1 - Y)P_2O_5 - YB_2O_3]$ glasses ($0.09 \leq Y \leq 0.64$).

5.4. Conclusion

The formation, atomic structure and transport properties of $0.45Li_2O - (0.55 - x)P_2O_5 - xB_2O_3$ ($0 \leq x \leq 0.55$) or equivalently $0.45Li_2O - 0.55[(1 - Y)P_2O_5 - YB_2O_3]$ ($0 \leq Y \leq 1$) borophosphate system were scrutinized by keeping the molar ratio of $Li_2O/(P_2O_5 + B_2O_3)$ constant to focus on the influence of cation mobility changes due to the mixed glass former effect. Glass forming region of the borophosphate system is within the range of $0 \leq Y \leq 0.73$ and $0.91 \leq Y \leq 1$ by using melt quenching method. Addition of B_2O_3 into lithium phosphate glasses increases glass transition temperature (T_g) and number density, decreases the molar volume, and generally renders the glasses more fragile.

Correlation between structure and conductivity were thoroughly investigated using FT-IR, Raman, XPS and impedance spectroscopy, as well as MD simulation and Bond Valence (BV) approach. FT-IR, Raman, XPS spectra and MD simulations indicate the formation of P – O – B bonds. A structural model is proposed to calculate the relative contributions of different bonds (i.e., NBOs, P – O – P, B – O – B and P – O – B bonds) in the borophosphate glasses, which turn out to closely harmonize with Raman and XPS data.

Optimized potential parameters for MD simulations also reproduce the reported bond lengths, coordinations, and the presence of both BO_3 and BO_4 units in this borophsphate system. Structural studies from BV analysis qualitatively agree with those from experimental data and the proposed structural model, which indicate the increase of P – O – B bonds (up to $Y \approx 0.5$) and B – O – B bonds, as well as the decrease of P – O – P bonds and non-bridging oxygens (NBOs) with rising B_2O_3 content.

The increase of cross-linking of the glass network through P – O – B bonds with B_2O_3 addition makes the glass chemically and structurally more heterogeneous, facilitating the formation of low energy pathways and thereby increasing the ionic conductivity. The linear rise of ionic conductivity (σ_{dc}) and reduction of activation energy (E_a) in the glass region of $0 \leq Y \leq 0.27$ can be linked to the increase of B-$(OP)_4$ bonds. The maximum fraction of P – O – B bonds at $Y = 0.55$ may be responsible for the maximum in σ_{dc} and the minimum in E_a for glass compositions of $0 \leq Y \leq 0.91$. In the region of $0.36 \leq Y \leq 0.55$, the decrease of B-$(OP)_4$ linkages and the increase of the

B-$(OP)_3$ linkages explains the less pronounced increase of σ_{dc} and decrease in E_a. For $0.64 \leq Y \leq 0.91$, the decrease of P – O – B bonds (and the emergence of crystalline Li_3PO_4 units in case of Y = 0.82) might account for the decrease of ionic conductivity.

A proposed model to estimate the ionic conductivity (σ_{dc}) at room temperature, which is based on the relative fractions of different bonds of bridging oxygens (i.e., P – O – P, B – O – B, P – O – B), is found to accurately describe the values of σ_{dc} found from the impedance spectroscopy. Consequently, σ_{dc} can be directly predicted from the structural model in the borophosphate glasses and the role of P – O – B units for the conductivity enhancement in this mixed glass former system could be quantified.

Analyses of impedance data in the conductivity and modulus formalisms as a function of temperature and frequency lead to single master curves for the reduced conductivity $\sigma(\omega)$ and the modulus M" at all temperatures, which clarifies that the relaxation mechanism is temperature independent. The analysis of the temperature variation of the M″ peak indicates that the observed relaxation process is thermally activated. The inferences drawn from the above analysis ((i) Arrhenius dependence of relaxation peak on temperature and (ii) comparable values of activation energy obtained from conductivity and modulus analysis) not only demonstrates that ion transport in the investigated materials follows the hopping mechanism, it also indicates the existence of a universal ionic relaxation process that essentially consists of a redistribution of the mobile Li^+ ions.

Experimental and simulated values of ionic conductivity (σ_{dc}) at room

temperature are in good agreement. The effect of B_2O_3 addition on the pathways for the mobility of Li^+ ions is also quantified using BV analysis for $0.45Li_2O - 0.55[(1 - Y)P_2O_5 - YB_2O_3]$ glasses ($0.09 \leq Y \leq 0.64$). The volume fraction of Li^+ ion transport pathways increases with the B_2O_3 content, in line with the increase of σ_{dc}, and the decrease of activation energy (E_a).

References

1. B. V. R. Chowdari, K. Radhakrishnan, J. Non-Cryst. Solids 108 (1989) 323.
2. A. Magistris, G. Chiodelli, M. Villa, J. Power Sources 14 (1985) 87.
3. R. V. Salodkar, V. K. Deshpande, K. Singh, J. Power Sources 25 (1989) 257.
4. B. K. Money, K. Hariharan, Solids State Ionics 179 (2008) 1273.
5. F. Munoz, L. Montagne, L. Pascual, A. Duran, J. Non-Cryst. Solids 355 (2009) 2571.
6. J. –M. Delaye, D. Ghaleb, J. Non-Cryst. Solids 195 (1996) 239.
7. J. –M. Delaye, D. Ghaleb, Phys. Rev. B 61 (2000) 14481.
8. W. Li, S. H. Garofalini, Solid State Ionics 166 (2004) 365.
9. L. G. Baikova, Y. K. Fedorov, V. P. Pukh, L. V. Tikhonova, T. P. Kazannikova, A. B. Sinani, S. I. Nikitina, Glass Phys. Chem. 29 (2003) 276.
10. K. Ito, C.T. Moynihan, C. A. Angell, Nature 398 (1999) 492.
11. E. I. Kamitsos, G. D. Chryssikos, J. Mol. Struct. 247 (1991) 1.
12. R. K. Brow, D. R. Tallant, S. T. Myers, C. C. Phifer, J. Non-Cryst. Solids 191 (1995) 45.
13. J. J. Hugdens, S. W. Martin, J. Am. Ceram. Soc. 76 (1993) 1691.
14. K. Meyer, J. Non-Cryst. Solids 209 (1997) 227.
15. G. B. Pakhomov, S. L. Neverov, Solid State Ionics 119 (1999) 235.
16. S. Kumar, P. Vinatier, A. Levasseur, K. J. Rao, J. Solid State Chem. 177 (2004) 1723.

17. E. I. Kamitsos, A. P. Patsis, M. A. Karakassides, G. D. Chryssikos, J. Non-Cryst. Solids 126 (1990) 52.
18. P. Y. Shih, Mater. Chem. Phys. 84 (2004) 151.
19. R. F. Bartholomew, J. Non-Cryst. Solids 7 (1972) 221.
20. J. J. Hudgens, R. K. Brow, D. R. Tallant, S. W. Martin, J. Non-Cryst. Solids 223 (1998) 21.
21. B. N. Nelson, G. J. Exarhos, J. Chem. Phys. 71 (1979) 2739.
22. M. Scagliotti, M. Villa, G. Chiodelli, J. Non-Cryst. Solids 93 (1987) 350.
23. J. Yifen, C. Xiangsheng, H. Xihuai, J. Non-Cryst. Solids 112 (1989) 147.
24. L. Koudelka, P. Mosner, J. Non-Cryst. Solids 293-295 (2001) 635.
25. B. N. Meera, J. Ramakrishna, J. Non-Cryst. Solids 159 (1993) 1.
26. T. Feng, P. Linzhang, J. Non-Cryst. Solids 112 (1989) 142.
27. E. C. Onyiriuka, J. Non-Cryst. Solids 163 (1993) 268.
28. R. K. Brow, J. Non-Cryst. Solids 194 (1996) 267.
29. A. Hayashi, M. Nakai, M. Tatsumisago, T. Minami, C. R. Chimie 5 (2002) 751.
30. Y. H. Yun, P. J. Bray, J. Non-Cryst. Solids 44 (1981) 227.
31. V. Nazabal, E. Fargin, C. Labrugere, G. L. Flem, J. Non-Cryst. Solids 270 (2000) 223.
32. P. S. Anantha, K. Hariharan, Mat. Sci. Eng. B 121 (2005) 12.
33. B. Roling, A. Happe, K. Funke, M. D. Ingram, Phys. Rev. Lett. 78 (1997) 2160.
34. A. Bhide, K. Hariharan, Mat. Chem. Phys. 105 (2007) 213.

35. K. Muruganandam, M. Seshasayee, S. Patnaik, Solid State Ionics 89 (1996) 313.
36. W. Soppe, C. V. D. Marel, H. W. D. Hartog, J. Non-Cryst. Solids 101 (1988) 101.

Chapter 6

Conclusions and Future Work

6.1. Conclusions

The overall objective of this PhD project was to study ion conduction mechanisms in fast ion conducting oxide glasses for all-solid-state rechargeable batteries. In view of this, various types of oxide glassy systems, such as lithium silicate glasses, lithium phosphate glasses doped with halide salt LiX (X = Cl, Br) and lithium borophosphate glasses, were synthesized and investigated using both experimental and simulation techniques.

Through the combination of impedance spectroscopy, Molecular Dynamics (MD) simulations and Bond Valence (BV) analysis, the ion conduction mechanisms in all the studied glasses can be clearly manifested by the following factors:

(a) *Lithium ion transport pathway has to run along sites with mixed oxide / halide or exclusive oxide coordination.*

In the investigated halide-doped phosphate glasses, this research has provided clear evidence that nearly all Li ions have mixed oxide / halide coordinations in the glass matrix and ion transport cannot be related to LiX aggregates since no such aggregates exist. This finding is consistent with experimental results.

(b) *Lithium ion transport follows the hopping mechanism.*

Analyses of impedance data in the conductivity and modulus formalisms as a function of temperature and frequency for both halide-doped phosphate and borophosphate glassy systems indicate

(i) the Arrhenius dependence of relaxation peak on temperature and (ii) comparable values of activation energy obtained from conductivity and modulus analysis. This confirms that ion transport in the investigated materials follows the hopping mechanism.

(c) *Density or volume fraction (F) of ion migration pathways – the increase in the density or F of ion migration pathways accounts for the increase of ionic conductivity (σ_{dc}) and a corresponding decrease in the activation energy (E_a).*

Firstly, for the lithium silicate glasses $xLi_2O - (1 - x)SiO_2$, the density or volume fraction (F) of ion conduction pathways rises with increasing modifier content x, which is in line with the rise of ionic conductivity (σ_{dc}) and the corresponding reduction of activation energy (E_a) in these glasses.

Secondly, in case of the halide-doped phosphate glasses $yLiX - (1 - y)(0.6Li_2O - 0.4P_2O_5)$, the density or F of ion conduction pathways is also found to slightly increase (i) when rising the lithium halide (LiX) dopant concentration (X = Cl, Br) or (ii) when doping by more polarisable halide X^- ions (e.g. the substitution of Cl^- by the same amount of Br^-), which corresponds to the small increment of σ_{dc} and the corresponding decrement of E_a.

Finally, for the borophosphate glasses $0.45Li_2O - 0.55[(1 - Y)P_2O_5 - YB_2O_3]$ ($0.09 \leq Y \leq 0.64$), the density or F of ion conduction pathways rises with the increase of B_2O_3 content, which is again in

proportion to the increase of σ_{dc} and the corresponding decrease of E_a.

For illustration, Figure 6.1 shows the local environment of the Li^+ ion sites located in the conduction pathways (yellow slices) of the investigated borophosphate glasses. The increase in the density of ion conduction pathways with the B_2O_3 addition can be clearly seen in this figure.

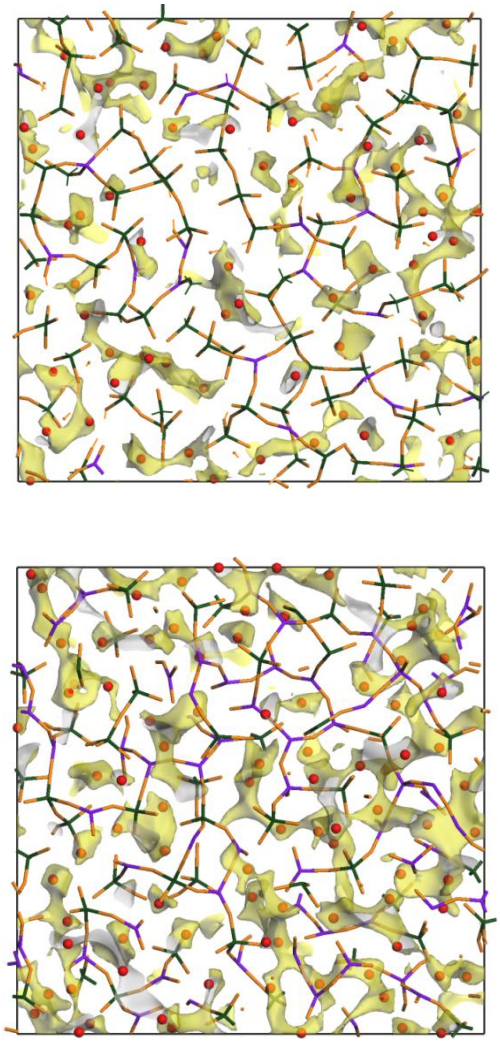

Figure 6.1. Slices through the lithium migration pathway network visualized as isosurfaces of constant Li bond valence sum mismatch |ΔV(Li)| for Y = 0.18 (top) and Y = 0.55 (bottom) superimposed on the respective glass structure model. Li atoms: red spheres.

Figure 6.2 shows the correlation between the scaled pathway volume fraction ($(F \times M^{1/2})^{1/3}$) and experimentally determined transport properties (i.e., σ_{dc}, E_a) in the silicate and halide-doped phosphate glassy systems, which follows the same trend as that observed from RMC-generated structure models in an earlier study of our group. As seen in Figure 6.2, it is evident that the higher volume fraction (F) of the ion percolating pathways in the phosphates contributes to the higher values of ionic conductivity (σ_{dc}) and lower values of activation energy (E_a) when compared to silicates.

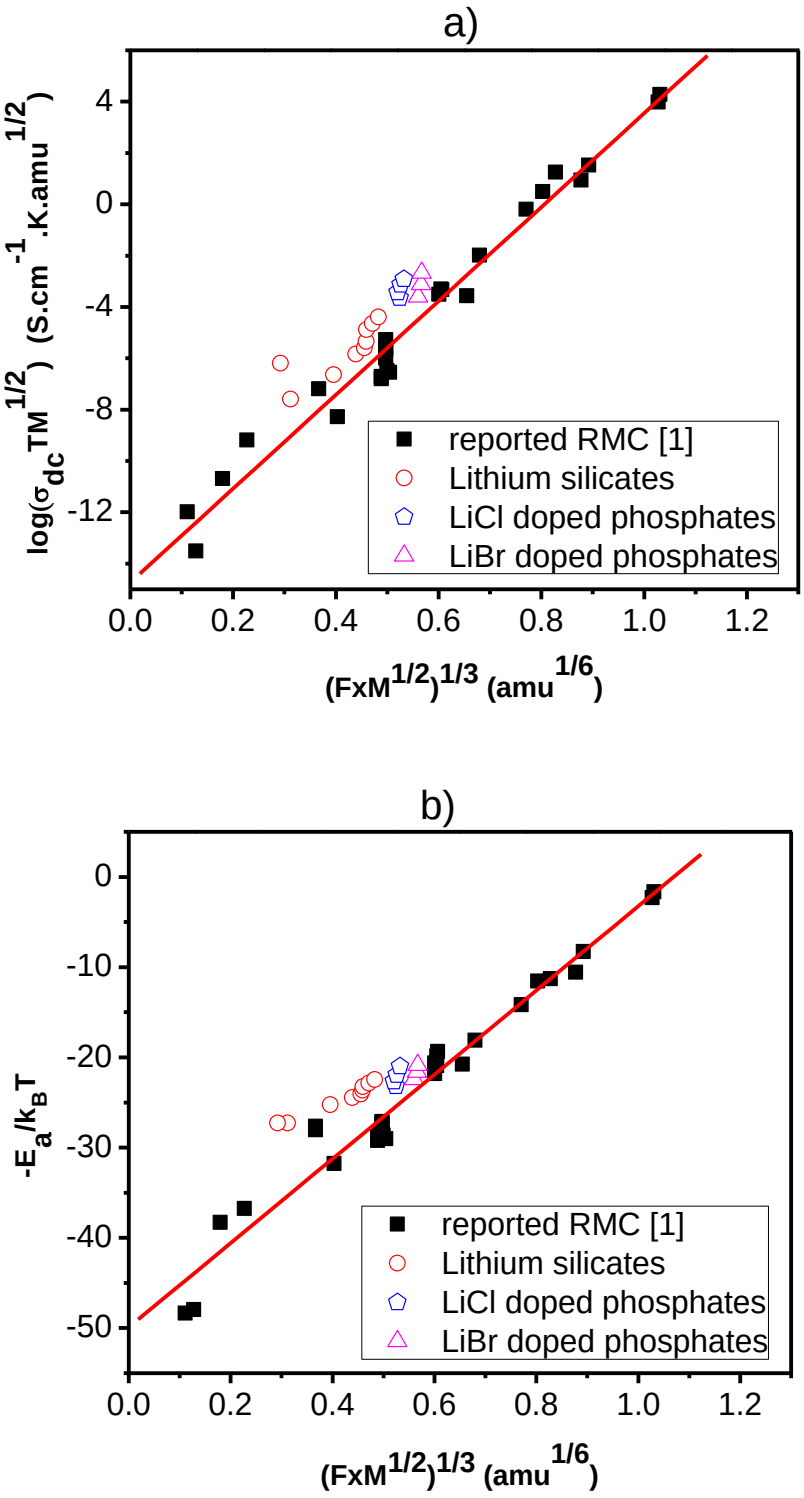

Figure 6.2. Variation of Li^+ ion pathway volume fractions with a) Experimental room temperature ionic conductivity; b) Activation energy. Solid symbols refer to data from RMC models [1]. Open symbols refer to MD simulated data of silicate glasses $xLi_2O - (1 - x)SiO_2$ (where x = 0.10, 0.15, 0.20, 0.25, 0.30, 0.33, 0.40, 0.45, 0.50) and halide-doped phosphate glasses $yLiX - (1 - y)(0.60Li_2O - 0.40P_2O_5)$ (where X = Cl, Br; y = 0.10, 0.15, 0.20, and 0.25 for LiCl only).

(d) *Minimum value of local pathway dimension as the effective bottleneck for ion transport is correlated to the ionic conductivity and its activation energy.*

As observed from lithium silicate and halide-doped phosphate glasses (see Figure 6.3), the rise in the minimum value of local pathway dimension (i) with increase of modifier content Li_2O (in case of silicates) or (ii) with the increase of LiX concentration or with the doping by more polarisable X^- ions (in case of halide-doped phosphates) is in proportion to the decrease of the activation energy and the increase in ionic conductivity. In addition, similar to volume fractions of ion transport pathways, the values of minimum local dimension of phosphates observed in this study are higher than those of silicates, which again explain the lower E_a and higher σ_{dc} of phosphate glasses when compared to silicate glasses (cf. Figure 6.3).

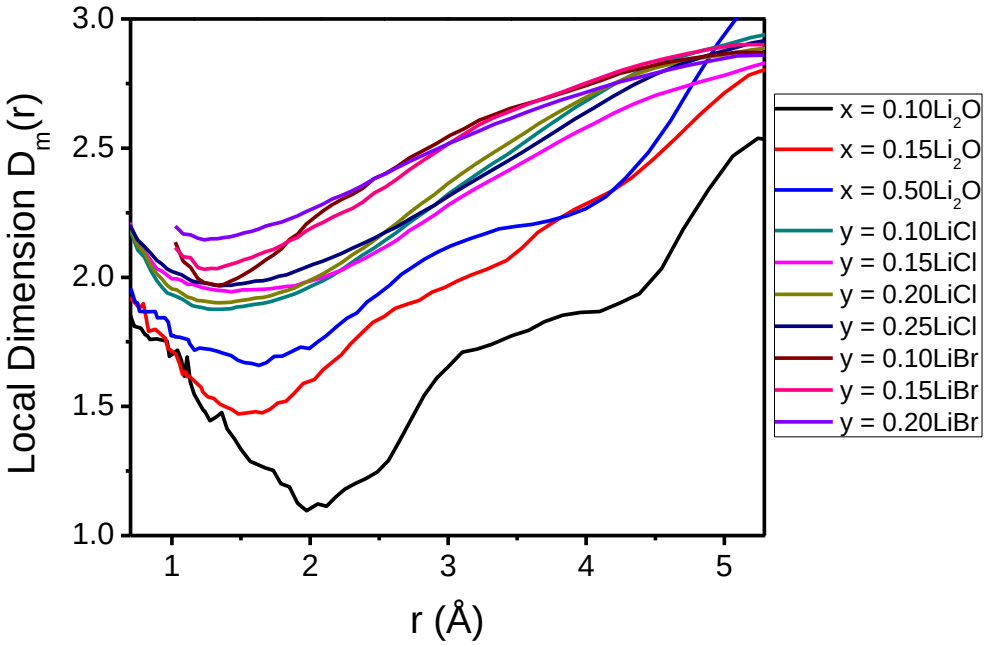

Figure 6.3. The local dimension of Li^+ ion transport pathway, $D_m(r)$ versus radius (r) for lithium silicate $xLi_2O - (1 - x)SiO_2$ and halide-doped phosphate $yLiX - (1 - y)(0.60Li_2O - 0.40P_2O_5)$ glasses.

Besides the ion conduction mechanisms, this project also explores the relaxation behavior of ions in the glassy solid electrolytes by analyzing frequency dependent conductivity ($\sigma(\omega)$) and modulus (M") formalism. In the halide-doped phosphate and borophosphate glasses, the comparable values of activation energy for hopping and dc conductivity suggest that the relaxation mechanism requires charge carriers to cross the same energy barriers as for the dc conduction process. The superposition of reduced conductivity ($\sigma(\omega)$) and imaginary modulus (M") onto single master curves at all temperatures proves that the relaxation mechanism is temperature independent. Additionally, the analysis of the temperature variation of the M″ peak also indicates that the observed relaxation process is thermally activated. As for dc ionic conductivity, temperature dependence of relaxation peak (ω_{max}) also obeys an Arrhenius-type relation. In particular, in the borophosphate glassy system

$0.45Li_2O - 0.55[(1 - Y)P_2O_5 - YB_2O_3]$ ($0 \leq Y \leq 1$), the overlap of master curves for different glasses onto a common super master curve in terms of $\sigma(\omega)$ and M" further reveals the existence of a universal ionic relaxation process in these materials.

During this research project, the combination of Molecular Dynamics (MD) simulation and Bond Valence (BV) analysis is found to be efficient in analyzing and predicting not only ion transport properties as mentioned above, but also the structure of the glassy solid electrolytes.

- In the lithium silicate glasses, the decrease of bridging oxygens and the variation of Q_n units (where n is the number of bridging oxygens) with the addition of network modifier Li_2O as estimated from BV analysis for MD-simulated structures qualitatively agree well with reported experimental results and bond order model.

- The optimised potential parameters for MD simulations in lithium halide-doped phosphate and borophosphate glassy systems, which have been derived in the frame of this project, can reproduce very well experimentally known bond lengths, coordination numbers of atoms in the structural networks, as well as their ionic conductivity within the experimental uncertainties. Structural analysis from BV approach for MD-simulated borophosphate glasses $0.45Li_2O - 0.55[(1 - Y)P_2O_5 - YB_2O_3]$ is qualitatively in good agreement with experimental results obtained from Raman and XPS analysis, which indicate the increase of P – O – B bonds (up to $Y \approx 0.5$) and

B – O – B bonds, as well as the decrease of P – O – P bonds and non-bridging oxygens with rising B_2O_3 content.

Moreover, a correlation between structure and conductivity in the borophosphate mixed glass former system $0.45Li_2O – 0.55[(1 – Y)P_2O_5 – YB_2O_3]$ ($0 \leq Y \leq 1$) was discovered. It was suggested that the increase of cross-linking through P – O – B bonds with B_2O_3 addition facilitates the formation of low energy pathways and thereby increasing the ionic conductivity (σ_{dc}). This study has also proposed two models (i.e., structure and conductivity model) to estimate the contributions of different bonds and σ_{dc} at room temperature in the borophosphate glasses, which well harmonize with the experimental results. The conductivity σ_{dc} can be directly predicted from the structural model in the borophosphate glasses. It has provided clear evidence that extended P – O – P regions will significantly reduce the conductivity, while the introduction of P – O – B units into a P – O – P region is the key factor for the conductivity enhancement. The maximum fraction of P – O – B bonds at Y = 0.55 may be responsible for the maximum in σ_{dc} and the minimum in activation energy (E_a) for the glass compositions $0 \leq Y \leq 0.91$.

In summary, the investigations on the ion conduction mechanisms of the above oxide glasses have provided the valuable insight of not only structure and ion transport properties, but also the relaxation behaviors in these glassy systems. The combination of the Molecular Dynamics (MD) simulation and the Bond Valence (BV) approach has shown to be a simple but efficient tool in predicting the variation of transport properties with compositions in the glassy solid electrolytes. It should be noticed that this formalism permits to estimate

the order of magnitude of ionic conductivity and activation energy for the glasses under study.

6.2. Future work

The ion conduction mechanism studies in the fast ion conducting oxide glasses were thoroughly investigated in this thesis. The oxide-based materials in this study are the promising candidates as solid electrolytes for the application of all-solid-state lithium rechargeable batteries, especially thin film or high temperature batteries, due to long-life cyclability, stability to humidity and high temperature [2 – 4]. Figure 6.4 illustrates a schematic diagram of a typical all-solid-state thin film battery for example, where oxide-based glassy solid electrolyte can be used [2]. To synthesize a thin film battery, all the components including anode (negative electrode such as metal Li, amorphous SnO, etc), solid electrolyte, cathode (positive electrode such as crystalline $LiCoO_2$, $LiMn_2O_4$, etc) and suitable current collectors (Pt or Pt/Cr) should be fabricated onto a multilayered thin film (cf. Figure 6.4).

Therefore, one possible direction for future work is to build the all-solid-state thin film or high temperature lithium rechargeable batteries employing the fast ion conducting glasses in this work as the solid electrolytes. Testing and optimizing the battery performance will also be conducted.

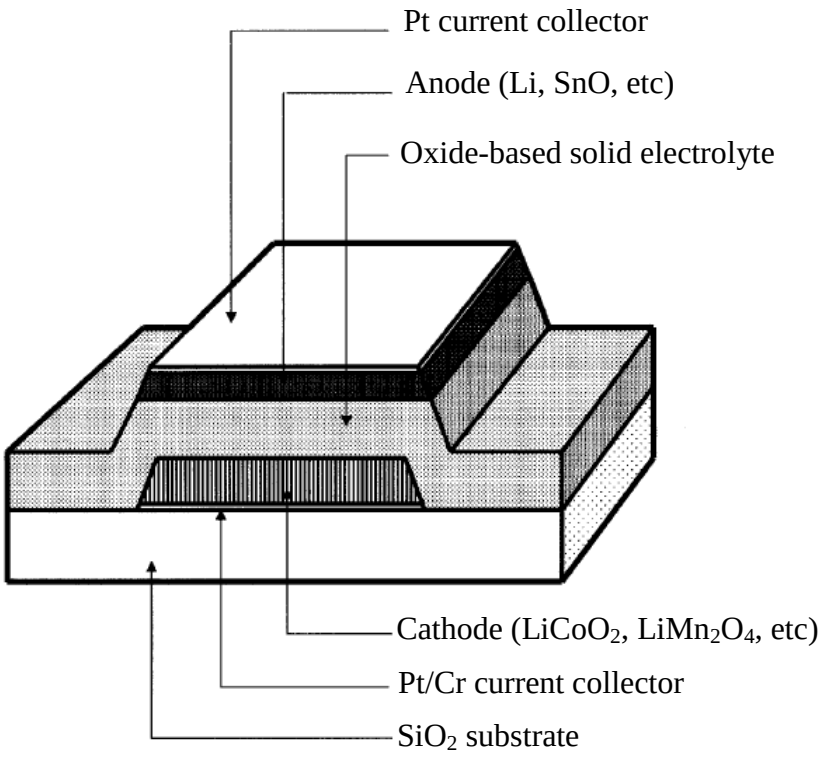

Figure 6.4. Schematic cross-sectional view of a typical all-solid-state thin film Li-ion rechargeable battery. Modified from Ref. [2].

Another direction for future research is to expand the investigations for sulfide glasses $xLi_2S - (1 - x)P_2S_5$ and $Li_2S - P_2S_5 - LiX$ (where X = Cl, Br, I), as well as borophosphide glass $Li_2S - P_2S_5 - B_2S_3$ with a similar approach (i.e., MD simulation, BV analysis, and impedance spectroscopy, etc) as the oxide glasses to clarify how replacement of oxygen by sulfur affects the local structure of glasses, ion transport pathways and thereby influences the ionic conductivity. In addition, ion transport in nanostructured heterogeneous solids, in particular glass ceramics formed by the partial crystallization of ion-conducting glasses, also needs to be explore. This will provide a more complete picture of ion transport in both glassy and glass-ceramic solid electrolytes.

Since sulfide glasses are highly sensitive to moisture and oxygen,

mechanical milling, which can eliminate both the risk of explosion due to high vapor pressure of P_2S_5 and the use of high temperatures in case of conventional melt quenching, is a very promising technique for the preparation of these glasses. Furthermore, formation of fine electrolyte powders from mechanical milling is expected to possess better interfacial contacts with the electrode materials, which are one of the key issues to improve battery performance, when compared to the use of the ground glasses. Therefore, it will be worthwhile to pursue this technique for sulfide glasses.

Another possible direction of research is to improve both ionic conductivity (σ_{dc}) and electrochemical stability by studying the mixed glass former effect for sulfide glasses and glass ceramics. In the oxysulfide glasses, the small addition (up to 5%) of Li_xMO_y (where M = Si, P, Ge, B, Al) to $60Li_2S - 40SiS_2$ glass was found to increase σ_{dc} up to 10^{-3} $S.cm^{-1}$ and widen the electrochemical window to more than 10 V [5]. Additionally, by controlled thermal treatment above T_g and below the crystallization temperature (T_c), obtained sulfide-based glass ceramics can exhibit a higher ionic conductivity than the corresponding original glasses [6 – 9]. Recently, Hayashi et al. have reported the highest ionic conductivity of 5.4 x 10^{-3} $S.cm^{-1}$ at room temperature for the glass ceramics $70Li_2S - 29P_2S_5 - 1P_2S_3$ and $98(0.7Li_2S - 0.3P_2S_5) - 2GeS_2$ [8, 9]. Therefore, further investigations on such mixed-glass-former glasses and glass ceramics (with and without dopants) might pave the way for the development of high conductivity solid electrolytes with high stability for application of bulk-type all-solid-state lithium rechargeable batteries.

References

1. S. Adams, J. Swenson, Phys. Chem. Chem. Phys. 4 (2002) 3179.
2. N. Kuwata, J. Kawamura, K. Toribami, T. Hattori, N. Sata, Electrochem. Commun. 6 (2004) 417.
3. N. Kuwata, N. Iwagami, Y. Tanji, Y. Matsuda, J. Kawamura, J. Electrochem. Soc. 157(4) (2010) A521.
4. J. M. Kim, G. B. Park, K. C. Lee, H. Y. Park, S. C. Nam, S. W. Song, J. Power Sources 189 (2009) 211.
5. T. Minami, A. Hayashi, M. Tatsumisago, Solid State Ionics 136-137 (2000) 1015.
6. Y. Seino, K. Takada, B. –C. Kim, L. Zhang, N. Ohta, H. Wada, M. Osada, T. Sasaki, Solid State Ionics 177 (2006) 2601.
7. K. Minami, A. Hayashi, M. Tatsumisago, Solid State Ionics 179 (2008) 1282.
8. A. Hayashi, K. Minami, S. Ujiie, M. Tatsumisago, J. Non-Cryst. Solids 356 (2010) 2670.
9. K. Minami, A. Hayashi, M. Tatsumisago, J. Non-Cryst. Solids 356 (2010) 2666.